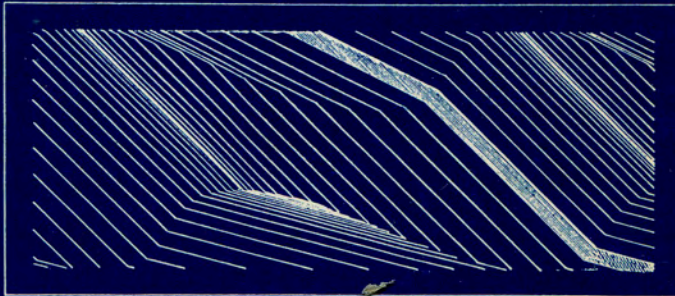


**GEOLOGICA ULTRAIECTINA**

**Mededelingen van het  
Instituut voor Aardwetenschappen der  
Rijksuniversiteit te Utrecht**

**No.60**

**DYNAMICS AND SEDIMENTARY FACIES ANALYSIS  
OF CLASTIC TIDAL DEPOSITS**



**Yang Chang-Shu**

Commy 1

**GEOLOGICA ULTRAIECTINA**

**Mededelingen van het  
Instituut voor Aardwetenschappen der  
Rijksuniversiteit te Utrecht**

**No.60**

**DYNAMICS AND SEDIMENTARY FACIES ANALYSIS  
OF CLASTIC TIDAL DEPOSITS**

PROF. SCHEFFT

TER VERVOLGING VAN DE GRAAD VAN DOCTORAAN  
DE RIJKS-UNIVERSITEIT TE UTRECHT OP GEZAG VAN  
DE RECTOR MAGNIFICUS PROF. DR. J. VAN GINKEL  
VOLGENS BESLUIT VAN HET COLLEGE VAN DEKANEN  
IN HET OPENBAARTE VERHOOR OP MAANDAG  
25 JUNI 1969 DES VORMIDDAGS TE 12.45 UUR

DOOR

Dynamics and sedimentary facies analysis of clastic tidal  
deposits by Yang-Chang Chen, Ph.D. Institute for  
Earth Sciences, Rijksuniversiteit Utrecht, 1969.  
Utrecht, The Netherlands. 128 p., 12 cm. - Met samenvatting  
in het Nederlands. - Met samenvatting in  
Engels. - Met Nederlandse samenvatting.  
ISBN 90-71377-13-9  
CDD 550.527.304123  
1969 - sedimentologie

Uitgeverij: De Persgroep, Utrecht

GEOLGICA ULTRAEICTINA

Mededelingen van het

Instituut voor Aardwetenschappen der

Rijksuniversiteit te Utrecht

No. 60

DYNAMICS AND SEDIMENTARY FACIES ANALYSIS  
OF CLASTIC TIDAL DEPOSITS

CIP-GEGEVENS KONINKLIJKE BIBLIOTHEEK, DEN HAAG

Yang, Chang-Shu

Dynamics and sedimentary facies analysis of clastic tidal  
deposits / Yang Chang-Shu. - [Utrecht : Instituut voor  
Aardwetenschappen der Rijksuniversiteit Utrecht]. -

(Geologica Ultraiectina, ISSN 0072-1026 ; no. 60)

Proefschrift Utrecht. - Met lit. opg. - Met samenvatting  
in het Nederlands.

ISBN 90-71577-13-9

SISO 563 UDC 551.3.051(043.3)

Trefw.: sedimentologie.

drukwerkverzorging : oosterijssel, ablasserdam

**DYNAMICS AND SEDIMENTARY FACIES ANALYSIS  
OF CLASTIC TIDAL DEPOSITS**

**DYNAMIEK EN SEDIMENTAIRE FACIES ANALYSE  
VAN KLASTISCHE GETIJDE AFZETTINGEN**

(met een samenvatting in het Nederlands)

**PROEFSCHRIFT**

**TER VERKRIJGING VAN DE GRAAD VAN DOCTOR AAN  
DE RIJKSUNIVERSITEIT TE UTRECHT OP GEZAG VAN  
DE RECTOR MAGNIFICUS PROF. DR. J.A. VAN GINKEL  
VOLGENS BESLUIT VAN HET COLLEGE VAN DEKANEN  
IN HET OPENBAAR TE VERDEDIGEN OP MAANDAG  
5 JUNI 1989 DES NAMIDDAGS TE 12.45 UUR**

**DOOR**

**CHANGSHU YANG**

**GEBOREN OP 27 JANUARI 1947 TE JIANGSU, CHINA**



Promotor: Prof. Dr. S.D. Nio

Co-promotor: Prof. Dr. J.B. Southard

PROFESCHRIJFT

TER VERKRIJGING VAN DE GRAAD VAN DOCTOR AAN  
DE RIJKSUNIVERSITEIT TE UTRECHT OP GEZAG VAN  
DE RECTOR MAGISTRUS PROF. DR. J.A. VAN GINKEL  
VULGENS BESLIJF VAN HET COLLEGE VAN DEKANS  
IN HET OPENBAAR TE VERBODIGEN OP MAANDAG  
3 JUNI 1889 DES NAMIDDAGS TE 12 1/2 UUR

DOOR

GEBOREN OP 27 JANUARIJ 1857 TE LANGENHOUT

# Contents

Chapter 1	
Introduction and summary .....	1
Chapter 2	
Bagnold's transport equation and its application .....	9
Chapter 3	
Time series analysis of subtidal deposits .....	33
Chapter 4	
Estimates of sand transport in the Oosterschelde tidal basin using current velocity measurements .....	51
Chapter 5	
An ebb delta depositional model - a comparison between the modern Eastern Scheldt Tidal Basin (SW Netherlands) and the Lower Eocene Roda Sandstone in the Southern Pyrenees (Spain) .....	81
Chapter 6	
An Early Holocene tidal delta of the Changjiang River - On the origin of Jianggang Radial Sand Ridges .....	105
Chapter 7	
Tidal sand ridges on the East China Sea shelf .....	117
Chapter 8	
Active, moribund and buried tidal sand ridges in the East China Sea and the Southern Yellow Sea .....	135
Samenvatting (Summary in Dutch) .....	157
Acknowledgements .....	161
Curriculum Vitae .....	162

# Chapter 1

## Introduction and summary

One of the most important dynamic processes in the ocean is that of tidal movement. The tides obtain their energy from the earth's rotation. Most of this energy is received in the major ocean basins, and from there transmitted into shallow waters. It is in these shallow waters that tidal energy is dissipated, in part by eroding and transporting sediments, resulting in very active sedimentary processes in the shelf and coastal areas.

Research in clastic tidal deposits has accumulated large amount of data on tidal processes and their products. In present-day tide-swept shelves large-scale tidal sandbodies with various bedforms has been a subject of extensive research, which mainly focussed on the southern bight of the North Sea (van Veen, 1935; Jones, Kain & Stride, 1965; Houbolt, 1968; Stride, 1970; Caston & Stride, 1970, 1973; McCave, 1971; Terwindt, 1971, 1973; Caston, 1972; Johnson et al., 1981; Kenyon et al., 1981; Langhorne, 1982; McCave & Langhorne, 1982; Nio & Nelson, 1982; Stride, 1982; de Boer, van Gelder & Nio, 1988), the English Channel and the French Atlantic shelf (Berné et al., 1986; Berné et al., 1988; Turcq et al., 1986) and the North American Atlantic shelf (Swift et al., 1972, 1979, 1981; Milliman et al., 1972; Sheridan et al., 1974; Knebel & Folger, 1976, Knebel, 1981; Swift & Field, 1981).

In estuaries and other inshore tidal basins, genesis, geometry, distribution pattern, dynamic behaviour and internal sedimentary structures of tidal bedforms have been studied intensively in the Netherlands (Boersma, 1969; Terwindt, 1970, 1981; de Raaf & Boersma, 1971; Boersma & Terwindt, 1981; Kohsiek & Terwindt, 1981; van den Berg, 1982, 1984, 1987; Terwindt & Brouwer, 1986; de Boer, van Gelder & Nio, 1988), U.K. (Langhorne, 1973; Allen & Friend, 1976; Elliott & Gardiner, 1981), France (Tastet et al., 1986), United States (Boothroyd & Hubbard, 1975; Bokuniewicz, et al., 1977), Canada (Swift et al., 1966; d'Anglejan, 1971; Dalrymple et al., 1975, 1978; Dalrymple, 1984) and other countries. Most of the studies were concentrated in intertidal areas. The subtidal deposits received less attention due to the difficulties in field observations. Preservation potential of subtidal deposits, however, is much higher. As a consequence subtidal deposits will occur more often in the geological record. It is from the detailed study of the subtidal deposits in the construction pits of the Oosterschelde, SW Netherlands that distinct diagnostic criteria for recognizing tide-dominated deposits were developed (Visser, 1980; Siegenthaler, 1982; van den Berg, 1982; Nio et al., 1983; de Mowbray & Visser, 1984; Yang & Nio, 1985).

Research on modern tidal deposits has resulted in a better understanding of tidal process. The characteristic feature of tidal movement is its periodicity, which makes it possible to relate tidal processes and their deposits to a time scale accurate to within a few hours. This has been proved first by the research of subtidal sequences in the Oosterschelde construction pit (Visser, 1980; Allen, 1981). This provides a basis for the quantitative study of the relationship between tidal processes and their cyclic deposits (Allen, 1981; Siegenthaler, 1982; Nio, Siegenthaler & Yang, 1983; Teyssen, 1984; Allen & Homewood, 1984; Yang & Nio, 1985).

The basic approach in establishing and testing such a quantitative process/product relationship is the comparative study of present-day processes and ancient deposits. The sub-recent tidal deposits of the Oosterschelde provide a unique link between modern processes and ancient deposits.

The purpose of this ph.D. study is to analyze quantitatively the dynamics of tidal sedimentation and to apply the results to ancient tidal deposits. Three aspects will be discussed in this study. Part 1 (Chapters 2 and 4) examines two basic problems of fluid and sediment movement. The application of these methods leads to the reconstruction of palaeotidal hydrodynamic conditions from ancient deposits (Part 2, Chapter 3) and the identification, interpretation and prediction of tidal deposits in modern and ancient tidal environments (Part 3, Chapters 4, 5, 6, 7 and 8).

One of the fundamental problems of fluid and sediment movement concerns the fields of bed shear stress and flow velocity in the boundary layer (Chapter 4: Yang, 1986b). In shallow marine environments with small-scale roughness elements (less than 10 cm in height), current velocities can be measured at 100 cm above the sea bed, and a single drag coefficient can be used. In areas with megaripples or sandwaves, however, serious questions arise as to the specification of the velocity field above the bed and the determination of the bed shear stress from boundary-layer velocity distributions. From field measurements and published data, a two-region composite boundary-layer model is used in this study to relate the local spatially averaged bed shear stress to velocity distributions over large bedforms. The two regions are divided at 100 cm above the bed, with an outer-region roughness length of 1.5 cm and an inner-region roughness length of 0.15 cm.

Another basic problem discussed in this study has to do with sediment transport formulas (Chapter 2: Yang, 1986a). The Bagnold sediment transport formula has proved important in tidal marine environments, but some questions need discussion. In the theoretical form, Bagnold's suspended-load transport formula  $q_s = \omega e_s \bar{U}_s (1 - e_b) / W$  and total-load transport formula  $q = \omega (e_b / \tan \alpha + e_s \bar{U}_s (1 - e_b) / W)$  are incorrect from the viewpoint of energy conservation. The correct form should be  $q_s = \omega e_s \bar{U}_s / W$  for suspended-load transport and  $q = \omega (e_b / \tan \alpha + e_s \bar{U}_s / W)$  for total-load transport. As for the practical form, the commonly used Bagnold transport coefficient  $K$  depends on the dimensionless excess shear

stress in the form of a power law. Sediment transport rates predicted from this modified Bagnold total-load transport formula compare very well with those derived from bedform migration measurements. This comparison indicates the difference of the term "bed-load" when used in bedform migration measurements and in sediment transport formulas. To avoid confusion, bed-material transport rate might be a better term for sediment transport rate estimated from bedform migration measurements.

With present knowledge of tidal hydraulics and sediment transport, palaeotidal hydrodynamic conditions can be reconstructed from preserved tidal deposits. Research in this field has advanced along two lines:

1. The estimation of palaeotidal current velocities and/or ranges using sediment transport formulas (J.R.L. Allen, 1981; Siegenthaler, 1982; Nio, Siegenthaler & Yang, 1983; Teysen, 1984) or based on preserved bedform types (P.A. Allen & Homewood, 1984). For ancient deposits the integral of the sediment transport rate over the dominant tidal semi-cycle is difficult to estimate due to unknown current-variation pattern, unknown integration limits and bedform lag effects. The total sediment transport, however, depends mainly on the peak velocities and is not very sensitive to the velocity variation over the whole dominant current phase. An empirical value for the integral of the velocity variation is therefore used in this study to derive the peak bed-material transport rate from bundle measurements (Chapter 3: Yang & Nio, 1985).

2. The resolution of palaeotidal movements into different periodic variations by means of time-series analysis (Chapter 3: Yang & Nio, 1985). This involves (1) Fourier analysis to test the periodicity of the bundle-thickness sequence and to estimate the periods and the phases of the most important periodic components, and (2) filtering analysis to resolve the bundle-thickness sequence into different components (i.e., diurnal components, random variations, neap/spring components and longer-period variations) and also to estimate the relative importance (e.g., amplitude) of each.

From these analyses useful information can be derived as to the palaeotidal hydrodynamic conditions (such as palaeotidal ranges, flow velocities, palaeotidal components and tidal character) and nontidal processes (such as the strength, duration, frequency and possible direction of storms). This opens up new prospects for the quantitative reconstruction of palaeotidal environments, in contrast to the traditional qualitative concept of high-energy or low-energy environments.

The above discussion suggests that the methods presented in this study may have wide application in modern and ancient tidal environments. The significance of this quantitative study is twofold. It provides not only a new means of reconstructing the palaeotidal processes and environments from a sedimentological viewpoint, but also a new way to identify, interpret or predict tidal deposits in terms of tidal hydrodynamics.



Chapter 4 (Yang, 1986b) discusses the prediction of sediment movement in modern tidal environments. Tidal current measurements in the Oosterschelde have been used for regional description of sand movement and estimation of sand transport. The calculations indicate very active sand movement in the present-day Oosterschelde tidal basin. Local sediment circulation may develop around shoals. Channel floor erosion may occur in parting areas of sediment transport. The net sediment transport is mainly in the ebb direction. The long-term sand budget indicates rapid adjustment of the tidal basin channel/shoal system to variations in the tidal prism.

In Chapter 5 (Yang & Nio, in press), the distinctive succession, external geometry, internal structural organization and sequential up-building of an ebb tidal delta and associated estuary channel sand bodies in the Lower Eocene Roda Sandstone in southern Pyrenees of Spain are documented and interpreted in terms of the comparison between preserved sequences of this fossil example and the sedimentary processes in the present-day estuary and ebb delta environment of the Oosterschelde mesotidal basin, SW Netherlands. Based on similarities and differences between these two ebb deltas, a depositional model has been constructed for the ebb delta and its associated estuary channel system. This consists mainly of: prograding terminal lobes at the delta front, extensive ebb-dominated subtidal shoals and wide, shallow ebb channels on the delta platform, as well as extensive intertidal shoals and relatively deep, actively migrating tidal channels in estuary basin. The common occurrence of submarine abandonment surfaces and erosional surfaces is an important feature of ebb delta and estuary channel sequences. Their sequential build-up is critically dependent upon the influences of marine transgressions and the tectonic movements of the tidal basin.

Chapter 6 (Yang, 1985) describes an example with strong tidal influence, i.e., the Jianggang Radial Sand Ridges in southern Yellow Sea (off Jiangsu coast). It was proposed that these gigantic sand ridges were formed by longshore currents, which brought sediments from the abandoned Old Huanghe River Delta in the north and the Recent Changjiang River Delta in the south. Our investigations, however, suggest that the Jianggang Radial Sand Ridges represents an early Holocene tidal delta of the Changjiang River characterized by huge radial tidal sand ridges. The major hydrodynamic factor responsible for the development of Jianggang Radial Sand Ridges is tidal currents. Because of the geomorphological boundary conditions in this area, the progressive tidal wave from the East China Sea and the amphidromic tidal wave from the southern Yellow Sea met off Jianggang coast, where the two sets of tidal waves had a phase difference of about one ebb-flood period and, therefore, could interfere constructively with each other, causing the increase of tidal ranges and forming the radial flow field of tidal currents, which controlled the radial distribution pattern of the tidal sand ridges.

An example of moribund tidal sand ridges is discussed in Chapter 7 (Yang & Sun, 1988). Widespread investigations have revealed for the first time the presence of these huge



tidal sand ridges on the shelf of the East China Sea. They are 10-60 km long, 2-5 km wide and 5-20 m high with a spacing of 8-14 km. They extend ESE-WNW (about  $120^{\circ}$ - $300^{\circ}$ ), and have asymmetrical profiles in transverse sections with steeper slopes facing SSW. They mainly consist of well-sorted fine sands with abundant debris of intertidal to shallow water marine shells. The shallow seismic profiles show an unconformity between the sand ridges and the underlying strata, and the very low-angle inclined layers within the sand ridges. The shallow marine fossils and the moribund morphology suggest that the tidal sand ridges on the East China Sea shelf probably developed during the post-glacial transgression when water depths were shallower and tidal currents were stronger than those of the present-day. As the sea level rose and the tidal currents became weaker, the sand ridges gradually ceased growing and became "relict" sand bodies on the shelf of the East China Sea.

Chapter 8 (Yang, in press) is a follow-up of the previous studies in Chapters 6 and 7. New shallow seismic profiles with a penetration of about 100 m below sea bottom and shallow borehole data have revealed not only the details of the active and moribund Holocene tidal sand ridges, but also the presence, characteristics and sequential development of buried Pleistocene sand ridges. They consist of relatively clean, well-sorted sands with rather uniform sequences. Their microfossil assemblage exhibits a high diversity including both euryhaline and stenohaline species. They are huge elongated sandbodies (several km wide, 10 to 60 km long and up to 20 m thick) and occur in groups with a spacing of several to more than 10 km. Normally they extend in the direction of tidal currents. The internal structures are characterized by very low angle inclined layers.

These tidal sand ridges were formed in estuary and shallow shelf environments, where strong tidal currents reworked, transported and redeposited large amount of relict sands from older delta and fluvial sediments. The development of tidal sand ridges in estuary-mouth areas is accompanied by a net sand transport from the shelf into the estuary. The evolution of tidal sand ridges is closely related to transgressions. Active tidal sand ridges are formed during a relative sea-level rise. They show distinct morphology and active migrations in a lateral as well as in a landward direction. They are generally in equilibrium with present-day tidal processes and their distribution patterns are related to the flow field of tidal currents. As the sea level rises further, these tidal sand ridges become moribund sandbodies with less distinct morphology. Their top surfaces are covered by a thin calcareous-rich layer with high contents of marine fossils, reflecting a submarine hiatus condition on the shelf during the high-stand period. During the subsequent steady fall of sea level, tidal sand ridges are often buried by fine-grained shelf and prodelta sediments. They have, therefore, a good chance to be preserved in stratigraphic records.

Above-discussed features have important implications for the subsurface recognition of fossil tidal sand ridges, for the reconstruction of the regional palaeogeography and transgressional history and for the prediction of potential reservoir sandstones.

## REFERENCES

- Allen, J.R.L. (1981) Paleotidal speeds and ranges estimated from cross-bedding sets with mud drapes. *Nature*, 293: 394-396.
- Allen, J.R.L. & Friend, P.F. (1976) Changes in intertidal dunes during two springneap cycles, Lifeboat Station Bank, Wells-next-the-Sea, Norfolk, England. *Sedimentology*, 23: 329-346.
- Allen, P.A. & Homewood, P. (1984) Evolution and mechanics of a Miocene tidal sandwave. *Sedimentology*, 31: 63-81.
- Berné, S., Augustin, J.M., Braud, F., Chene, G. & Walker, P. (1986) Cartographie et interprétation de la dynamique sédimentaire des plates-formes continentales: améliorations de la technique d'observation par sonar latéral. *Bull. Soc. géol. France*, 8(2): 437-446.
- Berné, S., Auffret, J.P. & Walker, P. (1988) Internal structure of subtidal sandwaves revealed by high-resolution seismic reflection. *Sedimentology*, 35: 5-20.
- Boersma, J.R. (1969) Internal structures of some tidal megaripples on a shoal in the Westerschelde estuary, the Netherlands. *Geol. Mijnbouw*, 48: 409-414.
- Boersma, J.R. & Terwindt, J.H.J. (1981) Neap-spring tide sequences of intertidal shoal deposits in a mesotidal estuary. *Sedimentology*, 28: 151-170.
- Bokuniewicz, H.J., Gordon, R.B. & Kastens, K.A. (1977) Form and migration of sand waves in a large estuary, Long Island Sound. *Mar. Geol.*, 24: 185-199.
- Boothroyd, J.C. and Hubbard, D.K. (1975) Genesis of bedforms in mesotidal estuaries. In: Cronin, L.E. (Ed.): *Estuarine Research*. Academic Press, New York, Vol.II, pp.217-234.
- Caston, V.N.D. (1972) Linear sand banks in the southern North Sea. *Sedimentology*, 18: 63-78.
- Caston, V.N.D. & Stride, A.H. (1970) Tidal sand movement between some linear sand banks in the North Sea off northeast Norfolk. *Mar. Geol.*, 9: M38-M42.
- Caston, V.N.D. & Stride, A.H. (1973) Influence of older relief on the location of sand waves in a part of the southern North Sea. *Estuarine Coastal Mar. Sci.*, 1: 379-386.
- Dalrymple, R.W. (1984) Morphology and internal structure of sandwaves in the Bay of Fundy. *Sedimentology*, 31: 365-382.
- Dalrymple, R.W., Knight, R.J. & Middleton, G.V. (1975) Intertidal sand bars in Gobequid Bay (Bay of Fundy). In: L.E. Cronin (Ed.): *Estuarine Research*. Academic Press, New York, Vol.II, pp.293-307.
- Dalrymple, R.W., Knight, R.J. & Lambiase, J.J. (1978) Bedforms and their hydraulic stability relationships in a tidal environment, Bay of Fundy, Canada. *Nature*, 275: 5676, 100-104.
- D'Anglejan, B.F. (1971) Submarine sand dunes in the St. Lawrence Estuary. *Can. J. Earth Sci.*, 8 (11): 1480-1486.
- de Boer, P.L., van Gelder, A. & Nio, S.D. (Eds) (1988) *Tide-influenced sedimentary environments and facies*. D. Reidel Publishing Company, 530 pp.
- de Mowbray, T. & Visser, M.J. (1984) Reactivation surfaces in subtidal channel deposits, Oosterschelde, southwest Netherlands. *J. Sediment. Petrol.*, 54: 811-824.
- de Raaf, J.F.M. & Boersma, J.R. (1971) Tidal deposits and their sedimentary structures. *Geol. Mijnbouw*, 59: 479-504.
- Elliott, T. & Gardiner, A.R. (1981) Ripple, megaripple and sandwave bedforms in the macrotidal Loughor Estuary, South Wales, U.K. In: S.D. Nio, R.T.E. Schuttenhelm & Tj C.E. van Weering (Eds): *Holocene marine sedimentation in the North Sea basin*. I.A.S. Spec. Publ. 5, Blackwell, Oxford, pp.51-64.
- Houbolt, J.J.H.C. (1968) Recent sediments in the southern Bight of the North Sea. *Geol. Mijnbouw*, 47: 245-273.
- Johnson, M.A., Stride, A.H., Belderson, R.H. & Kenyon, N.H. (1981) Predicted sand wave formation and decay on a large offshore tidal-current sand sheet. In: S.D. Nio, R.T.E. Schuttenhelm & Tj C.E. van Weering

- (Eds): Holocene marine sedimentation in the North Sea basin. I.A.S. Spec. Publ. 5, Blackwell, Oxford, pp.247-256.
- Jones, N.S., Kain, J.M. & Stride, A.H. (1965) The movement of sandwaves on Warts Bank, Isle of Man. *Mar. Geol.*, 3: 329-336.
- Kenyon, N.H., Belderson, R.H., Stride, A.H. & Johnson, M.A. (1981) Offshore tidal sand-banks as indicators of net sand transport and as potential deposits. In: S.D. Nio, R.T.E. Schuttenhelm & Tj C.E. van Weering (Eds): Holocene marine sedimentation in the North Sea basin. I.A.S. Spec. Publ. 5, Blackwell, Oxford, pp.257-268.
- Knebel, H.J. & Folger, D.W. (1976) Large sand waves on the Atlantic outer continental shelf around Wilmington Canyon off eastern United States. *Mar. Geol.*, 22: M7-M15.
- Knebel, H.J. (1981) Processes controlling the characteristics of the surficial sand sheet, U.S. Atlantic outer continental shelf. *Mar. Geol.*, 42: 349-368.
- Kohsiek, L.H.M. & Terwindt, J.H.J. (1981) Characteristics of foreset and topset bedding in megaripples related to hydrodynamic conditions on an intertidal shoal. In: S.D. Nio, R.T.E. Schuttenhelm & Tj C.E. van Weering (Eds): Holocene marine sedimentation in the North Sea basin. I.A.S. Spec. Publ. 5, Blackwell, Oxford, pp.27-37.
- Langhorne, D.N. (1973) A sandwave field in the Outer Thames Estuary. *Mar. Geol.*, 14: 129-143.
- Langhorne, D.N. (1982) A study of the dynamics of a marine sandwave. *Sedimentology*, 29: 571-594.
- McCave, I.N. (1971) Sand waves in the North Sea off the coast of Holland. *Mar. Geol.*, 10: 199-225.
- McCave, I.N. & Langhorne, D.N. (1982) Sand waves and sediment transport around the end of a tidal sand bank. *Sedimentology*, 29: 95-110.
- Milliman, J.D., Pilkey, O.H. & Ross, D.A. (1972) Sediments of the continental margin off the eastern United States. *Geol. Soc. Am. Bull.*, 83: 1315-1334.
- Nio, S.D. & Nelson, C.H. (1982) The North Sea and northeastern Bering Sea: a comparative study of the occurrence and geometry of sand bodies of two shallow epicontinental shelves. In: C.H. Nelson & S.D. Nio (Eds): The northeastern Bering shelf: new perspectives of epicontinental shelf processes and deposition products. *Geol. Mijnbouw*, 61: 105-114.
- Nio, S.D., Siegenthaler, C. & Yang, C.S. (1983) Megaripple cross-bedding as a tool for the reconstruction of the palaeo-hydraulics in a Holocene subtidal environment, S.W. Netherlands. *Geol. Mijnbouw* 62: 499-510.
- Sheridan, R.E., Dill, Jr.C.E. & Kraft, J.C. (1974) Holocene sedimentary environment of the Atlantic inner shelf off Delaware. *Geol. Soc. Am. Bull.*, 85: 1319-1328.
- Siegenthaler, C. (1982) Tidal cross-strata and the sediment transport rate problem: a geologist's approach. *Mar. Geol.*, 45: 227-240.
- Stride, A.H. (1970) Shape and size trends for sand waves in a depositional zone of the North Sea. *Geol. Mag.*, 107: 469-477.
- Stride, A.H. (Ed.) (1982) Offshore tidal sands: processes and deposits. Chapman and Hall, 222 pp.
- Swift, D.J.P., Cok, A.E. & Lyall, A.K. (1966) A subtidal sand body in the Minas Channel, eastern Bay of Fundy. *Marit. Sediments*, 2: 174-180.
- Swift, D.J.P., Kofoed, J.W., Saulsbury, F.P. & Sears, P. (1972) Holocene evolution of the shelf surface, south and central Atlantic shelf of North America. In: D.J.P. Swift, D.B. Duane & O.H. Pilkey (Eds): Shelf sediment transport: process and pattern. Dowden, Hutchinson & Ross, Stroudsburg, pp.499-574.
- Swift, D.J.P., Freeland, G.L. and Young, R.A. (1979) Time and space distribution of megaripples and associated bedforms, Middle Atlantic Bight, North American Atlantic Shelf. *Sedimentology*, 26: 389-406.
- Swift, D.J.P. & Field, M.E. (1981) Evolution of a classic sand ridge field: Maryland sector, North American inner shelf. *Sedimentology*, 28: 461-482.
- Swift, D.J.P., Young, R.A., Clarke, T.L., Vincent, C.E., Niedoroda, A. & Lesht, B. (1981) Sediment transport in the Middle Atlantic Bight of North America: synopsis of recent observations. In: S.D. Nio, R.T.E.

- Schuttenhelm & Tj C.E. van Weering (Eds): Holocene marine sedimentation in the North Sea basin. I.A.S. Spec. Publ. 5, Blackwell, Oxford, pp.361-383.
- Tastet, J.P., Fenies, H. & Allen, G.P. (1986) Facies, sequences et géométrie d'une barre tidale estuarienne: le banc de trompeloup dans l'estuaire de la Gironde. *Bull. Inst. Géol. Bassin d'Aquitaine*, 39: 165-184.
- Terwindt, J.H.J. (1970) Observation on submerged sand ripples with heights ranging from 30 to 200 cm occurring in tidal channels of S.W. Netherlands. *Geol. Mijnbouw*, 49: 489-501.
- Terwindt, J.H.J. (1971) Sand waves in the Southern Bight of the North Sea. *Mar. Geol.*, 10: 51-67.
- Terwindt, J.H.J. (1973) Sand movement in the in- and offshore tidal area of the S.W. part of the Netherlands. *Geol. Mijnbouw*, 52: 69-77.
- Terwindt, J.H.J. (1981) Origin and sequences of sedimentary structures in inshore mesotidal deposits of the North Sea. In: S.D. Nio, R.T.E. Schuttenhelm & Tj C.E. van Weering (Eds): Holocene marine sedimentation in the North Sea basin. I.A.S. Spec. Publ. 5, Blackwell, Oxford, pp.4-26.
- Terwindt, J.H.J. & Brouwer, M.J.N. (1986) The behaviour of intertidal sandwaves during neap-spring tide cycles and the relevance for palaeoflow reconstructions. *Sedimentology*, 33: 1-31.
- Teysse, T. (1984) Physical model and Fortran IV program to estimate paleotidal flow velocities from features of sand waves. *Computers & Geosciences*, 10(2-3): 237-244.
- Turcq, B., Cirac, P., Berné, S. & Weber, O. (1986) Caractéristiques des environnements sédimentaires de la plate-forme continentale nord-Aquitaine en relation avec les processus hydrodynamiques actuels. *Bull. Inst. Géol. Bassin d'Aquitaine*, 39: 149-164.
- Van den Berg, J.H. (1982) Migration of large-scale bedforms and preservation of crossbedded sets in highly accretional parts of tidal channels in the Oosterschelde, SW Netherlands. *Geol. Mijnbouw*, 61: 253-263.
- Van den Berg, J.H. (1984) Morphological changes of the ebb-tidal delta of the Oosterschelde during recent decades. *Geol. Mijnbouw*, 63: 363-375.
- Van den Berg, J.H. (1987) Bedform migration and bed-load transport in some rivers and tidal environments. *Sedimentology*, 34: 681-698.
- Van Veen, J. (1935) Sand waves in the North Sea. *Hydrogr. Rev.*, 12: 21-29.
- Visser, M.J. (1980) Neap-spring cycles reflected in Holocene subtidal large-scale bedform deposits: a preliminary note. *Geology*, 8: 543-546.
- Yang, C.S. (1985) On the origin of Jianggang Radial Sand Ridges in Yellow Sea. *Marine Geology & Quaternary Geology*, 5(3): 35-44 (in Chinese).
- Yang, C.S. (1986a) On Bagnold's sediment transport equation in tidal marine environments and the practical definition of bedload. *Sedimentology*, 33: 465-486.
- Yang, C.S. (1986b) Estimates of sand transport in the Oosterschelde tidal basin using current velocity measurements. *Marine Geology*, 72: 143-170.
- Yang, C.S. (in press) Active, Moribund and buried tidal sand ridges in the East China Sea and the Southern Yellow Sea. *Marine Geology*.
- Yang, C.S. & Nio, S.D. (1985) The estimation of paleohydrodynamic processes from subtidal deposits using time series analysis methods. *Sedimentology*, 32: 41-57.
- Yang, C.S. & Nio, S.D. (in press) An ebb-tide delta depositional model, a comparison between the modern eastern Scheldt Tidal Basin (SW Netherlands) and the lower Eocene Roda Sandstone in the southern Pyrenees (Spain). *Sedimentary Geology*.
- Yang, C.S. & Sun, J.S. (1988) Tidal sand ridges on the East China Sea shelf. In: P.L. de Boer, A. van Gelder and S.D. Nio (Eds): *Tide-Influenced Sedimentary Environments and Facies*. D. Reidel Publishing Company, pp.23-38.

## Chapter 2

### Bagnold's transport equation and its application

This chapter is published as:

Yang, C.S., 1986. On Bagnold's sediment transport equation in tidal marine environments and the practical definition of bedload. *Sedimentology*, 33: 465-486.



## On Bagnold's sediment transport equation in tidal marine environments and the practical definition of bedload

CHANG-SHU YANG\*

*Comparative Sedimentology Division, Institute of Earth Sciences, University of Utrecht, The Netherlands*

### ABSTRACT

Bagnold's sediment transport equation has proved to be important in studying tidal marine environments. This paper discusses three problems concerning Bagnold's transport equation and its practical application:

(1) Bagnold's suspended-load transport equation  $q_s = \omega \frac{e_s U_s}{W} (1 - e_b)$  and the total-load transport equation  $q = \left( \frac{e_b}{\tan \alpha} + \frac{e_s U_s}{W} (1 - e_b) \right) \omega$  with  $e_s (1 - e_b) = 0.01$  are incorrect from the viewpoint of energy conservation. In these equations the energy loss due to bedload transport has been counted twice. The correct form should be  $q_s = \omega \frac{e_s U_s}{W}$  for suspended-load transport and  $q = \left( \frac{e_b}{\tan \alpha} + \frac{e_s U_s}{W} \right) \omega$  for total-load transport with  $e_s = 0.016$ .

(2) The commonly used Bagnold's transport coefficient  $K$  varies as a non-linear function of the dimensionless excess shear stress, which can be represented best by the power law  $K = A (\tau_o/\tau_c - 1)^B$ , where the coefficient  $A$  and exponent  $B$  depend on sediment grain size  $D$ . The empirical values of  $A$  and  $B$  for fine to medium grain sands are determined using Guy *et al.*'s (1966) flume-experiment data.

(3) The sediment transport rates predicted from this equation are compared with bedform migration measurements in the flume and the field. This comparison shows that the sediment transport rates measured from bedform migrations are higher than the predicted bedload transport rates, but comparable to the calculated total-load (bedload plus intermittent suspended-load) transport rates. This indicates that bedform migration involves both bedload and intermittent suspended-load transport. As a logical conclusion, bedform migration data should be compared with Bagnold's total-load transport equation rather than with his bedload transport equation. In this respect the term 'bed material' might be more appropriate than the term 'bedload' for estimating sediment transport rate from bedform migration data.

The sediment transport rates predicted from this modified Bagnold transport equation are in good agreement with field measurements of bedform migration rates in four individual tidal marine environments, which cover a wide range of sediment grain size, flow velocity and bedform conditions (ranging from small ripples, megaripples to sandwaves).

### INTRODUCTION

The sediment transport problem is of great importance in sedimentology and marine geology. Numerous different theoretical and semi-empirical expressions have been developed for sediment transport rates (e.g. Einstein, 1950; Bagnold, 1963; Yalin, 1963; Engelund & Hansen, 1967; Ackers & White, 1973). A few

attempts have been made to test the applicability of such formulae in tidal marine environments (Kachel & Sternberg, 1971; Gadd, Lavelle & Swift, 1978; Heathershaw & Hammond, 1979; Heathershaw, 1981; Langhorne, 1981; Siegenthaler, 1982). All these efforts show that the sediment transport rates predicted by different sediment transport equations may differ from each other by as much as one order of magnitude. In view of this, the choice of the

\*Permanent address: Ministry of Geology and Mineral Resources, Marine Geological Survey, 526 Yan An Road West, Shanghai, China.



appropriate sediment transport equation for tidal marine environments is still an open question. The aim of this paper is to show how one particular sediment transport equation, that of Bagnold, can be used in practice in tidal environments.

Bagnold's transport equation is based on the considerations of energy balance and of mechanical equilibrium. However, in the theoretical derivation of this equation, some confusion remains concerning the efficiencies used by Bagnold (1966). The clarification of such confusion by Pantin (1979) is an essential step forward towards its practical use.

Concerning the practical utilization of Bagnold's transport equation in tidal marine environments, there are two basic problems. (1) While the basis of Bagnold's sediment transport equation is derived from purely theoretical considerations, the expression still involves four dimensionless coefficients whose values must be determined experimentally. (2) When the predicted sediment transport rates are compared with results from flume and field measurements, it is difficult to distinguish between 'bed-load' and 'total-load'. Where sediment transport rates are calculated from bedform migration rates, there is the further complication that both 'bed-load' and 'suspended-load' are present in the cross-bedded sands.

In this paper, the correct form of Bagnold's transport equation is discussed and a practical version of Bagnold's formula is developed which allows a comparison of predicted sediment transport rates with those measured from bedform migration rates.

## THE CORRECT FORM OF BAGNOLD'S SEDIMENT TRANSPORT EQUATION

Bagnold's sediment transport equation is based on the principle of energy conservation (Bagnold, 1966, 1968). Regarding the flowing fluid as a 'transporting machine', the energy conservation law can be written as:

$$\begin{aligned} \text{rate of doing work on the sediment} \\ = \text{available power} \times \text{efficiency.} \quad (1) \end{aligned}$$

The sediment load is transported by a variety of different mechanisms. As a first approximation, Bagnold (1966) divided the load into bedload and suspended-load. The bedload immersed weight is balanced by a momentum transfer from solid/solid collisions, while the immersed weight of the suspended load is balanced by an upward momentum transfer from fluid turbulence. The available flow power  $\omega$

constitutes the single common supply of energy to both transport mechanisms. For bedload transport, the bedload work rate is  $q_b \tan \alpha$ , and the bedload transport rate is given by (Bagnold, 1966):

$$q_b = \frac{e_b}{\tan \alpha} \omega \quad (2)$$

where  $q_b$  is the bedload transport rate expressed in terms of immersed weight of load,  $e_b$  is bedload transport efficiency,  $\tan \alpha$  is the coefficient of dynamic bedload friction,  $\omega$  is the total available flow power, expressed in terms of boundary shear stress  $\tau_o$  and mean flow velocity  $\bar{U}$  as:

$$\omega = \tau_o \bar{U} \quad (3)$$

For suspended-load transport, the suspended-load work rate is  $q_s \frac{W}{\bar{U}_s}$ , and the suspended-load transport rate is given by:

$$q_s = \omega \frac{e_s \bar{U}_s}{W} (1 - e_b) \quad (4)$$

where  $q_s$  is the suspended-load transport rate also expressed in terms of immersed weight,  $e_s$  is the suspension efficiency,  $W$  is the terminal fall velocity of suspended solids,  $\bar{U}_s$  is the mean transport velocity of suspended solids (Bagnold, 1966).

Adding equations (2) and (4), Bagnold's (1966) expression for the total transport rate  $q$  is:

$$q = q_b + q_s = \left( \frac{e_b}{\tan \alpha} + \frac{e_s \bar{U}_s}{W} (1 - e_b) \right) \omega. \quad (5)$$

This expression has a clear physical meaning in terms of the sediment transporting power of the fluid. However, as discussed by Pantin (1979), there is some confusion in equations concerning the efficiencies used by Bagnold (1966).

As an equivalent form, the principle of energy conservation can be expressed as:

$$\begin{aligned} \text{available power} \\ = \text{rate of doing work} + \text{unutilized power.} \quad (6) \end{aligned}$$

Since sediment transport consists of two mechanisms (the bedload transport and the suspended-load transport), the total available flow power  $\omega$  can be divided into two parts. The part  $(\omega_1 + \omega_2)$  is available for bedload transport, where  $\omega_1$  is the effective power used in bedload transport and  $\omega_2$  is the ineffective power dissipation in bedload transport. The remaining part  $(\omega_3 + \omega_4)$  is available for suspended-load transport, where  $\omega_3$  is the effective power used in

suspended-load transport and  $\omega_4$  is the ineffective power dissipation other than  $\omega_2$  (Pantin, 1979).

Bagnold's bedload transport efficiency  $e_b$  can be defined as  $\omega_1/\omega$ . The two factors of  $e_b$  as used by Bagnold (1966), i.e.  $e_c$  and  $e_g$ , can be defined as  $(\omega_1 + \omega_2)/\omega$  and  $\omega_1/(\omega_1 + \omega_2)$  respectively. The suspended-load transport efficiency  $e_s$  can be defined in the same way. However, Pantin (1979) found that  $e_s$  of Bagnold (1966) had two meanings. In fact Bagnold (1966) used  $e_s$  in three different senses.  $e_s$  was first introduced into his suspended-load and total-load transport equations as  $\omega_3/(\omega_2 + \omega_3 + \omega_4)$  (Bagnold, 1966, equations 8 and 9; presented in this paper as equations 4 and 5). Then  $e_s$  was assigned the value of 0.016 in the sense of  $\omega_3/\omega$  (Bagnold, 1966, equation 17). Finally this value was reduced by the factor 2/3 in the sense of  $\omega_3/(\omega_3 + \omega_4)$  (Bagnold, 1966, pp. 1-14 and equation 20). This suggests that there is a contradiction in Bagnold's suspended-load and total-load transport equation which influences the energy balance, because the energy loss due to bedload transport has been counted twice. Since the suspension efficiency  $e_s$  of 0.016 already includes the energy loss due to bedload transport, it should not be reduced again by the factor 2/3 on account of the same energy loss.

Therefore Bagnold's suspended-load transport formula (equation 4) and total-load formula (equation 5) with  $e_s(1 - e_b) = 0.01$  are incorrect from the viewpoint of energy conservation. The correct form of Bagnold's suspended-load transport formula is:

$$q_s = \omega \frac{e_s \bar{U}_s}{W} \quad (7)$$

and the correct form of Bagnold's total-load transport formula is:

$$q = \left( \frac{e_b}{\tan \alpha} + \frac{e_s \bar{U}_s}{W} \right) \omega \quad (8)$$

where  $e_s$  has the value of 0.016 as derived by Bagnold (1966) in the sense of  $\omega_3/\omega$ .

### THE COEFFICIENT $K$ OF BAGNOLD'S SEDIMENT TRANSPORT EQUATION

Bagnold's total-load transport equation (and its correct form in equation 8) is derived from purely theoretical principles. As Bagnold (1966) stated: '... its derivation seems straight forward and logical. It involves neither assumption nor approximation, and it is applicable both to turbulent and to laminar fluid flow'.

However, for the practical use of these equations, it is necessary to assign values to the coefficients  $e_b$ ,  $\tan \alpha$ ,  $e_s$  and  $\bar{U}_s/W$ . These four dimensionless coefficients are all functions of the fluid-solid two-phase motion system, but they cannot be theoretically determined. The only way to determine the values of these four coefficients is by experiment.

Bagnold (1966) suggested that the theoretical suspension efficiency  $e_s$  has the universally constant value 0.016 for fully developed suspension by turbulent shear flow. This is based on a theoretical calculation of the maximum asymmetry of turbulence available to suspended sediment and the actual measurements of turbulence near the boundary. A similar result was derived by Irmay (1960) using an entirely different approach along the line of Reynolds' (1895) treatment of the Navier-Stokes equations. Leeder's (1983) test of Bagnold's dynamic suspension theory from actual turbulence data broadly confirmed Bagnold's results. Substituting 0.016 for the coefficient  $e_s$ , equation (8) becomes:

$$q = \omega \left( \frac{e_b}{\tan \alpha} + 0.016 \frac{\bar{U}_s}{W} \right) \quad (9)$$

which gives a suspended-load transport rate of about 50% larger than in the previous incorrect equations. However, it is worth noting that Leeder's (1983) test suggests an upward-directed residual Reynolds stress for supporting suspended-load which is about 0.3  $\tau_0$ . This is equivalent to an  $e_s$  of 0.01 (in the sense of  $\omega_3/\omega$ ), giving a similar suspended-load transport rate as in previous incorrect equations (an  $e_s$  of 0.016 reduced by a factor of 2/3). Although Leeder's result is valid only for transport over flat beds, the comparison with experimental data (Bagnold, 1966) also suggests that 0.01 seems to be a better estimate of  $e_s$  than Bagnold's estimate of 0.016. Bagnold had already noticed this difference and reduced 0.016 by a factor of 2/3 on account of the energy loss in bedload transport. However, this difference is not due to such an energy loss. It may simply reflect the fact that Bagnold's estimation of  $e_s$  was derived from the theoretical maximum asymmetry of turbulence, and therefore is larger than the actual value of  $e_s$ .

The ratio  $e_b/\tan \alpha$  was assigned the value of 0.17 in the case of mean sand grain size  $D < 0.5$  mm and dimensionless shear stress  $\theta < 1$  (Bagnold, 1966). For  $D > 0.5$  mm and for  $\theta > 1$ , Bagnold (1966) gave special graphs for determining the bedload transport efficiency  $e_b$  and the dynamic bedload friction coefficient  $\tan \alpha$ .

A further simplification can be made by substituting the average velocity  $\bar{U}_s$  of the suspended solids with the average velocity  $\bar{U}$  of the flow. The effective mean fall velocity is defined as  $\bar{W} = \Sigma P W_p$ , in which  $P$  is the percentage of any individual constituent grade within the sand grain size distribution, whose fall velocity is  $W_p$ .  $\bar{W}$  can be calculated from the actual grain size distribution of the suspended material (Bagnold, 1966).

However, some problems still remain:

(1) Yalin (1972) concluded from a theoretical analysis of Bagnold's total-load transport equation that it would not hold for flow stages (defined as  $U_* / U_{*c}$  by Francis, 1973 and Abbott & Francis, 1977) which have the values of  $\theta$  that are less than 0.4.

(2) Although the four coefficients ( $e_b, \tan \alpha, e_s$  and  $\bar{U}/W$ ) have been assigned empirical values, each of them is still evaluated from experimental data with some assumptions or approximations. Therefore as a different approach, it would be equally valid, but much more simple, to combine all the coefficients in Bagnold's formula into one single coefficient  $K$  and evaluate  $K$  directly by flume-experiment data or field measurements. In terms of  $K$ , Bagnold's transport equation can be expressed as:

$$q_b = K_b \omega \tag{10}$$

where  $K_b = e_b / \tan \alpha$  for bedload transport, and

$$q = K \omega \tag{11}$$

where  $K = e_b / \tan \alpha + e_s \bar{U}/W$  for total-load transport.

In marine geological investigations, the immersed weight transport rate  $q$  is commonly substituted by the dry mass transport rate  $j$  where  $j = \frac{\rho_s}{(\rho_s - \rho)} q$ . Also, the flow power  $\omega$  is commonly replaced by the power expended against bottom friction, i.e.  $\omega_t$ , which can be expressed as:

$$\omega_t = \rho U_*^3 \quad (\text{Inman, 1963}). \tag{12}$$

Thus equation (10) becomes:

$$\frac{\rho_s - \rho}{\rho_s} g j_b = K_b' \rho U_*^3 \tag{13}$$

and equation (11) becomes:

$$\frac{\rho_s - \rho}{\rho_s} g j = K' \rho U_*^3 \tag{14}$$

where  $K_b'$  and  $K'$  differ from  $K_b$  and  $K$  by a factor of  $C_D^{1/2}$  ( $C_D$  being the drag coefficient):

$$K_b' = K_b / C_D^{1/2} \text{ and } K' = K / C_D^{1/2}. \tag{15}$$

From theoretical considerations, Bagnold (1973) pointed out that, in the case of sands transported by water, as the flow stage is increased, the coefficient  $K_b$  and  $K$  rise from zero at the threshold of sediment movement to a maximum constant value at high flow stages. Therefore, in water there is a lower, transitional range of flow stage in which the transport rate increases rapidly (due to an increase of the coefficient  $K_b$  and  $K$ ) to an ultimate near-proportionality to the flow power (due to the constant coefficient  $K_b$  and  $K$ ). Ripples and megaripples appear to be confined to the lower, transitional flow stage (Fig. 1). Since most practical sediment transport problems are related to bedform migrations, the values of  $K_b$  and  $K$  being considered here are not constant.

However, Bagnold does not give a function to enable the increasing values of  $K_b$  or  $K$  to be calculated within this lower, transitional flow stage. We must

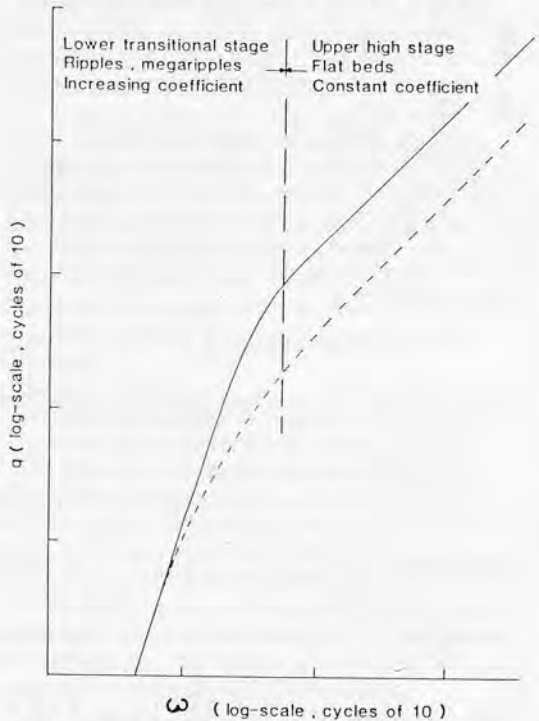


Fig. 1. General relation of transport rate to flow power. —: bedload transport rate  $q_b$  in water; —: total-load transport rate  $q$  in water. In lower transitional stage, the transport rate increases rapidly (due to an increase of the coefficient  $K_b$  and  $K$ ) to an ultimate near-proportionality to the power (due to the constant coefficient  $K_b$  and  $K$ ). Ripples and megaripples appear to be confined to this lower transitional stage (modified after Bagnold, 1968).

therefore consider this problem in more detail. Since both the coefficients  $K_b$  and  $K$  show the same tendency of variation with flow stage (Fig. 1), we can confine our discussion to Bagnold's bedload transport coefficient  $K_b$ .

Different functions have been proposed for the evaluation of Bagnold's bedload transport coefficient (Table 1). In the case of mean sand grain size  $D < 0.5$  mm and dimensionless shear stress  $\theta < 1$ , as a first approximation, Bagnold (1966) assigned the constant value 0.17 for  $K_b$ . Since the critical values of  $\theta$  (i.e. the value of  $\theta$  above which the lower transitional flow stage will change into the upper high flow stage) ranges from about 0.5 for grains smaller than 0.3 mm to about 0.25 for grains larger than 2.0 mm, the above assigned constant value of  $K_b$  (0.17) for  $\theta < 1$  certainly covers the whole lower, transitional range of flow stages. In early work, Bagnold derived other empirical estimates for  $K_b$  as a constant, mainly dependent on sediment characteristics (Table 1). Obviously, as Bagnold himself points out, it is not very satisfactory to use a constant as an approximation to a variable function.

Sternberg (1972) also suggested that  $K_b'$  is not constant but shows a strong dependence on both the sediment size  $D$  and the dimensionless excess shear stress  $E = (\tau_o - \tau_c)/\tau_c$ , in which  $\tau_c$  is the critical shear stress for initiation of sediment movement and  $\tau_o$  is the boundary shear stress. Sternberg developed the relationship:

$$K_b' = A \exp(BE) \quad (16)$$

where coefficient  $A$  and exponent  $B$  can be estimated according to grain size. In the case of the grain size less than 0.3 mm,  $K_b'$  varies mainly as a function of the excess shear stress. For sand of 0.19 mm in mean diameter, the relationship can be expressed as (Sternberg, 1972, fig. 24-A):

$$K_b' = 0.005 \exp(0.69E). \quad (17)$$

Langhorne (1981), based on sediment transport rates measured across a sandwave crest in Start Bay, Devon, U.K., studied the dependence of  $K_b'$  on dimensionless excess shear stress. He concluded that, within the range of flow velocities that were considered, there was no indication that  $K_b'$  becomes a constant at high flow velocities. But the dependence of  $K_b'$  upon dimensionless excess shear stress is not as strong as proposed by Sternberg. Langhorne derived an empirical relationship between  $K_b'$  and excess shear stress as follows:

$$K_b' = 0.18E. \quad (18)$$

Siegenthaler (1982) suggested that the exponential growth of the transport coefficient  $K_b'$  in Sternberg's formula may not exceed a limiting value, which is set between 6 and 9:

$$\begin{cases} K_b' = 0.005 \exp(0.69E) \\ K_b' < K_{b \text{ lim}} = 6-9. \end{cases} \quad (19)$$

Although these functions fit the experimental data within a certain range of flow stages, they still deviate from the general trend of the experimental data over the whole lower transitional stage. Most workers agree

**Table 1.** Functions for the evaluation of Bagnold's (1963) bedload transport coefficient

Author	Function	Condition	
Bagnold (1941)	$K_b = C (D/250)^{1/2}$	$C = \begin{cases} 1.5 \text{ near uniform sand} \\ 1.8 \text{ naturally graded sand} \\ 2.8 \text{ wide range of grain size} \end{cases}$	$K_b$ dependent on grain size and sorting
Bagnold (1963)	$K_{b \text{ max}} = \frac{1}{2} \log_{10}(H/D)$	Small gravity slope	$K_b$ dependent on grain size and flow depth
Bagnold (1966)	$K_b = 0.17$	$D < 0.5$ mm $\theta < 1$	$K_b$ constant
Sternberg (1972)	$K_b' = 0.005 \exp(0.69E)$	$D = 0.19$ mm	$K_b'$ dependent on excess shear stress and grain size
Langhorne (1981)	$K_b' = 0.18E$	$D = 0.32$ mm	$K_b'$ dependent on excess shear stress and grain size
Siegenthaler (1982)	$\begin{cases} K_b' = 0.005 \exp(0.69E) \\ K_b' \leq K_{b \text{ lim}} \\ K_{b \text{ lim}} = 6-9 \end{cases}$	$D = 0.19$ mm	$K_b'$ dependent on excess shear stress and grain size



that  $K'_b$  depends on the excess shear stress, but the exact form of this relationship is still a matter of discussion. Therefore the determination of the sediment transport coefficient  $K'$  and  $K'_b$  requires further investigation.

### THE EVALUATION OF $K'$ AND $K'_b$ USING GUY *ET AL.*'S FLUME EXPERIMENT DATA

To evaluate the sediment transport coefficient  $K'$  and  $K'_b$ , the flume experiment data of Guy, Simons & Richardson (1966) were used. These experiments were conducted in a large recirculating flume, 8' wide, 2' deep and 150' long, with a wide range of flow velocities, sediment grain sizes and bedforms. Data were collected after the runs had reached equilibrium. The measurements relating to shear velocity  $U_*$ , suspended sediment discharge  $j_s$  and total bed material discharge  $j'$  for four different grain sizes, i.e. 0.19, 0.28, 0.45 and 0.93 mm, were used in this study (Guy *et al.*, 1966, cols 20, 21, and 22 of their tables 2, 4, 5, 6). Since the problem being considered here is the sediment transport rate in lower transitional stages, only the data within this range were used.

Simons, Richardson & Nordin (1965) developed a formula which gives a bed material discharge which is only half of the value of the bed material transport rate as calculated by Kachel & Sternberg (1971). This represents the difference between the absolute mass transport  $j$  and the net sediment transport  $j'$ . As a ripple migrates one wavelength in a given direction, each sedimentary particle involved must be moved twice on average. The total height of the ripple, not the mean height, moves through this distance (i.e. a wavelength) (Kachel & Sternberg, 1971, appendix I). Therefore, the measured values of total bed material discharge  $j'$  of Guy *et al.* have been doubled to get the value of absolute bed material transport rate  $j$ .

Purely empirical values of  $K'$  can be calculated from the experimental data using equation (14). Rearrangement of equation (14) gives the expression:

$$K' = \frac{\rho_s - \rho}{\rho_s} g j / (\rho U_*^3). \quad (20)$$

It is now possible to investigate how  $K'$  varies with the dimensionless excess shear stress  $E = (\tau_o - \tau_c) / \tau_c$ . The shear stress  $\tau_o$  can be calculated from experimental data on  $U_*$  using the expression:

$$\tau_o = \rho U_*^2. \quad (21)$$

The critical shear stress  $\tau_c$  can be estimated from the

threshold shear velocity curve (Inman, 1963; Sternberg, 1971). Three different models for the relationship between  $K'$  and  $E$  were tested:

$$K' = A E^B \quad (22)$$

$$K' = A E \quad (23)$$

$$K' = A \exp(B E) \quad (24)$$

where  $A$  and  $B$  are coefficient and exponent respectively in the  $K'$  formulae.

The experimental values of  $K'$  are plotted against  $E$  on a double-log scale (Fig. 2). For each of the three models,  $A$  and  $B$  were calculated using the least squares method. The resulting best fit curves are presented in the same  $K'$ - $E$  plot. In these graphs,  $K' = A \exp(B E)$  appears as a rapidly rising curve which shows a large deviation from the experimental data at low and high flow velocities. At high flow velocities especially, the exponential growth of coefficient  $K'$  reaches an unrealistic value. This is the reason why Siegenthaler set an upper limit for  $K'$ . On the other hand,  $K' = A E$  is represented by a straight line with a constant slope of 1. This does not agree well with the experimental data. Although the experimental data do show the strong trend of following a straight line with a constant slope, this slope is not always the same for different data sets (i.e. for different grain sizes), and generally the slope does not equal 1. Those straight lines with slopes other than 1 on double-log scale graphs represent the power law of  $K' = A E^B$ . Therefore the data are best represented by this model.

We can conclude:

(1) The relationship between  $K'$  and  $E$  is best represented by the power law  $K' = A E^B$ .

(2) The coefficient  $A$  and exponent  $B$  of this function are dependent on the sediment grain size  $D$ . Empirical  $K'$  formulae for different grain sizes are determined using the data of Guy *et al.* (1966) and are listed in Table 2. For fine-medium grained sands ( $D = 0.19$ – $0.45$  mm) it appears that when  $D$  increases,  $A$  increases while  $B$  decreases correspondingly (Fig. 3). Therefore, for convenience, the values of  $A$  and  $B$  can be estimated by interpolation. These values are listed in Table 3, covering the range of most common sand grain sizes.

(3) While the formula  $K' = A E^B$  gives good results for fine and medium grained sands (0.19, 0.28 and 0.45 mm grain sizes), the situation becomes more complicated for coarse grained sand. With  $E$  in the range 4.1–5.6 (corresponding to  $U_*$  of 5.2–5.9 cm s<sup>-1</sup>),  $K'$  seems to decrease as  $E$  increases (Fig. 2).

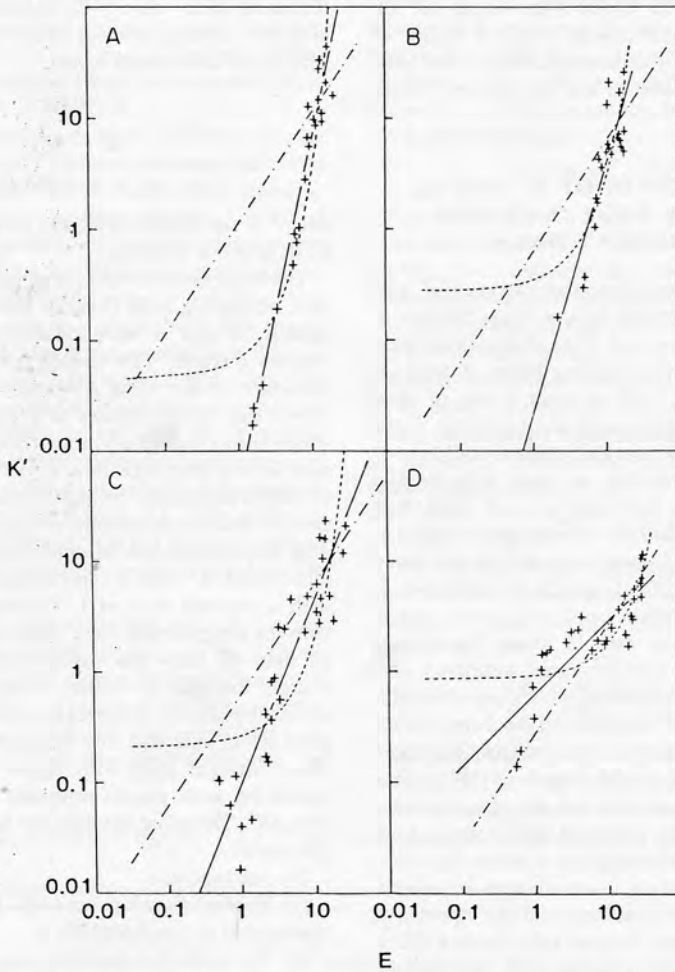


**Fig. 2.** Bagnold's total-load transport coefficient  $K'$  versus dimensionless excess shear stress  $E = (\tau_o - \tau_c)/\tau_c$ . + : data from Guy *et al.*'s (1966) flume experiments; —: calculated from  $K' = A E^B$ ; - - - - -: calculated from  $K' = A E$ ; - · - · -: calculated from  $K' = A \exp(BE)$ . (A) 0.19 mm sands; (B) 0.28 mm sands; (C) 0.45 mm sands; (D) 0.93 mm sands.

Therefore, a reliable evaluation of  $K'$  may only be possible within a certain range of excess shear stress.

In Fig. 4, the measured total-load transport rates

**Table 2.** Evaluation formulae of Bagnold's total-load transport coefficient  $K'$  in equation (14)

$D$ mm	$\tau_c$ dyne $\text{cm}^{-2}$	$K'$ evaluation formulae	Correlation coefficient
0.19	1.9	$K' = 0.0042E^{3.128}$	0.97
0.28	2.18	$K' = 0.0209E^{2.244}$	0.88
0.45	2.8	$K' = 0.0972E^{1.665}$	0.92
0.93	5.27	$K' = 0.6680E^{0.664}$	0.86

from Guy *et al.*'s experiments are plotted against shear velocities. In association with these are the curves derived from  $K'$  evaluation formulae (equation 22) for the same grain size. These curves follow the experimental data very well, indicating that the power law is a suitable model. The curves of the other two models (not shown in Fig. 4) fit the data only in certain range of flow stages. They deviate from the general trend of the data, even though they are also derived from the least-squares fit of the same experimental data. The poor fit arises from the use of inappropriate models (Davis, 1973).



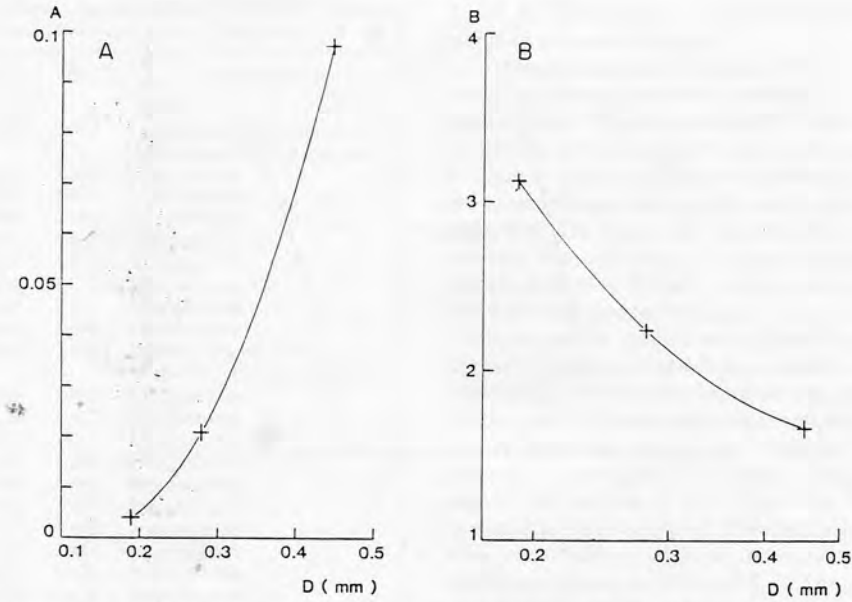


Fig. 3. (A) The coefficient  $A$  of the  $K'$  evaluation equation versus sediment grain size  $D$ . (B) The exponent  $B$  of  $K'$  evaluation equation versus sediment grain size  $D$ .

A similar procedure as used to evaluate  $K'$  above can also be used for  $K'_b$ . Since the bedload transport rate cannot be measured directly, it is calculated as the total bed material discharge  $j'$  minus the suspended sediment discharge  $j'_s$  (also doubled for the same reason as mentioned above):

$$j_b = 2(j' - j'_s). \quad (25)$$

Similar analyses show that the bedload discharge data are also best fitted by the model:

$$K'_b = A_b E^{B_b}. \quad (26)$$

The empirical  $K'_b$  evaluation formulae determined using the data of Guy *et al.* (1966) are listed in Table 4. The coefficient  $A_b$  and exponent  $B_b$  of these formulae are dependent on the sediment grain size  $D$ .

Table 3. Coefficient  $A$  and exponent  $B$  of the  $K'$  evaluation equation estimated from Guy *et al.*'s (1966) flume data

$D$ mm	$A$	$B$	Determined by:	$D$ mm	$A$	$B$	Determined by:
0.19	0.0042	3.128	Least square fit of Guy <i>et al.</i> 's flume data for 0.19 mm sand	0.32	0.0336	2.026	Interpolation
0.20	0.0053	2.990		0.33	0.0373	1.981	Interpolation
0.21	0.0065	2.864	Interpolation	0.34	0.0411	1.941	Interpolation
0.22	0.0080	2.750	Interpolation	0.35	0.0452	1.903	Interpolation
0.23	0.0096	2.646	Interpolation	0.36	0.0495	1.869	Interpolation
0.24	0.0115	2.551	Interpolation	0.37	0.0540	1.837	Interpolation
0.25	0.0135	2.464	Interpolation	0.38	0.0587	1.808	Interpolation
0.26	0.0158	2.385	Interpolation	0.39	0.0636	1.782	Interpolation
0.27	0.0182	2.312	Interpolation	0.40	0.0687	1.758	Interpolation
0.28	0.0209	2.244	Least square fit of Guy <i>et al.</i> 's flume data for 0.28 mm sand	0.41	0.0740	1.735	Interpolation
0.29	0.0238	2.183		0.42	0.0795	1.715	Interpolation
0.30	0.0268	2.126	Interpolation	0.43	0.0852	1.697	Interpolation
0.31	0.0301	2.074	Interpolation	0.44	0.0911	1.680	Interpolation
				0.45	0.0972	1.665	Least square fit of Guy <i>et al.</i> 's flume data for 0.45 mm sand

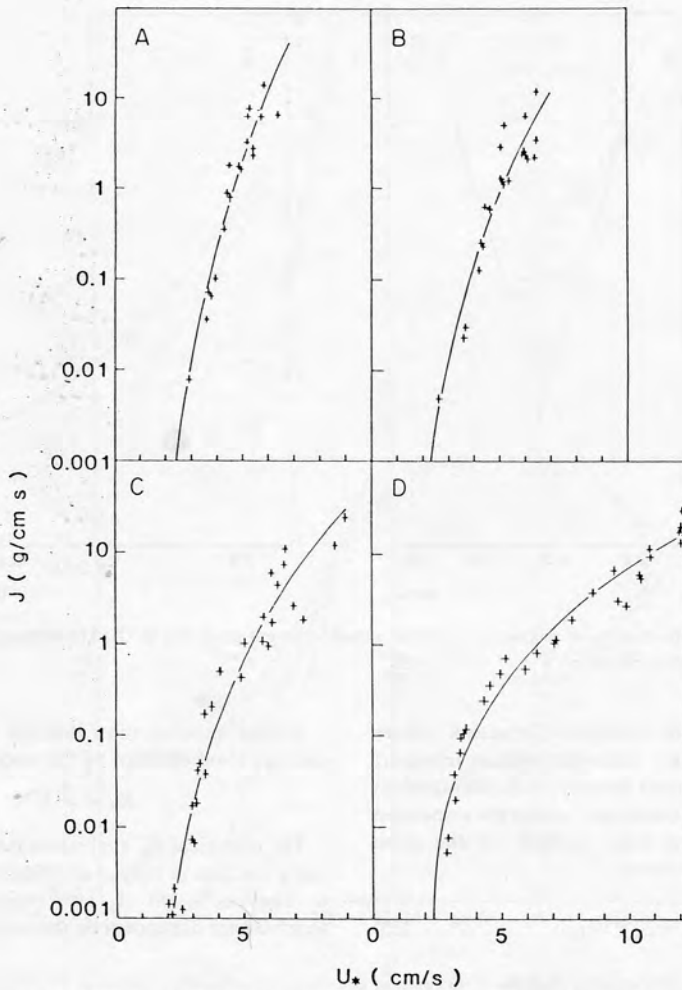


**Fig. 4.** Total-load transport rate  $j$  versus shear velocity  $U_*$ . +: data from Guy *et al.*'s (1966) flume experiments; —: predicted from the modified Bagnold's total-load transport equation (equations 14 and 22 with values of  $A$  and  $B$  from Table 2). (A) 0.19 mm sands; (B) 0.28 mm sands; (C) 0.45 mm sands; (D) 0.93 mm sands.

For fine to medium grained sands ( $D = 0.19\text{--}0.45$  mm), they show a similar variation as the  $K'$  formulae. The

**Table 4.** Evaluation formulae of Bagnold's bedload transport coefficient  $K'_b$  in equation (13)

$D$ mm	$\tau_c$ dyne $\text{cm}^{-2}$	$K'_b$ evaluation formulae	Correlation coefficient
0.19	1.9	$K'_b = 0.0058E^{2.553}$	0.92
0.28	2.18	$K'_b = 0.0561E^{1.521}$	0.68
0.45	2.8	$K'_b = 0.1048E^{1.443}$	0.87
0.93	5.27	$K'_b = 0.7358E^{0.389}$	0.56

interpolated values of  $A_b$  and  $B_b$  for  $K'_b$  formulae are listed in Table 5.

The calculated bedload transport rates from these  $K'_b$  evaluation formulae are plotted against shear velocities (Fig. 5). For comparison, the predicted total-load transport rates from  $K'$  formulae for the same grain size are also plotted in the same figures, which clearly show that bedload transport rates are smaller than total-load transport rates for the same grain size. The difference between these two mainly depends on the shear velocity. At the threshold of

**Table 5.** Coefficient  $A_b$  and exponent  $B_b$  of the  $K_b'$  evaluation equation estimated from Guy *et al.*'s (1966) flume data

$D$ mm	$A_b$	$B_b$	Determined by:
0.19	0.0058	2.553	Least square fit of Guy <i>et al.</i> 's flume data for 0.19 mm sand
0.20	0.0123	2.366	Interpolation
0.21	0.0185	2.203	Interpolation
0.22	0.0245	2.060	Interpolation
0.23	0.0303	1.935	Interpolation
0.24	0.0359	1.827	Interpolation
0.25	0.0412	1.732	Interpolation
0.26	0.0464	1.650	Interpolation
0.27	0.0514	1.580	Interpolation
0.28	0.0561	1.521	Least square fit of Guy <i>et al.</i> 's flume data for 0.28 mm sand
0.29	0.0606	1.516	Interpolation
0.30	0.0650	1.511	Interpolation
0.31	0.0691	1.507	Interpolation
0.32	0.0730	1.502	Interpolation
0.33	0.0767	1.498	Interpolation
0.34	0.0802	1.493	Interpolation
0.35	0.0835	1.489	Interpolation
0.36	0.0866	1.484	Interpolation
0.37	0.0894	1.479	Interpolation
0.38	0.0921	1.475	Interpolation
0.39	0.0945	1.470	Interpolation
0.40	0.0968	1.466	Interpolation
0.41	0.0988	1.461	Interpolation
0.42	0.1006	1.457	Interpolation
0.43	0.1022	1.452	Interpolation
0.44	0.1036	1.447	Interpolation
0.45	0.1048	1.443	Least square fit of Guy <i>et al.</i> 's flume data for 0.45 mm sand

movement,  $j$  is almost equal to  $j_b$ . However, when shear velocity increases, their difference will also increase.

### THE COMPARISON OF PREDICTED AND MEASURED SEDIMENT TRANSPORT RATES

#### Tests using measurements of bedform migration rates in tidal marine environments

To examine the applicability of this modified Bagnold's sediment transport equation (equations 13 and 26 for bedload, and equations 14 and 22 for total load), bedform migration rates from field measurements in tidal marine environments were compared with the sediment transport rates predicted for the same hydrodynamic conditions using equation (14) (evaluating  $K'$  from equation (22) with values of  $A$  and  $B$  from Table 3 for total-load transport) and equation (13) (evaluating  $K_b'$  from equation (26) with values of

$A_b$  and  $B_b$  from Table 5 for bedload transport). Four examples are presented here:

(1) Megaripple migration data (Berben *et al.*, 1978). The observations were made in the Plaat van Ossensisse intertidal shoal, Westerschelde, SW Netherlands (Fig. 6). The shoal was covered by fine grained sands of 0.15 mm in mean size. The area was characterized by strong semidiurnal tides with a mean tidal range of about 4 m. The shoal was dominated by flood tidal currents. The data collected during two spring tidal periods (July 26 to August 2, and August 9 to August 14, 1976) were used in the study.

The measuring station was situated in a field of relatively uniform, sinuous megaripples which had heights of 0.3–0.4 m and a mean wavelength of about 6 m. In order to observe the megaripple migrations, a line of reference stakes was deployed at 4.5 m intervals, crossing the megaripple crests at right angles. The heights of the stakes were fixed with reference to mean sea-level. Detailed measurements were made between adjacent stakes using a special megaripple-measuring device (Fig. 7). The megaripple profiles were obtained by measuring the vertical distance between the horizontal reference level  $AB$  of the megaripple-measuring device and the bottom at 0.41 m intervals. Megaripple migration rates were determined from the comparison of the megaripple profiles during successive flood/ebb cycles (Fig. 8). The migration data for a representative megaripple were selected for detailed analysis.

Boundary layer current velocities were measured by means of a vertical array of five or six Ott-meters mounted on a vertical frame at the crest of the megaripple. Because the measurements were made during the day time, only seven and five flood/ebb tidal cycles were observed during the two spring periods respectively. Analyses indicate that the measured velocity data fit a logarithmic velocity profile with a correlation coefficient of 0.97–0.99. Using a mean drag coefficient  $C_{100}$  of  $3 \times 10^{-3}$  (Sternberg, 1968, 1972; Collins, Amos & Evans, 1981), the shear velocity  $U_*$  was calculated from  $U_{100}$  as:

$$U_* = C_{100}^{1/2} U_{100} \quad (27)$$

The critical shear stress, estimated from the mean grain size using a competence curve (Inman, 1963; Sternberg, 1971), is 1.9 dyne  $\text{cm}^{-2}$ .

Following Bagnold (1941), Kachel & Sternberg (1971) and Langhorne (1981), the mean rate of sediment transport as dry mass per unit length of the megaripple crest,  $j_r$ , was derived from the equation:

$$j_r = \rho_b h_r d_r/t \quad (28)$$

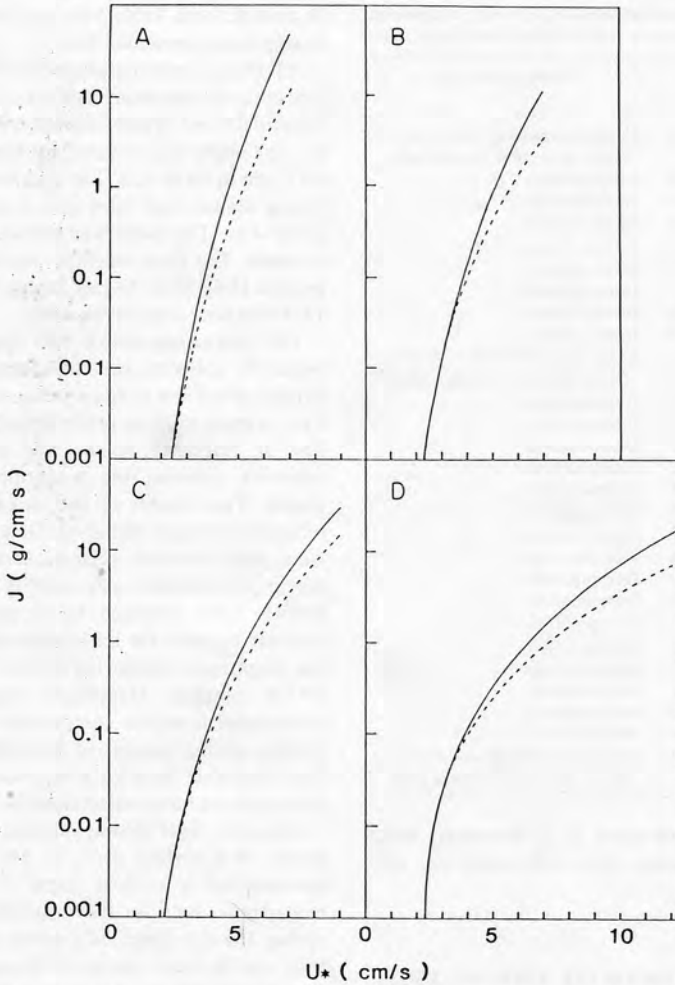


**Fig. 5.** Comparison of total-load transport rate  $j$  and bedload transport rate  $j_b$ . —: total-load transport rate  $j$  predicted from modified Bagnold's total-load transport equation (equation 14 and 22 with values of  $A$  and  $B$  from Table 2); - - -: bedload transport rate  $j_b$  predicted from the modified Bagnold's bedload transport equation (equations 13 and 26 with values of  $A_b$  and  $B_b$  from Table 4). (A) 0.19 mm sands; (B) 0.28 mm sands; (C) 0.45 mm sands; (D) 0.93 mm sands.

where the sediment bulk density  $\rho_b$  is taken as  $1.6 \text{ g cm}^{-3}$ ,  $h_r$  is the megaripple height and  $d_r$  the migration distance of the measured megaripple during the time  $t$ , which is defined as the period during a flood (dominant) tide when  $U_{100}$  is larger than  $U_{100c}$ , the threshold velocity for sand movement at 100 cm above the bottom. Assuming a  $U_{100c}$  value of about  $20 \text{ cm s}^{-1}$  (Langhorne, 1981),  $t$  is estimated as about 135 min during spring tides at the measurement position. Corresponding to the mean sediment transport rate  $j_r$ ,

the cubic shear velocity  $U_*^3$  was also averaged over the same period  $t$ , in order to get the mean shear velocity  $\bar{U}_*$ . The results are given in Table 6.

(2) Small-scale ripple migration data (Kachel & Sternberg, 1971). These measurements were made in a subtidal channel in Puget Sound with a water depth of 31 m and mean bottom sand grain size of 0.37 mm. The sea bed in the study area was deformed into small-scale ripples with a ripple height of 1–5 cm and a ripple wavelength of 10–50 cm. The critical shear

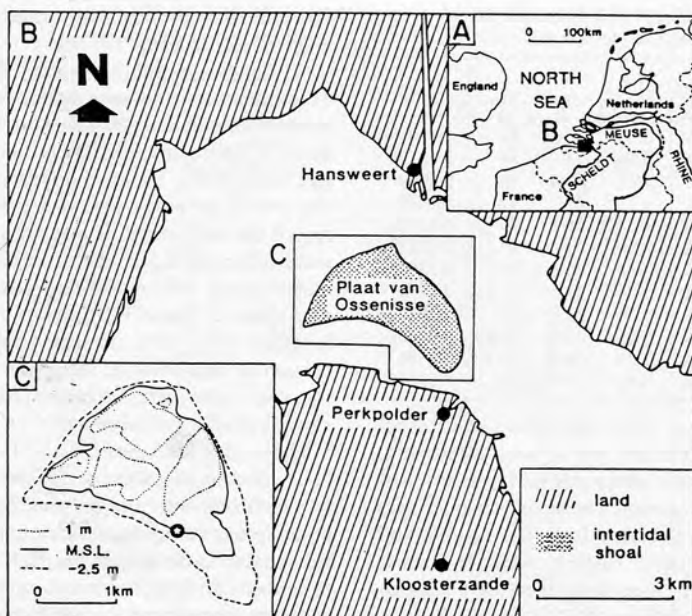


Fig. 6. Location of the Plaat van Ossensisse study area, Westerschelde, SW Netherlands. The asterisk indicates the position of the measuring station (modified after Berben *et al.*, 1978).

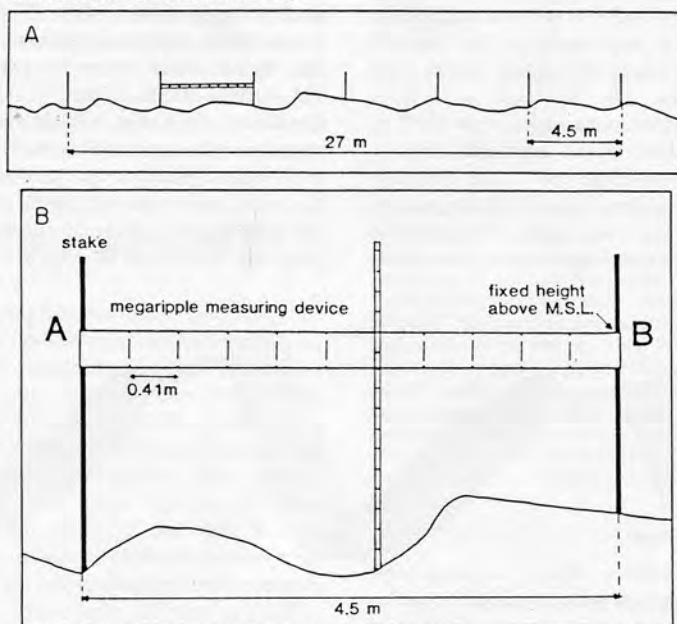


Fig. 7. The megaripple profile measurement as used by Berben *et al.* (1978). (A) The deployment of a line of reference stakes at 4.5 m intervals, crossing the megaripple crests at right angles. The heights of the stakes were fixed with reference to the mean sea-level. (B) The observation of the megaripple profiles by measuring the vertical distance between the horizontal reference level *AB* of the megaripple measuring device and the bottom at 0.41 m intervals.

**Table 6.** Sediment transport measurements in Plaats van Oostenisse, Westerschelde, SW Netherlands

	$U_{100\text{max}}$ $\text{cm s}^{-1}$	$U_{*max}$ $\text{cm s}^{-1}$	$\bar{U}_*$ $\text{cm s}^{-1}$	$h_r$ cm	$d_r$ cm	$j_s$ $\text{g (cm s)}^{-1}$
ST <sub>2</sub> -7	84	4.59	3.85	20.5	42	0.1701
ST <sub>2</sub> -5	86	4.70	3.94	24	34	0.1612
ST <sub>2</sub> -3	90	4.92	4.12	41.4	36	0.2944
ST <sub>2</sub> -1	88	4.81	4.03	42	37	0.3070
ST <sub>2</sub> +1	99	5.42	4.54	39.1	79	0.6102
ST <sub>2</sub> +3	83	4.54	3.80	37.4	30.5	0.2253
ST <sub>2</sub> +5	75	4.10	3.44	36.6	18	0.1301
ST <sub>3</sub> -5	77	4.21	3.53	31.4	27.6	0.1712
ST <sub>3</sub> -3	82	4.49	3.76	32	21	0.1327
ST <sub>3</sub> -1	82	4.49	3.76	34.5	32.8	0.2235
ST <sub>3</sub> +1	74	4.05	3.39	34.5	25.7	0.1751
ST <sub>3</sub> +3	90	4.92	4.12	28.5	26	0.1464

stress of  $2.25 \text{ dyne cm}^{-2}$  was determined by extrapolating the ripple migration rate to zero (Sternberg, 1971). The observations were made during a period of relatively strong ebb current. The mass transport rates of sediments were calculated from the heights and migration rates of small ripples, while the shear velocities were determined from measured velocity profiles (Kachel & Sternberg, 1971).

(3) Subtidal megaripple cross-bedding set (tidal bundle sequence) data (Oosterschelde, SW Netherlands). The recent Oosterschelde subtidal megaripple cross-bedding sets were deposited in a tidal channel with a water depth of about 14.5 m and a mean sand grain size of 0.19 mm. The preserved set heights indicate that the original megaripples were 1.5–2 m high. The critical shear stress, estimated from a competence curve, is  $1.9 \text{ dyne cm}^{-2}$ . The sediment transport rates were calculated from the field measurements of these recent megaripple cross-bedding deposits, while the shear velocities were determined

from present-day tidal range data of this area (Nio, Siegenthaler & Yang, 1983).

(4) Sandwave migration data (Langhorne, 1981). These measurements were carried out in a tidal marine environment in Start Bay, Devon, U.K. with a water depth of approximately 10 m and a mean sand grain size of 0.32 mm. Detailed observations were carried out over a nine-day period around spring tides to record the movement of one sandwave crest with a wave height of 3.5 m and a wavelength of approximately 180 m. The critical shear stress, estimated from a competence curve, is  $2.3 \text{ dyne cm}^{-2}$ . The sediment transport rates were calculated from the volume of erosion or deposition at the sandwave crest, and the shear velocities were determined from boundary layer velocity profile measurements.

The data of examples 2, 3 and 4 are shown in Table 7. The measured sediment transport rates from these four environments, and the predicted sediment transport rates from equations (13) and (14), are plotted against shear velocities in Fig. 9. It might be expected that the sediment transport rate calculated from bedform migration data would be comparable with the minimum value of the predicted bedload transport rate. However, it turns out that for megaripple and sand wave migration data (Fig. 9A, C, D), the measured sediment transport rates are generally larger than the calculated bedload transport rates, but agree well with the calculated total-load transport rates. For Sternberg's data (Fig. 9B), the measured sediment transport rates agree well with the predicted rates of both bedload transport and total-load transport, since these data were collected during the early stage of an ebb flow before substantial quantities of sand were taken into suspension (Kachel & Sternberg, 1971).

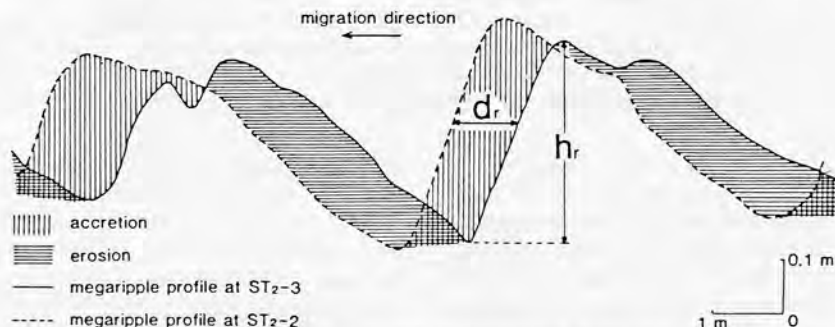


**Fig. 8.** The determination of megaripple migration rates from the comparison of the megaripple profiles during successive flood/ebb cycles.  $h_r$ : megaripple height;  $d_r$ : horizontal migration distance of the megaripple during one dominant tidal current; ST2-3 and ST2-2: three and two tides before the spring tide ST2 (modified after Berben *et al.*, 1978).



**Table 7.** Sediment transport measurements in tidal marine environments (example 2, 3 and 4) used for testing modified Bagnold's transport equation

Small-ripple migration Puget Sound $\tau_c = 2.25 \text{ dyne cm}^{-2}$		Megaripple cross-bedding Oosterschelde $\tau_c = 1.90 \text{ dyne cm}^{-2}$		Sand wave migration Start Bay $\tau_c = 2.30 \text{ dyne cm}^{-2}$	
$U_*$	$j$	$U_*$	$j$	$U_*$	$j$
$\text{cm s}^{-1}$	$\text{g}(\text{cm s})^{-1}$	$\text{cm s}^{-1}$	$\text{g}(\text{cm s})^{-1}$	$\text{cm s}^{-1}$	$\text{g}(\text{cm s})^{-1}$
2.54	0.0084	4.12	0.4957	3.3	0.07
2.8	0.0341	5.35	2.1029	4.0	0.19
3.0	0.0670			4.3	0.25
3.13	0.0256			4.4	0.34
3.37	0.0803			4.7	0.64
3.6	0.0317			4.8	0.37
3.84	0.1034			4.9	0.56
4.5	0.1002			4.9	0.76
				5.0	0.56
				5.2	0.54

There are several possible reasons for the discrepancy between the bedform migration data and the calculated bedload transport rates. First, the large differences in hydrodynamic conditions between natural tidal environments and artificial flume experiments must be taken into account, especially in terms of the non-steady flow and the greater water depth of the tidal currents. Secondly, the technical difficulty of field measurements in tidal marine environments may introduce some errors. Finally, this discrepancy may also be attributed to the different meanings of 'bedload' when used in field measurements and in sediment transport rate predictions.

#### Tests using bedform migration data from flume experiments

We can test whether the first two factors (the difference between flume and natural tidal environments, and the errors in field measurements) are the cause of this discrepancy. To do this, we use the flume experiment data of Guy *et al.* In their experiments with 0.19, 0.28 and 0.93 mm sands, they also calculated ripple and megaripple migration rates (Guy *et al.*, 1966, tables 2, 4 and 6, cols 15 and 16). These data are the most suitable for testing the results of our work for two reasons. First, they include bedform migration rates and sediment transport rates measured simultaneously from the same run with exactly the same grain size, flow velocity, flow depth and other hydraulic conditions. Secondly, in their experiments, bedform migration was observed through a window in the flume wall marked by a grid, and the bedform migration data

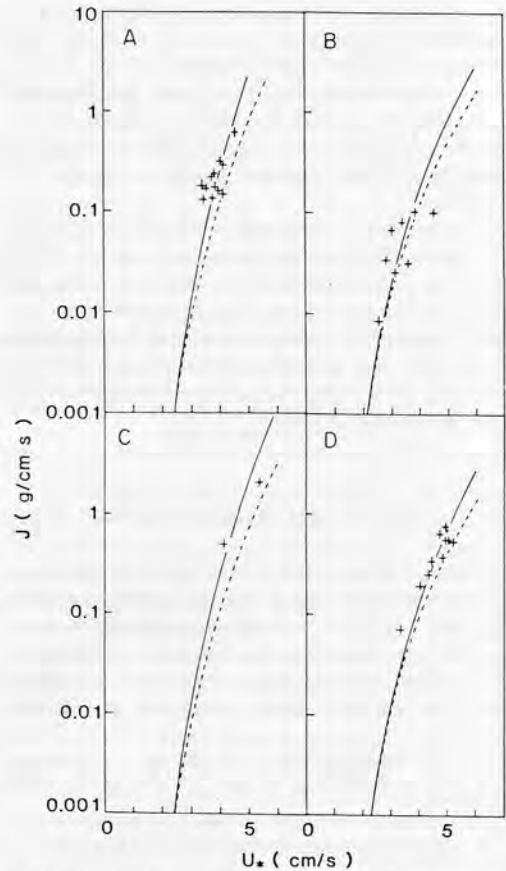


**Fig. 9.** Sediment transport rates versus shear velocity. +: data from bedform migration measurements in tidal environments; —: predicted from modified Bagnold's total-load transport equation (equations 14 and 22 with values of  $A$  and  $B$  from Table 3); - - -: predicted from the modified Bagnold's bedload transport equation (equations 13 and 26 with values of  $A_b$  and  $B_b$  from Table 5). (A) example 1: megaripple migration data, Plaat van Ossenisse, Westerschelde (data from Berben *et al.*, 1978); (B) example 2: small-ripple migration data, Puget Sound (data from Kachel & Sternberg, 1971); (C) example 3: megaripple cross-bedding data, Oosterschelde (data from Nio *et al.*, 1983); (D) example 4: sand wave migration data, Start Bay (data from Langhorne, 1981).

were measured under controlled conditions. This reduced the possible measurement error to a negligible level. The sediment transport rates were derived from these bedform migration measurements using the equation:

$$j_r = \rho_b h_r U_r \quad (29)$$

which is equivalent to equation (28) with the term  $d_r/t$  substituted for the migration velocity  $U_r$  of the ripple or megaripple. The results are listed in Table 8. With these considerations, any discrepancy in comparison can safely be attributed to the inconsistency in the meaning of bedload when used in bedform migration measurements and sediment transport equation calculations.

The results of these comparisons are shown in Fig. 10. Again, the bedform migration data are higher than the calculated bedload transport rates, but comparable with the total-load transport rates. This result confirms the previous tests with field measurement data and provides clear evidence that the meaning of the term bedload is not consistent when used in different situations.

### BEDLOAD DEFINITIONS

The tests above lead us to a basic problem in sediment transport: the meaning of bedload. Although bedload is a basic concept in sediment transport, its meaning is still very confusing. A comparison of different bedload definitions is shown in Table 9. Numerous investigations have been carried out to calculate

**Table 8.** Sediment transport rates derived from bedform migration measurements in Guy *et al.*'s (1966) flume experiments

0.19 mm sand		0.28 mm sand		0.93 mm sand	
$U_*$	$j$	$U_*$	$j$	$U_*$	$j$
$\text{cm s}^{-1}$	$\text{g}(\text{cm s})^{-1}$	$\text{cm s}^{-1}$	$\text{g}(\text{cm s})^{-1}$	$\text{cm s}^{-1}$	$\text{g}(\text{cm s})^{-1}$
2.19	0.00073	2.62	0.0144	3.35	0.0595
2.44	0.00042	2.68	0.0409	3.38	0.0867
2.83	0.00216	3.60	0.0201	3.51	0.0520
2.90	0.0178	3.66	0.0396	3.60	0.0595
3.90	0.0317	4.21	0.114	4.30	0.312
4.24	0.0793	4.30	0.218	4.54	0.297
4.33	0.570	4.33	0.461	4.94	0.357
4.42	0.758	4.45	0.141	5.15	0.713
4.45	0.258	4.63	0.139	5.91	0.515
4.79	0.773	5.06	1.189	6.37	0.803
4.88	0.446	5.09	0.609	7.07	1.031
5.12	2.093	5.15	0.681	7.13	1.179
5.33	1.843	5.33	0.669	7.74	2.071
5.33	0.743	5.94	0.850	8.56	2.485
5.67	2.029	5.97	0.870	9.54	2.274
6.31	1.586	6.13	1.937	9.88	3.456
5.15	0.644	6.40	1.011	10.39	4.757
5.09	1.932	6.46	1.229	10.42	4.311
		6.04	2.448	10.79	6.610
		6.49	2.051	9.39	4.073
				12.01	14.245

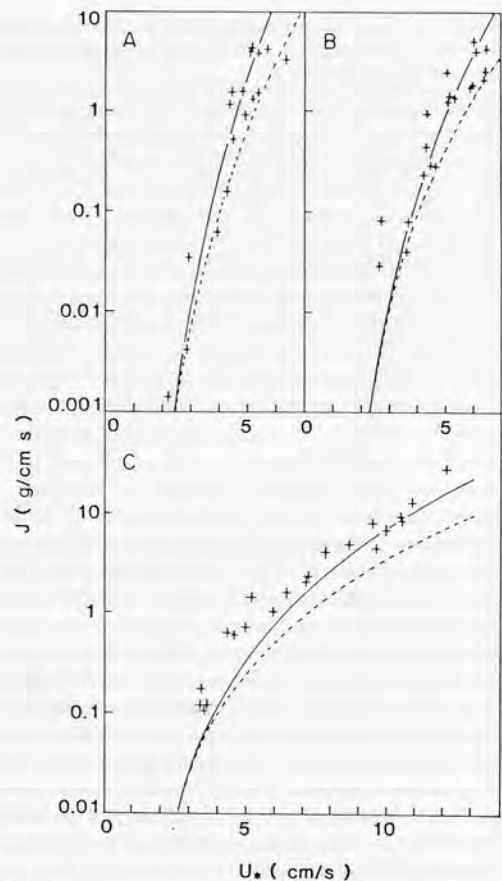


**Fig. 10.** Sediment transport rate versus shear velocity. +: data from bedform migration measurements in Guy *et al.*'s flume experiments, —: predicted from modified Bagnold's total-load transport equation (equations 14 and 22 with values of  $A$  and  $B$  from Table 2), - - -: predicted from modified Bagnold's bedload transport equation (equations 13 and 26 with values of  $A_b$  and  $B_b$  from Table 4). (A) 0.19 mm sands; (B) 0.28 mm sands; (C) 0.93 mm sands.

'bedload' transport rates from bedform migration data and to compare them with the 'bedload' transport rates predicted from sediment transport equations. This approach seems to be a commonly accepted practice in marine geological research. In doing so, it is seldom considered if the term bedload has a consistent meaning when used in different situations (Middleton, 1980). The foregoing analysis shows that this conventional approach might not be the appropriate way, since 'bedload' used in sediment transport equations does not necessarily have the same meaning

**Table 9.** Comparison of bedload definitions. Definitions from Bagnold (1966, 1973), Middleton & Southard (1978), Leeder (1979, 1982) and Blatt *et al.* (1980)

Bedform migration measurements	Sand grain size distribution	Mode of grain movement	Mechanism of momentum transfer	Sediment transport function	
'Bedload' definition A bed material discharge	Traction population	Sliding	Bedload definition B	Bedload transport function	Total sediment transport function
		Rolling			
	Intermittent suspension population	Saltation	Momentum transfer by solid/solid contacts (collisions)		
		Intermittent suspension	Suspended-load momentum transfer by fluid turbulence	Suspended-load transport function	
	Suspension population	Suspension (wash load)		Wash load transport does not depend on local flow hydrodynamics	

as the 'bedload' when used in bedform migration calculations.

It is, therefore, essential to determine whether the two bedload meanings are identical before any reliable comparison can be made between calculated bedload transport rates and bedload transport rates measured from bedform migration data.

#### Bedload defined in terms of bedform migration (definition A)

From the practical viewpoint, bedload can be defined as the sediment which is trapped in the lee of a bedform, i.e. the sediment that moves within the migrating bedform, rather than over it (Middleton & Southard, 1978). Therefore, in the field, the measurements of bedform migration are commonly used to estimate 'bedload' transport rate.

In fact, this approach has become widely used for the estimation of bedload transport rate (Bagnold, 1941; Simons *et al.*, 1965; Allen, 1981). A variety of techniques have been developed in actual measurements. Kachel & Sternberg (1971) measured the heights and migration rates of small ripples on time-lapse stereo photographs to calculate bedload transport. Langhorne (1981) observed sandwave migration using a bottom stake profiling technique, and calculated bedload transport rates. Others have used echosounding profiles to measure megaripple or sandwave migration rates and the corresponding bedload transport. Though different techniques can be used, the underlying concept is the same: bedload is the sediment passing the crest of a migrating bedform which is trapped in the lee side.

The fact that this definition of bedload is so widely used in marine geological practice is not fortuitous. For practical reasons, engineers are mainly concerned with bedform migration. For sedimentologists, the migration of bedforms and the resultant cross-bedding structures are of major interest. In addition, since the direct measurement of bedload transport in marine environments is still difficult, observation of bedform migration rates has been the only alternative. Therefore 'bedload' defined in terms of bedform migration is generally used in marine environments. However, it should be noted that bedform migration data are only an indirect measurement of the sediment transport, i.e. the result of sediment transport, it is not the direct observation of the sediment transport process itself.

#### The dynamic definition of bedload (definition B)

From the theoretical viewpoint, bedload can be defined in terms of the mode of grain movement, or the mechanism of momentum transfer. In this dynamic definition, bedload includes rolling, sliding, saltating and collision-interrupted 'saltating' grains. These grains transfer momentum to the stationary bed surface by solid/solid contacts (collisions) (Bagnold, 1966). The immersed weight of bedload grains is balanced by this solid/solid momentum transfer mechanism. Suspended-load, however, includes all the grains kept aloft by fluid turbulence; the immersed weight of the suspended grains is balanced by an upward momentum transfer from the fluid turbulence (Bagnold, 1966, 1973; Leeder, 1979, 1982).

This dynamic definition of bedload transport is

derived from basic physical principles. The distinction between suspended-load and bedload is based on the mode and mechanism of grain movement, i.e. the sediment transport process itself. This dynamic bedload definition is widely used in bedload transport equations.

Since most field measurements of bedload transport are based on bedload definition A, whereas the calculated bedload transport rates from bedload transport equation (e.g. Bagnold's bedload formula) refer to bedload definition B, and the two approaches give different results, it is obvious that these two meanings of 'bedload' are not identical.

### THE CONTRIBUTION OF INTERMITTENT SUSPENDED LOAD TO THE DEVELOPMENT OF CROSS-BEDDED DEPOSITS

The migration of bedforms and the development of cross-bedded deposits involve both bedload and suspended-load transport, in contrast to the commonly held opinion that only bedload is important. In many cases, the foreset laminae of a cross-bedded set are clearly visible because of a distinct alternation of coarse-grained laminae with fine-grained laminae (Fig. 11). As proposed by Jopling (1966), one dominant process in the development of such foreset laminae is the selective transport related to differential settling velocity of grains. The layers composed of coarse grains of 'bedload' (definition B) origin are produced by the process of avalanching, which tends to be intermittent rather than continuous at low flow stage. On the other hand, the material comprising the fine-grained laminae is derived mainly from the suspension load. It is commonly observed that many of the

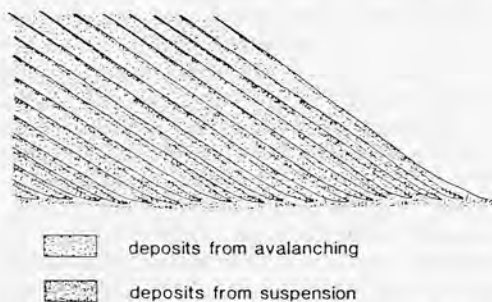


Fig. 11. The foreset lamination showing a distinct alternation of the coarse material laminae deposited from avalanching with the fine material laminae deposited from suspension.

laminae of the lee face can be traced from the lower foreset through the toeset into the distal bottomset. This continuity is important evidence of the contribution to bedform migration from suspension transport. Thus, the relative proportion of fine-grained laminae to coarse-grained laminae would provide an approximate index of the relative importance of bedload and suspended-load. Variation in bedload/suspended-load proportion will also determine the shape of the cross-bedded set (Allen, 1968; Reineck & Singh, 1973; Blatt, Middleton & Murray, 1980).

A convincing argument was provided by White & Williams (1967), who applied the hydraulic equivalence concept to cross-bedded sands. In the unimodal population of bottomset laminations and the finer population of foreset laminations, quartz and tourmaline have approximately the same settling velocities, indicating that the quartz and tourmaline grains are hydraulically equivalent, i.e. they were deposited by settling from suspension. On the other hand, in the coarser population of foreset laminations, tourmaline grains have settling velocities considerably smaller than that of quartz, suggesting that the quartz and tourmaline grains are not hydraulically equivalent. They were deposited from bedload. Heavy minerals, once deposited, are more difficult to entrain than quartz. Thus heavy minerals in bedload sands have a smaller settling velocity than associated quartz.

Therefore the so-called 'bedload' transport rate measured from bedform migration data includes not only bedload transport, but also a considerable amount of suspended-load transport. Although it is difficult to measure bedload and suspended-load transport rates separately, the total bed material transport rate should be comparable with the sediment transport rate estimated from bedform migration. This explains the results of our testing.

However, the suspended load involved in bedform migration has only an intermittent character. It differs from wash load which is held almost continuously in suspension. Intermittent suspended-load is not held continuously in suspension and drops back frequently on to the bed whenever the intensity of the turbulence is low relative to the settling velocity of the grains. In the case of sediment deposition on megaripples, this may be related to flow separation downstream of a megaripple crest during the dominant tidal current, and will depend on the character of the local boundary layer in the lee of the megaripple crest. Substantial suspended sediment may be caught in a region of separated flow behind the crest and deposited on the lee slope.



When flow separation occurs, the mean backflow velocity in the local boundary layer within the separation cell,  $U_{sep}$ , is a function of the external free stream mean velocity  $\bar{U}$  (Allen, 1982):

$$U_{sep} = K_u (h_r/H, Re) \bar{U} \quad (30)$$

where  $K_u$  is a numerical coefficient which depends on the megaripple height  $h_r$ , the mean water depth  $H$  and the Reynolds number  $Re$ . From experimental studies, the coefficient  $K_u$  varies between 0.15 and 0.3 according to the relative roughness (Allen, 1982). A similar value of 0.2–0.25 for  $K_u$  was estimated by Reineck & Singh (1973).

Therefore, assuming a representative sand movement threshold velocity ( $U_{ces}$ ) of  $20 \text{ cm s}^{-1}$  (Allen, 1982), the corresponding threshold velocity of the external stream for the sand to deposit beneath the separation cell may range from 67 to  $133 \text{ cm s}^{-1}$ . Considering the logarithmic velocity profile, an even higher velocity range at the water surface is needed. Such a threshold velocity range is too high to be exceeded in most natural tidal flows. This implies that

while the tidal current velocity over the megaripple crest is larger than  $U_{ces}$ , the local boundary layer current velocity, within the separation cell, is still lower than  $U_{ces}$ , causing sands to deposit on the lee slope and in the trough (Fig. 12).

Intermittent suspension is an important mode of movement of fine to medium grained sand movement in natural subaqueous environments. As Middleton & Southard (1978) have proposed, among the three major populations of sand-size distributions, namely, sliding and rolling, intermittent suspension and suspension, the intermittent suspension population makes up the greatest part of the size distribution in most sandy environments. Sand within cross-bedded sets (which is of 'bedload' origin according to definition A because it is trapped in the lee of megaripples) generally has a size distribution composed of two different fractions: a relatively small sliding and rolling population and a large intermittent suspension population. Although the intermittent suspension population here may include some saltation movement, the size distribution of most cross-

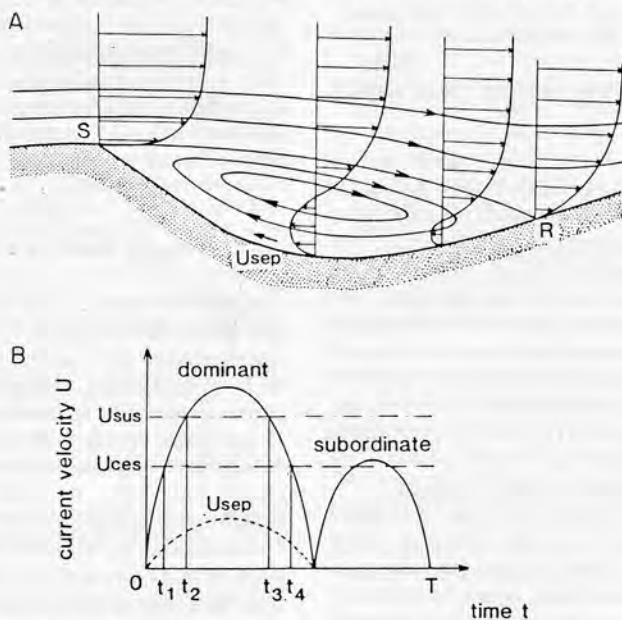


Fig. 12. The effects of flow separation on sand transport and deposition. (A) The flow separation and current velocity pattern during the dominant tidal current down stream of megaripple crest. S: separation; R: reattachment;  $U_{sep}$ : the mean backflow velocity in the boundary layer within the separation cell (modified after Allen, 1982). (B) During the interval  $t_4-t_1$  sand is deposited in the megaripple lee-slope and the trough at the same time as it is passing the crest in the form of bedload (during the intervals of  $t_2-t_1$  and  $t_4-t_3$ ) or intermittent-suspended load (during the interval of  $t_3-t_2$ ). —: current velocity at megaripple crest; - - - - : mean backflow velocity  $U_{sep}$  in the boundary layer within the separation cell (no separation during subordinate current stage);  $U_{ces}$ : threshold velocity of sand movement;  $U_{sus}$ : threshold velocity of sand suspension.



bedded sands shows a strong evidence that intermittent suspended-load transport also contributes to the bedform migration and the development of cross-bedded sets. Our calculation of bedform migration data and sediment transport rates confirms Middleton & Southard's theory.

## CONCLUSIONS

Due to its clear physical basis and great flexibility, Bagnold's sediment transport equation is very popular among sedimentologists and marine geologists. However, its successful application depends critically on a number of factors and in particular the following points need to be considered:

(1) The widely used Bagnold suspended-load transport equation (equation 4) and total-load transport equation (equation 5) with  $e_s(1 - e_b) = 0.01$  are incorrect from the viewpoint of energy conservation. In these two equations the energy loss due to bedload transport has been counted twice. The correct form

should be  $q_s = \omega \frac{e_s \bar{U}_s}{W}$  for suspended-load transport and  $q = \left( \frac{e_b}{\tan \alpha} + \frac{e_s \bar{U}_s}{W} \right) \omega$  for total-load transport with  $e_s = 0.016$ .

(2) The coefficient  $K'$  in the modified form of Bagnold's total-load transport equation (equation 14) is not constant, but varies as a function of dimensionless excess shear stress  $E$  and grain size  $D$  within lower transitional flow stages, which are the case in all natural tidal environments with rippled beds. The relation giving the best fit of  $K'$  to  $E$  is a power law  $K' = A E^B$ , where coefficient  $A$  and exponent  $B$  depend on  $D$ . The empirical values of  $A$  and  $B$  for commonly occurring fine to medium grained sand (0.19–0.45 mm in grain size) have been tabulated for convenience (Table 3). Similar results have been presented for Bagnold's bedload transport equation (Table 5).

(3) The wide use of the term 'bedload' in different applications may result in some confusion. With respect to sediment transport problems, the term 'bedload' is used in two different senses. In the case of bedform migration measurements, bedload is used in the first sense (definition by bedform migration), while in sediment transport equations, the second sense of bedload is meant (dynamic definition). To avoid confusion, it is advisable that the sediment transport rate measured from bedform migration is designated as 'bed material' transport rate rather than the

problematical 'bedload' transport rate. This bed material is moved by sliding, rolling, saltation, and intermittent suspension (Blatt *et al.*, 1980). The bed material transport rates thus defined are directly comparable with bedform migration rate.

(4) The bedload transport rate calculated from the bedload transport equation, and the bed material transport rate measured from bedform migration are not identical. Therefore the direct comparison of the two can hardly be regarded as appropriate. Since bedform migration involves both bedload and intermittent suspended-load transport, the 'bed material' transport rates measured from bedform migrations should be compared with Bagnold's total-load transport equation, namely, bedload plus intermittent suspended-load. Wash load should be excluded because it is not derived from the bed, and its occurrence depends mainly on the availability of fine material rather than on the local hydraulics (Blatt *et al.*, 1980).

(5) The applicability of our modified Bagnold transport equation to both flume experiments and the tidal marine environment is well supported by experimental data. In particular, sediment transport rates predicted from the modified equation are in good agreement with independent measurements of bedform migration rates in tidal marine environments, and bedform migration rates from flume experiments, which cover a wide range of flow velocities, grain sizes and bedform conditions.

## ACKNOWLEDGMENTS

The author wishes to thank S.-D. Nio for his support and helpful discussions in this work. Appreciation and thanks are also due to T. de Mowbray and P. L. de Boer who made numerous suggestions for the improvement of the manuscript. M. R. Leeder, A. D. Heathershaw and J. S. Bridge kindly reviewed the manuscript and made valuable suggestions and comments. The author is greatly indebted to G. V. Middleton, J. B. Southard and J. H. J. Terwindt for a critical reading of the manuscript and fruitful discussions. M. R. Leeder and G. Middleton kindly provided reprints of very interesting papers.

## REFERENCES

- ABBOTT, J.E. & FRANCIS, J.R.D. (1977) Saltation and suspension trajectories of solid grains in a water stream. *Phil. Trans. R. Soc. A*, **284**, 225–254.

- ACKERS, P. & WHITE, W.R. (1973) Sediment transport: new approach and analysis. *J. Hydraul. Div., Proc. Am. Soc. Civ. Engrs.* **99**, 2041–2060.
- ALLEN, J.R.L. (1968) *Current Ripples: their Relation to Patterns of Water and Sediment Motion*. North-Holland, Amsterdam, 433 pp.
- ALLEN, J.R.L. (1981) Palaeotidal speeds and ranges estimated from cross-bedding sets with mud drapes. *Nature*, **293**, 394–396.
- ALLEN, J.R.L. (1982) Mud drapes in sand-wave deposits: a physical model with application to the Folkestone Beds (early Cretaceous, southeast England). *Phil. Trans. R. Soc. A*, **306**, 291–345.
- BAGNOLD, R.A. (1941) *The Physics of Blown Sand and Desert Dunes*. Morrow, New York, 265 pp.
- BAGNOLD, R.A. (1963) Beach and near-shore processes, I: mechanics of marine sedimentation. In: *The Sea* (Ed. by M. N. Hill), pp. 507–549. Wiley (Interscience), New York.
- BAGNOLD, R.A. (1966) An approach to the sediment transport problem from general physics. *Prof. Pap. U.S. geol. Surv.* **422-1**.
- BAGNOLD, R.A. (1968) Deposition in the process of hydraulic transport. *Sedimentology*, **10**, 45–56.
- BAGNOLD, R.A. (1973) The nature of saltation and of 'bed-load' transport in water. *Proc. R. Soc. A*, **332**, 473–504.
- BERBEN, F.M.L., BROUWER, M.J.N., KOHSIEK, L.H.M., LEMKES, J.C.A. & STEYAERT, F.H.I.M. (1978) *Ribbelvormen, waterbeweging en hun onderlinge samenhang in een getijdengebied (Plaats van Ossensisse, Westerschelde)*. Geografisch Instituut, Rijksuniversiteit Utrecht.
- BLATT, H., MIDDLETON, G. & MURRAY, R. (1980) *Origin of Sedimentary Rocks*. Prentice-Hall, Englewood Cliffs, New Jersey, 782 pp.
- COLLINS, M.B., AMOS, C.L. & EVANS, G. (1981) Observations of some sediment-transport processes over intertidal flats, the Wash, U.K. In: *Holocene Marine Sedimentation in the North Sea Basin* (Ed. by S.-D. Nio, R. T. E. Shüttenhelm & Tj. C. E. van Weering). *Spec. Publ. int. Ass. Sediment.* **5**, 81–98. Blackwell Scientific Publications, Oxford.
- DAVIS, J.C. (1973) *Statistics and Data Analysis in Geology*, pp. 192–221. Wiley, London.
- EINSTEIN, H.A. (1950) The bedload function for sediment transportation in open channel flows. *U.S. Dept. Agric. Soil Conserv. Ser., Tech. Bull.* **1026**, 1–71.
- ENGELUND, F. & HANSEN, E. (1967) *A Monograph on Sediment Transport in Alluvial Streams*. Teknisk Forlag, Copenhagen, 62 pp.
- FRANCIS, J.R.D. (1973) Experiments on the motion of solitary grains along the bed of water stream. *Proc. R. Soc. A*, **332**, 443–471.
- GADD, P.E., LAVELLE, J.W. & SWIFT, D.J.P. (1978) Estimates of sand transport on the New York shelf using near-bottom current meter observations. *J. sedim. Petrol.* **48**, 239–252.
- GUY, H.R., SIMONS, D.B. & RICHARDSON, E.V. (1966) Summary of alluvial channel data from flume experiments, 1956–1961. *Prof. Pap., U.S. geol. Surv.* **462-1**, 96 pp.
- HEATHERSHAW, A.D. (1981) Comparisons of measured and predicted sediment transport rates in tidal currents. *Mar. Geol.* **42**, 75–104.
- HEATHERSHAW, A.D. & HAMMOND, F.D.C. (1979) Swansea Bay (Sker) Project; offshore sediment movement and its relation to observed tidal current and wave data. *Inst. Oceanogr. Sci. Rep. No. 93*, 119 pp.
- INMAN, D.L. (1963) Sediments: physical properties and mechanics of sedimentation. In: *Submarine Geology* (Ed. by F. P. Shepard), pp. 101–151. Harper & Row, New York.
- IRMAV, S. (1960) Accelerations and mean trajectories in turbulent channel flow. *Trans. Am. Soc. Mech. Engrs.* **82**, 961–972.
- JOPLING, A.V. (1966) Some principles and techniques used in reconstructing the hydraulic parameters of a paleo-flow regime. *J. sedim. Petrol.* **36**, 5–49.
- KACHEL, N.B. & STERNBERG, R.W. (1971) Transport of bed load as ripples during an ebb current. *Mar. Geol.* **10**, 229–244.
- LANGHORNE, D.N. (1981) An evaluation of Bagnold's dimensionless coefficient of proportionality using measurements of sand wave movement. *Mar. Geol.* **43**, 49–64.
- LEEDER, M.R. (1979) 'Bed load' dynamics: grain-grain interactions in water flows. *Earth Surf. Processes*, **4**, 229–240.
- LEEDER, M.R. (1982) *Sedimentology, Process and Product*. Allen & Unwin, London, 344 pp.
- LEEDER, M.R. (1983) On the dynamics of sediment suspension by residual Reynolds stresses—confirmation of Bagnold's theory. *Sedimentology*, **30**, 485–491.
- MIDDLETON, G.V. (1980) Physical processes. In: *Sedimentary Processes and Animal-Sediment Relationships in Tidal Environments* (Ed. by S. B. McCann). *Short Course Notes, geol. Ass. Can.* **1**, 25–58.
- MIDDLETON, G.V. & SOUTHARD, J.B. (1978) Mechanics of sediment movement. *Short Course Soc. econ. Paleont. Miner., Tulsa, No. 3*.
- NIO, S.D., SIEGENTHALER, C. & YANG, C.S. (1983) Mega-ripple cross-bedding as a tool for the reconstruction of the palaeo-hydraulics in a Holocene subtidal environment, S.W. Netherlands. *Geologie Mijb.* **62**, 499–510.
- PANTIN, H.M. (1979) Interaction between velocity and effective density in turbidity flow: phase-plane analysis, with criteria for autosuspension. *Mar. Geol.* **31**, 59–99.
- REINECK, H.E. & SINGH, I.B. (1973) *Depositional Sedimentary Environments*. Springer-Verlag, Berlin, 439 pp.
- REYNOLDS, O. (1895) On the dynamic theory of viscous incompressible fluids and the determination of the criterion. *Phil. Trans. R. Soc. A*, **186**, 123.
- SIEGENTHALER, C. (1982) Tidal cross-strata and the sediment transport rate problem: a geologist's approach. *Mar. Geol.* **45**, 227–240.
- SIMONS, D.B., RICHARDSON, E.V. & NORDIN, C.F. Jr (1965) Bedload equation for ripples and dunes. *Prof. Pap. U.S. geol. Surv.* **462-H**, 9 pp.
- STERNBERG, R.W. (1968) Friction factors in tidal channels with differing bed roughness. *Mar. Geol.* **6**, 243–260.
- STERNBERG, R.W. (1971) Measurements of incipient motion of sediment particles in the marine environment. *Mar. Geol.* **10**, 113–119.

STERNBERG, R.W. (1972) Predicting initial motion and bedload transport of sediment particles in the shallow marine environment. In: *Shelf Sediment Transport* (Ed. by D. J. P. Swift, D. B. Duane and O. H. Pilkey), pp. 61-82. Dowden, Hutchinson & Ross, Stroudsburg.

WHITE, J.R. & WILLIAMS, E.G. (1967) The nature of a fluvial

process as defined by settling velocities of heavy and light minerals. *J. sedim. Petrol.* **37**, 530-539.

YALIN, M.S. (1963) An expression for bedload transportation. *J. Hydraul. Div. Proc. Am. Soc. civ. Engrs.* **89**, 221-250.

YALIN, M.S. (1972) *Mechanics of Sediment Transport*. Pergamon Press, Oxford, 298 pp.

(Manuscript submitted 17 July 1984; revision received 29 August 1985)

## APPENDIX: NOTATION

$A$	coefficient of the $K'$ evaluation formula	$K_u = U_{sep}/\bar{U}$ , coefficient of mean backflow velocity in separation boundary layer of ripple or megaripple	
$A_b$	coefficient of the $K'_b$ evaluation formula	$P$	percentage of individual constituent grade within the sand grain size distribution, whose fall velocity is $W_p$
$B$	exponent of the $K'$ evaluation formula	$q$	total-load transport rate by immersed weight per unit width ( $\text{g}(\text{cm s})^{-1}$ )
$B_b$	exponent of the $K'_b$ evaluation formula	$q_b$	bedload transport rate by immersed weight per unit width ( $\text{g}(\text{cm s})^{-1}$ )
$C$	factor of the $K_b$ evaluation formula proposed by Bagnold	$q_s$	suspended-load transport rate by immersed weight per unit width ( $\text{g}(\text{cm s})^{-1}$ )
$C_D = (U^*/\bar{U})^2$	drag coefficient	$\bar{U}$	mean flow velocity ( $\text{cm s}^{-1}$ )
$C_{100} = (U^*/U_{100})^2$	drag coefficient, $3 \times 10^{-3}$	$U_{ces}$	threshold flow velocity of sand movement ( $\text{cm s}^{-1}$ )
$D$	grain size (cm)	$U_{sus}$	threshold flow velocity of sand suspension ( $\text{cm s}^{-1}$ )
$d_r$	horizontal migration distance of ripple or megaripple during one dominant tide (cm)	$U_{sep}$	mean backflow velocity in boundary layer within separation cell downstream of megaripple crest ( $\text{cm s}^{-1}$ )
$E = (\tau_o - \tau_{oc})/\tau_{oc}$	dimensionless excess shear stress	$U_{100}$	flow velocity 100 cm above bottom ( $\text{cm s}^{-1}$ )
$e_b$	bedload transport efficiency	$U_{100c}$	critical flow velocity 100 cm above bottom ( $\text{cm s}^{-1}$ )
$e_c$	factor of $e_b$ used by Bagnold (1966)	$U^* = (\tau_o/\rho)^{1/2}$	shear velocity ( $\text{cm s}^{-1}$ )
$e_g$	factor of $e_b$ used by Bagnold (1966)	$U_{*c}$	critical shear velocity ( $\text{cm s}^{-1}$ )
$e_s$	suspension efficiency	$\bar{U}_s$	mean transport velocity of suspended grains ( $\text{cm s}^{-1}$ )
$g$	acceleration due to gravity, $981 \text{ cm s}^{-2}$	$U_r$	migration velocity of ripple or megaripple ( $\text{cm s}^{-1}$ )
$H$	flow depth (cm)	$W$	fall velocity of suspended grains
$h_r$	height of ripple or megaripple (cm)	$\bar{W} = \Sigma P W_p$	effective mean fall velocity of heterogeneous suspended grains
$j$	total-load transport rate by dry mass per unit width ( $\text{g}(\text{cm s})^{-1}$ )	$W_p$	fall velocity of individual constituent grade (percentage $P$ ) within the sand grain size distribution
$j_b$	bedload transport rate by dry mass per unit width ( $\text{g}(\text{cm s})^{-1}$ )	$\omega = \tau_o \bar{U}$	total flow power per unit boundary area
$j_s$	suspended-load transport rate by dry mass per unit width ( $\text{g}(\text{cm s})^{-1}$ )	$\omega_t = \rho U_*^3$	the flow power expended against bottom friction per unit boundary area
$j'$	total-load transport rate in Guy <i>et al.</i> 's flume data ( $\text{g}(\text{cm s})^{-1}$ )	$\omega_1$	effective power used in bedload transport
$j'_s$	suspended load transport rate in Guy <i>et al.</i> 's flume data ( $\text{g}(\text{cm s})^{-1}$ )		
$j_r$	bed material transport rate from bedform migration measurements by dry mass per unit width ( $\text{g}(\text{cm s})^{-1}$ )		
$K$	total-load transport coefficient (bedload plus intermittent suspended-load)		
$K_b$	bedload transport coefficient		
$K' = K/C_D^{1/2}$	total-load transport coefficient		
$K'_b = K_b/C_D^{1/2}$	bedload transport coefficient		
$K'_{lim} = 6-9$	a limiting value of $K'_b$ proposed by Siegenthaler		

$\omega_2$	ineffective power dissipation in bedload transport	$\rho$	density of water ( $1 \text{ g cm}^{-3}$ )
$\omega_3$	effective power used in suspended-load transport	$\rho_s$	density of the sediment grains ( $2.65 \text{ g cm}^{-3}$ )
$\omega_4$	ineffective power dissipation other than $\omega_2$	$\rho_b$	bulk density of sediment ( $1.6 \text{ g cm}^{-3}$ )
$\tan \alpha$	coefficient of dynamic bedload friction	$\tau_o$	boundary shear stress ( $\text{dyne cm}^{-2}$ )
		$\tau_c$	critical shear stress ( $\text{dyne cm}^{-2}$ )
		$\theta$	$\theta = \tau_o / ((\rho_s - \rho)gD)$ , dimensionless shear stress

## Chapter 3

### Time series analysis of subtidal deposits

This chapter is published as:

Yang, C.S. & Nio, S.D., 1985. The estimation of palaeohydrodynamic processes from subtidal deposits using time series analysis methods. *Sedimentology*, 32: 41-57.



## The estimation of palaeohydrodynamic processes from subtidal deposits using time series analysis methods

CHANG-SHU YANG\* and SWIE-DJIN NIO†

\*Ministry of Geology and Mineral Resources, Marine Geological Survey, 526 Yan An Road West, Shanghai, China and †Comparative Sedimentology Division, Institute of Earth Sciences, University of Utrecht, The Netherlands

### ABSTRACT

Tidal bundle sequences are the characteristic large-scale cross-bedded sets with mud drapes deposited by strongly asymmetrical bidirectional tidal currents. By means of time series analysis of the bundle thickness of such sequences, the palaeohydrodynamic processes can be reconstructed. This technique involves: (1) Fourier analysis to test the periodicity of the bundle-thickness sequence and to estimate the periods and the phases of the most important periodic components; (2) filtering analysis to resolve the bundle-thickness sequence into different components (i.e. diurnal components, random variations, neap/spring components and longer period variations) and also to estimate the relative importance (amplitude) of each component.

From these analyses, useful information can be derived as to the palaeotidal regime (whether semi-diurnal or mixed) and also about the possible influence of non-tidal processes, such as storms (their strength, duration, frequency and direction). Results from a subrecent and an ancient example show that tidal currents and storm-induced currents are the most important hydrodynamic processes in the transport and deposition of sediment in these shallow marine environments.

### INTRODUCTION

#### Tidal bundle sequences

Large-scale cross-bedded sets are commonly formed in the channelized inshore parts of estuaries or tidal embayments, where bidirectional tidal currents are spatially separated into flood-dominated and ebb-dominated zones. The predominance of one of the tidal currents produces stable megaripples (sand waves) with a consistent asymmetry (Terwindt, 1970; de Raaf & Boersma, 1971; Allen, 1982). These megaripples show a regular pattern of behaviour during a flood/ebb cycle. A flood/ebb cycle consists of four stages, each reflected in the deposits of the megaripple: (1) the dominant current stage during which active megaripple migration results in the deposition of sandy foreset and bottomset laminae; (2) the slack-water stage following the dominant current during which a mud drape is deposited on the foresets and bottomsets; (3) the subordinate current stage during which a thin sandy layer is deposited on the megaripple slipface. There may also be some

erosion of the dominant-current deposits; (4) the slack-water stage following the subordinate current during which a second mud drape is deposited (Visser, 1980). The sandy foresets deposited during a single dominant tidal current make up a bundle (Visser, 1980; Siegenthaler, 1982; Nio, Siegenthaler & Yang, 1983). Each bundle is bounded by slack water mud drapes or, in the case of a slightly stronger subordinate current, by a mud drape and an erosional reactivation surface (de Mowbray & Visser, 1984). A series of bundles laid down by successive dominant currents is described as a tidal bundle sequence (Fig. 1). Preservation of a bundle sequence attests to high deposition rates, for example, lateral accretion on the inner bank of a curved tidal channel (van den Berg, 1982; Siegenthaler, 1982; Nio & Yang, 1983).

Since the sediment transport rate depends on the third or fourth power of the current velocity, a relatively minor change in tidal current velocity can bring about a major change in sediment transport

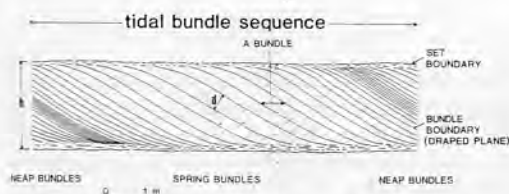


Fig. 1. Schematic drawing of a tidal bundle sequence. The bundle boundaries have thin mud drapes and/or erosional reactivation surfaces.  $d$ : thickness of a bundle measured perpendicular to the bundle boundary.  $h$ : set height, which can be used to estimate the original megaripple height provided the erosion due to subordinate currents is small and can be estimated.

rate. Changes in dominant tidal current velocity are therefore recorded in the thickness variation of successive bundles (provided the velocities remain high enough to allow active migration of the megaripples). Evidence of two tidal periodicities can be detected: neap/spring/neap tidal variations cause the thickening (towards spring) and thinning (towards neap) of successive bundles (Visser, 1980; Allen, 1981a; Allen & Homewood, 1984); and diurnal tidal variations cause the alternation of successive thick and thin bundles (Visser & de Boer, 1982). Superimposed on this regular pattern are random storm events and other non-tidal processes (such as growth and decay of individual megaripples and variations in river discharge) which can cause deviations of bundle thicknesses from the ideal pattern.

In the last few years, a number of fossil bundle sequences have been recognized: the Holocene deposits of the Oosterschelde basin, SW Netherlands (Visser, 1980; Van den Berg, 1982; Siegenthaler, 1982; Nio *et al.*, 1983), the Lower Cretaceous Folkestone Beds, SE England (Allen, 1981a, 1982), the Miocene in the vicinity of Fribourg, west Switzerland (Homewood & Allen, 1981; Allen & Homewood, 1984). The megaripple migration patterns and associated internal structures related to periodic tidal currents have also been observed in modern intertidal environments (Boersma, 1969; Terwindt, 1981; Boersma & Terwindt, 1981). Allen (1982) developed a physical model of tidal bundle deposition and applied it to the Folkestone Beds.

### Reconstruction of palaeotidal hydrodynamics

The recognition of tidal bundle sequences offers the possibility of analysing palaeotidal hydrodynamics. Research in this field has developed along two lines:

firstly the estimation of palaeotidal current velocities and/or ranges, and secondly the resolution of palaeotidal currents into different periodic components. Attempts to estimate palaeotidal current velocities and/or ranges have been made by Allen (1981b), Siegenthaler (1982), Nio *et al.* (1983), Allen & Homewood (1984) and Teysen (1984). Nio *et al.* (1983) estimated the palaeotidal range from tidal bundle-sequence data through a series of steps described briefly below.

It is assumed that the total bed material transport during a single dominant tide is represented by the material trapped on the leeside of the megaripple, which can be estimated from the bundle thickness and the megaripple height. The original megaripple height can only be estimated from the height of the preserved cross-bedded set. This will introduce some errors. However, the presence of brinkpoint structures in the upper part of some of the cross-bedded sets in the Oosterschelde Holocene section (van den Berg, 1982, fig. 12) suggests that the original megaripple height was not very much greater than the preserved set height.

There will be a relationship between the total amount of bed-material transported during a single dominant tide and the peak instantaneous bed-material transport rate, dependent on some integral of the velocity variation during the dominant current stage. The pattern of this velocity variation cannot, however, be determined for ancient deposits. In addition, the unknown limits of this integration bring about further complications in the calculation (Teysen, 1984), as do bedform lag effects. However, since most of the sediment transport occurs during times of peak velocity, the total sediment transport will depend mainly on these peak velocities and will not be very sensitive to the velocity variation over the whole dominant current phase. An empirical value for the integral of the velocity variation is therefore used to derive the peak instantaneous bed-material transport rate from the total bed-material transport during a dominant tide (Nio *et al.*, 1983).

Using an appropriate sediment transport function, the peak shear velocity during the dominant tide can be calculated from the peak bed material transport rate. The tidal range  $R$  can be estimated from the peak shear velocity  $U_*$  (Nio *et al.*, 1983):

$$R = U_*^2 T' / [\pi(gH)^{1/2}] \quad (1)$$

in which  $T'$  is the period of an ebb/flood cycle,  $g$  the acceleration due to gravity and  $H$  the water depth. For ancient deposits, the water depth can only be

inferred from the position of the tidal bundle-sequence with respect to the thickness of the whole fining-upward channel sequence. Estimations of palaeotidal ranges have also been made in different ways. Allen (1981b) calculated the ratio between neap and spring tidal ranges. Klein (1971, 1972) estimated the tidal range from considerations of the thickness of intertidal deposits.

This article concentrates on the second aspect of the palaeotidal hydrodynamic reconstruction, i.e. the resolution of different periodicities of current variation recorded in the tidal bundle sequence. These periodicities consist mainly of semidiurnal, diurnal and fortnightly (neap/spring/neap) tidal components, and non-tidal components (such as meteorological events). An important problem is how to separate all these different components and how to estimate the relative importance of each. In this article time series analysis methods are used in order to solve this problem.

## DATA

Two examples of subtidal deposits showing tidal bundle sequences were analysed. The first example is from a Holocene section in a construction pit at the mouth of the Oosterschelde tidal basin, south-western Netherlands (Fig. 2). Palaeogeographic reconstructions from old maps and the occurrence of *Mya arenaria* (a bivalve species imported by man from the Atlantic coast of North America at the end of the sixteenth century, Hessland, 1964) indicate that deposition took place during the seventeenth or eighteenth centuries (van den Berg, 1982). The bundle sequences are exposed at a depth of 17–12 m below present Mean Sea Level (Fig. 3), which, in view of the relatively young age of the deposits, should be similar to the original depositional depth. These bundle sequences consist of large-scale cross-bedded sets which were deposited within an actively migrating

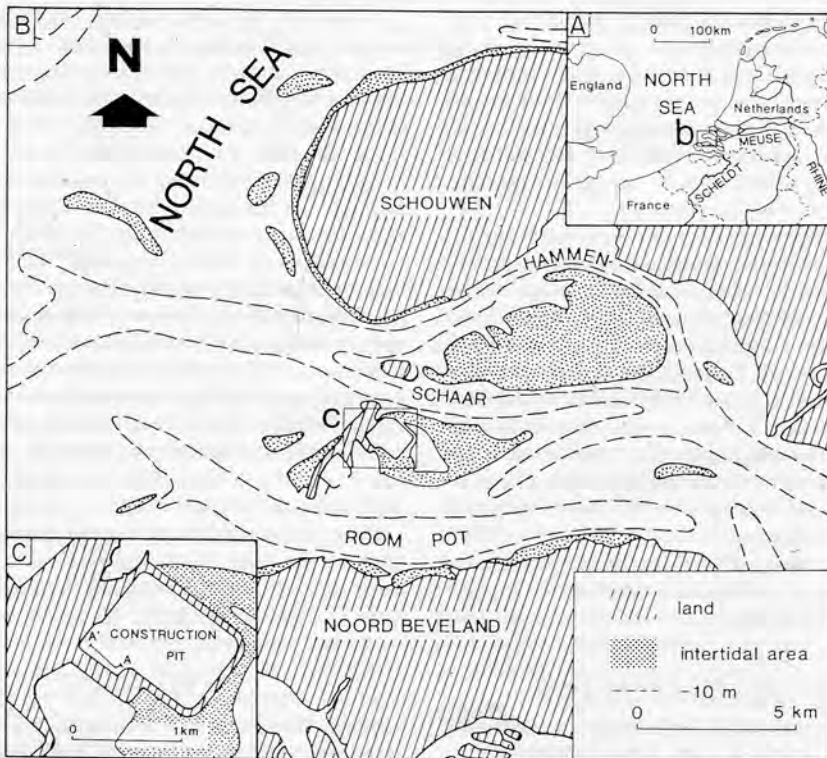


Fig. 2. Location of the construction pit, Oosterschelde tidal basin, SW Netherlands.

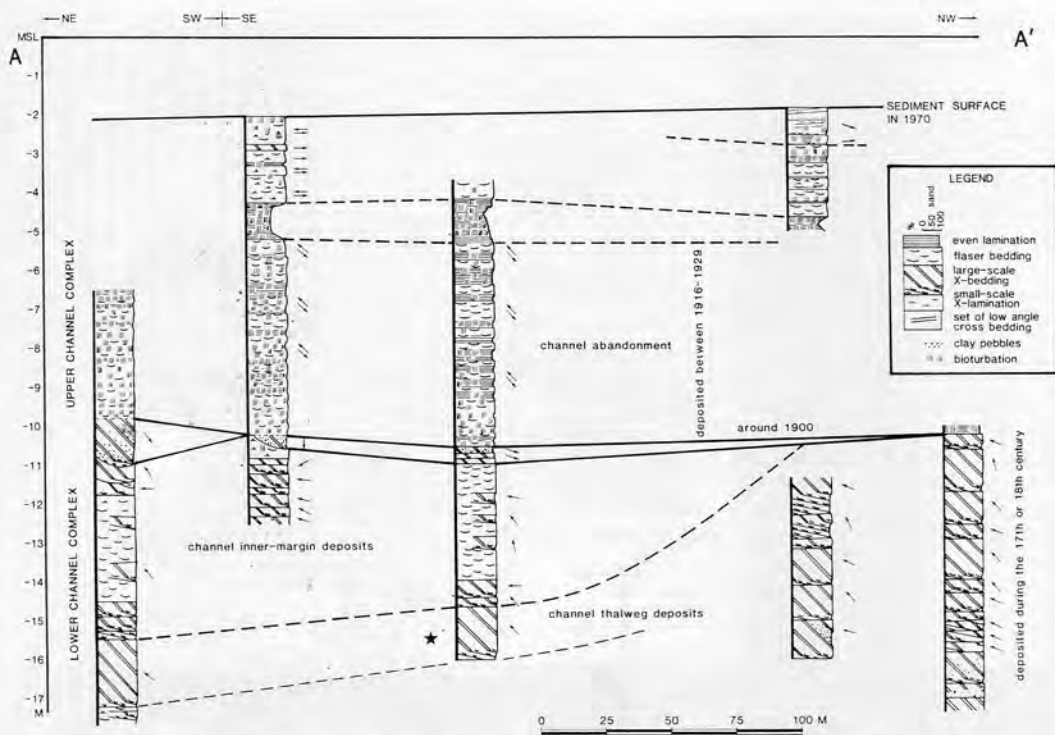


Fig. 3. Holocene stratigraphic framework of the Schaar construction pit, showing the superposition of two tidal channel sequences. The large-scale cross-bedded sets with tidal bundle sequences occur in the channel thalweg deposit unit. Asterisk indicates the position of the measured bundle sequence. For location of this section, see A-A' in Fig. 2(C) (modified after van den Berg, 1981).

tidal channel (van den Berg, 1982; Nio & Yang, 1983). The sets are about 2 m high and consist of fine-grained sand with a mean diameter of 0.19 mm. The foreset dip directions (NW) indicate that these sets were produced by a dominant ebb-current. The exposure displays a clear tidal bundle sequence from thin neap bundles to thick spring bundles, and then thin neap bundles again (Fig. 4). The thicknesses of 131 successive bundles measured by Visser (1980) will be used for this analysis.

The second example is from the Lower Tertiary (Eocene) Roda Sandstone Fm, southern Pyrenees, northern Spain (Fig. 5). The sediments were deposited in the channelized part of a subtidal estuarine environment (Nio & Siegenthaler, 1978). The sets are very similar in appearance to those of the Oosterschelde, showing a tidal bundle sequence of thick spring bundles and thin neap bundles (Fig. 6). The thicknesses of 41 successive tidal bundles were

measured in a set with a height of 1.5 m and a mean grain size of about 1 mm.

#### APPLICABILITY OF TIME SERIES ANALYSIS TO SUBTIDAL BUNDLE THICKNESS SEQUENCES

Time series analysis methods have proved to be powerful and effective tools. However, they can only be used where: (1) the observed variable is measurable quantitatively; (2) each observation of the variable represents an equal time interval; and (3) the successive observations are continuous, that is, no observations have been missed from the sequence. In the case of the bundle sequence data, the variable in question is the bundle thickness which can be measured quantitatively. Moreover, since each bundle is deposited by one dominant tidal current, each



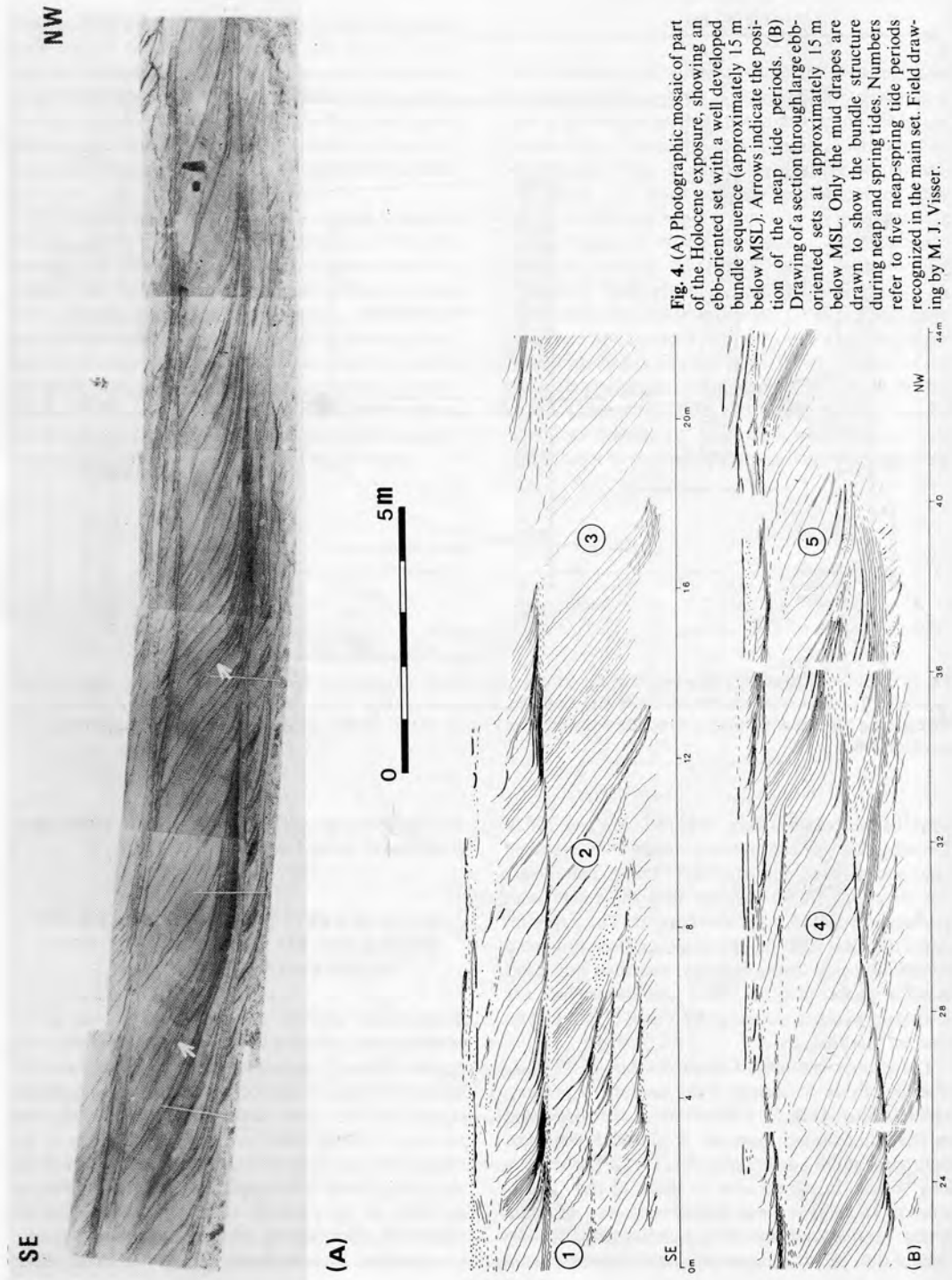


Fig. 4. (A) Photographic mosaic of part of the Holocene exposure, showing an ebb-oriented set with a well developed bundle sequence (approximately 15 m below MSL). Arrows indicate the position of the neap tide periods. (B) Drawing of a section through large ebb-oriented sets at approximately 15 m below MSL. Only the mud drapes are drawn to show the bundle structure during neap and spring tides. Numbers refer to five neap-spring tide periods recognized in the main set. Field drawing by M. J. Visser.



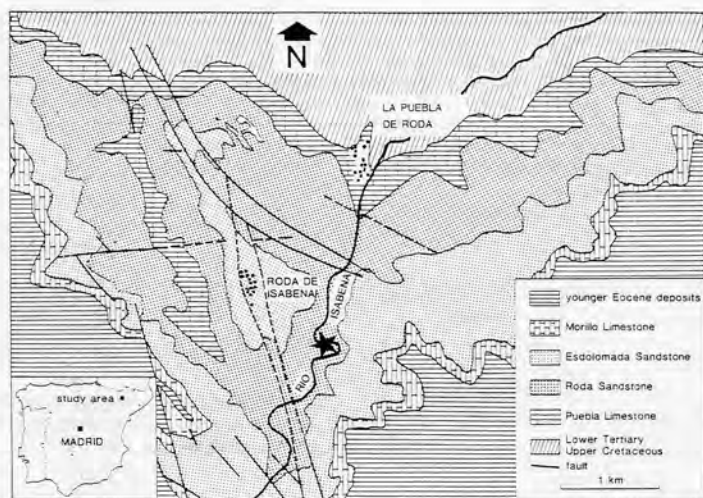


Fig. 5. Schematic geological map of the Isabena valley, southern Pyrenees, Spain. Asterisk indicates the position of the measured bundle sequence in Roda Sandstone.

SE

NW

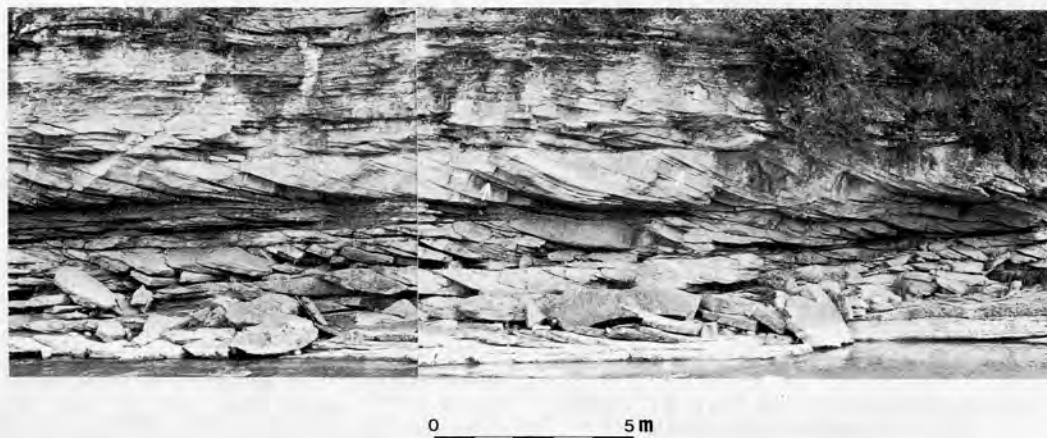


Fig. 6. Tidal bundle sequence of the Lower Tertiary (Eocene) Roda Sandstone, southern Pyrenees, Spain. Arrows indicate the position of the neap tide periods.

bundle represents the same period of time. Bundle formation is repeated at equal time intervals—the BTU (bundle time unit), which is 12.4 hr in a semidiurnal tidal system. However, the final requirement is not always met. The weaker currents of neap tide may not be able to bring about sand transport and megaripple migration will then cease. The resulting discontinuities in the bundle sequence may be the

major reason why time series analyses of some tidal bundle sequences from the Roda Sandstone did not show reasonable results.

Figure 7 shows the main procedures of the time series analysis. The data were processed by Fourier and filtering analysis. First, Fourier analysis was applied to examine the periodicity of the bundle-thickness sequence, and also to estimate the period

APPLICATION OF THE TIME SERIES ANALYSES

I. DATA: SUBTIDAL BUNDLE THICKNESS SEQUENCE

II. METHODS: TIME SERIES ANALYSIS

A. FOURIER ANALYSIS

1. Examine the periodicity of the bundle sequence
2. Determine { the frequencies (the periods) / the phase } of the dominant periodic components

B. TIME-TREND ANALYSIS ( FILTERING ) :

( using the period and phase parameters estimated from Fourier analysis )

1. resolve the bundle sequence into :
  - diurnal components
  - random variations
  - neap-spring components
  - longer period variations
2. Estimate the relative importance of each component.

III. RESULTS: PALEO-HYDRODYNAMIC PROCESSES

- A. PALEO-TIDAL REGIME : { semi-diurnal tide / mixed tide
- B. NON-TIDAL PROCESSES : storms etc.

Fig. 7. The application and results of the time series analyses.

(reciprocal of the frequency) and the phase of the most important periodic components. The phase gives the position of the first spring-tide bundle in the measured sequence with respect to the first measured bundle. Secondly, using these estimated periods and phases as parameters, the filtering analysis was carried out to resolve the bundle-thickness sequence into different components (such as the diurnal components, the random variations, the neap/spring components and the longer period variations). At the same time an estimation of the relative importance of each component (i.e. the amplitude averaged over the whole sequence) was made.

THE PERIODICITY OF THE BUNDLE THICKNESS SEQUENCES

Fourier analysis resolves the time sequence into its harmonic components, the contributions from each component being indicated by its amplitude or power (the square of amplitude). The resolution of the data can be displayed by plotting the power of the harmonic component versus its frequency, i.e. the power spectrum (Jenkins & Watts, 1968). Figures 8 and 9 are the power spectra of the tidal bundle sequences in the Oosterschelde and the Roda Sandstone. The most distinctive feature of all these power spectra is the existence of a very strong peak at frequencies of about

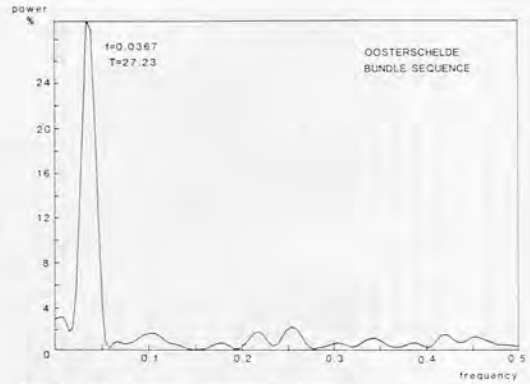


Fig. 8. The power spectrum from Fourier analysis of Subrecent tidal deposits in the Oosterschelde, SW Netherlands; bundle sequence 1 (N = 131).

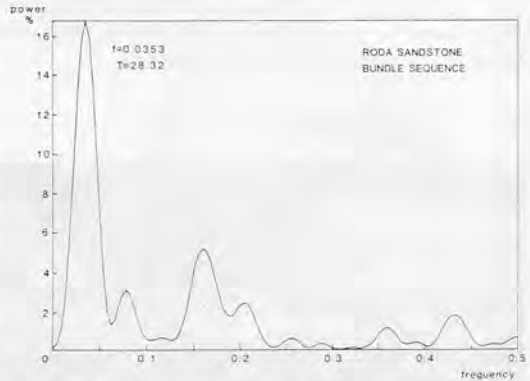


Fig. 9. The power spectrum from Fourier analysis of Lower Tertiary (Eocene) tidal deposits in the Roda Sandstone, southern Pyrenees, Spain; bundle sequence 2 (N = 41).

0.036 cycle BTU<sup>-1</sup>. The corresponding period is about 27.2–28.3 BTU, which tallies very well with the number of dominant-current events in a neap/spring/neap cycle in a semidiurnal system. The highest frequency that can be detected in the original data is 0.5 cycle BTU<sup>-1</sup>. The corresponding period is 2 BTU. Between these two frequencies there are a number of other peaks. Here we will consider mainly the dominant periodic component with the period of 27.2–28.3 BTU.

The period, phase and amplitude of the dominant periodic component are given in Table 1 and Fig. 10. These values should be considered as approximations because of the limited length of the analysed sequence and the consequently low-frequency resolution. The

**Table 1.** Summary of the frequencies, periods and phases of the most important periodic component estimated from Fourier analysis. The position of the first spring tidal bundle ( $M2$ ) is calculated from the phase (see Appendix B). The first neap tidal bundle differs from the first spring tidal bundle by  $M1$  (half the neap/spring period  $T$ ). These positions are not in integers because they are determined by least square fit of the dominant harmonic function over the whole measured bundle sequence rather than by the comparison within a few neighbouring bundles.

Example	Frequency $f$ (cycle/BTU)	Period $T=1/f$ (BTU)	$M1=T/2$ (BTU)	Phase (radian)	First spring tidal bundle position ( $M2$ )	First neap tidal bundle position	Amplitude $A$ (cm)
The subrecent Oosterschelde subtidal deposits bundle sequence 1 ( $N=131$ )	0.0367	27.23	13.61	-0.351	1.52	15.13	10.7
The Lower Eocene Roda Sandstone subtidal deposits bundle sequence 2 ( $N=41$ )	0.0353	28.32	14.16	-4.149	18.7	4.54	5.4

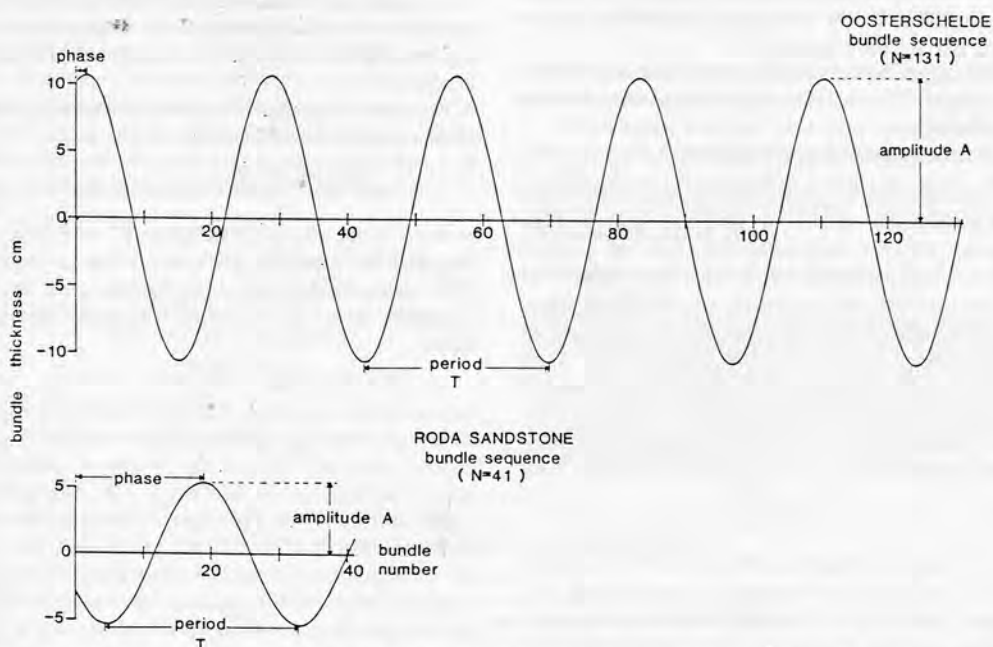


**Fig. 10.** The period, phase and amplitude of the most important periodic component estimated from Fourier analysis. The phase merely reflects at what point in the neap-spring cycle one happens to start measuring bundle thicknesses, and therefore as important only in characterizing a time-series.

frequency resolution is the reciprocal of  $N \cdot \Delta t$  where  $N$  is the total number of measurements, in this case the number of bundles, and  $\Delta t$  is the time interval represented by successive measurements, in this case the BTU (Jenkins & Watts, 1968). Although the period and the phase obtained from Fourier analysis agree well with the dominant periodic component of the bundle sequence data, the amplitude usually does

not. The constant value of the amplitude derived from Fourier analysis is the average amplitude over the whole sequence, while the actual amplitude of the dominant periodic component is not constant, but changes through the sequence. Theoretically, the changing amplitude of the dominant component implies that it may consist of several components with slightly different periods and frequencies, which

cannot be resolved by Fourier analysis in cases of low-frequency resolution. In order to estimate the changing amplitudes of this dominant periodic component, it is necessary to use filtering analysis. Filtering analysis requires a predetermined period and phase, which have already been derived from the Fourier analysis.

### FILTERING ANALYSIS TECHNIQUE

The results of the Fourier analysis show that the subtidal bundle thickness variation can be divided into different components:

- (1) Diurnal components with a period of about one day (2 BTU). This is the shortest period that can be detected from the original data.
- (2) Long-period components with a period of about a fortnight. This is the strongest component that can be detected.
- (3) Other superimposed variations.

The difference in periods allows separation of the components by means of filtering analysis. The filtering analysis technique (i.e. moving average method) has been widely used to separate a time series of observations into two parts: an underlying signal or meaningful pattern of variation, and a superimposed noise or random variation (Davis, 1973). It can also be used to separate a time series of observations into a lower frequency (longer period) variation part, and a higher frequency (shorter period) variation part. The filtering analysis is carried out step by step. With

each step, the higher-frequency component is separated out and the lower-frequency components are left in the residual data. In this way a series of components is derived with frequencies varying from the higher to the lower. The whole procedure is shown in the flow chart of Fig. 11.

The term 'filter' refers to the smoothing equation used in filtering analysis. This equation defines a smoothing interval known as the 'filter window' or 'data window', which is centred around the point whose smoothed value is to be estimated. Only the data within the window are used to calculate the smoothed value. For optimal separation of the different components, a special filter has been designed with appropriate 'filter window' length and smoothing equation for each component depending on its period and pattern of variations, as revealed by the Fourier analysis.

For separating diurnal periodic components from other components, a three-term filter is used:

$$\hat{d}_i = \frac{d_{i-1} + 2d_i + d_{i+1}}{4} \quad (i = 2 \text{ to } N-1) \quad (2)$$

where  $d_i$  is the measured thickness of the  $i$ th bundle and  $\hat{d}_i$  is the smoothed thickness of the  $i$ th bundle. This equation does not hold for the ends of the sequence, therefore we also have to apply one-sided filters:

$$\hat{d}_1 = \frac{2d_1 + d_2}{3} \quad (3)$$

$$\hat{d}_N = \frac{d_{N-1} + 2d_N}{3} \quad (4)$$

TIME-TREND ANALYSIS ( FILTERING ) PROCEDURE

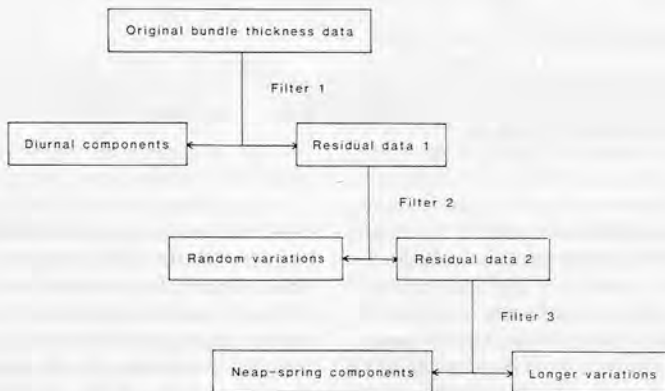


Fig. 11. Flow chart of the filtering analysis procedure.

In order to separate random variations from dominant periodic and other periodic components, the bundle thickness predicted by these periodic components must be estimated. To do this, the amplitude of the dominant periodic component must be known. However, this amplitude changes gradually through the whole sequence. Therefore the amplitude is calculated for a filter window of only 27 bundles (equivalent to dominant component period). In this way, harmonic analysis is carried out within a certain length of the sequence (the window) over which the change of the dominant harmonic amplitude is negligible. By moving the window along the sequence, we can apply harmonic analysis to the whole bundle thickness sequence with changing amplitude.

The equation for estimating the 'filter window' average value was derived from the least-square fit of the dominant harmonic function (see Appendix A). The calculation is carried out in two steps. First the amplitude  $A_i$  and the mean bundle-thickness  $\bar{d}_i$  of the dominant periodic component were estimated from the data window centred around the  $i$ th bundle:

$$A_i = (27 \sum d_j X_j - \sum d_j \sum X_j) / \{27 \sum X_j^2 - (\sum X_j)^2\} \quad (5)$$

$$\bar{d}_i = \{\sum d_j - A_i \sum X_j\} / 27 \quad (6)$$

$$X_j = \cos \{\pi(j - M2) / M1\} \quad (7)$$

$$(j = i - 13 \text{ to } i + 13, \quad i = 14 \text{ to } N - 13)$$

where  $d_j$  is the  $j$ th bundle thickness in the residual data from previous filtering.  $X_j$  represents the bundle thickness variation due to the dominant periodic component.  $M1$  is the number of flood/ebb cycles between neap and spring tides, and  $M2$  is the position of the first spring tidal bundle in the measured sequence. Using these estimates as parameters of the dominant harmonic function, the  $i$ th bundle thickness  $\bar{d}_i$  due to the dominant component is calculated using:

$$\bar{d}_i = \bar{d}_i + A_i \cos(\pi(i - M2) / M1) \quad (8)$$

For the ends of the sequence (i.e. the first and last 13 bundles)  $A_i$  and  $\bar{d}_i$  of the dominant periodic component cannot be estimated from equations (5) and (6). Therefore  $\bar{d}_{14}$  and  $A_{14}$  must be used for the first 13 bundles:

$$\bar{d}_i = \bar{d}_{14} + A_{14} \cos(\pi(i - M2) / M1) \quad (i = 1 \text{ to } 13) \quad (9)$$

and  $\bar{d}_{N-13}$  and  $A_{N-13}$  for the last 13 bundles:

$$\bar{d}_i = \bar{d}_{N-13} + A_{N-13} \cos(\pi(i - M2) / M1) \quad (i = N - 12 \text{ to } N) \quad (10)$$

This approximation will cause some distortions in the filtering results at the ends of the sequence.

For separating the fortnightly periodic component from the longer period variation, a filter with the same length (27 bundles) but a different smoothing equation is used:

$$\hat{d}_i = \frac{\sum_{j=i-13}^{i+13} d_j}{27} \quad (i = 14 \text{ to } N - 13) \quad (11)$$

For the ends of the sequence, a similar averaging equation with a shorter window length is used:

$$\hat{d}_i = \frac{\sum_{j=1}^{i+13} d_j}{i+13} \quad (i = 1-13) \quad (12)$$

$$\hat{d}_i = \frac{\sum_{j=i-13}^N d_j}{N - (i - 14)} \quad (i = N - 12 \text{ to } N) \quad (13)$$

where  $d_j$  is the  $j$ th bundle thickness in the residual data from the previous filtering.

The filtering analysis gives the bundle-thickness deviation due to each different component. According to the Error Propagation Law, the tidal range deviation  $s(R)$  can be estimated from the bundle-thickness deviation  $s(d)$ :

$$s(R) = s(d) \delta R / \delta d \quad (14)$$

where  $\delta R / \delta d$  is the derivative of the tidal range with respect to the bundle thickness, which can be derived from a series of functions relating the tidal processes to the bundle sequence deposits (Nio *et al.*, 1983, equations 10, 11, 14, 15 and 18). The final expression for this derivative is:

$$\frac{\delta R}{\delta d} = \frac{\bar{R}}{nd} \quad (15)$$

where  $\bar{d}$  is the mean tidal bundle thickness ( $\bar{d} = \sum_i^N d_i / N$ ),  $\bar{R}$  is the mean tidal range estimated from bundle-sequence deposits as discussed in the introduction and  $n$  is the exponent in a sediment transport function. The experimentally determined value of  $n = 3$  (Nio *et al.*, 1983) is used in this article. Substituting  $\bar{R}/nd$  for  $\delta R / \delta d$ , equation (14) becomes:

$$s(R) = s(d) \bar{R} / nd \quad (16)$$

### FILTERING ANALYSES OF THE OBSERVED SUBTIDAL BUNDLE SEQUENCES

The curves in Figs 12 and 13 (results summarized in Table 2) show different components resolved from the original data using filtering methods. Diurnal components (curve B) are greatest around spring tides and



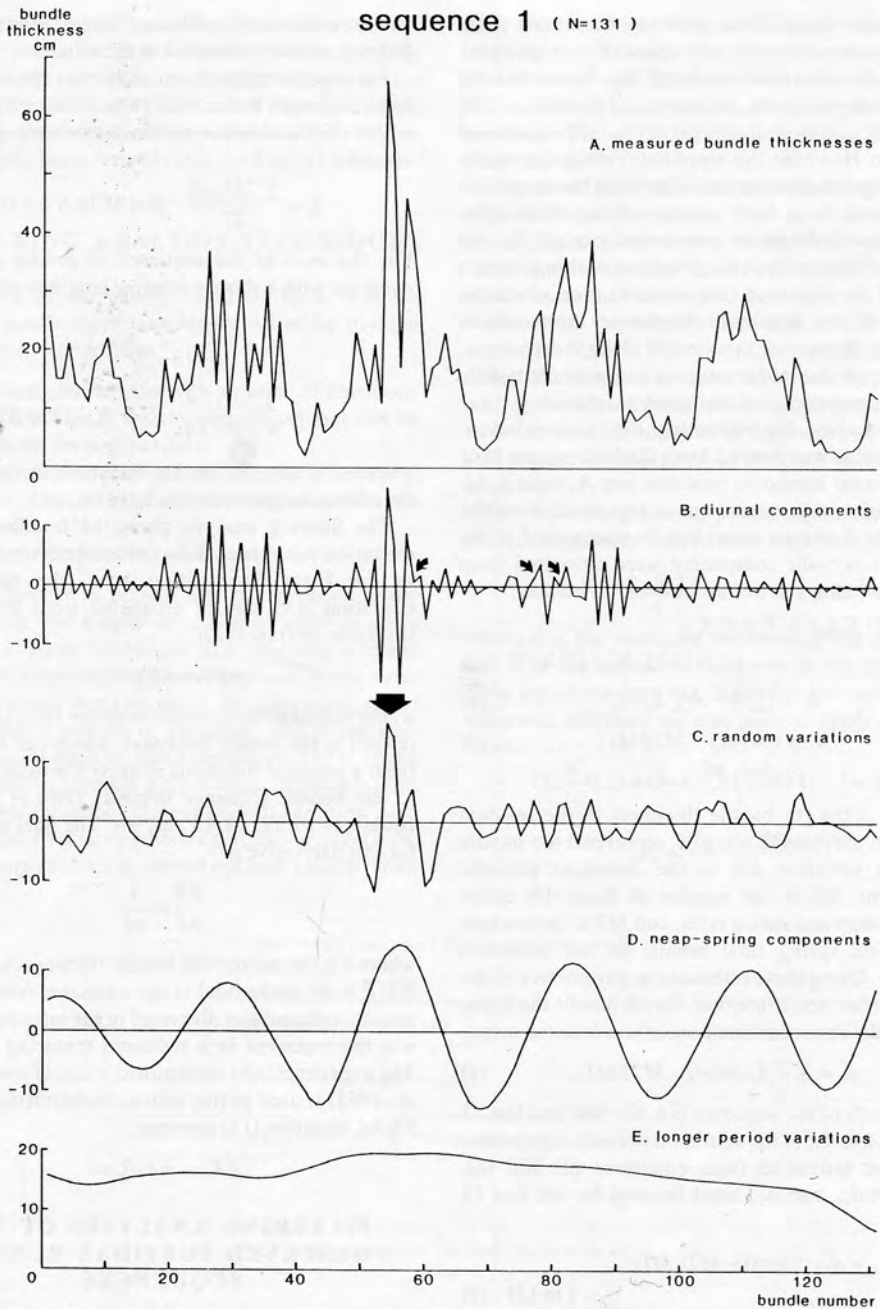


**Fig. 12.** Palaeotidal components, random variations and longer-period variations derived from filtering analysis, Subrecent tidal deposits in the Oosterschelde, SW Netherlands; bundle sequence 1 ( $N=131$ ). The arrows in curve B indicate the departures of the diurnal variation from the regular pattern. Arrowed large deviation in curve C is likely to have been caused by a storm event.

## sequence 2 (N=41)

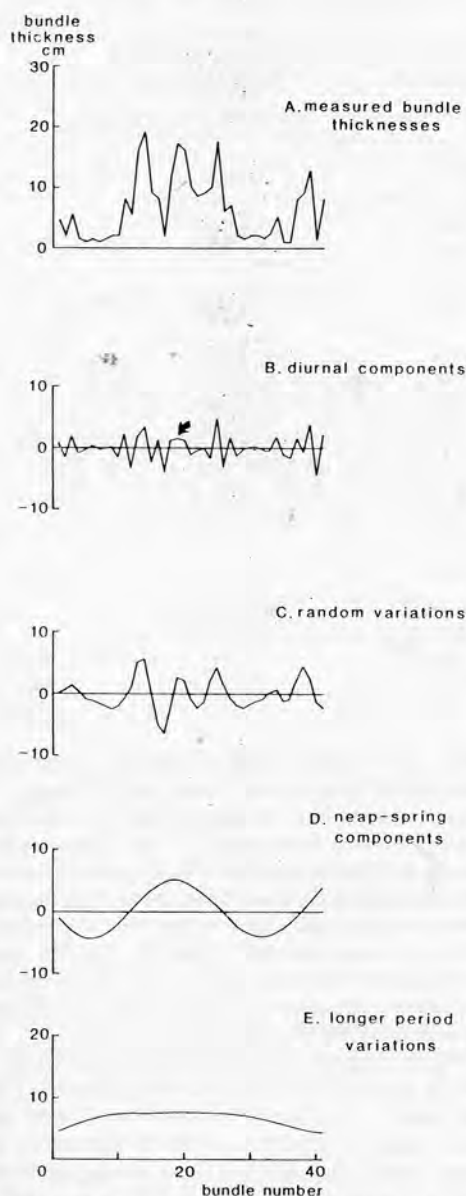


Fig. 13. Palaeotidal components, random variations and longer-period variations derived from filtering analysis. Lower Tertiary (Eocene) tidal deposits of the Roda Sandstone, southern Pyrenees, Spain; bundle sequence 2 ( $N=41$ ). The arrow in curve B indicates the departure of the diurnal variation from the regular pattern.

are least around neap tides. The mean tidal range deviations due to diurnal components estimated from equation (16) are 0.16 m (sequence 1) and 0.25 m (sequence 2). Normally diurnal variations show a regular alternation of successive thicker-than-average and thinner-than-average bundles, but in places there are departures from this regular pattern (arrowed in curve B, Figs 12 and 13). The regular diurnal variation must have been disturbed by some superimposed short-period fluctuation. These smaller departures may be caused by random factors, such as meteorological fluctuations, variations of megaripple dimensions, fluvial discharge fluctuations and measurement errors.

Curve C shows random variations with respect to the regular neap/spring cycle. The maximum tidal range deviations caused by these random variations are estimated to be 0.93 m (sequence 1) and 1.06 m (sequence 2). The random variations have a maximum duration of about 1–1.5 days and are irregularly distributed throughout the sequence.

The neap/spring tidal components (curve D) cause tidal range deviations of 0.81 m (sequence 1) and 0.84 m (sequence 2). The period of this variation is about 14 days (27–28 bundles). Therefore the bundle sequences described here were deposited within a relatively short time, about 2.5 months for sequence 1 and less than one month for sequence 2.

Longer period variations are apparent in curve E. Apart from the distortion at the ends of the sequence caused by the filtering analysis itself, there is still a general trend of, at first, a gradual increase in bundle thickness, and then a gradual decrease. It seems therefore that the megaripple developed and grew, reached its climax, and then declined. In other words, individual megaripples have a life-span.

## DISCUSSION AND CONCLUSIONS

## Tidal regime

The tidal regime is characterized by the value of the tide characteristic ratio  $F'$ :

$$F' = \frac{\text{major diurnal tidal component amplitude}}{\text{major semi-diurnal tidal component amplitude}}$$

If  $F'$  is less than 0.25, the tide is semidiurnal. If  $F'$  lies between 0.25 and 1.5, the tide is mixed, but predominantly semidiurnal. When  $F'$  lies between 1.5 and 3, the tide is said to be mixed, but predominantly diurnal.

**Table 2.** Summary of the estimated palaeotidal ranges, palaeotidal components and maximum random deviations. The mean tidal ranges are estimated from the bundle sequence data as discussed in the introduction, while the tidal ranges during neaps and springs are derived from the mean tidal ranges and the neap/spring amplitudes

Example	Oosterschelde subtidal bundle sequence 1	Roda Sandstone subtidal bundle sequence 2
Original data		
Mean bundle thickness (cm)	16.5	7.3
Megaripple height (cm)	197.7	150
Foreset dip (°)	30	30
Grain size:(cm)	0.0186	0.1
Time period of ebb/flood cycle (hr)	12.4	12.4
Inferred parameter		
Water depth (cm)	1450	1500
Results		
Tidal range $R$ (cm) { mean	276	359
neap	195	275
spring	357	443
Semidiurnal tidal components amplitude (cm)	179	222
Diurnal tidal components amplitude (cm)	16	25
Neap/spring tidal components amplitude (cm)	81	84
$F' = \frac{\text{major diurnal components}}{\text{major semidiurnal components}}$	0.09	0.11
Tide type	Mesotidal semidiurnal	Meso/macrotidal semidiurnal
Maximum random deviation { amplitude (cm)	93	106
duration (day)	1-1.5	1-1.5

Finally, the tide is diurnal if  $F'$  exceeds 3 (Lisitzin, 1974). The necessary component amplitudes can be derived from the results of the filtering analysis. The amplitude of the major semi-diurnal tidal components (the sum of the main lunar semi-diurnal component and the main solar semi-diurnal component) is assumed to be half the spring tidal range (equation 1). The amplitude of the major diurnal component is approximately the mean tidal range deviation due to diurnal tidal components. The calculated value of  $F'$  is 0.09 for sequence 1, which is quite similar to the present-day value in the Oosterschelde of 0.10. For sequence 2 the ratio is 0.11. Therefore these tidal bundle sequences were deposited in a semi-diurnal tidal regime.

### Random variations

The random variations as shown in curve C may be caused by many factors, such as storms, spatial and temporal variations in megaripple dimensions, variable fluvial discharges, and measurement errors. How-

ever, it is unlikely that changes in megaripple dimensions would cause such abrupt changes in bundle thicknesses. In addition, fluvial discharges were relatively unimportant in the Oosterschelde during the deposition of the bundle-sequence because the discharge of the River Schelde had been diverted to the Westerschelde Inlet by this time (Gottschalk, 1971). It seems probable, therefore, that the large random deviations with rapid variations (e.g. the one indicated by the arrow in Fig. 12, curve C, sequence 1) were caused by storm events.

As an example of storm effects, Fig. 14 (M. J. Visser, pers. comm.) shows a recent storm event near the mouth of the Oosterschelde. The wind speed was about  $20 \text{ m s}^{-1}$  (about 8-9 on the Beaufort scale), the duration was 1.5-2 days and the tidal range deviation due to this storm was about 1 m. This is very similar to the inferred major storm events from the subrecent Oosterschelde subtidal bundle sequence.

A storm tends to displace water and so influences tidal currents. After a storm, the water will seek its own equilibrium level, resulting in a reverse influence

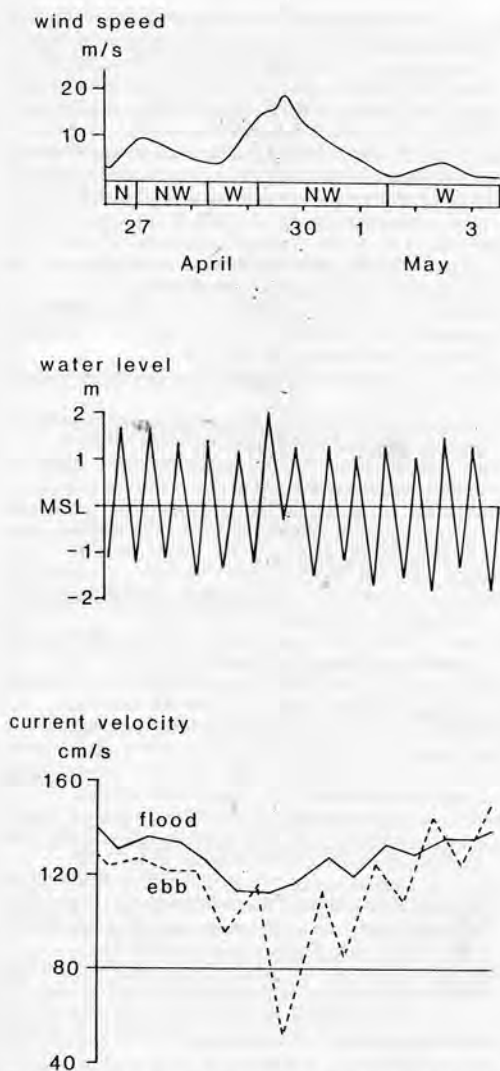


Fig. 14. The wind speed, water level fluctuations and tidal current velocity variation during a recent storm event near the mouth of Oosterschelde (see text for explanation; M. J. Visser, pers. comm.).

on the currents. This auto-compensation effect must also be recorded in the tidal bundle-thickness sequence, resulting in the characteristic feature of several successive unusually thick bundles followed by several successive unusually thin bundles, or vice versa. The direction of the storm event in sequence 1 (arrowed in Fig. 12, curve C) seems to be coincident

with the dominant ebb current direction, resulting in thicker tidal bundle deposits.

As for the Lower Tertiary (Eocene) Roda Sandstone, the maximum tidal range deviations for the presumed storm events are 1.06 m (estimated from the maximum random deviation of the bundle thickness). Since the grain size of these deposits is very coarse (1 mm), storm-induced currents would have had an important influence in the transport of sediments which had a relatively high threshold of movement. Storms may not only have disturbed the regular diurnal component pattern, but may also have affected the regular neap/spring component pattern.

### Long-period variations

The reason for the long-period variations reflected in curve E is not clear. Although megaripple variations are unlikely to cause sudden changes in bundle thicknesses, they may influence the long-period variations. A possible example is the climbing of one megaripple on to another. In such a case, the sediment transported by the dominant tidal currents will be trapped at the lee-side of the new (upper) megaripple; the migration of the old megaripple will slow down until it is finally overtaken by the new one. Allen (1982) discussed the relative movement and mutual influence of neighbouring bedforms and the resulting processes of bedform creation/destruction. In addition, any change in the orientation of the section through the cross-bedded sets of three-dimensional megaripples may cause some variations in the observed bundle sequence.

Besides these factors, some long-period tidal components such as the monthly components group, the semi-annual and annual components group, etc. (Lisitzin, 1974) may also have some influence on the longer-period variations. For example, in curve D of Fig. 12 the amplitude of the neap/spring component shows a longer-period variation. This changing amplitude suggests that it may consist of two or more components with slightly different frequencies. When these components are in phase, the amplitude will be largest, and when these components are out of phase, the amplitude will be smallest. However, in order to resolve these different components, a considerably longer time series would be required. In practice, the bundle sequence data available at present are much too short to allow this kind of analysis.

In conclusion, we can reconstruct the palaeohydrodynamic regime of tidal-bundle sequences with the aid of time series analysis. A summary of the results is

given in Table 2. The subrecent Oosterschelde subtidal bundle sequence was deposited in a semi-diurnal mesotidal environment (tidal range: 1.95–3.57 m, semi-diurnal component amplitude: 1.79 m, diurnal component amplitude: 0.16 m, neap/spring component amplitude: 0.81 m) with some large random deviations (amplitude: 0.93 m), which are likely to have been caused by storm events. This is quite similar to the modern Oosterschelde environment (tidal range: 2.06–3.46 m, semi-diurnal component amplitude: 1.73 m, diurnal component amplitude: 0.18 m, neap/spring component amplitude: 0.70 m. Data from Getijtafels voor Nederland, 's-Gravenhage, 1966, in Siegenthaler, 1982). The Lower Tertiary (Eocene) Roda Sandstone subtidal bundle sequence was deposited in a semi-diurnal meso-macrotidal regime (tidal range: 2.75–4.43 m, semi-diurnal component amplitude: 2.22 m, diurnal component amplitude: 0.25 m, neap/spring component amplitude: 0.84 m). The large irregular deviations of this bundle sequence may reflect a strong storm influence.

### ACKNOWLEDGMENTS

The authors wish to acknowledge and thank A. M. H. Nolet (Theoretical Geophysical Department, Institute of Earth Sciences, University of Utrecht) and P. L. de Boer for their assistance with the calculation of Fourier analysis. Appreciation and thanks are also due to C. Siegenthaler, J. H. van den Berg, M. J. Visser, D. B. Smith, and the members of the Comparative Sedimentology Division for their helpful and interesting discussion. The manuscript has benefited from critical reviews by Tessa de Mowbray and P. L. de Boer. We are grateful for the constructive criticism and valuable suggestions from J. S. Bridge and P. A. Allen.

### REFERENCES

- ALLEN, J.R.L. (1981a) Lower Cretaceous tides revealed by cross-bedding with mud drapes. *Nature*, **289**, 579–581.
- ALLEN, J.R.L. (1981b) Palaeotidal speeds and ranges estimated from cross-bedding sets with mud drapes. *Nature*, **293**, 394–396.
- ALLEN, J.R.L. (1982) Mud drapes in sand wave deposits: a physical model with application to the Folkestone Beds (Early Cretaceous, Southeast England). *Phil. Trans. R. Soc. A*, **306**, 291–345.
- ALLEN, P.A. & HOMEWOOD, P. (1984) Evolution and mechanics of a Miocene tidal sandwave. *Sedimentology*, **31**, 63–81.
- BERG, J.H. VAN DEN (1981) Rhythmic seasonal layering in a mesotidal channel fill sequence, Oosterschelde Mouth, the Netherlands. In: *Holocene Marine Sedimentation in the North Sea Basin* (Ed. by S.-D. Nio, R. T. E. Schüttenhelm and Tj. C. E. van Weering). *Spec. Publ. int. Ass. Sediment.* **5**, 147–159. Blackwell Scientific Publications, Oxford.
- BERG, J.H. VAN DEN (1982) Migration of large-scale bedforms and preservation of crossbedded sets in highly accretional parts of tidal channels in the Oosterschelde, SW Netherlands. *Geologie Mijnb.* **61**, 253–263.
- BOERSMA, J.R. (1969) Internal structures of some tidal megaripples on a shoal in the Westerschelde estuary, the Netherlands. *Geologie Mijnb.* **48**, 409–414.
- BOERSMA, J.R. & TERWINDT, J.H.J. (1981) Neap-spring tide sequences of intertidal shoal deposits in a mesotidal estuary. *Sedimentology*, **28**, 151–170.
- DAVIS, J.C. (1973) *Statistics and Data Analysis in Geology*. Wiley, London.
- GOTTSCHALK, M.K.E. (1971) *Stormloeden en rivieroverstromingen in Nederland I: de periode vóór 1400*. Assen.
- HESSLAND, J. (1964) On the Quaternary Mya period in Europe. *Ark. Zool.* **37A**, 1–51.
- HOMEWOOD, P. & ALLEN, P.A. (1981) Wave-, tide- and current-controlled sandbodies of Miocene Molasse, western Switzerland. *Bull. Am. Ass. Petrol. Geol.* **65**, 2534–2545.
- JENKINS, G.M. & WATTS, D.G. (1968) *Spectral Analysis and its Applications*. Holden-Day, New York.
- KLEIN, G. DE V. (1971) A sedimentary model for determining paleotidal range. *Bull. geol. Soc. Am.* **82**, 2585–2592.
- KLEIN, G. DE V. (1972) Sedimentary model for determining paleotidal range. *Bull. geol. Soc. Am.* **83**, 539–546.
- LISITZIN, E. (1974) *Sea-level Changes*. Elsevier, Holland.
- MOWBRAY, T. DE & VISSER, M.J. (1984) Reactivation surfaces in subtidal channel deposits, Oosterschelde, Southwest Netherlands. *J. sedim. Petrol.* in press.
- NIO, S.-D. & SIEGENTHALER, C. (1978) A Lower Eocene estuarine-shelf complex in the Isabena valley, Spain. *Com. Studies sedim. Univ. Utrecht, Rep. no. 18*, pp. 1–44.
- NIO, S.-D., SIEGENTHALER, C. & YANG, C.S. (1983) Megaripple cross-bedding as a tool for the reconstruction of the palaeohydraulics in a Holocene subtidal environment, S.W. Netherlands. *Geologie Mijnb.* **62**, 499–510.
- NIO, S.-D. & YANG, C.S. (1983) Dynamics, geometry and sequential upbuilding of large subtidal bedforms. *Proc. int. Symp. Sedimentation on the Continental Shelf, with Special Reference to the East China Sea*, pp. 20–36. China Ocean Press, Beijing.
- RAAF, J.F.M. DE & BOERSMA, J.R. (1971) Tidal deposits and their sedimentary structures. *Geologie Mijnb.* **59**, 479–504.
- SIEGENTHALER, C. (1982) Tidal cross-strata and the sediment transport rate problem: a geologist's approach. *Mar. Geol.* **45**, 227–240.
- TERWINDT, J.H.J. (1970) Observation on submerged sand ripples with heights ranging from 30 to 200 cm occurring in tidal channels of S.W. Netherlands. *Geologie Mijnb.* **49**, 489–501.
- TERWINDT, J.H.J. (1981) Origin and sequences of sedimentary structures in inshore mesotidal deposits of the North Sea. In: *Holocene Marine Sedimentation in the North Sea Basin* (Ed. by S.-D. Nio, R. T. E. Schüttenhelm and Tj. C. E. van Weering). *Spec. Publ. int. Ass. Sediment.* **5**, 4–26. Blackwell Scientific Publications, Oxford.



TEYSSEN, T. (1984) Physical model and FORTRAN IV program to estimate paleotidal flow velocities from features of sandwaves. *Comput. Geosci.* in press.

VISSER, M.J. (1980) Neap-spring cycles reflected in Holocene subtidal large-scale bedform deposits: a preliminary note. *Geology*, **8**, 543-546.

VISSER, M.J. & DE BOER, P.L. (1982) The effect of the diurnal inequality on tidal sediments: a tool in the recognition of tidal influences. *Abstr. int. Ass. Sediment. 3rd Eur. Meeting*, Copenhagen, pp. 88-90.

(Manuscript received 30 June 1983;  
revision received 15 June 1984)

### APPENDIX A: DERIVATION OF HARMONIC LEAST-SQUARE ESTIMATION FOR 'FILTER WINDOW' AVERAGE VALUE

According to harmonic analysis, the  $i$ th tidal bundle thickness can be estimated as:

$$\begin{aligned} \hat{d}_i &= \bar{d}_i + A_i \cos\left(\frac{2\pi i}{2M1} + \phi\right) \\ &= \bar{d}_i + A_i \cos\left(\frac{2\pi(i-M2)}{2M1}\right) \end{aligned} \quad (A1)$$

where

- $\hat{d}_i$ : the  $i$ th tidal bundle thickness calculated from the harmonic function of the dominant periodic component;
- $\bar{d}_i$ : the mean tidal bundle thickness estimated from the data window centred around the  $i$ th bundle;
- $A_i$ : the amplitude of the dominant periodic component estimated from the data window centred around the  $i$ th bundle;
- $\phi$ : the phase of the dominant periodic component;
- $M1$ : the number of the bundles from neap to spring tide;
- $M2$ :  $-2M1\phi/2\pi$  the position of the first spring tidal bundle.

$\bar{d}_i$  and  $A_i$  can be found by taking the least-squares fit of the harmonic function  $\hat{d}_j$  in the bundle thickness data within the filter window centred around the  $i$ th bundle. This leads to:

$$\sum_{j=i-13}^{i+13} (\hat{d}_j - d_j)^2 = \min \quad (A2)$$

where  $d_j$  is the  $j$ th bundle thickness in the residual data from previous filtering. Substituting (A1) into (A2):

$$\sum_{j=i-13}^{i+13} \left[ \bar{d}_i + A_i \cos\left(\frac{2\pi(j-M2)}{2M1}\right) - d_j \right]^2 = \min. \quad (A3)$$

For the sum to reach the minimum, its derivative with respect to  $\bar{d}_i$  and  $A_i$  must be zero, giving the simultaneous normal equation set:

$$\begin{vmatrix} 27 & \sum X_j \\ \sum X_j & \sum X_j^2 \end{vmatrix} \begin{vmatrix} \bar{d}_i \\ A_i \end{vmatrix} = \begin{vmatrix} \sum d_j \\ \sum d_j X_j \end{vmatrix} \quad (A4)$$

where

$$X_j = \cos\left(\frac{2\pi(j-M2)}{2M1}\right). \quad (A5)$$

The sum  $\sum$  is over the whole window ( $J=i-13$  to  $i+13$ ).

The solution to equation (A4) gives the least-square estimate of  $\bar{d}_i$  and  $A_i$  for the window centred around the  $i$ th bundle:

$$A_i = \frac{27 \sum d_j X_j - \sum d_j \sum X_j}{27 \sum X_j^2 - (\sum X_j)^2} \quad (A6)$$

$$\bar{d}_i = (\sum d_j - A_i \sum X_j) / 27. \quad (A7)$$

### APPENDIX B: NOTATION

- $A_i$  dominant harmonic amplitude estimated by least-square fit of dominant harmonic function within data window centred around the  $i$ th bundle.
- $d_i$  measured thickness of the  $i$ th tidal bundle.
- $\hat{d}_i$  smoothed thickness of the  $i$ th tidal bundle.
- $d_j$  the  $j$ th bundle thickness in the residual data from previous filtering.
- $\bar{d}_i$  mean bundle thickness estimated by least-squares fit of dominant harmonic function within data window centred around the  $i$ th bundle.
- $\bar{d} = \sum_{i=1}^N d_i / N$ , mean tidal bundle thickness over whole measured sequence.
- $F'$  characteristic ratio of tide.
- $f$  frequency of dominant harmonic component.
- $g$  acceleration due to gravity.
- $H$  water depth.
- $M1 = T/2$ , number of tidal bundles from neap to spring tide.
- $M2 = -2M1\phi/2\pi$ , position of the first spring tidal bundle in measured sequence as counted from the first measured bundle.
- $N$  number of measured tidal bundles.
- $n$  exponent of sediment transport function.
- $R$  tidal range.
- $\bar{R}$  mean tidal range.

- $s(x)$  standard deviation of  $x$ .  
 $T$  period of dominant harmonic component.  
 $T'$  period of ebb/flood cycle.  
 $t$  time interval between the  $i$ th bundle and the first bundle of the sequence.
- $U_*$  shear velocity during peak tidal current.  
 $X_j = \cos\{\pi(j - M2)/M1\}$ , thickness variation pattern due to dominant harmonic component.  
 $\Delta t$  time interval between successive observations.  
 $\phi$  phase of dominant harmonic component.

## Chapter 4

### Estimates of sand transport in the Oosterschelde tidal basin using current velocity measurements

This chapter is published as:

Yang, C.S., 1986. Estimates of sand transport in the Oosterschelde tidal basin using current velocity measurements. *Marine Geology*, 72: 143-170.

## ESTIMATES OF SAND TRANSPORT IN THE OOSTERSCHELDE TIDAL BASIN USING CURRENT-VELOCITY MEASUREMENTS\*

CHANG-SHU YANG\*\*

*Comparative Sedimentology Division, Institute of Earth Sciences, University of Utrecht, Utrecht (The Netherlands)*

(Received July 27, 1984; revised and accepted September 30, 1985)

### ABSTRACT

Yang, C.-S., 1986. Estimates of sand transport in the Oosterschelde tidal basin using current-velocity measurements. *Mar. Geol.*, 72: 143-170.

Estimates of sand transport have been made from mid-depth velocity measurements in the Oosterschelde tidal basin, southwestern Netherlands. This involves: (1) The use of a two-region composite boundary-layer model in deriving the local spatially averaged bed shear stress from velocity distributions over large bedforms (megaripples and sandwaves). The two regions are divided at 100 cm above the bed, with an outer-region roughness length of 1.5 cm and an inner-region roughness length of 0.15 cm. (2) The application of a modified Bagnold's transport equation with the transport coefficient  $K$  depending on dimensionless excess shear stress in the form of a power law.

The calculations indicate very active sand movement in the present-day Oosterschelde tidal basin. Local sediment circulation may develop around shoals. Channel-floor erosion may occur in parting areas of sediment transport. The net sediment transport is mainly in the ebb direction.

Estimates of sediment budget for the last 20 years show that large amounts of sand have been eroded from the Oosterschelde tidal basin and transported to the ebb-delta area. These results are comparable with other estimates from echo-sounding data, reflecting the rapid adjustment of the basin to the increased tidal prism. Such active sediment redistribution and major morphological evolution processes would have important influence on the structural organization and sequential development of estuary-ebb delta deposits. Information about the sedimentary processes in present-day estuary tidal basins is valuable for a better understanding of ancient examples.

### INTRODUCTION

The estimation of sediment transport in marine environments is of particular importance to marine geology and sedimentology. Based on the compilation of existing boundary-layer and sediment-transport measurements in marine environments, Sternberg (1972) proposed a procedure for predicting the

\*Comparative Sedimentology Division, Publ. No. 57.

\*\*Present address: Ministry of Geology and Mineral Resources, Marine Geological Survey, 526 Yan An Road West, Shanghai, China.

mass transport rates of sands over the sea floor. Gadd et al. (1978) made a regional description of the sediment movement on the New York Shelf by applying the transport formulae of Bagnold (1941, 1956, 1963), Einstein (1950) and Yalin (1963) to observations of near-bottom current velocity and surficial grain size.

Sternberg's and Gadd et al.'s methods were applied in shallow marine environments with small-scale roughness elements (less than 10 cm in height) where current velocities can be measured at 100 cm above the sea bed and a single constant drag coefficient of  $3 \times 10^{-3}$  can be used. In the case of areas with megaripples or sandwaves, however, serious problems arise as to the specification of the velocity field above the bed and the determination of the bed shear stress from boundary-layer velocity distributions. In addition, some problems remain in the application of the sediment transport equation. Although Bagnold's transport equation has been widely applied in marine environments, its exact form is still controversial.

There has been a remarkable progress in the field of boundary layers and sediment transport in recent years (Nowell, 1983), which provided a good base for sediment transport estimations. In this paper a two-region composite boundary-layer model is used to allow the determination of the local spatially averaged bed shear stress from mid-depth velocity measurements over megaripples. These data, combined with a modified version of Bagnold's transport equation, are used for the regional description of sand movements and the estimation of sand transport in the Oosterschelde tidal basin, southwestern Netherlands. The results are comparable with sand transport determined from successive echo-sounding data, indicating active sand redistribution and rapid adjustment of the estuary tidal basin to tidal prism variations. This suggests that the methods presented in this paper may have wide application in tidal marine environments with large bedforms.

#### DATA

The Oosterschelde tidal basin is one of the tidal inlets and estuaries related to the Rijn-Maas-Schelde fluvial system in southwestern Netherlands (Fig.1). The present-day Oosterschelde basin has three major tidal channels: the Roompot in the south, the Hammen in the north and the Schaar between. These large tidal channels are 20-40 m deep and separated by several shoals. The tides are semidiurnal. At Zierikzee the mean tidal ranges are 206 cm at neap and 346 cm at spring tide respectively (Siegenthaler, 1982). The bottom deposits consist mainly of fine sand with mean grain size about 0.2 mm. These sediments have been studied by many authors. Terwindt (1973) discussed the sand movement along the tidal inlets and estuaries of southwestern Netherlands. The sediment movement in connection with tidal hydrodynamic processes in the Oosterschelde basin were also discussed by Van den Berg (1982), Siegenthaler (1982), Nio et al. (1983), and Yang and Nio (1985). Van den Berg (1984) discussed the morphological changes and sand movement in the ebb-delta area of the Oosterschelde based on echo-sounding data.



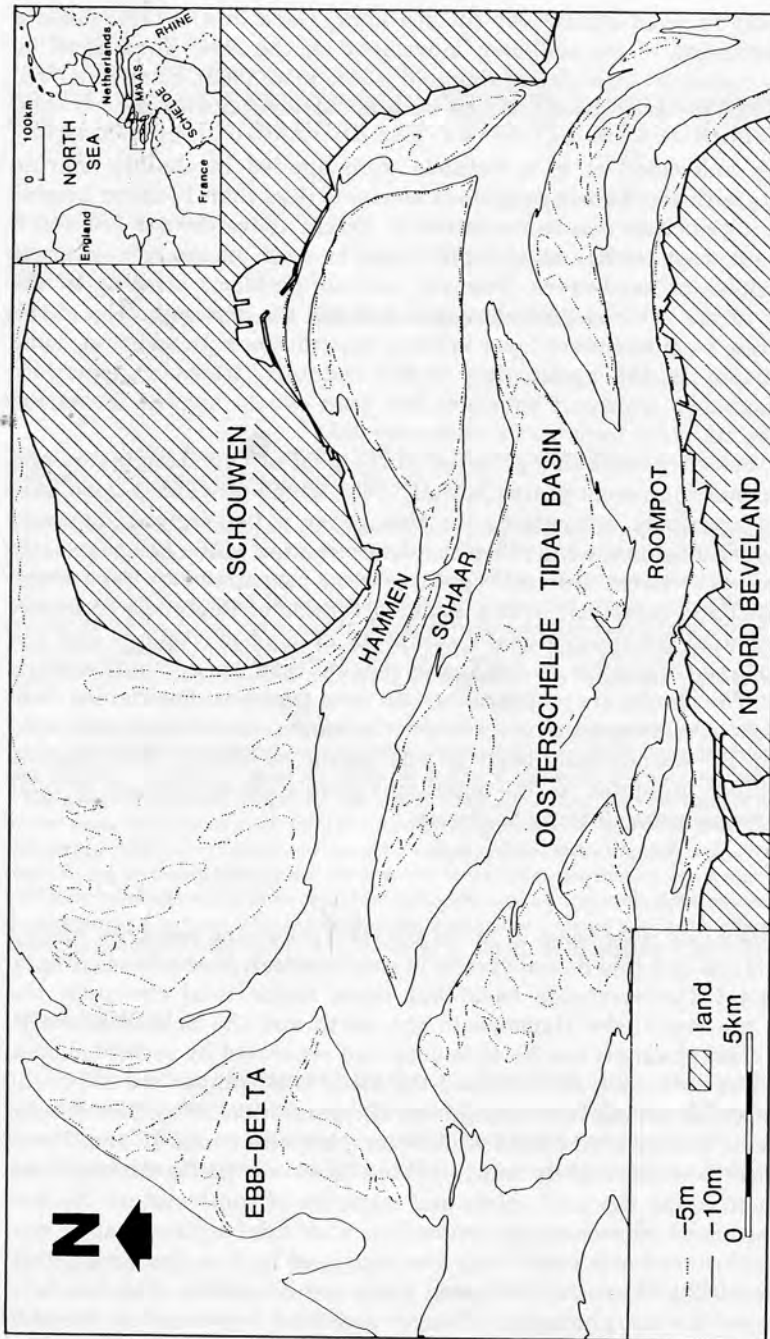


Fig.1. The Oosterschelde tidal basin in the southwestern Netherlands.

As part of the extensive measurement program of the Delta Project, 19 measuring stations were occupied within the major tidal channels of the Oosterschelde during the spring of 1980 and an additional three measuring stations in 1981 (Fig.2). Interval-averaged velocities and current directions were recorded at 0.5 lunar hour intervals using Flachsee (a self-recording, automatic propeller current meter) at half the water depth. The mid-depth velocities were used for two reasons: (1) to estimate the local spatially averaged bed shear stress over megaripples instead of the bed shear stress from near-bottom velocity measurements which are spatially variable over megaripples; (2) they show less disturbance from outside than the velocities near the water surface.

Data obtained at seven locations in the Vuilbaard on December 22, 1983 were used to examine the velocity profile over megaripples (Fig.3). Velocities and current directions were measured at 1 m, 2 m, and 4 m above the bottom, as well as 8 m (or 4 m, depending on water depth) and 2 m below the water surface. Wave activities during the measurements were negligible. Mean velocity and current direction averaged over a 2-min period were recorded during a complete flood/ebb cycle using AZTM, i.e. an Acoustic sand-transport meter developed at the Delft Hydraulics Laboratory. It determines the velocity of suspended-particles from the Doppler frequency shift between the received acoustic signal and the transmitted acoustic signal (Jansen, 1978).

#### BOUNDARY LAYER VELOCITY PROFILE

##### *The boundary layer over large bedforms*

Numerous measurements have verified the general existence of a logarithmic velocity distribution in the lower region of fully turbulent currents (approximately below 1 m from the bed) (Bowden, 1962; Sternberg, 1968; Langhorne, 1981). Such velocity profiles can be described by the Karman-Prandtl equation:

$$U(Z) = U_* / k \ln (Z/Z_0) \quad (1)$$

where  $U(Z)$  is the velocity at the height  $Z$  above the bed,  $U_*$  is the shear velocity,  $k$  is Von Karman's constant (0.4) and  $Z_0$  is the roughness length. Equation (1) has been widely used to determine the bed shear stress from near-bottom velocity measurements over rippled and plane beds.

In the case of non-uniform flow over large bedforms (megaripples or sandwaves), however, the bed shear stress changes over the bedform. Taylor and Dyer (1977) calculated a 75% reduction in shear stress from the crest to the trough of a sandwave. Bed shear stresses calculated using the Karman-Prandtl equation therefore pertain to local positions on a bedform; they cannot be considered to be values local-spatially averaged over a number of bedforms (Bridge and Jarvis, 1982).

Local-spatially averaged value of bed shear stress over large bedforms can

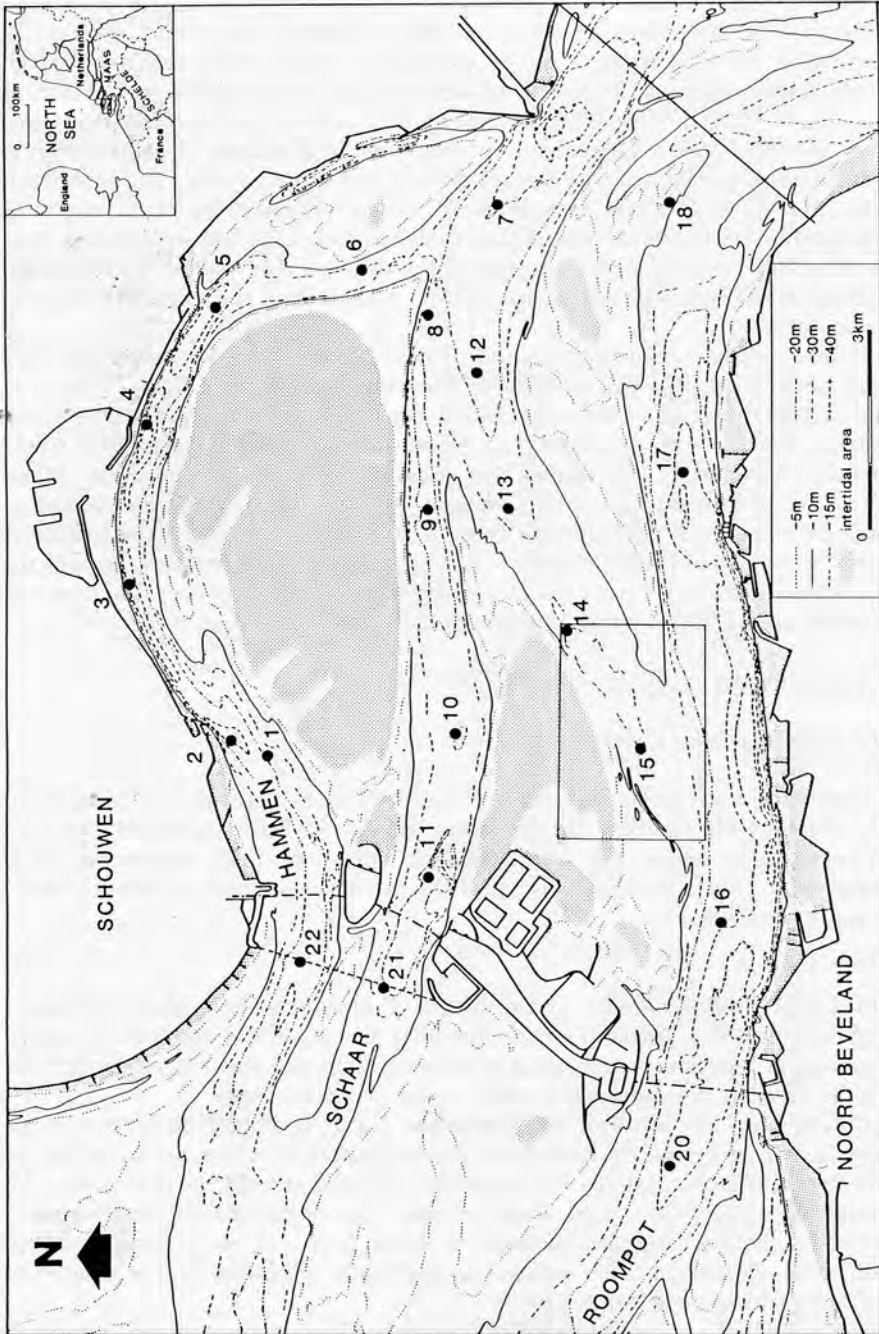


Fig.2. Measurement stations for the mid-depth tidal current velocity in the Oosterschelde tidal basin, southwestern Netherlands. Box denotes Fig.3.

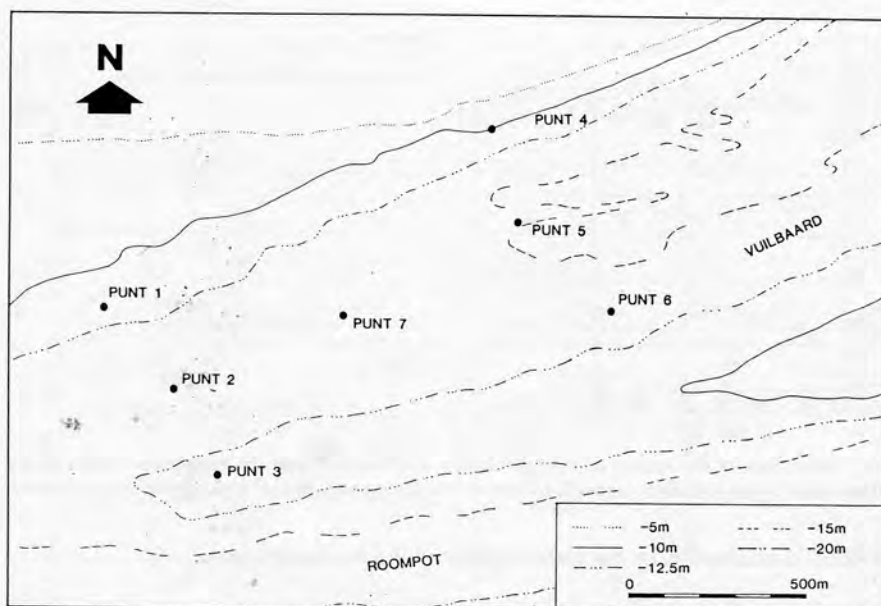


Fig.3. Measurement sites for tidal-current velocity profiles at the Vuilbaard. The location of this figure is indicated in Fig.2 (near station 15).

be determined from velocity measurements at some distance from the bed (Dyer, 1970). As Rubin and McCulloch (1980) noted, the bedforms are contained in a flow layer having a thickness of several bedform heights. Large bedforms will therefore have thick boundary layers, which should be taken into consideration for the estimation of the local spatially averaged bed shear stress.

It is commonly accepted that the logarithmic velocity profile has proved to be a good approximation to the velocity distribution observed throughout the full depth of wide open-channel flows (Blatt et al., 1980). It is also well known, however, that the law of the wall can be applied only to the lower region of the boundary layer, i.e., approximately below 100 cm from the bed. This raises an interesting question: why is it impossible to extrapolate the slope of the velocity profile at heights of more than 2 m directly to the vicinity of the bed? In other words, what is the difference in the velocity distributions between the two regions? We will therefore discuss the velocity distributions in two regions: an inner-region where the law of the wall is valid (approximately below 100 cm from the bed) and an outer-region where the law of the wall cannot be applied (above approximately 100 cm from the bed).

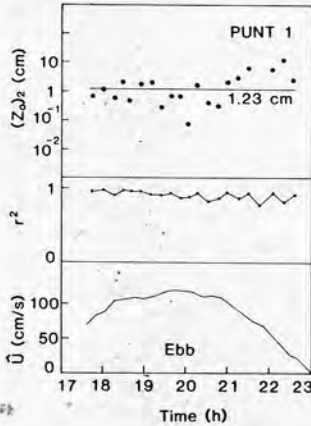


Fig.4. Variations of the square of the correlation coefficient  $r^2$  and the roughness length in the outer-region of the boundary layer  $(Z_0)_2$  over an ebb period at punt 1.  $\bar{U}$  is the depth-mean velocity.

#### *Velocity distribution in the outer-region of the boundary layer*

The velocity profiles from 1 m above the bed to 2 m below the water surface were measured over a complete flood/ebb cycle at seven locations in the Vuilbaard. Velocities  $U(Z)$  were plotted against  $\ln Z$ ; straight lines were fitted by least-squares to the points, with five points in each profile. The velocity distribution was considered logarithmic if the square of the correlation coefficient  $r^2$  is larger than 0.8, and for these profiles the value of  $(Z_0)_2$ , the roughness length in the outer-region, was calculated from the least-squares fit of straight lines to the  $U(Z) - \ln Z$  plots. In the case of  $r^2$  smaller than 0.8, the velocity distribution was classified as non-logarithmic, and no value for roughness length was calculated.

The square of the correlation coefficient  $r^2$  and the roughness length  $(Z_0)_2$  obtained from each measuring location are shown in Figs.4 and 5. Also shown are the time-velocity curves of the tidal currents at each location. Around peak tidal currents, the velocity distribution was logarithmic approximately 95% of the time (ranging from 90 to 100% at individual locations; Table 1). The mean  $r^2$  value is 0.93. During late decelerating stages and around slack-water periods, however, the velocity distribution was logarithmic only 34% of the time (ranging from 10 to 75% at individual locations; Table 1). The mean  $r^2$  value is 0.54, indicating larger velocity fluctuations during the turning of tidal currents than those during established tidal currents.

The dispersion range and the mean value of the roughness lengths during peak currents show little variation between flood and ebb currents and among different measuring locations. The mean value of  $(Z_0)_2$  varies from 0.99 to 2.46 cm at individual locations (Table 1). It is therefore possible to derive a temporally and spatially averaged value of  $(Z_0)_2$ . In Fig.6 all data are



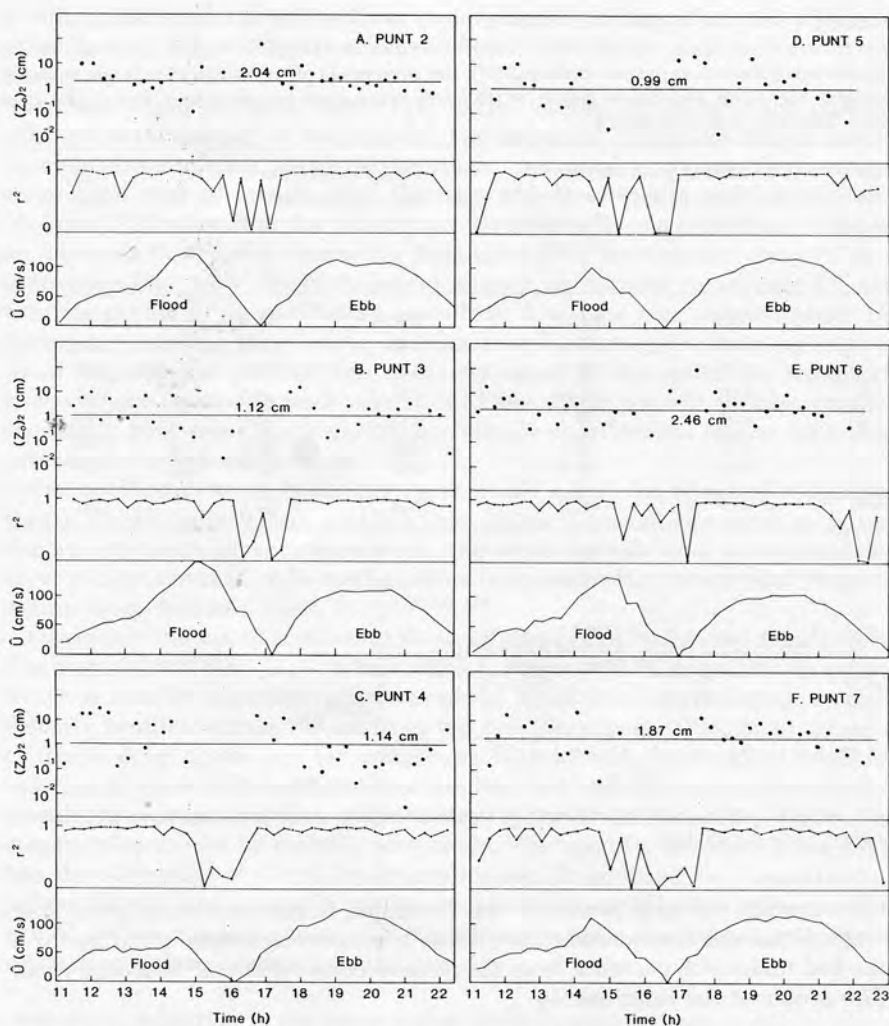


Fig.5. Variations of the square of the correlation coefficient  $r^2$  and the roughness length in the outer-region of the boundary layer  $(Z_0)_2$  over a complete flood/ebb cycle at punts 2-7.  $\bar{U}$  is the depth-mean velocity.

superimposed on the same time scale. The temporally and spatially averaged value of  $(Z_0)_2$  for all data is found to be 1.5 cm.

This mean value of roughness length reflects the overall effects of the megaripples. It is comparable with the roughness length associated with large roughness elements calculated from rivers or theoretical considerations. Middleton and Southard (1978) estimated a roughness length of 2.3 cm from a

TABLE 1

The square of mean correlation coefficient ( $\bar{r}^2$ ), the percentage of time when  $r^2$  is larger than 0.8 (%) and the mean roughness length in the outer-region of the boundary layer ( $(Z_0)_2$ ) at seven locations in the Vuilbaard

Punt	Around peak current		Late deceleration and slack water		$(Z_0)_2$ (cm)
	$\bar{r}^2$	% of time $r^2 > 0.8$	$\bar{r}^2$	% of time $r^2 > 0.8$	
1	0.93	100.0	0.86	75.0	1.23
2	0.93	93.8	0.48	28.6	2.04
3	0.95	96.8	0.51	37.5	1.12
4	0.96	100.0	0.61	45.5	1.14
5	0.92	89.7	0.42	10.0	0.99
6	0.93	96.6	0.64	42.9	2.46
7	0.92	90.0	0.40	21.4	1.87
Mean	0.93	94.9	0.54	33.8	1.50

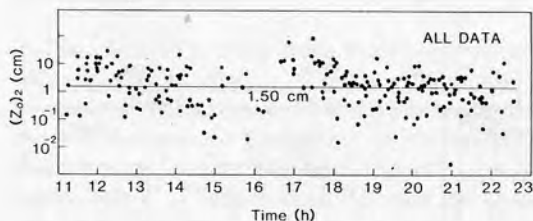


Fig.6. Variation of the roughness length in the outer region of the boundary layer  $(Z_0)_2$  over a flood/ebb cycle for all data.

66-min-average velocity profile in the Columbia River (maximum grain size: 28 cm). Allen and Homewood (1984) chose a roughness length of 1.0 cm for a dune bed under ebb currents from theoretical considerations. Wooding et al. (1973) proposed the relationship

$$Z_0 = 2h(h/\lambda)^{1.4} \quad (15 < \delta/Z_0 < 1000) \quad (2)$$

between roughness length  $Z_0$  and bedform dimensions, where  $h$  is bedform height,  $\lambda$  is bedform wavelength and  $\delta$  is boundary-layer thickness. Using eqn.(2), megaripples with heights of 0.5 m and wavelengths of 10 m, as commonly observed in the Oosterschelde, should have a roughness length of 1.51 cm, which is in close agreement with the average value of 1.50 cm. This is only an approximate comparison, however, because the mean roughness length is related not only to megaripple dimensions, but also to the overall distribution pattern of the megaripples.

The individual value of  $(Z_0)_2$  calculated from each logarithmic velocity-

profile measurement (Fig.6) still varies considerably. This reflects the effects of other factors, e.g. acceleration, wave effects, turbulence, and bedform variations.

In fact, Fig.6 suggests that  $(Z_0)_2$  varies according to whether current velocity is increasing or decreasing. The apparent roughness length would become larger during accelerating stage, and smaller during decelerating stage than that of steady flow. Soulsby and Dyer (1981) and Lavelle and Mofjeld (1983) show that the velocity profile departs from a logarithmic form in an unsteady flow, and a correction term related to "acceleration length" or a time-dependent eddy viscosity model should be applied in solving for the velocity profile of an oscillatory turbulent flow. One can underestimate  $U_*$  during accelerating stage and overestimating  $U_*$  during decelerating stage if usual logarithmic profiles are used. As most of the sediment transport, however, occurs during peak velocities (Allen, 1982), we will mainly consider the steady peak flows and logarithmic velocity distributions can be applied to determine the bed shear stress.

The oscillatory wave boundary layer would affect the effective roughness length significantly (Grant and Madsen, 1979). However, the wave activities during our measurements were weak, therefore the effects of wave boundary layer can be assumed to be negligible as compared with strong tidal currents within deep channels.

Obviously the use of a constant mean value of  $(Z_0)_2$  will cause some errors. The dispersion of most  $(Z_0)_2$  values in Fig.6, however, is within a certain range, which is smaller than the variations of the roughness length estimated from velocity profiles within 100 cm from the bed (Sternberg, 1968, fig.6). Since a constant drag coefficient (or roughness length) has been widely used for velocity profiles within 100 cm from the bed, the use of a constant roughness length for velocity profiles in the outer-region of the boundary layer over megaripples should be equally acceptable. The use of a constant mean  $(Z_0)_2$  has the advantage of simplicity in application. In addition, in reconstructing palaeo-hydrodynamic conditions the actual velocity profiles are unknown. The use of such a constant mean  $(Z_0)_2$  therefore provides the only simple way of estimating palaeo-current parameters.

#### *Velocity distribution in the inner-region of the boundary layer*

The inner-region of the boundary layer (less than 100 cm from bed) is the region where the Karman-Prandtl equation or the quadratic stress law (Sternberg, 1968, 1972) have been widely used for direct estimation of the bed shear stress. Although numerous investigations have verified the general existence of the logarithmic velocity distribution in the inner region, there is still a wide range of estimates for  $(Z_0)_1$ , the mean roughness length in the inner-region of the boundary layer. Dyer (1970) used a constant roughness length of 0.15 cm for the local spatially averaged bed shear stress over megaripples. This value lies between Sternberg's (1968) estimate of 0.067 cm

over small ripples and Langhorne's (1981, 1982) estimate of 0.55 cm over sandwave crests where higher bed shear stresses are expected. On the grounds of the similarity in conditions (local spatially averaged shear stress of the currents over megaripples in tidal channels), 0.15 cm is considered as a suitable value of  $(Z_0)_1$ .

#### *The composite boundary-layer structure*

The above discussion suggests that although logarithmic velocity profiles are good approximations to the velocity distribution throughout the whole boundary layer, the roughness lengths in the outer-region are different from those in the inner-region. This implies a composite boundary-layer structure.

The existence of such a composite boundary-layer structure is verified by observations that two or more scales of bedforms commonly exist in equilibrium with a single steady flow (Guy et al., 1966; Harms et al., 1974; Southard, 1975; Boothroyd and Hubbard, 1975; Dalrymple et al., 1978). As discussed by Rubin and McCulloch (1980), where ripples are superimposed on sandwaves the flow within a distance of several ripple heights from the bed should have a velocity profile with a slope that defines a shear velocity within the ripple range. The overlying flow, within several sandwave heights of the bed, should have a velocity profile with a slope that defines a shear velocity within the sandwave range. Shear velocity can vary with height above the bed because the effective hydraulic roughness varies with height above the bed. Away from the bed, the roughness is that associated with large bedforms. Approaching the bed, the surface of a large bedform approximates a plane bed, and the roughness decreases to that associated with smaller superimposed bedforms or individual grains. This decrease of roughness in the vicinity of the bed increases the slope of the velocity profile, and causes a decrease in the shear velocity near the bed, where small bedforms can exist on large bedforms.

Smith and McLean (1977) measured detailed velocity profiles of spatially averaged flow over three orders of superimposed bedforms in the Columbia River. These velocity profiles can be divided into three logarithmic profile sections with different slopes. In the innermost region the velocity field is related to the local skin friction. The roughness length varies from about 0.055 to 0.3 cm, being associated with grain sizes or the thickness of the saltation zone. In the outer region the velocity field is related to the spatially averaged bed shear stress, including form drag on bedforms. The roughness length ranges from about 1 cm to 6 cm, being related to the dimensions of the largest bedforms. Based on an experiment on the Oregon shelf, Chriss and Caldwell (1982) also demonstrated a velocity profile consisting of two distinct logarithmic profile regions. The stress calculated from the upper one reflects the influence of form drag, while that determined from the lower one reflects the skin friction.

In fact there is only one velocity profile, which reflects both the small and the large roughness elements of the bed. The transition between the inner-

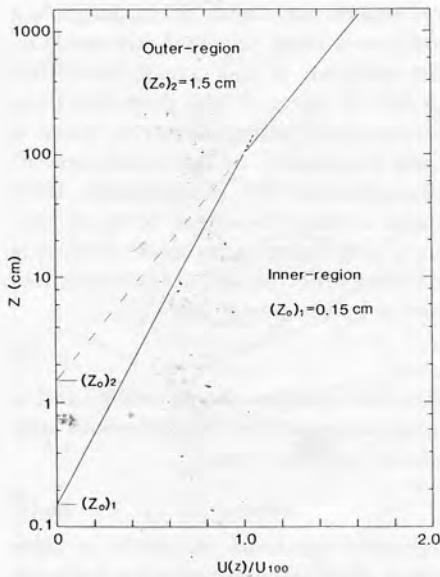


Fig.7. Normalized velocity profile of the two-region composite boundary-layer model. The two regions are divided at 100 cm from the bed. They differ in the slope of the logarithmic velocity profiles, with an outer-region roughness length of 1.5 cm and an inner-region roughness length of 0.15 cm. The actual transition between these two regions is gradual.

region, dominated by the smaller roughness elements, and the outer-region, dominated by the larger roughness elements, takes place gradually over a zone instead of sharp inflexion at a specific height. The division of the inner-region and the outer-region at 100 cm from the bed is therefore somewhat arbitrary. For the practical application of such a composite boundary-layer model in the estimation of the bed shear stress, however, simplification is necessary. Due to the logarithmic nature of the velocity profile this model is not very sensitive to the height of the transition between the two regions.

The two-region composite boundary-layer model discussed above is shown conceptually in Fig.7. The two regions differ in the slope of the logarithmic velocity profiles, with an outer-region roughness length of 1.5 cm and an inner-region roughness length of 0.15 cm.

#### BAGNOLD'S TRANSPORT EQUATION

Bagnold's (1966, 1968) transport equation is generally expressed as:

$$\frac{\rho_s - \rho}{\rho_s} g j = K \rho U_*^3 \quad (3)$$

where  $\rho_s$  is the density of the sediment,  $\rho$  is water density,  $g$  is gravitational



acceleration,  $j$  is the mass sediment transport rate, and  $K$  is Bagnold's transport coefficient. This equation is based on a clear physical concept, i.e., the principle of energy conservation. In addition it has great flexibility, allowing for the form drag as well as the skin friction. It has therefore been widely used in marine geology. For practical application, however, there is still the important problem concerning the evaluation of the coefficient  $K$ . Although most workers (Sternberg, 1972; Langhorne, 1981; Siegenthaler, 1982) agree that  $K$  depends on the excess shear stress, the exact form of this relationship is still a matter of discussion. Using flume experiment data, it is found (Yang, 1986) that  $K$  varies as a non-linear function of the dimensionless excess shear stress, which is best represented by the power law:

$$K = A(\tau_0/\tau_c - 1)^B \quad (4)$$

where  $\tau_c$  is the critical shear stress for initiation of sediment movement, and  $\tau_0$  is the bed shear stress. The coefficient  $A$  and exponent  $B$  depend on grain size. For fine sands of about 0.19 mm, this equation has the form:

$$K = 0.0042(\tau_0/\tau_c - 1)^{3.128} \quad (5)$$

The applicability of this modified Bagnold's transport equation to tidal marine environments receives strong support from good agreements between the sediment transport rates predicted from this equation and the field measurements in tidal environments, which cover a wide range of sediment grain size, flow velocity and bedform conditions.

## RESULTS

### *Tidal current pattern*

The tidal current patterns at 21 of the 22 measuring stations are summarized concisely by vector plots (Fig.8). One station (station 19) will not be discussed here due to the difference in water depth and current velocities. In Fig.8 the vector plots over a flood/ebb cycle at all stations show a clear bidirectional pattern, indicating strongly channelized tidal currents. The peak flood and ebb currents at each station are usually unequal. This asymmetrical pattern of tidal currents reflects the differentiation of tidal currents in the channel into flood-dominant and ebb-dominant zones. Most stations are dominated by ebb currents. Flood currents are dominant mainly along the southern Roompot (stations 16 and 17) and part of the southern Hammen (station 22 around spring tide). This reflects the influence of Coriolis effects and the lateral water-surface gradient caused by tidal-wave progradation (J.H.J. Terwindt, pers. commun., 1984). Flood currents are also dominant at stations 1 and 5 in the Hammen, where they become directed towards the shoal, while strong ebb currents follow the curved channel-bend. This is because the peak flood currents occur later in the flooding stage, they are less confined by meandered channels and may flow directly over shoals. During ebbing stage, drainage of

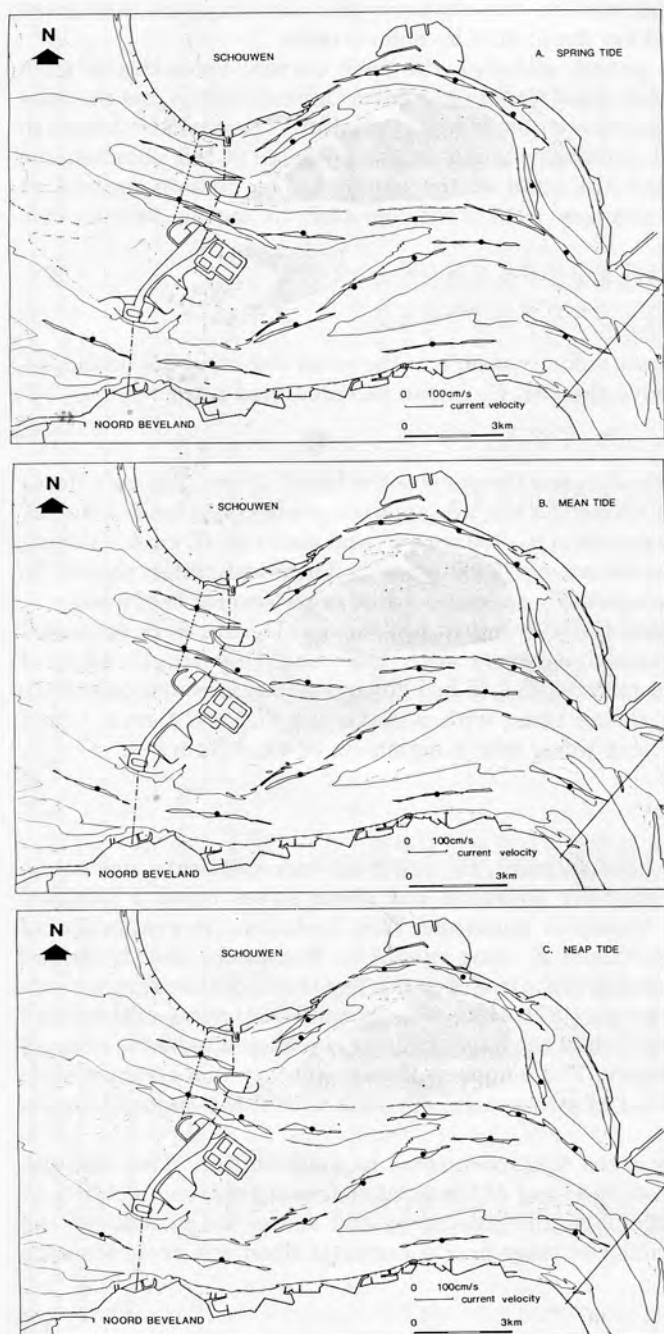


Fig.8. Vector plots of the tidal current pattern at 21 measuring stations. (A) spring tide; (B) mean tide; (C) neap tide.

water becomes concentrated in the channel; this also explains why most stations in the channel are dominated by ebb currents.

Over a neap/spring period, although the peak current velocities at each station vary in magnitude considerably, the basic current pattern and the tidal asymmetry at individual stations show little variation. These patterns seem to be controlled by local conditions, such as the position in the channel, the bottom topography, and the bend of the channel. The current pattern at station 22, however, changes from flood-dominant at spring tide to ebb-dominant at neap tide.

### *The boundary layer*

Assuming a logarithmic velocity profile in the outer-region of the boundary, the velocity 100 cm above the bed,  $U_{100}$ , can be calculated using:

$$\bar{U}_{100} = U(Z) \ln(100/(Z_0)_2) / \ln(Z/(Z_0)_2) \quad (6)$$

where roughness length  $(Z_0)_2$  has the constant value of 1.5 cm. The calculated peak velocities 100 cm above the bed are approximately 60–85 cm s<sup>-1</sup> during spring tides, with a maximum of 95–100 cm s<sup>-1</sup>, and about 45–65 cm s<sup>-1</sup> during neap tides, with a maximum of 75–80 cm s<sup>-1</sup>. These estimates should be understood as the local-spatially averaged value (over several bedforms).

From  $U_{100}$  the local spatially averaged bed shear velocities were estimated using the Karman-Prandtl equation with the roughness length  $(Z_0)_1$  of 0.15 cm. The estimated peak values of bed shear velocity are approximately 3.7–5.2 cm s<sup>-1</sup> during spring tides, with a maximum of 5.8–6.2 cm s<sup>-1</sup>, and 2.8–4.0 cm s<sup>-1</sup> during neap tides, with a maximum of 4.6–4.9 cm s<sup>-1</sup>.

### *Total sediment transport*

For each half-lunar-hour interval, the sediment transport rate was calculated from the local spatially averaged bed shear stress using a modified version of Bagnold's transport equation. This includes: (1) evaluation of Bagnold's transport coefficient  $K$  using eqn.(5) for fine sands, and (2) estimation of the sediment transport rate from eqn.(3). The threshold shear stress was determined from Sternberg's (1971, 1972; after Inman, 1963) curve of threshold shear velocity. The direction of the transport was considered to be the same as that of the current velocity. The influence of wave activity was assumed to be small compared with that of strong tidal currents within the major channels (deeper than 10 m).

Table 2 lists the sediment transport rates at each station. The absolute transport rate  $|J|$  reflects the level of the total sediment transport activity at each station. It is calculated by averaging the scalar magnitude of the individual sediment transport rates over a complete flood/ebb cycle for each station:

$$|J| = 1/T \int_0^T |j| dt \quad (7)$$

TABLE 2

Sediment transport rates at 21 stations. The absolute transport rate is the scalar average of the sediment transport rate over a flood/ebb cycle, and the net transport rate is the vectorial average of the transport rate over a flood/ebb cycle. The net transport rates averaged over a neap/spring/neap cycle were also calculated

Station	Sediment transport rates						
	Spring tide		Mean tide		Neap tide		Averaged over a neap/spring/neap cycle
	Absolute ( $\text{g cm}^{-1} \text{s}^{-1}$ )	Net ( $\text{g cm}^{-1} \text{s}^{-1}$ , degree)	Absolute ( $\text{g cm}^{-1} \text{s}^{-1}$ )	Net ( $\text{g cm}^{-1} \text{s}^{-1}$ , degree)	Absolute ( $\text{g cm}^{-1} \text{s}^{-1}$ )	Net ( $\text{g cm}^{-1} \text{s}^{-1}$ , degree)	
1	0.106	0.026, 67°	0.024	0.001, 152°	0.005	0.002, 231°	0.006, 74°
2	0.409	0.403, 238°	0.140	0.139, 238°	0.044	0.044, 239°	0.181, 238°
3	0.105	0.057, 258°	0.033	0.019, 257°	0.011	0.006, 257°	0.025, 257°
4	0.102	0.045, 288°	0.024	0.011, 288°	0.005	0.002, 290°	0.017, 288°
5	0.097	0.086, 131°	0.020	0.015, 132°	0.003	0.002, 131°	0.030, 131°
6	0.071	0.050, 346°	0.019	0.015, 346°	0.005	0.004, 346°	0.021, 346°
7	0.383	0.248, 310°	0.123	0.095, 311°	0.041	0.037, 313°	0.119, 311°
8	0.576	0.519, 285°	0.164	0.147, 285°	0.035	0.029, 286°	0.210, 285°
9	0.204	0.127, 262°	0.068	0.053, 263°	0.022	0.019, 263°	0.063, 263°
10	0.303	0.201, 266°	0.069	0.048, 266°	0.014	0.010, 266°	0.077, 266°
11	0.888	0.291, 274°	0.263	0.140, 282°	0.075	0.052, 286°	0.155, 279°
12	0.428	0.406, 269°	0.125	0.119, 269°	0.028	0.027, 270°	0.168, 269°
13	0.279	0.268, 247°	0.080	0.076, 247°	0.020	0.018, 250°	0.110, 247°
14	0.404	0.403, 237°	0.107	0.107, 237°	0.024	0.023, 238°	0.160, 237°
15	0.449	0.369, 247°	0.109	0.099, 248°	0.020	0.019, 249°	0.146, 247°
16	2.115	0.212, 154°	0.837	0.138, 129°	0.299	0.036, 136°	0.128, 140°
17	1.692	0.930, 88°	0.462	0.187, 90°	0.130	0.028, 96°	0.333, 89°
18	2.419	0.818, 301°	0.919	0.438, 296°	0.353	0.185, 295°	0.469, 298°
20	0.437	0.381, 292°	0.156	0.135, 292°	0.048	0.040, 292°	0.173, 292°
21	0.420	0.195, 285°	0.139	0.094, 286°	0.044	0.038, 286°	0.105, 286°
22	1.289	0.079, 136°	0.340	0.124, 285°	0.097	0.070, 288°	0.063, 277°

where  $j$  is the sediment transport vector during each sampling interval and  $T$  is the flood/ebb period.

The directional distribution of the total sediment transport is shown in Fig.9. The length of each radial bar represents the total amount of sediment transport within that direction class over a cross section 1 cm wide during a flood/ebb cycle. The bidirectional distribution of the total sediment transport during a flood/ebb cycle is a distinctive feature of this plot. Also, the sediment transport in one direction was usually dominant over that in the other. The general level of sediment transport during spring tides was about one order of magnitude greater than that during neap tides.

#### *Net sediment transport rate*

The net sediment transport rate  $J$  (Table 2) reflects the preferential movement of sediment in a certain direction during a flood/ebb cycle. It is obtained by vectorially averaging the individual sediment transport vector over a complete flood/ebb cycle for each station:

$$J = 1/T \int_0^T j \, dt \quad (8)$$

In addition, the net sediment transport rates averaged over a neap/spring/neap cycle were also estimated. These net sediment transport rates are plotted in Fig.10.

It is obvious that at most stations the net sediment transport was in the ebb direction. In the Schaar, ebb-oriented net sediment transport dominated throughout the channel. Such a sediment transport pattern indicates a major transit channel for tidal discharge and sediment transport. This pattern is also in accordance with the morphological evolution of the Schaar from an early equilibrating stream running NW-SE between the Hammen and the Roompot to a major tidal channel. Such change has been attributed to the increase in its tidal discharge which already shares 20% of the total tidal discharge in the mouth of the Oosterschelde (Van den Berg, 1984).

Net sediment transport in the flood direction was less common, occurring mainly along the southern Roompot and part of the southern Hammen, reflecting the effects of the Coriolis force and the lateral water-surface gradient associated with tidal-wave progradation. At stations 1 and 5 in the Hammen, flood-dominant net sediment transport was towards shoals, indicating that peak flood currents occurred later in the flooding stage, therefore, they were less confined by meandered channels and might flow directly over submerged shoals, while ebb-oriented net transport mainly concentrated in the channel and followed the meandered channel thalweg. These features agree well with the distribution pattern of ebb and flood currents in the meandered Hammen where the tidal discharge has declined to about 20% of the total tidal discharge in the mouth of the Oosterschelde.

Where net sediment transport at neighbouring stations was in opposite directions (the parting of the net sediment transport), channel-floor erosion is



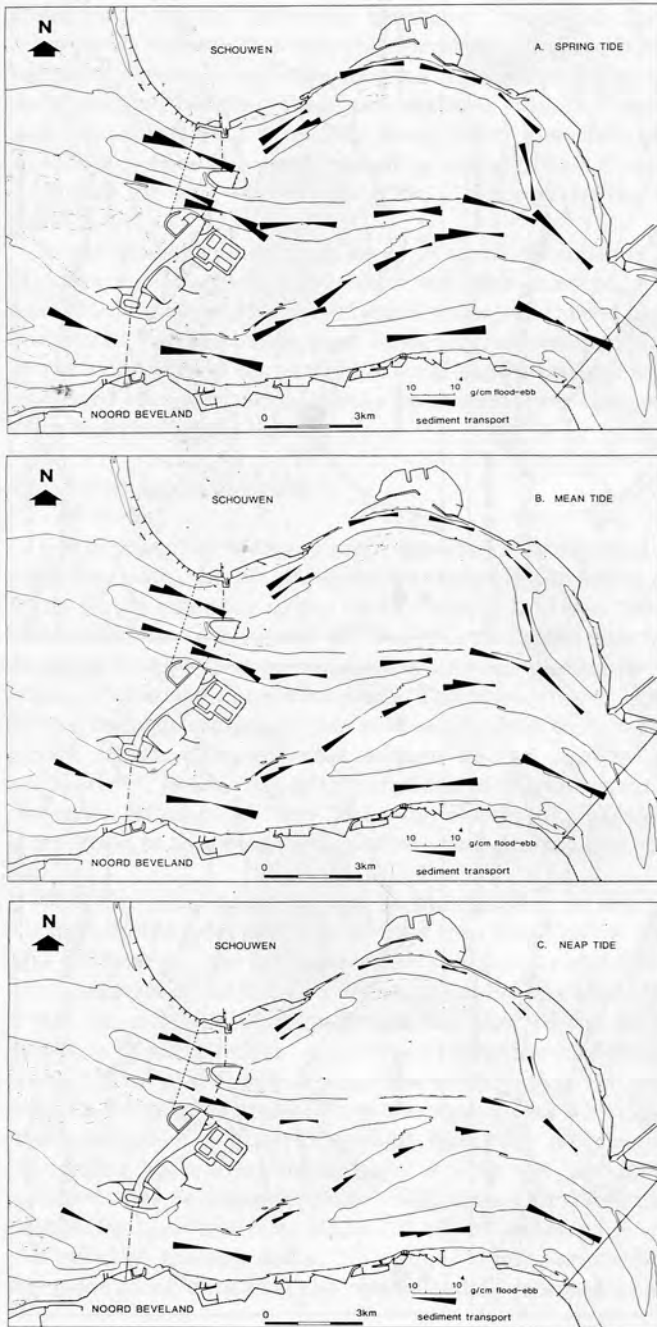


Fig.9. Directional distribution of the total sediment transport at 21 measuring stations. Radial bar length (in log scale) represents the total amount of sediment transport within that direction class over a cross section 1 cm wide during a flood/ebb cycle. (A) spring tide; (B) mean tide; (C) neap tide.

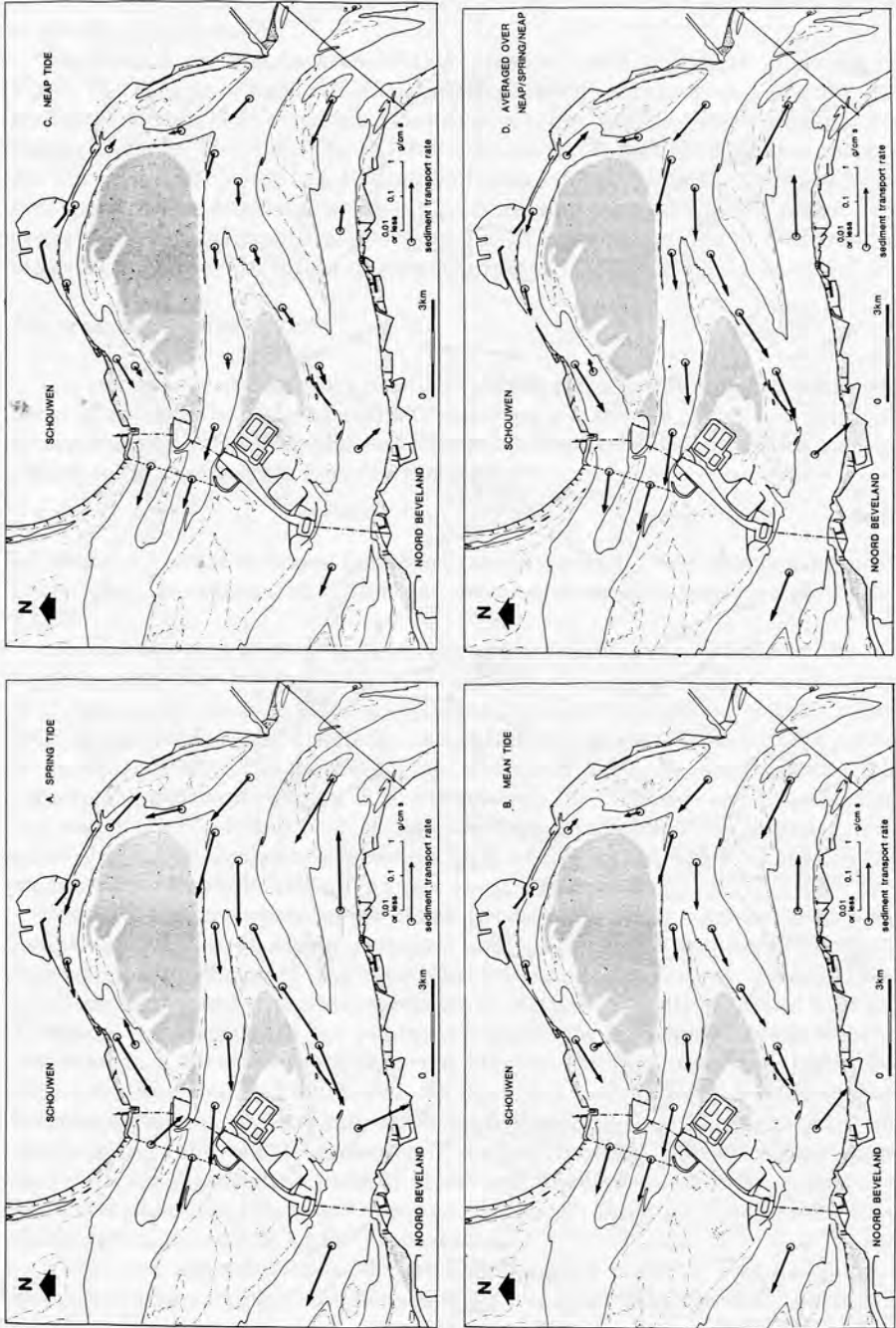


Fig. 10. Net sediment transport rates at 21 measuring stations. Arrow length (in log scale) represents the magnitude of the net sediment transport rate ( $\text{g cm}^{-1} \text{s}^{-1}$ ). (A) spring tide; (B) mean tide; (C) neap tide; (D) average over a neap/spring/neap cycle.

to be expected. This is indeed the case between stations 16 and 20 in the Roompot. The net sediment transport at station 16 was flood-dominant, whereas at station 20 it was ebb-dominant. Channel-flood erosion is therefore expected between these two stations. This is confirmed by the existence of the deep channel between these two stations (Fig.2). Comparisons of successive echo sounding data (Van den Berg, 1984) also indicates the widening and deepening of the Roompot caused by the increase of its tidal discharge which accounts for 60% of the total tidal discharge in the mouth of the Oosterschelde.

Local sand circulation can be recognized. At stations 12, 13, 14 and 15 in the Vuilbaard, net sediment transport was ebb-oriented, while along stations 16 and 17 in the Roompot, net sediment transport turned to the flood direction. At station 18, further to the east, however, net sediment transport was again in the ebb direction. This pattern of local sand circulation suggests that the total sediment transport activity may be much larger than what can be estimated from morphological changes.

#### *Long-term sediment budget*

For comparison with sediment movement determined from successive echo-sounding data, the net sediment transport in the major channels (deeper than 10 m) at the entrance in the east (stations 7, 17 and 18) and at the exit in the west (stations 1, 2, 11 and 20) was calculated for the last 20 years (Table 3). Stations 21 and 22 were not used in this calculation because they were in the vicinity of artificial constructions. The net sediment transport rates averaged over a neap/spring/neap cycle at these stations were considered to be representative of the channel cross section at the station, and of the period of comparison. In the case of two stations in one channel (stations 1 and 2 in the Hammen, stations 17 and 18 in the Roompot), estimates were made of the proportion of the cross-section where each station can be regarded as representative.

The estimated sand budget is summarized in Fig.11. For simplicity the Oosterschelde tidal basin is divided into three parts: the inner-basin (east of the study area), the mid-basin (the study area) and the outer-basin (between the study area and the ebb delta). Calculations show that during the last 20 years about  $10.7 \times 10^6 \text{ m}^3$  sediment has entered the study area from the east, which is thought to have been eroded from the inner-basin. Meanwhile, about  $17.6 \times 10^6 \text{ m}^3$  of sediment has left the study area in the west, implying a net loss of  $6.9 \times 10^6 \text{ m}^3$  of sediment from the study area, which is thought to represent the amount of sediments eroded from the mid-basin during this period. According to echo-sounding data, during the last 20 years  $11.5 \times 10^6 \text{ m}^3$  of sediment has been eroded from the Roompot in the outer-basin area (Van den Berg, 1984). As much as  $29.1 \times 10^6 \text{ m}^3$  of sediment may therefore have been delivered to the ebb delta. This figure is comparable with the estimate from echo-sounding data that the ebb delta has received  $37.2 \times 10^6 \text{ m}^3$  of sediment,

TABLE 3

Estimation of net sediment transport in the major channels (deeper than 10 m) at the entrance and the exit of study area for the last 20 yr. (+) represents entering the study area; (-) represents leaving the study area

Station	Net transport rate ( $\text{g cm}^{-1} \text{ s}^{-1}$ )	Current width ( $10^2 \text{ cm}$ )	Duration ( $10^8 \text{ s}$ )	Sediment transport ( $10^6 \text{ m}^3$ )	
Entrance					
7	+0.119	1600	6.3072		+7.5
17	-0.333	600	6.3072	-7.9	+3.2
18	+0.469	600	6.3072	+11.1	
Total					+10.7
Exit					
1	+0.006	300	6.3072	+0.07	-3.5
2	-0.181	500	6.3072	-3.57	
11	-0.155	800	6.3072		-4.9
20	-0.173	1350	6.3072		-9.2
Total					-17.6

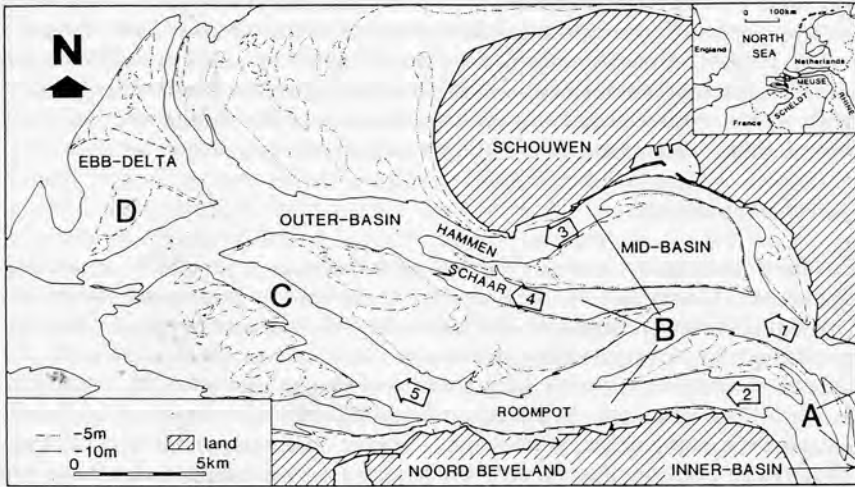
derived mainly from the Oosterschelde Basin during the last 20 years (Van den Berg, 1984).

The sand budget estimated from the current data agrees very well with the morphological evolution of the Oosterschelde (Van den Berg, 1984). Considerable erosion has occurred in the tidal basin in the form of channel development and shoal retreat. In the mid-basin, the major channel Roompot has deepened and widened further at the expense of neighbouring shoals. The equilibrating channel Schaar has become a major transit channel. In the outer-basin (proximal part of ebb-delta) major ebb channels have deepened and extended rapidly towards the sea, leading to the coalescence of ebb channels and the complete disappearance of some large intertidal shoals. As a large part of the eroded sediments has been deposited in the distal part of the ebb tidal delta, it has shown a remarkable seaward expansion.

The major reason responsible for the sediment redistribution and the morphological evolution of the estuary tidal basin is the increase of tidal prism (Van den Berg, 1984). The closure of the Volkerak in 1969 increased the tidal prism of the Oosterschelde by about 9%. The damming of the Geul in 1972 caused a further increase in tidal discharges through the Roompot and the Schaar with some loss of tidal discharge in the Hammen. In addition, a 4% increase of the tidal prism along the Dutch coast over the past century has been reported (De Ronde, 1983). There exists an equilibrium between tidal discharges and tidal channel system in the Oosterschelde tidal basin which can be described by the empirical formula:

$$A_c = 1.17 \hat{Q} \quad (9)$$

A.



B.

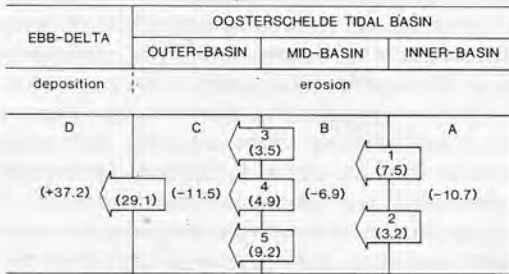


Fig.11. Box model of the sand budget in the Oosterschelde tidal basin for the last 20 years. (A) Locations of boxes (indicated by letters) and boxed arrows (numbered) in the model; (B) sand budget. Figures in boxed arrows (in parentheses) are net sand fluxes (in  $10^6 \text{ m}^3$ ) passing across the boundary of the box during this period. Figures in boxes (in parentheses) represent net deposition (+) or erosion (-) of sediment (in  $10^6 \text{ m}^3$ ) in the area during the same period. For further explanation, see text.

where  $A_c$  is the cross-sectional area of the estuary mouth below M.S.L. and  $\bar{Q}$  is the maximum tidal discharge (Van de Kreeke and Haring, 1979). Therefore, in response to the increase of tidal prism, erosion has been dominant in the Oosterschelde tidal basin with further development of the tidal channel system.

As for the sediment deposited in the ebb delta, there is still some difference between the estimate from current data and that from echo sounding data. This difference is attributable to: (1) only sediment transport in the major channels (deeper than 10 m) was considered in the budget; (2) exceptional storms may



influence sediment movement; (3) the ebb delta may receive sediment from other sources; and (4) the processes of ebb channel expansion in the tidal basin and net sedimentation in the tidal delta were accelerated after 1969 when the damming of the Volkerak caused a sudden increase in tidal prism (Van den Berg, 1984). Such processes would, however, begin to slow down when current measurements were carried out in the Oosterschelde tidal basin in 1980. Therefore these measurements would give relatively low estimates.

### *Geological implications*

The above discussion shows very active sedimentary processes in modern tidal basins. During period of stability, these active processes reached a certain equilibrium in terms of the bidirectional sediment-transport circulation and the local spatial sediment-transport circulation. The active sediment movement therefore produced only small morphological changes. When the basin conditions changed, however, this equilibrium was replaced by unbalanced sediment movements, which then brought about important morphological changes and rapid adjustment of the basin to new conditions. Such change has been observed in the present-day Oosterschelde tidal basin, where large amounts of sediment have been eroded from the basin and delivered to the ebb delta at the mouth in response to the increase of the tidal prism. This sediment redistribution process would have important influence on the structural organization and sequential build-up of estuary-ebb delta deposits.

In the estuary tidal basin, tidal channels became the most active elements with deposition mainly along the inner-bend of these actively migrating channels. As shown in Fig.8, tidal currents in confined channels commonly show a differentiation into ebb-dominated and flood-dominated zones. Such asymmetrical tidal currents would produce unidirectional megaripple cross-bedding in the direction of dominant currents. A Holocene section from the Schaar construction pit at the mouth of the Oosterschelde (Visser, 1980; Van den Berg, 1982; Siegenthaler, 1982; Nio et al., 1983; Yang and Nio, 1985) shows distinct tidal channel sequences, which mainly consist of cosets of ebb-oriented megaripple cross-beddings. Foresets were well organized into a series of bundles. Each bundle is the foreset unit formed during one dominant tidal current (Boersma, 1969; Visser, 1980). Thus a bundle with its characteristic boundaries represents clearly a single ebb/flood tidal cycle. The sequential arrangement of bundle units laid down during successive ebb/flood cycles is described as a tidal bundle sequence, which shows diurnal and fortnightly periodic variations of successive bundle thicknesses in response to the diurnal tidal inequality and the neap-spring tidal variations.

The periodicity of the tidal bundle sequence reveals that the deposition of the bundle sequence was very fast. As suggested in our estimations, in response to the variation of tidal prism, major changes in the channel and shoal pattern would occur in tens of years. Measurements in the Oosterschelde mouth showed a channel migration of several hundred meters within one year

(Nio and Yang, 1983). Such rapid migration implies that tidal channel sequences were often interrupted by channel abandonment or erosion, and later succeeded by channel deposit of a new generation. The 17 m deep section at the Schaar construction pit in the mouth of the Oosterschelde exhibits the superposition of two tidal channel sequences, including channel thalweg deposits, channel inner-margin deposits and channel abandonment deposits. Based on numerous studies of tidal sediments in mesotidal basins around the North Sea, Terwindt (1981) proposed that in tidal channels as well as on shoals, deposition is followed by erosion and non-deposition, causing the absence of a general fining-upward macro-sequence (in tens-of-meters scale). Although there are many types of micro-sequence (in decimeter-meter scale), they are all cut off by erosional surfaces and abrupt changes in lithofacies. The frequent occurrence of erosional contacts and abrupt facies changes are the most striking features in these inshore tidal sediments (Terwindt, 1981).

Due to the redistribution of sediments from the tidal basin to the ebb delta, the distal parts of the ebb delta show a gradual seaward expansion. The major depositional areas were the terminal lobe at the delta front with a concave-upward seaward-dipping accretional surface where bedforms were rare, and the ebb shoals on delta platform fed by ebb channels which were covered by ebb-oriented megaripple fields (Van den Berg, 1984). Therefore two types of structural organizations could be expected for such expanding ebb delta deposits: (1) a simple structural organization characterized by very large to giant low-angle inclined bedding; (2) a composite structural organization consisting of cosets of ebb-oriented megaripple cross-bedding. In the more proximal part of the ebb delta the tidal channel sand bodies with erosional base might cut into the lobe-shaped units.

The estimates from tidal current measurements indicate about  $29.1 \times 10^6 \text{ m}^3$  sediments have been delivered to the ebb tidal delta during the last 20 years. Morphological studies (Van den Berg, 1984) also indicate that the progradation of the ebb tidal delta locally amounted to 700 m and a layer of more than 9 m of sediment was deposited. Such active sediment movement and major morphological change mean that the tidal basin could adjust to the change of hydrodynamic conditions and reach new equilibrium with increased tidal discharge very fast, and then the processes of sediment redistribution and ebb-delta progradation would slow down. Therefore the expansions of the ebb tidal delta were rather short-period, intermittent processes, producing major units of the ebb tidal delta, while most of the time the ebb tidal delta area underwent a long period of non-deposition or erosion, producing non-depositional submarine abandonment surfaces or erosional surfaces. This implies that the sequential build-up of the ebb tidal delta would be characterized by a vertical stack of different delta lobes, which represent relative short periods of delta progradation, separated from each other by non-depositional submarine abandonment surfaces or erosional surfaces, which represent rather long periods of delta modification. A fossil analogue of such an ebb delta has been observed in the Eocene Roda Sandstone, southern Pyrenees, Spain, where an ebb tidal

delta complex shows a vertical stack of five ebb delta lobes separated from each other by submarine abandonment surfaces (Nio et al., 1984).

The above discussion shows only some typical cases within a whole spectrum. Estuary sand bodies would change over a wider range in response to the increased tidal discharge. In estuaries with high fluvial influx and small tidal discharge, large-scale transverse sand bars might develop at the mouth of the estuary. As the tidal prism increases, tidal channels in the estuary would develop further and become more active with erosion dominant in most parts of the estuary tidal basin, whereas the major sand accumulation would change to an ebb delta which expands in size and progrades farther seawards onto the shelf sediments. In estuaries with an even larger tidal prism, the tidal channels would widen and extend further, becoming the dominant morphological elements, while sand would mainly be deposited in elongated sand bodies, i.e. the tidal sand ridges.

#### CONCLUSIONS

(1) Based on measurements in the Oosterschelde tidal basin and literature data a simplified composite boundary-layer model with two regions is used to estimate the local spatially averaged bed shear stress over megaripples. The two regions are divided at 100 cm above the bed and differ in the slope of the logarithmic velocity distribution. The mean roughness length in the outer-region is found to be 1.5 cm, reflecting the large bedforms; the inner-region has a roughness length of 0.15 cm, corresponding to small bedforms and sediment grains.

(2) Applying this composite boundary-layer model and a modified version of Bagnold's transport equation, the mid-depth velocity measurements in the Oosterschelde tidal basin were used to make a regional description of sediment movement. The results show the total sediment transport processes are very active in the basin. The net sediment transport is mainly in the ebb direction. Local sediment circulation may develop around shoals. Channel-floor erosion may occur in parting areas of sediment transport.

(3) Estimates of the long-term sediment budget show that large amounts of sand have been eroded from the Oosterschelde basin and transported to the ebb-delta, reflecting that the change of tidal discharge and its distribution pattern would cause a remarkable sediment redistribution in the estuary tidal basin. The scale and magnitude of this sediment redistribution have been estimated using current measurements and a general pattern has been outlined, which shows good agreement with morphological evolutions of the basin as revealed by echo-sounding data.

(4) The active sediment redistribution and major morphological evolution processes in the present-day Oosterschelde tidal basin would have important influence on the structural organization and sequential development of estuary-ebb delta deposits. In response to increased tidal discharge it is expected that estuarine tidal deposits would be characterized by the superposi-

tion of truncated sequences of channel or shoal deposits and the general existence of abandonment surfaces or erosional surfaces, while the ebb delta would expand in size and prograde farther seaward onto the shelf deposits. Information about the sedimentary processes in a present-day estuary tidal basin is valuable for a better understanding of ancient examples.

#### ACKNOWLEDGEMENTS

The author wishes to thank S.D. Nio for his support and suggestions in this research. Appreciation and thanks are also due to the technique team of the Delta Project for obtaining the field measurements, and to the members of Rijkswaterstaat/Deltadienst (Ministry of Transport and Public Works, Delta Department) in Zierikzee and Den Haag for their cooperation and supply of data. The manuscript has benefitted considerably from numerous comments by J.B. Southard. The author is greatly indebted to J.H.J. Terwindt for critical reading of the manuscript, and also to J.H. Van den Berg, T. de Mowbray and the members of the Comparative Sedimentology Division for their fruitful discussions.

#### REFERENCES

- Allen, J.R.L., 1982. Mud drapes in sand-wave deposits: a physical model with application to the Folkestone Beds (early Cretaceous, Southeast England). *Philos. Trans. R. Soc. London, Ser. A*, 306: 291-345.
- Allen, P.A. and Homewood, P., 1984. Evolution and mechanics of a Miocene tidal sandwave. *Sedimentology*, 31: 63-81.
- Bagnold, R.A., 1941. *The Physics of Blown Sand and Desert Dunes*. Morrow, New York, N.Y., 265 pp.
- Bagnold, R.A., 1956. The flow of cohesionless grains in fluids. *Philos. Trans. R. Soc., Ser. A*, 249: 235-297.
- Bagnold, R.A., 1963. Beach and near-shore processes, I: Mechanics of marine sedimentation. In: M.N. Hill (Editor), *The Sea*. Wiley-Interscience, New York, N.Y., pp.507-549.
- Bagnold, R.A., 1966. An approach to the sediment transport problem from general physics. *U.S. Geol. Surv., Prof. Pap.*, 422-I: 96 pp.
- Bagnold, R.A., 1968. Deposition in the process of hydraulic transport. *Sedimentology*, 10: 45-56.
- Blatt, H., Middleton, G. and Murray, R., 1980. *Origin of Sedimentary Rocks*. Prentice-Hall, Englewood Cliffs, N.J., 782 pp.
- Boersma, J.R., 1969. Internal structures of some tidal megaripples on a shoal in the Westerschelde estuary, The Netherlands. *Geol. Mijnbouw*, 48: 409-414.
- Boothroyd, J.C. and Hubbard, D.K., 1975. Genesis of bedforms in mesotidal estuaries. In: L.E. Cronin (Editor), *Estuarine Research*, Vol. II. Academic Press, New York, N.Y., pp.217-234.
- Bowden, K.F., 1962. Turbulence. In: M.N. Hill (Editor), *The Sea: Ideas and Observations*. Vol. III. Wiley, New York, N.Y.
- Bridge, J.S. and Jarvis, J., 1982. The dynamics of a river bend: a study in flow and sedimentary processes. *Sedimentology*, 29: 499-541.
- Chriss, T.M. and Caldwell, D.R., 1982. Evidence for the influence of form drag on bottom boundary layer flow. *J. Geophys. Res.*, 87: 4148-4154.
- Dalrymple, R.W., Knight, R.J. and Lambiase, J.J., 1978. Bedforms and their hydraulic stability relationships in a tidal environment, Bay of Fundy, Canada. *Nature*, 275(5676): 100-104.



- De Ronde, J.G., 1983. Changes of relative mean sea-level and of mean tidal amplitude along the Dutch coast. In: A.R. Ritsema and A. Gurpinar (Editors), *Seismicity and Seismic Risk in the Offshore North-Sea Area*, pp.131-142.
- Dyer, K.R., 1970. Current velocity profiles in a tidal channel. *Geophys. J. R. Astron. Soc.*, 22: 153-161.
- Einstein, H.A., 1950. The bed-load function for sediment transportation in open channel flows. U.S. Dep. Agric., Soil Conservation Ser., Tech. Bull., 1026: 1-71.
- Gadd, P.E., Lavelle, J.W. and Swift, D.J.P., 1978. Estimates of sand transport on the New York shelf using near-bottom current meter observations. *J. Sediment. Petrol.*, 48: 239-252.
- Grant, W.D. and Madsen, O.S., 1979. Combined wave and current interaction with a rough bottom. *J. Geophys. Res.*, 84: 1797-1808.
- Guy, H.R., Simons, D.B. and Richardson, E.V., 1966. Summary of alluvial channel data from flume experiments, 1956-1961. U.S. Geol. Surv., Prof. Pap., 462-I: 96 pp.
- Harms, J.C., Choquette, P.W. and Brady, M.J., 1974. Carbonate sand waves, Isla Mujeres, Yucatan. In: A.E. Weidie (Editor), *Field Seminar on Water and Carbonate Rocks of The Yucatan Peninsula, Mexico*. Geol. Soc. Am. Annu. Meeting, Miami, Fla., pp.123-147.
- Inman, D.L., 1963. Sediments: physical properties and mechanics of sedimentation. In: F.P. Shepard (Editor), *Submarine Geology*. Harper and Row, New York, N.Y., pp.101-151.
- Jansen, R.H.J., 1978. The in-situ measurement of sediment transport by means of ultrasonic scattering. Delft Hydraulic Laboratory, Delft, Publ. 203.
- Langhorne, D.N., 1981. An evaluation of Bagnold's dimensionless coefficient of proportionality using measurements of sandwave movement. *Mar. Geol.*, 43: 49-64.
- Langhorne, D.N., 1982. A study of the dynamics of a marine sandwave. *Sedimentology*, 29: 571-594.
- Lavelle, J.W. and Mofjeld, H.O., 1983. Effects of time-varying viscosity on Oscillatory turbulent channel flow. *J. Geophys. Res.*, 88: 7607-7616.
- Middleton, G.V. and Southard, J.B., 1978. *Mechanics of sediment movement*. Soc. Econ. Paleontol. Mineral., Short Course, 3.
- Nio, S.D. and Yang, C.S., 1983. Dynamics, geometry and sequential upbuilding of large subtidal bedforms. Proc. Int. Symposium on Sedimentation on The Continental Shelf with Special Reference to The East China Sea. China Ocean Press, Beijing, Vol. 1, pp.20-36.
- Nio, S.D., Siegenthaler, C. and Yang, C.S., 1983. Megaripple cross-bedding as a tool for the reconstruction of the palaeo-hydraulics in a Holocene subtidal environment, S.W. Netherlands. *Geol. Mijnbouw*, 62: 499-510.
- Nio, S.D., Siegenthaler, C. and Yang, C.S., 1984. Facies pattern and development of the Lower Eocene Roda Sandstone, Isabena Valley, Southern Pyrenees, Spain. Abstr. Int. Assoc. Sedimentol. 5th Eur. Meeting, Marseilles, pp.328-329.
- Nowell, A.R.M., 1983. The benthic boundary layer and sediment transport. *Rev. Geophys. Space Phys.*, 21: 1181-1192.
- Rubin, D.M. and McCulloch, D.S., 1980. Single and superimposed bedforms: a synthesis of San Francisco Bay and flume observations. *Sediment. Geol.*, 26: 207-231.
- Siegenthaler, C., 1982. Tidal cross-strata and the sediment transport rate problem: a geologist's approach. *Mar. Geol.*, 45: 227-240.
- Simons, D.B. and Richardson, E.V., 1962. The effect of bed roughness on depth-discharge relations in alluvial channels. U.S. Geol. Surv. Water Supply Pap. 1498-E.
- Smith, J.D. and McLean, S.R., 1977. Spatially averaged flow over a wavy surface. *J. Geophys. Res.*, 82: 1735-1746.
- Soulsby, R.L. and Dyer, K.R., 1981. The form of the near-bed velocity profile in a tidally accelerating flow. *J. Geophys. Res.*, 86: 8067-8074.
- Southard, J.B., 1975. Bed configurations. In: *Depositional environments as interpreted from primary sedimentary structure and stratification sequences*. Soc. Econ. Paleontol. Mineral., Short Course, 2: 5-43.
- Sternberg, R.W., 1968. Friction factors in tidal channels with differing bed roughness. *Mar. Geol.*, 6: 243-260.
- Sternberg, R.W., 1971. Measurements of incipient motion of sediment particles in the marine environment. *Mar. Geol.*, 10: 113-119.



- Sternberg, R.W., 1972. Predicting initial motion and bedload transport of sediment particles in the shallow marine environment. In: D.J.P. Swift, D.B. Duane and O.H. Pilkey (Editors), *Shelf Sediment Transport: Process and Pattern*. Dowden, Hutchinson and Ross, Stroudsburg, Pa., pp.61-82.
- Taylor, P.A. and Dyer, K.R., 1977. Theoretical models of flow near the bed and their implications for sediment transport. In: E.D. Goldberg (Editor), *The Sea*, 6. Wiley-Interscience, New York, N.Y., pp.579-601.
- Terwindt, J.H.J., 1973. Sand movement in the in- and offshore tidal area of the S.W. part of The Netherlands. *Geol. Mijnbouw*, 52: 69-77.
- Terwindt, J.H.J., 1981. Origin and sequences of sedimentary structures in inshore mesotidal deposits of the North Sea. In: S.D. Nio, R.T.E. Shuttenhelm and Tj.C.E. van Weering (Editors), *Holocene Marine Sedimentation in The North Sea Basin*. Spec. Publ. Int. Assoc. Sedimentol., Vol. 5: 4-26.
- Van de Kreeke, J. and Haring, J., 1979. Equilibrium flow areas in the Rhine-Meuse Delta. *Coastal Eng.*, 3: 97-111.
- Van den Berg, J.H., 1982. Migration of large-scale bedforms and preservation of crossbedded sets in highly accretional parts of tidal channels in the Oosterschelde, SW Netherlands. *Geol. Mijnbouw*, 61: 253-263.
- Van den Berg, J.H., 1984. Morphological changes of the ebb-tidal delta of the Eastern Scheldt during recent decades. *Geol. Mijnbouw*, 63: 363-375.
- Visser, M.J., 1980. Neap-spring cycles reflected in Holocene subtidal large-scale bedform deposits: a preliminary note. *Geology*, 8: 543-546.
- Wooding, R.A., Bradley, E.F. and Marshall, J.K., 1973. Drag due to regular arrays of roughness elements of varying geometry. *Boundary Layer Meteorol.*, 5: 285-308.
- Yalin, M.S., 1963. An expression for bedload transportation. *J. Hydraul. Div. Proc. Am. Soc. Civ. Eng.* HY3, 89: 221-250.
- Yang, C.S., 1986. On Bagnold's sediment transport equation in tidal marine environments and the practical definition of bedload. *Sedimentology* (in press).
- Yang, C.S. and Nio, S.D., 1985. The estimation of palaeo-hydrodynamic processes from subtidal deposits using time series analysis methods. *Sedimentology*, 32: 41-57.

## Chapter 5

### **An ebb-tide delta depositional model - a comparison between the modern Eastern Scheldt Tidal Basin (SW Netherlands) and the Lower Eocene Roda Sandstone in the Southern Pyrenees (Spain)**

Chang-Shu Yang\* and Swie-Djin Nio

Comparative Sedimentology Division, Institute of Earth Sciences, University of Utrecht, Budapestlaan 4, 3508 TA Utrecht, The Netherlands

\*Present address: International Geoservices BV, Statenhof, Reaal 5, 2353 TK, Leiderdorp, The Netherlands.

#### **ABSTRACT**

This paper documents the succession, internal structural organization and sequential up-building of an ebb-tide delta in the Lower Eocene Roda Sandstone in southern Pyrenees, Spain. Special attention is given to the relationship between preserved sequences of this fossil ebb-tide delta and sedimentary processes in the present-day estuary and ebb-delta environment of the Eastern Scheldt mesotidal basin, SW Netherlands. Based on similarities and the differences between these two ebb deltas, a depositional model has been constructed for the ebb delta and its associated estuary channel system. This consists mainly of: prograding terminal lobes at the delta front, extensive ebb-dominated subtidal depositional lobes and wide shallow ebb channels on the delta platform, as well as extensive intertidal shoals and relatively deep, actively migrating tidal channels in estuary basin.

Distinctive geometry and internal structures of both ebb delta and estuary channel

---

This chapter has been accepted for publication as:

Yang, C.S. & Nio, S.D., 1989. An ebb-tide delta depositional model - a comparison between the modern Eastern Scheldt Tidal Basin (SW Netherlands) and the Lower Eocene Roda Sandstone in the Southern Pyrenees (Spain). *Sedimentary Geology* (in press).

sand bodies clearly reflect the characteristic hydrodynamic and morphological conditions in the estuaries. The common occurrence of submarine abandonment surfaces and erosional surfaces is an important feature of ebb deltas and estuary channel sequences. Their sequential buildup is critically dependent upon the influences of marine transgressions and the tectonic movements of the tidal basin.

## INTRODUCTION

Many investigators of ebb-tide deltas have focussed on the sediment and bedform distribution pattern and the morphological evolution of ebb-tide deltas in present-day micro- and mesotidal environments (Hayes, 1975; Wright & Sonu, 1975; Hine, 1975; Hubbard, 1975; Oertel, 1975; Finley, 1975; van den Berg, 1984). Hayes (1975) presented a morphological model of an ebb-tidal delta which includes a main ebb channel with channel-margin linear bars, a terminal lobe, a broad swash platform with swash bars and marginal flood channels. The internal structural and sequential organization of ebb deltas are, however, still less known.

This paper documents the succession of an ebb delta and its associated estuary channel deposits recognized in the Roda Sandstone. An attempt is made to relate sand-body geometry, structural organization and sequential up-building in this ancient example to the morphological features and bedform patterns in the modern environments of the Eastern Scheldt tidal basin where the hydrodynamic conditions are known. From such comparative studies a generalized depositional model of ebb deltas in mesotidal environments can be established, and the roles of regional transgressions and basin tectonic movements will be discussed. The resulting information on the formation, preservation, dimensions, geometry, internal structural organization, sequential development and distribution pattern of an ebb delta and its associated estuary channel sand bodies is particularly important to the exploration of oil and gas in such basins.

## EBB-TIDE DELTA AND ESTUARY CHANNEL DEPOSITS IN THE EASTERN SCHELDT TIDAL BASIN

### General Setting

A good example of a present-day mesotidal ebb delta is found at the mouth of the Eastern Scheldt tidal basin. It is one of the estuaries previously connected to the Rhine-Meuse-Scheldt fluvial system. The basin is characterized by semidiurnal tides with mean tidal ranges of 2.8 m to 3.4 m in the ebb delta area (van den Berg, 1984). Sediment deposited in the mouth of the basin is predominantly sand. The mean grain size varies from 0.15 mm to more than 0.25 mm (Terwindt, 1973). Morphologically the Eastern Scheldt tidal basin and the adjacent shelf area can be divided into three zones (Fig.1):

A. The Eastern Scheldt tidal basin, an elongated inshore tidal basin, consists of three

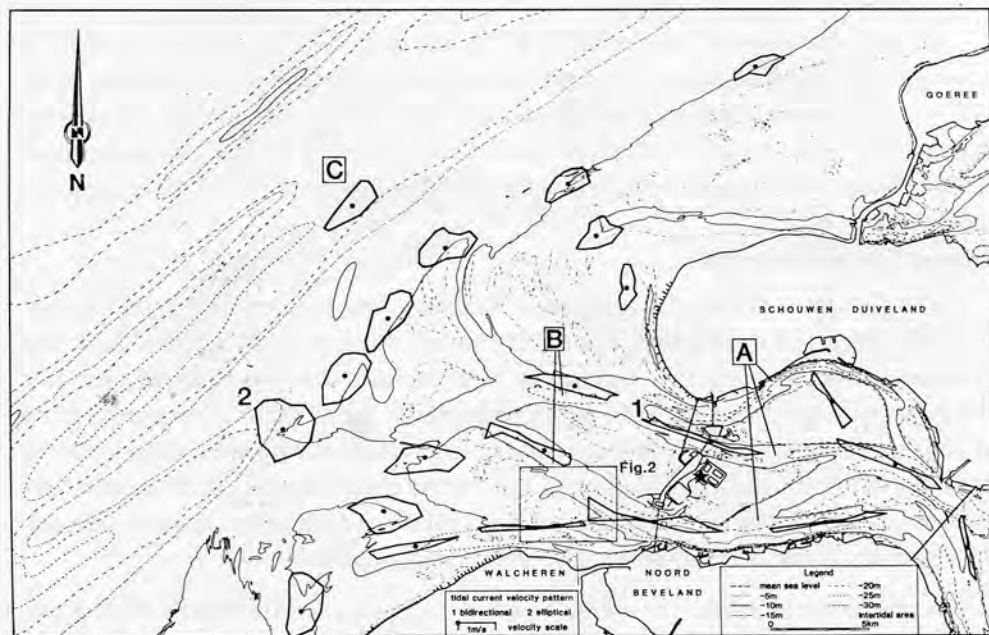


Fig.1 Physiographic map of the Eastern Scheldt tidal basin and the adjacent shelf area with tidal ellipses for mean spring tidal currents. A. Channelized estuary tidal basin; B. Ebb-tide delta; C. Offshore shelf (after Nio & Yang, 1983, data from Rijkswaterstaat; tidal current pattern modified after Siegenthaler, 1982).

major tidal channels separated from each other by extensive intertidal shoals. The shoals are dissected by smaller tidal channels. Accretion, erosion and shifting of these large sandy shoals is dependent mainly on the lateral migration of the major or intershoal tidal channels. In relatively narrow channels the tidal currents exhibit a distinct bidirectional current pattern. Peak flood and ebb current velocities at any one location are usually unequal. This asymmetrical current pattern causes the development of flood-dominated and ebb-dominated channels. Peak velocities of the dominant tidal currents may be as high as 1.5 m/s or more. Wave action generally plays a subordinate role, mainly in sediment entrainment. During storms, however, wave action plays a dominant role in the erosion of sandy shoals. Megaripples with wavelengths of more than 5 m are present within the channels as well as on the intertidal shoals.

B. The large ebb-tide delta consists of ebb delta lobes and large tidal channels which feed the lobes. A distinct feature is the shallowing and widening of these ebb channels towards the continental shelf. Compared with the inshore tidal basin, tidal currents are less confined by channels and the tidal current ellipses begin to lose their linear character. Especially over the outer section of the ebb delta, tidal currents exhibit a distinct rotating pattern. Peak tidal current velocities are about 1 m/s. In addition, wave action is more impor-

tant. Megaripples may occur within the channels and on the ebb delta lobes.

C. The offshore shelf area seaward of the ebb delta exhibits a pattern of SW-NE oriented elongated sand ridges. Superimposed on these sandy ridges are sandwaves, which also occur independently in sandwave fields. The tidal currents turn through 360 degrees during a tidal cycle, so that here tidal currents are always present. Peak velocities are about 0.8 m/s. Wave action, especially during storms, plays an important role in the erosion and sedimentation pattern.

### **Estuary Channel Sequence**

The present-day Eastern Scheldt basin has three major tidal channels, ranging from 20 to 40 m deep, and many smaller intrashoal channels which are less than 15 m deep. The asymmetrical bidirectional tidal currents in these confined channels commonly produce stable megaripples (Terwindt, 1970). Megaripple heights within channels may reach 1 to 2 m, and their migration usually produces unidirectional cross-bedding in the direction of the dominant current. A distinctive feature of these active channels is the rapid lateral migration with accretion along the inner margin of the channel bend. Therefore megaripple cross-bedded cosets in the channels have a high preservation potential.

A typical example from the southern part of the Eastern Scheldt tidal basin is shown in Fig.2. Echo-sounding made by Rijkswaterstaat (Dutch Ministry of Transport and Public Works) shows that flood-oriented megaripples develop along the flood-dominated inner bend (Fig.2b). The highest megaripples occur at the deeper part of the accretionary inner bend, and the size of the megaripples usually decreases towards the shallow parts of the inner bend. Measurements of accretion and erosion in this area between 1977 and 1978 by Rijkswaterstaat revealed that the channel thalweg migrated approximately 250 metres towards the NW. Within the same period a vertical accretion of more than 10 m occurred along the inner bend (Fig.2a).

Such rapid lateral migration and high accretion rates along the inner bend favour the preservation of tidal channel sequences in stratigraphical records. A Holocene section down to 17 m below M.S.L. in the Schaar construction pit at the mouth of the Eastern Scheldt (Visser, 1980; Nio et al., 1980; van den Berg, 1982; Siegenthaler, 1982; Nio, Siegenthaler & Yang, 1983; Yang & Nio, 1985) clearly shows the superposition of two channel complexes (Fig.3). The upper channel complex represents an abandoned tidal channel sequence (van den Berg, 1981). The lower channel complex represents an active tidal channel sequence, which consists mainly of cosets of ebb-oriented megaripple cross-beddings with distinct tidal-bundle sequences of thick spring bundles and thin neap bundles (Fig.4) (Visser, 1980). The lateral distance of a neap to spring to neap bundle sequence is on average about 15 to 20 m. This is also confirmed by the observation that megaripples with a height of 2 m in present-day tidal channels may migrate in the direction of the dominant current at a mean rate of 5 to 15 metres within a neap to spring to neap cycle (van den Berg, 1982). This reflects a very high accretion rate and high preservation potential along the



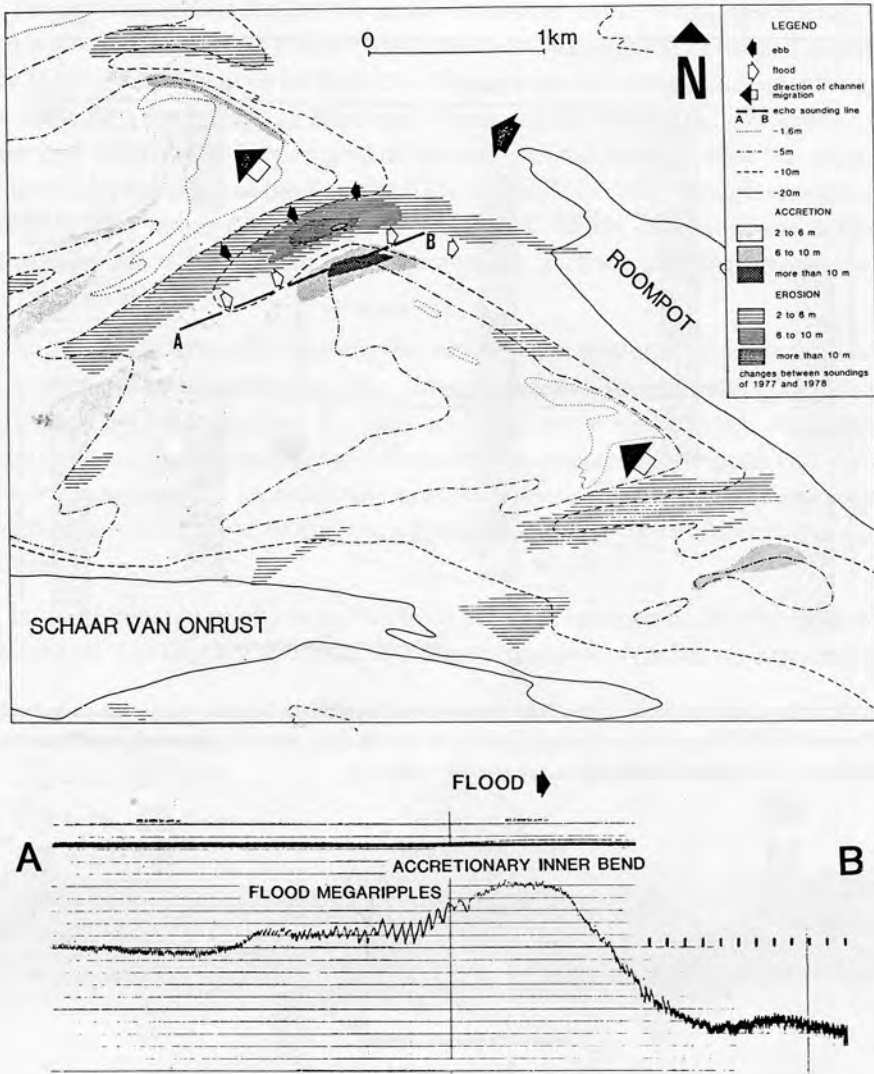


Fig.2 (a)The accretionary and erosional pattern of a migrating channel at the Onrust area in the mouth of the Eastern Scheldt during 1977-1978. (b) Echo-sounding profile for the transect A-B (Fig.2a) across the accretionary inner bend and part of the flood-dominated channel at the Onrust area. Note the increase of megaripple height towards the lobate complex of the accretionary inner bend (after Nio & Yang, 1983, data from Rijkswaterstaat).

inner bends of channels.

### Ebb-Tide Delta

The ebb-tide delta consists of ebb delta lobes and large tidal channels which feed the

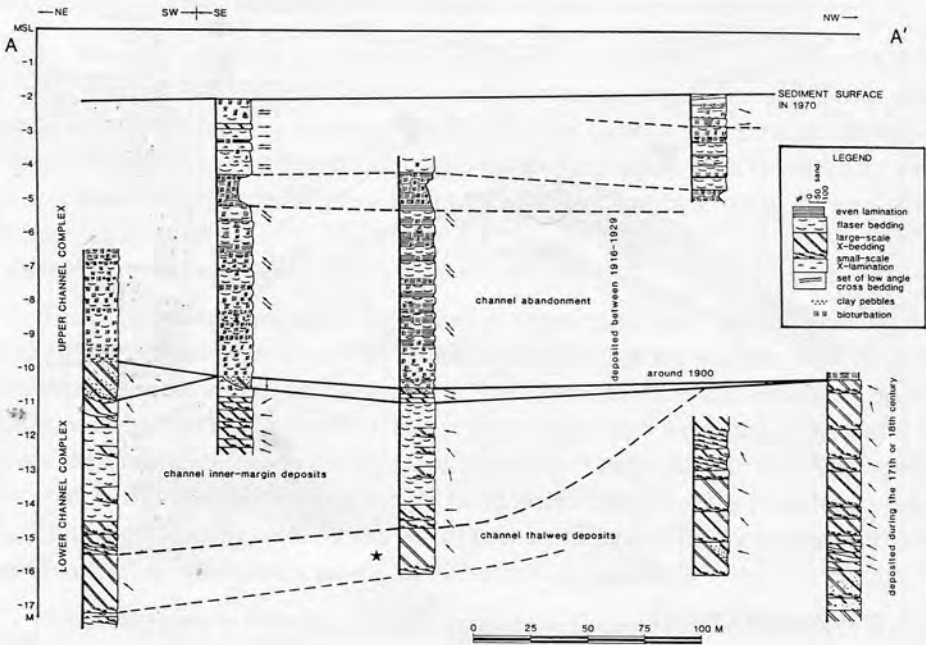


Fig.3 Stratigraphical scheme of part of the Holocene sequence found in the Schaar construction pit in the mouth of the Eastern Scheldt estuary. Note the superposition of the two tidal-channel sequences (modified after van den Berg, 1981, for location of this section, see asterisk in Fig.1).

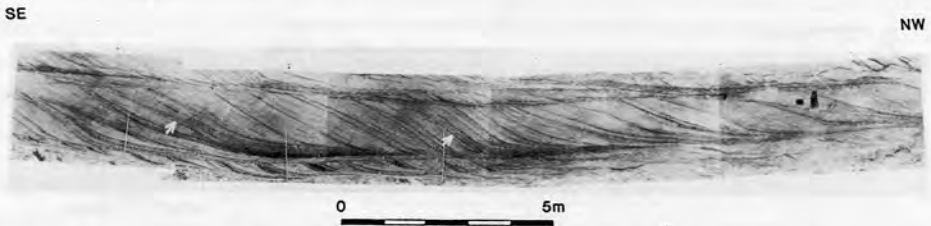


Fig.4 Part of the Holocene exposure, showing an ebb-oriented set with a well developed bundle sequence deposited approximately 15 m below M.S.L. The arrows indicate the position of neap-tide bundles. The measuring scale on the photograph is 1.5 m (For location of this exposure, see asterisk in Fig.3).

lobes. Comparison of detailed hydrographic surveys made in the last 25 years have revealed remarkable morphological changes (van den Berg, 1984). As a result of increased tidal discharge, major ebb channels in the proximal part of the ebb delta have deepened and extended in a seaward direction and the distal part of the ebb delta has shown a gradual seaward progradation. The major depositional areas are the terminal lobe at the delta front and the subtidal ebb-dominated depo-lobes on the delta platform (Fig.5).

The terminal lobe at the delta front has a width of several kilometres parallel to the shore. It is 6 m high and has a concave upward seaward-facing slope between 7 m and 13 m below M.S.L. The gradient varies from 12 to 4 degrees along the slope. Side-scan sonar data show a relatively flat surface on this slope. Measurements of accretion and erosion in the period 1960-1980 revealed that a gradual expansion of this terminal lobe has taken place over the innermost ridge of the Zeeland Ridges. The descending concave seaward-facing slope prograded rather rapidly onto the inner shelf. In the northwest, the delta front prograded for about 700 m, and a sand layer over 9 m thick was deposited in a period of 20 years (van den Berg, 1984).

Above - , m developed a relatively flat subtidal delta platform, on which subtidal ebb-dominated depo-lobes are present. They show a horseshoe-shaped morphology about 2-3 km wide and 3-4 km long (Fig.5, B). They are fed by major ebb channels. Echo sounding records show that these depo-lobes are covered by ebb-oriented megaripples (van den Berg, 1984). Measurements of accretion and erosion of these subtidal depo-lobes revealed a seaward expansion of about 1000 m and a sand layer 2-4 m thick was deposited in a period of 20 years.

In such a prograding ebb delta, two types of structural organizations can be expected to be formed. The first would consist of a simple structural organization characterized by

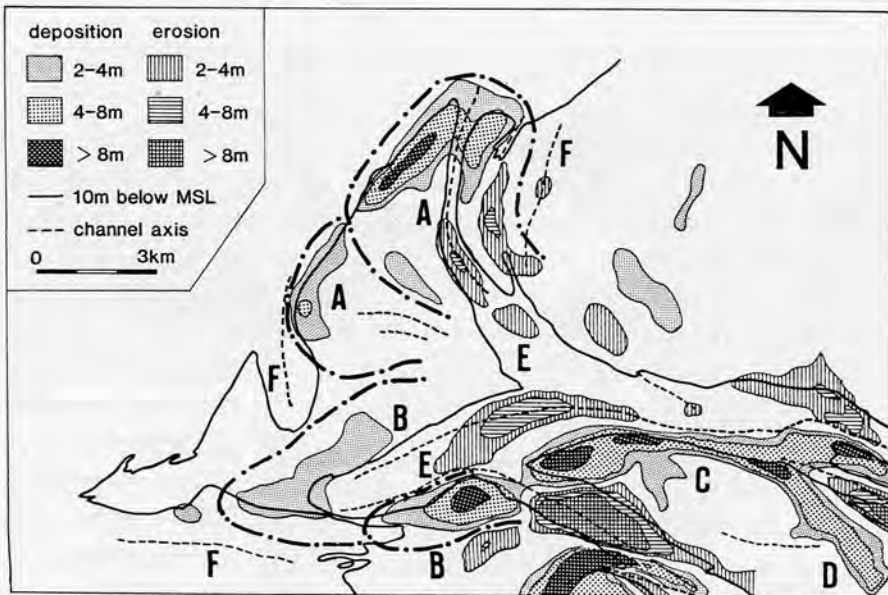


Fig.5 Net deposition and erosion on part of the ebb delta of the Eastern Scheldt estuary between 1960 and 1980. A. terminal lobe at the delta front; B. ebb-dominated subtidal depo-lobes; C. accretionary inner bend of ebb channel; D. abandoned channel; E. ebb channels at the proximal part of the ebb delta; F. flood channels at the edge of the ebb delta (modified after van den Berg, 1984).

very large to giant low-angle inclined layers. The second would contain a composite structural organization consisting of cosets of ebb-oriented megaripple cross-bedding. At the edge of the ebb delta, flood-oriented megaripple cross-beds can be observed (Fig.5, F). In the more proximal part of the ebb delta, ebb channel sand bodies with an erosional base might cut into the lobe-shaped units (Fig.5, E). Owing to intensive wave action and the continuously rotating tidal current pattern, sediments deposited in the distal part of the ebb-tide delta would contain few, if any, mud laminae.

### Surfaces of Abandonment or Erosion

The ebb delta expansion and the tidal channel migration are very rapid on a geological time-scale. This implies that the deposition of major sand units are rather short, intermittent processes in a continuously changing system while most of the time the tidal basins and ebb deltas undergo long periods of non-deposition or erosion, producing submarine abandonment surfaces or erosional surfaces. The research on tidal sediments in channels as well as on shoals has shown that the frequent occurrence of erosional contacts and abrupt facies changes are important features in these inshore tidal sediments (Terwindt, 1981).

## EBB-TIDE DELTA AND ESTUARY CHANNEL DEPOSITS IN THE RODA SANDSTONE

### Geological Setting

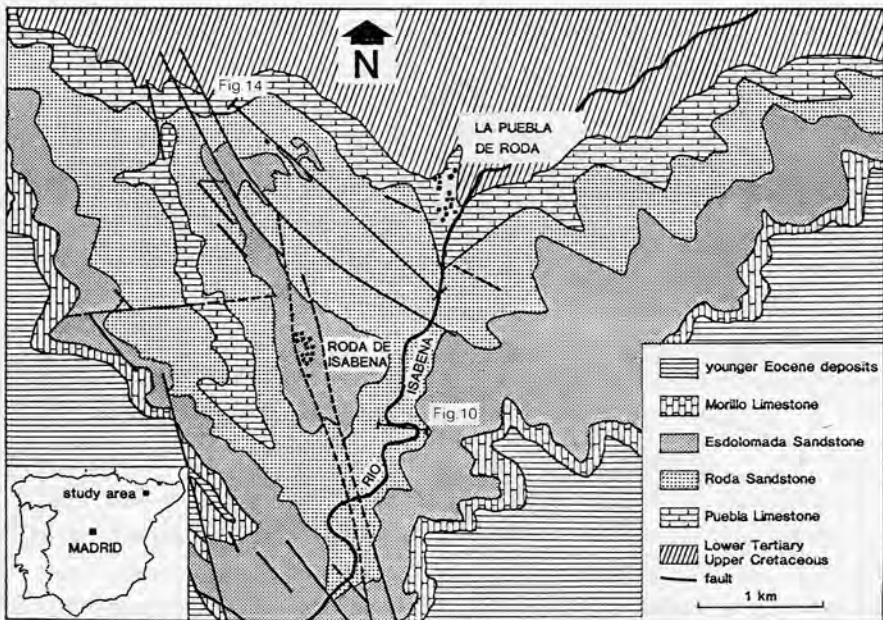


Fig.6 Geological map of the Roda Sandstone.

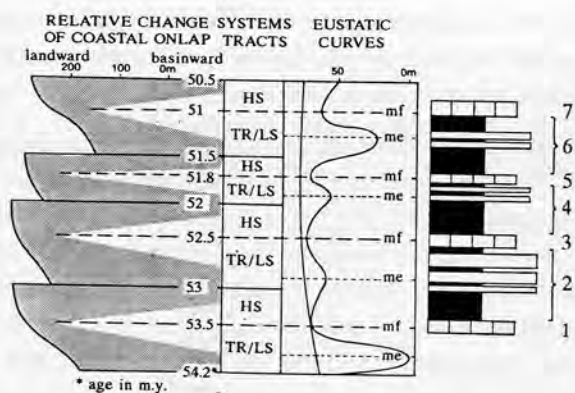


Fig.7 Schematic stratigraphic section of part of the Lower Eocene in Isabena valley. Systems tracts follow the definition of Vail (1987): HS-High Stand systems tract; TR-Transgressive systems tract; LS-Low Stand systems tract. Two surfaces are indicated: MF-Maximum Flooding surface; ME-Maximum Emergence surface. Major stratigraphy sequences are numbered: 1. Puebla Limestone Fm; 2. Roda Sandstone Mbr; 3. Plateau Limestone Bed; 4 and 6. Esdolomada Mbr; 5. El Villar Limestone Bed; 7. Morillo Limestone Fm. Relative change of coastal onlap and the eustatic curves follow Vail (1987).

The Roda Sandstone were discussed by Nio (1976), Nio & Siegenthaler (1978), Nio & Yang (1984) and Nio & Yang (in prep.).

The Roda Sandstone Member is bounded by two bioclastic fossiliferous wackestone and grainstone layers: the "Puebla Limestone" at the base and the "Plateau Limestone" at the top (Figs.6 and 7). Both can be traced over tens of kilometres. The overlying Esdolomada Member consists of thinly-bedded fine sandstones with small scale structures and thick marl intervals. It represents a distal analogue of the Roda Sandstone Member and is covered by the "Morillo Limestone", a laterally persistent major limestone horizon which is homogenous in both lithology and thickness over a distance of at least 10-15 km. The Morillo Limestone exhibits the highest content and diversity of marine fossils within the entire Eocene succession. It reflects an extensive transgression during the Ypresian.

The Roda Sandstone Member is well exposed on both sides of the Isabena River, near the Village of La Puebla de Roda (Figs.8 and 9). It can be divided into two parts. The lower part consists of a thick marl interval with intercalations of thin and laterally persistent bioclastic limestone beds. This is interpreted as the distal inner to middle shelf deposits. The upper part of the Roda Sandstone Member consists of medium to coarse arkosic sandstone units with various distinct sedimentary structures, separated from each other by marl intervals. Based on geometry, lithology and internal structures, eight sandstone units can be differentiated (Units I, II, III, A, B, C, D and E; Figs.8 and 9). These units are always

The Lower Eocene Roda Sandstone is the lowermost paleogene fill of the Tresp-Graus basin in the Isabena valley, northern Spain (Mey et al., 1968; Nijman & Nio, 1975; Nio, 1976). The Tresp-Graus basin forms the south-central part of the larger southern Pyrenean foreland basin (Puigdefabregas et al., 1986). The basin is approx. 100 km long in the ESE-WNW direction and 20 km wide. It deepens towards the west (Nijman & Nio, 1975). The stratigraphy, the tectonic setting, the transgression history and the distribution of major sedimentary facies of the Roda



capped by thin and laterally persistent calcareous sandstone beds. These fossiliferous and intensively bioturbated beds are submarine hardgrounds. Laterally, all sandstone units grade into thin bioclastic limestone beds, which represent the distal shelf facies.

Biochronostratigraphic data indicate that the Puebla Limestone was deposited during the Maximum Flooding at about 53.5 Ma (Fig.7). The overlying marl interval represents the deposits of the subsequent Highstand Systems Tract. The first coarse clastic influx (sandstone Unit I) reached the Roda area during the Maximum Emergence at about 53 Ma. The major sandstone units of the Roda Sandstone Member were built up as the Lowstand Systems Tract (Unit I, II and III) and the subsequent Transgressive Systems Tract (Unit A, B, C, D and E). The overlying Plateau Limestone represents the Maximum Flooding at about 52.5 Ma.

Within Roda sandstone units three major facies are recognized: the transverse sand bar facies (Units I, II and III); the estuarine channel facies (Units A, B, C and E) and the ebb-tide delta facies (mainly in Unit D) (Fig.9).

#### Estuarine Channel Facies

**Isabena Valley Section** This facies is exposed in a vertical section of more than 20 m high along the Isabena valley (Fig.10). The section exhibits a lower part of channel thalweg deposits and an upper part of channel inner bend deposits, similar to the Holocene tidal

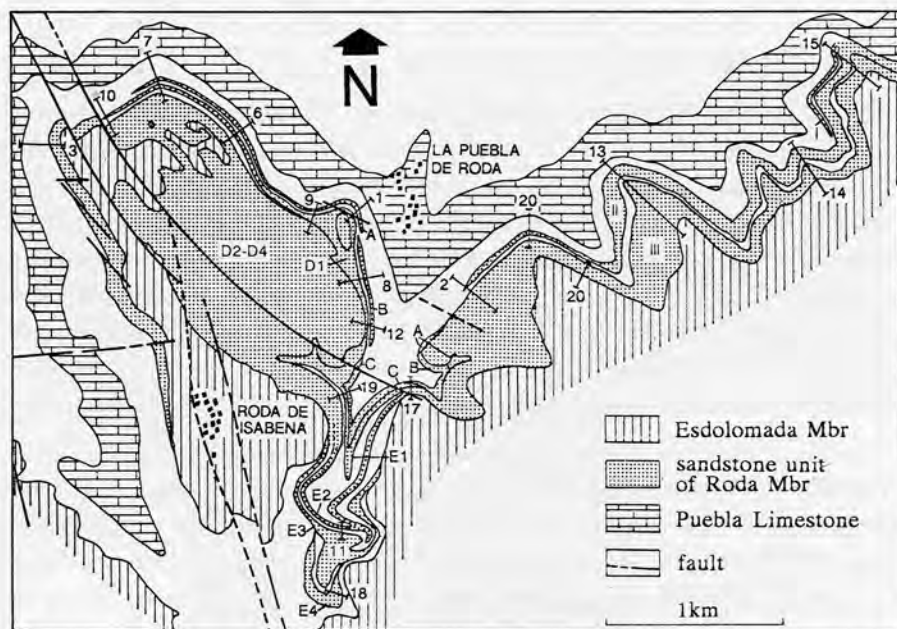


Fig.8 Major sandstone units of the Roda Sandstone. Unit I, II, III, A, B, C, D and E refer to the major sandstone units. Figures refer to the columnar section numbers.

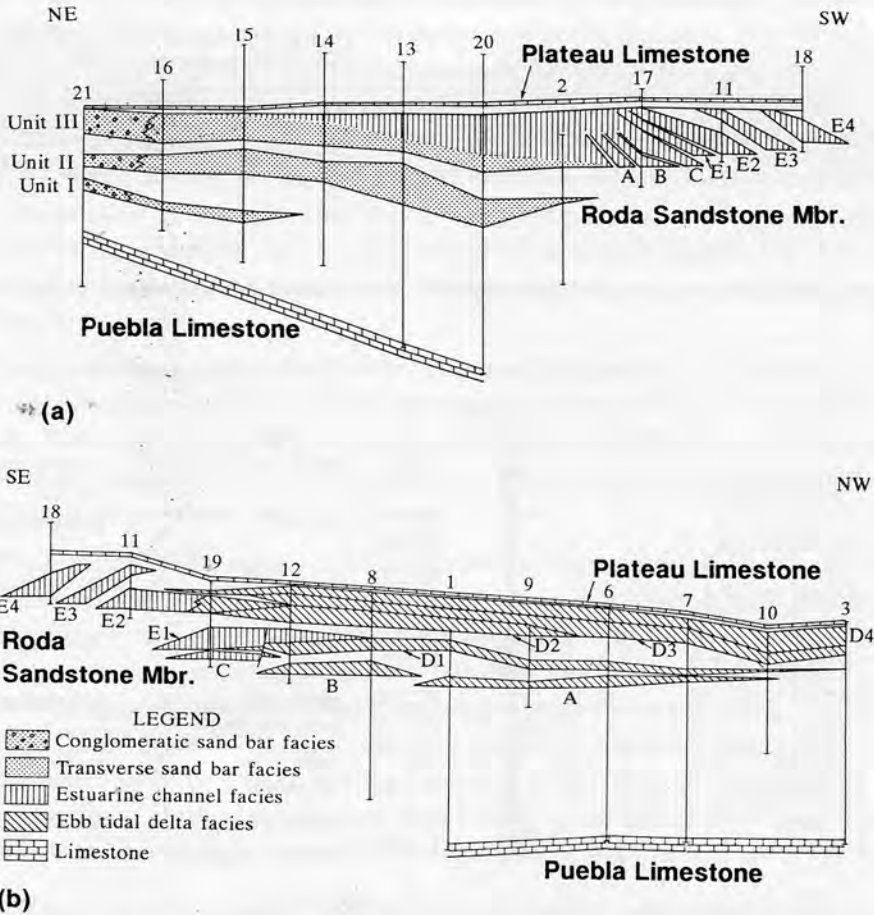


Fig.9 Cross-sections along the eastern side (9a) and the western side (9b) of the Isabena Valley, showing major facies of the Roda Sandstone. Unit I, II, III, A, B, C, D and E refer to the major sandstone units. Figures refer to the columnar section numbers. Ebb-tide delta facies and estuary channel facies are exposed mainly in sandstone unit A, B, C, D and E.

channel section found in the Eastern Scheldt.

Vertical Sequence A typical sequence of the estuary facies was measured in the Isabena Valley Section (Fig.11). The sequence is fining and thinning upwards. It can be divided into two parts. The lower part consists mainly of coarse quartz sandstone with distinct cosets of megaripple cross-bedding. Set heights can reach 150 cm, but thins upward rapidly to 20-40 cm. Foresets show a series of bundles with mud drapes. The thicknesses of successive bundles clearly display the diurnal and the fortnightly periodic variations corresponding to the diurnal tidal inequality and neap to spring tidal variations. Foreset dip directions (WNW) show that the bundle sequence was deposited by dominant ebb tidal cur-

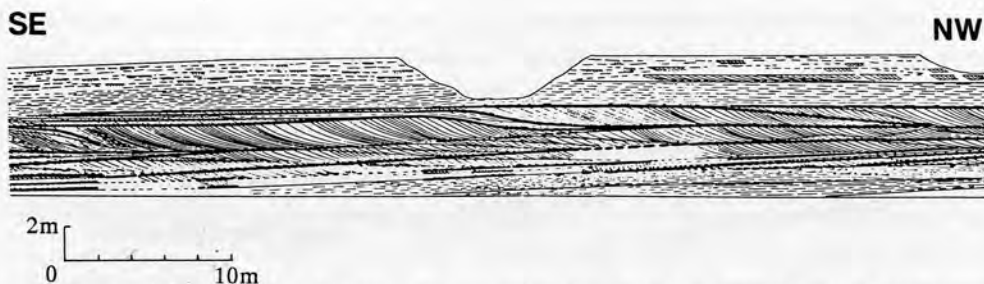


Fig.10 Part of the estuary channel facies section exposed in Unit E2 along the Isabena valley (see Fig.6 for location).

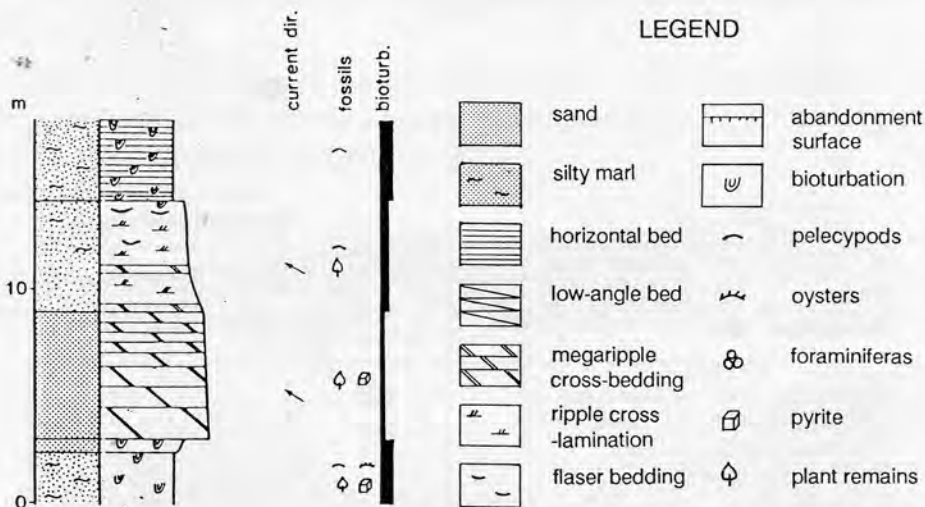


Fig.11 A typical vertical sequence of Estuary Facies in Unit E2 (for location see columnar section 11 in Fig.8 and 9).

rents. From time series analysis of successive bundle thicknesses it has been estimated that these bundle sequences were deposited in a semidiurnal meso- to slightly macrotidal regime with an estimated palaeotidal range between 2.75 and 4.43 m, a semidiurnal component amplitude of 2.22 m, a diurnal component amplitude of 0.25 m, and a neap to spring component amplitude of 0.84 m (Yang & Nio, 1985). Bioturbation, especially in the bottomset, is common. Plant remains and pyrite are also found.

The upper part of the Isabena Valley section consists mainly of fine sandstones, siltstones and intercalated mud beds. There is, in general, an upward increase in mud content and number of intercalated mud beds. Sedimentary structures are confined to megaripple cross-bedding with set heights less than 20 cm, small-ripple cross-lamination and flaser bedding. Bioturbation is rather strong. Burrows in vertical, horizontal or oblique directions are common, while bivalve and plant remains are also found within the sets.

The distinct fining-upward sequence of this section is related to a lateral migration of tidal channels. The lower part of the sequence represents the active channel thalweg deposits, whereas the upper part of the sequence was formed along the inner bend of the channel and on a shallow shoal. The presence of flaser bedding (mud flasers about 0.5 cm thick alternating with sand layers 3-5 cm thick) implies that periods of current activity (sand transport) alternated with periods of quiescence (mud deposition). This is in good agreement with the inferred channelized tidal currents as indicated by the bundle sequence (Yang & Nio, 1985). Because of the rapid lateral migration of the channel thalweg, the whole section is characterized by a lateral stacking of different channels.

### Ebb-Tide Delta Facies

**Las Forcas Section** The ebb-tide delta facies is well exposed at Las Forcas to the west of the Isabena Valley (Fig.9). A vertical stacking of several ebb-delta lobes is observed (Fig.12). The largest lobes are 1 to 2 km wide and 3 to 4 km long. Each lobe is truncated by a laterally persistent, sub-horizontal calcareous bed. These fossiliferous and strongly bioturbated beds represent abandonment and abrasion planes.

The sequential and structural development of a single ebb delta exhibits a distinct two-tier subdivision (Fig.13). The lower part, 6 to 8 m thick, consists of very large, low-angle inclined layers, which are slightly concave upward and dip towards the NW at an angle of 10 to 15 degrees. This is clearly comparable with the terminal lobe at the delta front in the Eastern Scheldt, which is 6 m high and has a concave upward seaward-facing slope with a gradient of 12 to 4 degrees. The upper part of the ebb delta, 2 to 4 m thick, consists of cosets of ebb-oriented megaripple cross-bedding. Sets are normally 20-70 cm high, but reach 1 to 2 m in some cases. Foreset dip directions show a wider variation than those in the estuary channels. No mud drapes were observed. This represents the ebb-dominated subtidal depo-



Fig.12 The geometry of ebb-delta complexes in Unit D at the Las Forcas showing a vertical stacking of several ebb-delta lobes.

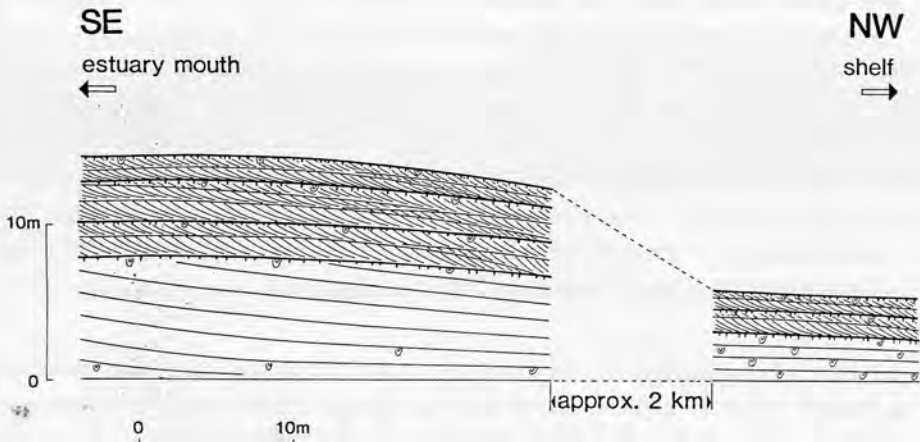


Fig.13 A schematic section of the ebb-delta facies exposed at the Las Forcas (see Fig.6 for location).

lobes on the delta platform.

The prograding ebb delta was fed by wide, shallow ebb channels. Fig.14 shows such a prograding ebb-delta complex with an offlapping of two delta lobes, separated from each other by a marl interval, which represents an abandonment phase. Each ebb delta lobe consists of a depo-lobe and an ebb channel which fed the lobe. The depo-lobe is several metres high and exhibits large-scale cross-beds dipping towards NW, i.e. the shelf. The ebb channel is characterized by an offlap stacking of megaripple cross-bed sets. The set height increases towards the depo-lobe. The paleocurrent directions show a wider range than those of the channel thalweg deposits within the estuary. Several offlap bounding surfaces of the cross-bed sets (C1) show clear evidence of erosion and reactivation. They dipped at a low angle, truncated underlying bedding surfaces, and were overlain by cross-bed sets with the same orientation. They represent stage changes, or the offlap stacking of the cross-bed sets produced when a faster-moving megaripple overtook a slower-moving one downstream of it (de Mowbray & Visser, 1984). Erosion and reactivation surface produced by counter currents, however, is also present (C2), similar to those produced by subordinate current erosion in a bidirectional flow system (de Mowbray & Visser, 1984). These internal reactivation surfaces (C1 and C2) are quite analogous to Miall's third order surfaces, while the abandonment surface (D), which capped the ebb-delta lobe, is comparable to Miall's fourth order surfaces (Miall, 1988 a, b & c).

At the edge of the ebb delta in Las Forcas, however, flood-oriented megaripple cross-beds with set heights of 20 to 100 cm can be observed. Herring-bone cross-beddings with both flood- and ebb-oriented megaripple cross-bed are also clearly visible.

Vertical Sequence A typical sequence of this facies is shown in Fig.15. Two ebb-tidal delta sequences are present.





Fig.14 Detailed view of a prograding ebb-delta complex, showing the offlap pattern of two ebb-delta lobes. Each lobe consists of a depo-lobe with large cross beddings (A) and a feeding channel with an offlap stacking of megaripple sets (B). Several offlap bounding surfaces (C1) show erosion and reactivation due to stage changes or megaripple overtaking. Some reactivation surface (C2) was produced by subordinate flood currents. The ebb-delta lobe is capped by an abandonment surface (D). Arrow indicates megaripple cross-bedded set of flood currents.

Each sequence starts with horizontally-bedded, bioturbated siltstones and marl (Fig.15, a and d). Individual bed thickness is about 20-60 cm with a general thickening-upward trend. Marine fossils point to a muddy shelf environment.

These fine-grained deposits are overlain by coarsening-upward, low-angle bedded sandstones (Fig.15, b and e). The bulk of the sandstone consists of coarse sand. The individual low-angle beds are about 10 cm thick at the lower part and 20 to 50 cm thick in the middle to upper part. They are slightly concave upward and dip towards the WNW-WSW ( $250^{\circ}$  to  $315^{\circ}$ ). Some beds, however, dip at a rather high angle of about  $20^{\circ}$ . Bioturbation is strong, especially near the upper surface of a sequence. Cross-bedding structures are not visible in the uppermost decimetres of the sandstone layer.

The low-angle bedded sandstones are, in turn, covered by medium to coarse sandstones with megaripple cross-bedded cosets (Fig.15, f). Individual sets vary from 15 to 40 cm in height. Foresets dip in a WNW-WSW direction ( $235^{\circ}$  to  $305^{\circ}$ ). Several strongly bioturbated abandonment surfaces are clearly visible (35 m to 45 m, Fig.15).

At the proximal part of this facies, some fining-upward megaripple cross-bedded sequence can be recognized (Fig.15, c). Megaripple sets are 20-50 cm high. Foreset dips show a wide range in direction. Mud drapes are absent.

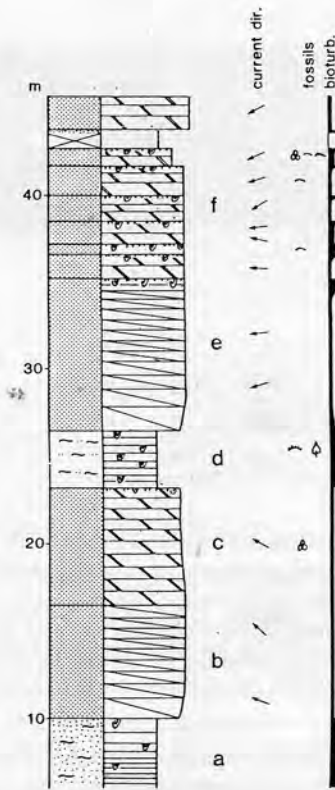


Fig.15 A typical vertical sequence of the ebb-tide delta facies in unit D (for location see columnar section 12 in Fig.8 and 9).

strong bioturbation and abundant marine fauna, such as corals, foraminifera, molluscs etc. Laterally they grade into thin bioclastic limestone beds in the more distal or inner shelf part of the basin. These are ancient submarine hardgrounds and represent long periods of low clastic influx and high marine macrobenthic productivity. The common appearance of these ancient submarine hardground surfaces in the section reveals that the deposition of estuary channel and ebb delta sand bodies were rather short-period events which can probably be related to the episodic supply of clastic sediments, whereas during most of the time, the depositional rates were very low. Such conditions would also occur when further transgression pushed the whole depositional system shoreward.

## DISCUSSIONS

### Depositional Model

The sequences described above were built up by a prograding ebb-tide delta system with the superposition of two ebb delta complexes, separated from each other by an abandonment phase when mud sedimentation prevailed. Within each ebb delta complex, the coarsening-upward, low-angle bedded sequences (Fig.15, b and e) represent the progradation of terminal lobes onto the silty and muddy shelf. The megaripple cross-bedded cosets (Fig.15, f) represent the build-up of smaller depo-lobes on the delta platform. The fining-upward megaripple-cross-bedded sequence (Fig.15, c) reflects the ebb channel which feeds the depo-lobe. This main ebb channel was wider than the estuary channel and ebb currents were thus not so well confined. They might therefore build up these lobe-like ebb-dominated sand bodies. Slight shifts of the main ebb channel would cause slight variations in the progradation direction of the new lobe, which in turn would result in vertical stacking of several ebb lobes with slight variations in megaripple foreset directions.

### Abandonment Surface

The Roda Sandstone units are always capped by thin laterally persistent calcareous sandstone beds. These are characterized by

The preserved sequences of the fossil ebb-delta and estuary channel deposits from the Roda Sandstone show many important features which are inferred to be the result of processes analogous to present-day sedimentary processes observed in the Eastern Scheldt tidal environment. Based on the comparison of both systems a depositional model is proposed for such an ebb-tide delta and estuarine channel system (Fig.16).

The ebb-tide delta has terminal lobes at the delta front, and extensive ebb-dominated subtidal depo-lobes and wide ebb tidal channels on the delta platform. A seaward progradation of the terminal lobe would produce large sand bodies many km long, a few km wide and 4-8 m thick with large-scale, low-angle inclined bedding. Compared with inshore tidal channels the main ebb channel on the delta platform would be much wider, perhaps more than 1 km, but shallower, normally less than 10 m (Fig.16, C-C'). They can therefore build up extensive ebb-dominated subtidal depo-lobes which are commonly covered by ebb-oriented megaripples (Fig.16, A-A'). This would produce sheet-like or lobe-shaped sand bodies 2-3 km wide, 3-4 km long and 2-4 m thick with internal cosets of megaripple cross-bedding. The sets would range from decimetres to 2 m in height. Progradation of a new depo-lobe over a former one would produce an offlap stacking of such lobe-shaped sand bodies. As tidal currents are less confined, megaripple foresets would show a wider range of dip directions than those found in the inshore tidal channels. The less confined tidal currents and the stronger wave influence would also inhibit the deposition of mud drapes in sand deposits. At the edge of the ebb delta, some flood-oriented megaripple cross-beddings with set heights of 20-100 cm could be expected to be formed in flood-dominated channels (Fig.16, B-B'). At the more proximal part of the ebb-delta, tidal channel sandbodies sometimes cut into the large delta lobes with a distinct erosional base.

The inshore channel deposits consist of a lower part of active channel sequences and an upper part of channel inner bend or abandoned channel sequences. In estuaries the active channels are generally narrower (hundreds of metres to 1 km) but much deeper (20 m or more) than those in the ebb delta area (Fig. 16, D-D' and E-E'). The strongly asymmetrical and rectilinear character of tidal current ellipses would produce stable megaripples up to 2 m high. They have high preservation potential along the inner bend of channels due to very high accretion rates there. In these circumstances they would produce sand bodies several kilometres long, hundreds of metres wide, and over 10 m thick with internal cosets of megaripple cross-bedding. The sets would vary from a few decimetres to 2 m in height. Continuous lateral migration of the channel could produce a much wider belt of active tidal-channel sand deposits. As the tidal currents are confined laterally by the channels, megaripple foresets would show a narrower range of dip directions than those in the ebb delta. The strongly channelized tidal currents with pronounced slack water periods and the relatively weak wave influence favour the deposition of mud drapes. The upper part of the channel inner bend and lower intertidal shoal sequences would comprise mainly of fine sand and silt with increased mud content and intercalations of mud layers. These sequences are usual-

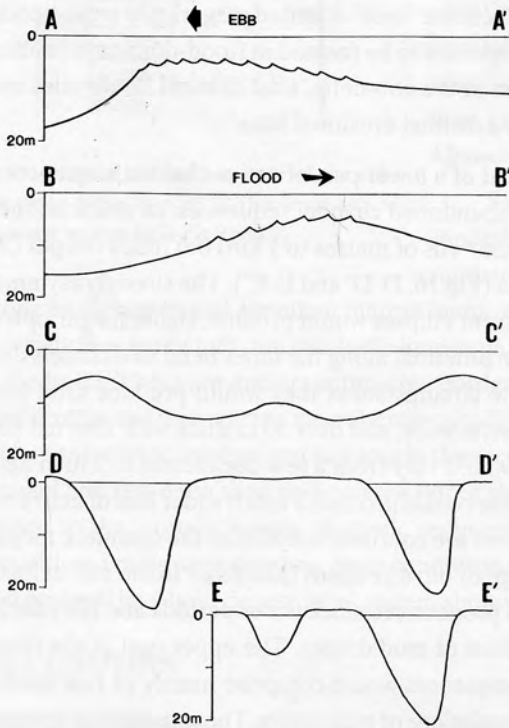
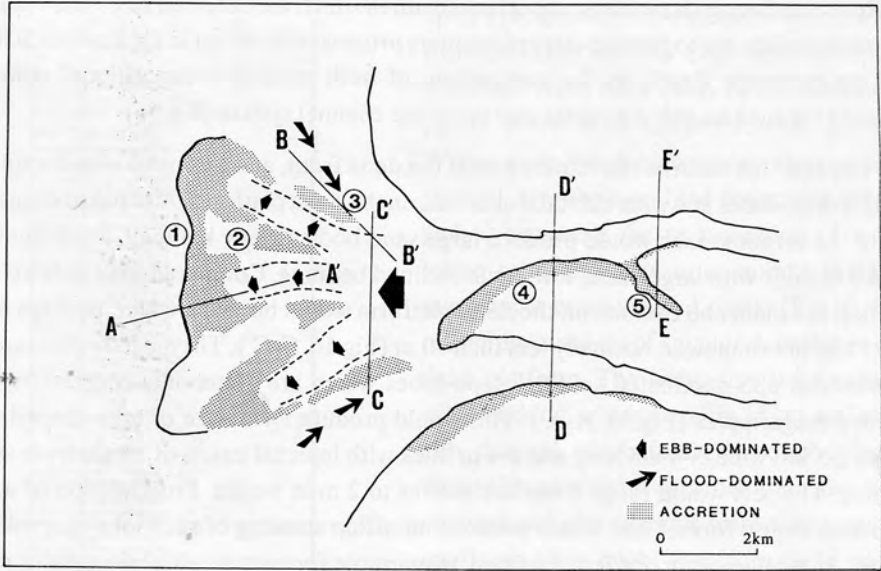
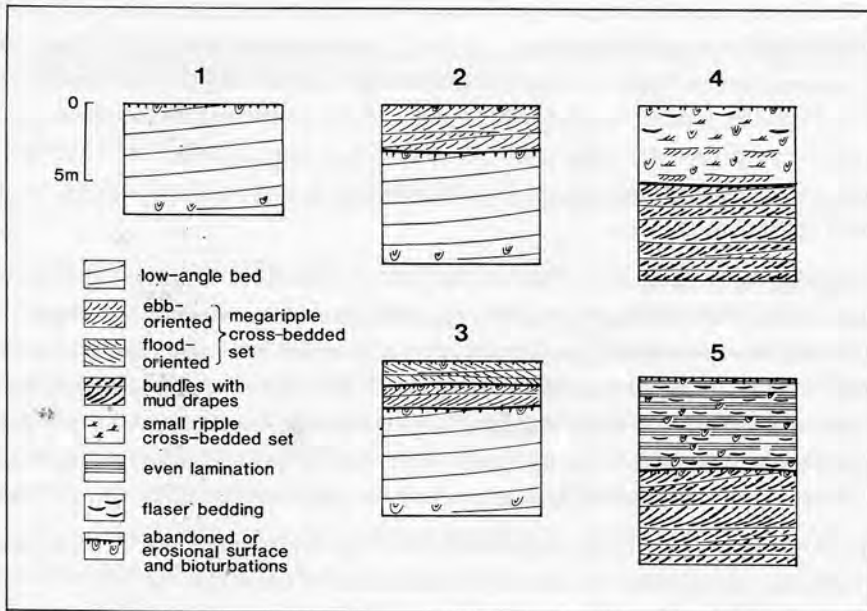


Fig.16 Depositional model of the ebb-tide delta and its associated estuary channel system. (a) Major morphological units; (b) Profiles showing morphology and bedforms; (c) Expected structures. 1.-terminal lobe at the delta front; 2. ebb-dominated depo-lobe on the delta platform; 3. marginal flood channel; 4. active estuary channel; 5. abandoned estuary channel.



ly several metres to over 10 metres thick. Small megaripple cross-bedding with set heights of 15-20 cm, small ripple cross-lamination and flaser bedding are typical structures. They reflect the increased effects of wave action and decreased influence of tidal currents. In an abandoned channel sequence, parallel lamination may be important (van den Berg, 1981). Bioturbation, however, can destroy these structures.

This depositional model of an ebb delta and its associated estuary channel is based on the examples of the Eocene Roda Sandstone and the present-day Eastern Scheldt. The overall dimensions of major sand bodies are inevitably determined by conditions within these basins, such as the scale, tectonics, sediment supply and hydraulic conditions of the basin. The model outlined above is in many respects similar to the ebb-delta model of Hayes (1975). A major difference concerns the bifurcating ebb channel. The model of Hayes, which was based on studies of tidal inlets in microtidal environments, includes a single main ebb channel, whereas our model, which is based on mesotidal ebb deltas at estuary mouths, shows a better developed tidal channel system with several ebb channels separated by sub-tidal shoals, thus producing a much larger ebb delta complex with several delta lobes.

#### Sequential Up-building

Despite many similarities, there are also important differences between the modern Eastern Scheldt ebb delta and the fossil Roda ebb delta.

The development of the present-day ebb delta differs considerably from the sequential build-up found in the fossil counterpart. The first and most important of these is the time scale. The development of a modern ebb delta involves a time scale of hundreds of



years. That is very short in the geological sense. This suggests that the active upbuilding of an ebb delta and its associated estuary channel units occurs during short, intermittent events, whereas for the rest of the time the ebb delta undergoes long periods of non-deposition and/or erosion, producing submarine abandonment surfaces and/or erosional surfaces. These surfaces represent the stage of ebb-delta abandonment or further sea-level rise. The common occurrence of such surfaces is a characteristic feature in the ebb delta as well as in estuary channel sequences.

Secondly, the build-up and preservation of an ebb delta and its related estuarine channel deposits depends critically on such factors as basin tectonics and relative sea level movements. While these factors are less important in a geographical model for a modern ebb delta environment, they are paramount in a geological model for sequential development and preservation of a fossil ebb delta. Such factors must be incorporated into the depositional model if a sequential build-up is to be achieved. The sequential development of the Roda Sandstone ebb-tide delta (Fig. 17) demonstrates the important effects of such factors.

As illustrated in Fig. 17, the stage before the delta development was characterized by a lateral shifting of the basin depocentre. Whereas some of the shifts may reflect the migration of major channels, there is nevertheless a consistent trend in shift direction from Unit A (in NNE) to Unit C (in SSW). As a result, the ebb-dominated subtidal depo-lobes in

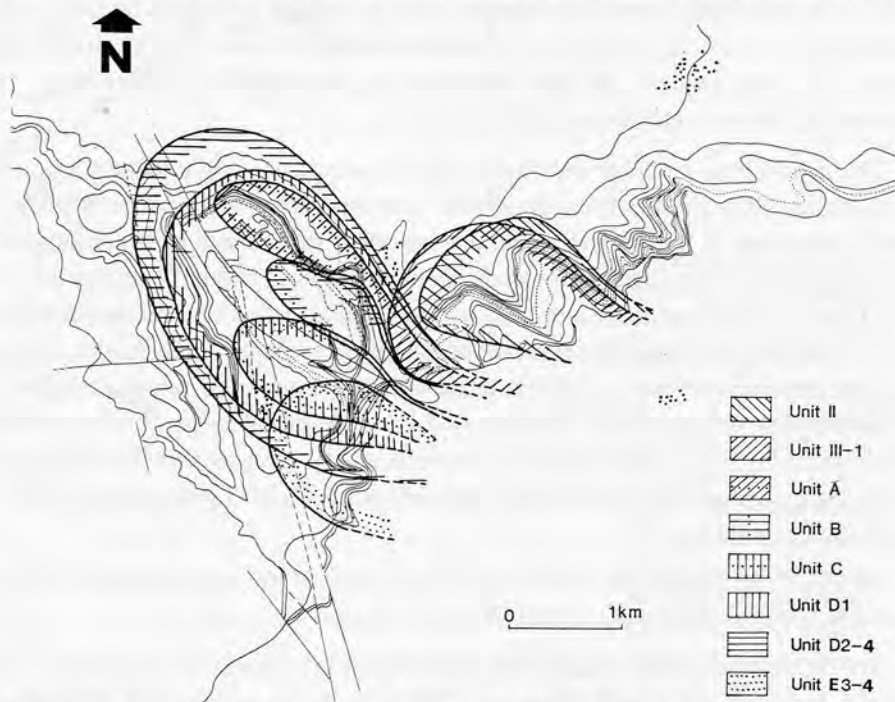


Fig. 17 Sequential development of the Lower Eocene Roda Sandstone, showing the development of major sandstone units.



Fig.18 A section of sandstone Unit B, showing the initial stage of an ebb-dominated subtidal depo-lobe (5-6 m high).

Units A, B and C only reached the initial stage (Fig.18).

This was followed by a major depositional stage, during which a stable depocenter was formed by continuous subsidence at the estuary mouth. Meanwhile, the influx of coarse clastics increased due to the uplift in the source area, located to the NE. As a result of basin subsidence and eustatic sea-level rise, tidal discharges were increased significantly. These conditions led to the build-up of major ebb-tide delta sand bodies seaward of the estuary mouth (Unit D). In the inshore estuary channels tidal channel sequences were built up over the same period (E1-2). Further transgression during the deposition of Unit E4 pushed the ebb-delta system to the ESE (Fig.17).

The sequential development of major sand bodies was controlled mainly by two factors:

1. Tectonic movements of the basin. The build-up of major sand bodies coincides with episodic ramping thrust events along the northern margin of the foreland basin, during which the thrusting sheets in the north supplied abundant clastics, and the progressive subsidence of the basin due to tectonic loading effects created a major depocentre and caused a relative sea-level rise with increasing tidal discharges in the basin. These ramping thrust episodes alternated with episodes during which the southward migration of the thrust belt resulted in a southward shift of the depocentre, as can be seen in the depositional stages of Unit A, B and C.

2. Marine transgression. The Roda Sandstone represents the deposits of the lowstand and the subsequent transgression periods. This relative sea-level rise was due to progressive basin subsidence, and superimposed on that, was a regional eustatic sea-level rise. In response to the continuous transgression and the associated increase in tidal discharge, the major sand bodies changed from a giant transverse sand bar system at the estuary mouth (Unit II and III) to a large ebb-tide delta complex outside the mouth (Unit D) (Fig.9). As the transgression continued, the whole depositional system was pushed towards the ESE. In the Isabena Valley, the major sand bodies of Unit D are exposed west of the Isabena Valley, while those of Unit E4 are exposed east of the valley (Fig.17). The overlying Esdolomada Member represents a more distal inner to middle shelf analogue to the Roda Sandstone Member. In fact, a thick medium- to coarse-grained sandstone sequence with large-scale cross-bedding has been found in a stratigraphical position equivalent to the Es-

dolomada Member in a valley about 4 km to the SE of the Isabena Valley.

The distribution of these major sandstone bodies was controlled by basin tectonic movements and the regional transgression history. The southward migration of the thrust belt caused a southward shift of the major depocenter, while continuous marine transgression pushed the whole depositional system to the ESE. Major sandstone units are therefore exposed to the SE in a successively higher stratigraphical position.

The present-day Eastern Scheldt is also characterized by continuous basin subsidence and a Holocene marine transgression. In this case the build-up of a significant ebb delta sequence depends on the sediment supply. The Eastern Scheldt tidal basin lost its connection with the Scheldt River in 1867 (van den Berg, 1984). As a consequence, no terrigenous clastic sediments are supplied to the present-day Eastern Scheldt tidal basin by fluvial systems. Ebb-delta progradation in the present-day Eastern Scheldt essentially involves the redistribution of the estuarine sediments caused by variations in tidal discharges (Yang, 1986). If the present-day trend of basin subsidence and marine transgression would continue, more sediments might be eroded from the inner-part of the estuary, and be transported and redeposited at the estuary mouth, building up an ebb-delta sequence.

## CONCLUSIONS

1. The fossil ebb delta from the Lower Eocene Roda Sandstone in southern Pyrenees, Spain shows many features which can be related to depositional processes observed in the present-day ebb-delta environment of the Eastern Scheldt estuary, SW Netherlands. Such similarities allow the construction of a depositional model for an ebb delta and estuary channel system. The ebb delta consists mainly of prograding terminal lobes at the delta front, extensive ebb-dominated subtidal depo-lobes and wide, shallow ebb channels on the delta platform flanked by marginal flood channels. The estuarine tidal basin consists of extensive intertidal shoals and relatively deep, actively migrating tidal channels.

2. The deposition of an ebb delta and its related estuary-channel sand bodies probably occurs as short-period, intermittent events when viewed on a geological time-scale. During most of the time the ebb delta area must undergo long periods of non-deposition or erosion brought about by ebb delta abandonment or further sea-level rise, producing submarine abandonment surfaces and/or erosional surfaces. The common occurrence of such surfaces is a characteristic feature in fossil ebb delta as well as estuary channel sequences.

3. The sequential development of an ebb delta and its estuary channel deposits depends critically on the marine transgressional histories and tectonic movements of the basin. The depositional patterns of sand bodies are determined mainly by the balance between sediment supply and tidal discharge (Nio & Yang, in prep.). In response to an increasing tidal discharge, brought about by a continuous basin subsidence and regional eus-

tatic sea-level rise, and the increase of sediment supply due to the uplift in the source area or the redistribution of estuary sediments caused by variations in tidal discharges, the ebb-tide delta can grow and expand, leading to a significant sequential build-up with vertical stacking of different ebb-delta complexes, provided that a stable depocentre at the estuary mouth can be maintained by continuous basin subsidence.

## ACKNOWLEDGMENTS

The authors wish to thank the technical team and the members of the Rijkswaterstaat (especially J.H. van den Berg) for collecting data in the Eastern Scheldt. Grateful thanks are due to A.D. Miall for stimulating discussion and the reprints of his interesting papers. We are grateful to P.L. de Boer, B.W. Flemming, D.B. Smith, and the members of the Comparative Sedimentology Division for helpful discussions and valuable comments, and to Miss Yolanda Furster for typing of the manuscript.

## REFERENCES

- de Mowbray, T. & Visser, M.J., 1984. Reactivation surfaces in subtidal channel deposits, Oosterschelde, southwest Netherlands. *J. Sediment. Petrol.*, 54: 811-824.
- Finley, R.J. (1975) Hydrodynamics and tidal deltas of North Inlet, South Carolina. In: Cronin, L.E. (Ed.): *Estuarine Research*, vol.II, Academic Press, New York, 277-291.
- Hayes, M.O. (1975) Morphology of sand accumulation in estuaries: an introduction to the symposium. In: Cronin, L.E. (Ed.): *Estuarine Research*, vol.II, Academic Press, New York, 3-22.
- Hine, A.C. (1975) Bedform distribution and migration patterns on tidal deltas in the Chatham Harbor Estuary, Cape Cod, Massachusetts. In: Cronin, L.E. (Ed.): *Estuarine Research*, vol.II, Academic Press, New York, 235-252.
- Hubbard, D.K. (1975) Morphology and hydrodynamics of the Merrimack River ebb-tidal delta. In: Cronin, L.E. (Ed.): *Estuarine Research*, vol.II, Academic Press, New York, 253-266.
- Mey, P.H.W., Nagtegaal, P.J.C., Roberti, K.J. & Hartevelt (1968) Lithostratigraphic subdivision of post-Hercynian deposits in the south-central Pyrenees, Spain. *Leidse geol. meded.*, 41, 221-228.
- Miall, A.D., 1988. Facies architecture in clastic sedimentary basins. In: K.L. Kleinspehn & C. Paola (Editors), *Frontiers in Sedimentary Geology, New Perspectives in Basin Analysis*. Springer-Verlag, New York, pp.67-81.
- Miall, A.D., 1988. Architectural elements and bounding surfaces in fluvial deposits: anatomy of the Kayenta Formation (Lower Jurassic), southwest Colorado. *Sediment. Geol.*, 55: 233-262.
- Miall, A.D., 1988. Reservoir heterogeneities in fluvial sandstones: lessons from outcrop studies. *AAPG Bulletin* 72 (6): 682-697.
- Nijman, W. & Nio, S.D. (1975) The Eocene Montanana delta. In: *Sedimentary evolution of the Paleogene south Pyrenean basin*. IXe Congress Int. Assoc. Sediment., excursion guide no.19.
- Nio, S.D. (1976) Marine transgressions as a factor in the formation of marine sand wave complexes. *Geol. Mijnbouw*, 55: 18-40.
- Nio, S.D. & Siegenthaler, C. (1978) A Lower Eocene estuarine- shelf complex in the Isabena valley, Spain. *Comparative studies in sedimentology*, University of Utrecht, report no.18: 1-44.
- Nio, S.D., Van den Berg, J.H., Goesten, M. & Smulders, F. (1980) Dynamics and sequential analysis of a mesotidal shoal and intershoal channel complex in the Eastern Scheldt (southwestern Netherlands). *Sediment. Geol.* 26: 263-279.



- Nio, S.D., Siegenthaler, C. & Yang, C.S. (1983) Megaripple cross-bedding as a tool for the reconstruction of the palaeo-hydraulics in a Holocene subtidal environment, S.W. Netherlands. *Geol. Mijnbouw* 62: 499-510.
- Nio, S.D. & Yang, C.S. (1983) Dynamics, geometry and sequential upbuilding of large subtidal bedforms. *Proc. Int. Symp. Sedimentation on the Continental Shelf, with special reference to the East China Sea*, 20-36, China Ocean Press, Beijing.
- Nio, S.D. & Yang, C.S. (1984) Facies pattern and sequential development of the Lower Eocene Roda Sandstone, Isabena Valley, southern Pyrenees, Spain. *Abstr. Int. Ass. Sediment. 5th European Meeting*.
- Nio, S.D. & Yang, C.S. (in prep.) Sea-level fluctuations and the geometric variability of tide-dominated sandbodies. *Bulletin de la Societe Geologique de France*.
- Oertel, G.F. (1975) Ebb-tidal deltas of Georgia Estuaries. In: Cronin, L.E. (Ed.): *Estuarine Research*, vol.II, Academic Press, New York, 267-276.
- Puigdefabregas, C., Munoz, J.A. & Marzo, M. (1986) Thrust belt development in the eastern Pyrenees and related depositional sequences in the southern foreland basin. In: Allen, P.A. & P. Homewood (eds): *Foreland Basins. Spec. Publ. Int. Ass. Sediment. 8*, Blackwell Scientific Publications, Oxford, 229-246.
- Siegenthaler, C. (1982) Tidal cross-strata and the sediment transport rate problem: a geologist's approach. *Mar. Geol.* 45: 227-240.
- Terwindt, J.H.J. (1970) Observation on submerged sand ripples with heights ranging from 30 to 200 cm occurring in tidal channels of S.W. Netherlands. *Geol. Mijnbouw*, 49: 489-501.
- Terwindt, J.H.J. (1973) Sand movement in the in- and offshore tidal area of the S.W. part of the Netherlands. *Geol. Mijnbouw*, 52: 69-77.
- Terwindt, J.H.J. (1981) Origin and sequences of sedimentary structures in inshore mesotidal deposits of the North Sea. In: Nio, S.D., R.T.E. Shuttenthelm & Tj.C.E. van Weering (eds): *Holocene Marine Sedimentation in the North Sea Basin. Spec. Publ. Int. Ass. Sediment. 5*, Blackwell Scientific Publications, Oxford, 4-26.
- Vail, P.R. (1987) Seismic stratigraphy interpretation using sequence stratigraphy, Part 1: Seismic stratigraphy interpretation procedure. In: A.W. Bally (ed.): *Atlas of seismic stratigraphy, AAPG studies in geology no.27*, Tulsa, Oklahoma, Vol.1, 1-10.
- Van den Berg, J.H. (1981) Rhythmic seasonal layering in a mesotidal channel fill sequence, Oosterschelde mouth, the Netherlands. In: Nio, S.D., R.T.E. Shuttenthelm & Tj.C.E. van Weering (eds): *Holocene marine sedimentation in the North Sea basin. Spec. Publ. Int. Ass. Sediment. 5*, Blackwell Scientific Publications, Oxford, 147-159.
- Van den Berg, J.H. (1982) Migration of large-scale bedforms and preservation of crossbedded sets in highly accretional parts of tidal channels in the Oosterschelde, SW Netherlands. *Geol. Mijnbouw*, 61: 253-263.
- Van den Berg, J.H. (1984) Morphological changes of the ebb-tidal delta of the Eastern Scheldt during recent decades. *Geol. Mijnbouw* 63: 363-375.
- Visser, M.J. (1980) Neap-spring cycles reflected in Holocene subtidal large-scale bedform deposits: a preliminary note. *Geology* 8: 543-546.
- Wright, L.D. & Sonu, C.J. (1975) Processes of sediment transport and tidal delta development in a stratified tidal inlet. In: Cronin, L.E. (Ed.): *Estuarine Research*, vol.II, Academic Press, New York, 63-76.
- Yang, C.S. & S.D. Nio (1985) The estimation of paleo-hydrodynamic processes from subtidal deposits using time series analysis methods. *Sedimentology* 32: 41-57.
- Yang, C.S. (1986) Estimates of sand transport in the Oosterschelde tidal basin using current-velocity measurements. *Mar. Geol.*, 72: 143-170.



## Chapter 6

### An Early Holocene tidal delta of the Changjiang River

#### On the origin of Jianggang Radial Sand Ridges

Chang-Shu Yang

Ministry of Geology and Mineral Resources, Bureau of Marine Geological Survey, 526  
Yan An Road West, Shanghai, China

#### ABSTRACT

Based on large-scale investigations of marine geology in Jianggang Radial Sand Ridges off Jiangsu coast and the adjacent area in SW Southern Yellow Sea, this paper discusses the sedimentary and hydrodynamic features of Jianggang Radial Sand Ridges. Available data indicate: (1) Jianggang Radial Sand Ridges formed during early-Holocene, i.e. in the period from about 10000 B.P., when the Holocene transgression reached this area, to about 7500 B.P. before the maximum Holocene transgression. (2) The sediments of Jianggang Radial Sand Ridges were mainly derived from Changjiang River. (3) The major hydrodynamic factor responsible for the development of Jianggang Radial Sand Ridges was not long-shore currents, but tidal currents. Because of the geomorphological boundary conditions in this area, the progressive tidal wave from the East China Sea and the amphidromic tidal wave from southern Yellow Sea met off Jianggang coast, where the two sets of tidal waves had a phase difference of about one ebb-flood period and therefore could interfere constructively with each other, causing the increase of tidal ranges and forming the radial flow field of tidal currents, which controlled the radial distribution pattern of the tidal sand ridges. (4) Jianggang Radial Sand Ridges represent an Early Holocene tidal delta of the Changjiang River characterized by huge radial tidal sand ridges. When Early Holocene transgression

---

This chapter is published as:

Yang, C.S., 1985. On the origin of Jianggang Radial Sand Ridges in Yellow Sea. *Marine Geology & Quaternary Geology*, 5(3): 35-44 (in chinese).

reached this area, a wide funnel-shaped estuary was established and a large tidal delta begun to develop as the sands from the Changjiang River were deposited in the estuary mouth and the adjacent shallow shelf area under the control of strong tidal currents. During the subsequent abandonment stage, tidal processes became dominant, modifying this tidal delta further into radial sand ridges.

## INTRODUCTION

Jianggang Radial Sand Ridges are situated to the north of the Modern Changjiang River Delta and to the south of the Old Huanghe River Delta. The major sand bodies extend in the shallow shelf area of the SW Southern Yellow Sea off the Subei coast. The distinctive radial distribution pattern and huge dimensions of these sand ridges have drawn extensive attentions of marine geologists and sedimentologists in China. Due to difficult working conditions, however, the research of this area is still limited, and the explanation for the origin of this important sedimentary system is rather controversial (Li et al., 1979; Zhou & Sun, 1981; Li & Li, 1981; Zhang et al., 1984).

The correct explanation for the origin of the Jianggang Radial Sand Ridges is the key to the understanding of the whole evolution history of the Holocene Changjiang River Delta. Based on large-scale marine geological survey in Jianggang Radial Sand Ridges and the adjacent area carried out by the Bureau of Marine Geological Survey in Shanghai, Ministry of Geology and Mineral Resources, this paper describes the general features of the Jianggang Radial Sand Ridges and discusses three problems concerning their origin: the time and history of their formation, the source of their sediments and the hydrodynamic conditions during the deposition, which are essential to further research of the evolution history of the Holocene Changjiang River Delta.

## JIANGGANG RADIAL SAND RIDGES

Jianggang Radial Sand Ridges are situated to the north of the modern Changjiang River Delta, off the Subei coast. It covers a shallow shelf area of about 35000 km<sup>2</sup> (250 km N-S and 140 km E-W) with the shape of a huge fan (Fig.1). Main sand ridges are distributed in a radial pattern with Jianggang as the apex. Individual sand ridges are elongated. Water depths to the top of these sand ridges range from 5 to 20 m. Between these sand ridges are wide troughs. Approaching the apex near Jianggang, individual sand ridges merge together, forming large shallow subtidal to intertidal shoals which emerge during low tides. Part of the shoals in the apex has merged into the present-day coastal plain of Subei.

These sand ridges are characterized by huge dimensions. Individual sand ridges are 60-100 km long, 10-15 km wide and 10-15 m high. These sand ridges consist of grey, well-sorted fine sands with shell debris, silty sands and sandy silt. There is a gradual decrease of the grain size from well-sorted fine sands with enrichment of heavy minerals in the shoals near apex to silty sands and sandy silt in distal parts of the sand ridge. Deposits in the troughs,

however, are mainly muddy silt.

## THE AGE OF JIAGANG RADIAL SAND RIDGES

A commonly hold opinion considered Jiagang Radial Sand Ridges as the associated facies of modern Changjiang River Delta. Its sediments are mainly derived from Changjiang River in the south and the abandoned Old Huanghe River Delta in the north. The sediments from Changjiang River mouth and the materials eroded from abandoned Old Huanghe River Delta are transported by northward and southward longshore currents, respectively. They meet in the area near Jiagang where they are deposited under the influence of shelf process, forming radial sand ridges. Data on hydrodynamic conditions and sediment movements, however, suggest that this is not the case.

In the western part of Southern Yellow Sea there exists southward flowing Yellow Sea Longshore Current which transports cold, low-salinity water of the Yellow Sea to the East China Sea (Fig.2). It is the counter current of the northward flowing Yellow Sea Warm Current (a branch of the warm, high-salinity Kuroshi Current). As the Yellow Sea Warm Current flows northward all year round, for the exchange and equilibrium of sea water in the

Southern Yellow Sea, the southward flowing Yellow Sea Longshore Current does not show a seasonal change in current direction. Although the south wind in summer might reverse the surface current, the flow under the surface is still southward.

Along the west coast of the Southern Yellow Sea, there exists the Subei Longshore Current, which is the right flank of the Yellow Sea Longshore Current. Due to shallow water depth (often smaller than 10 m) Subei Longshore Current exhibits low velocities (15-

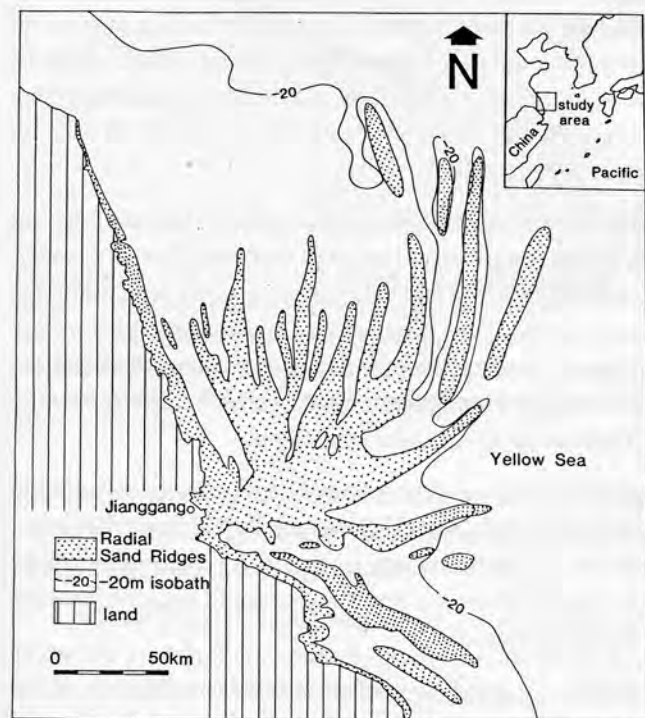


Fig.1 Distribution of the Jiagang Radial Sand Ridges.

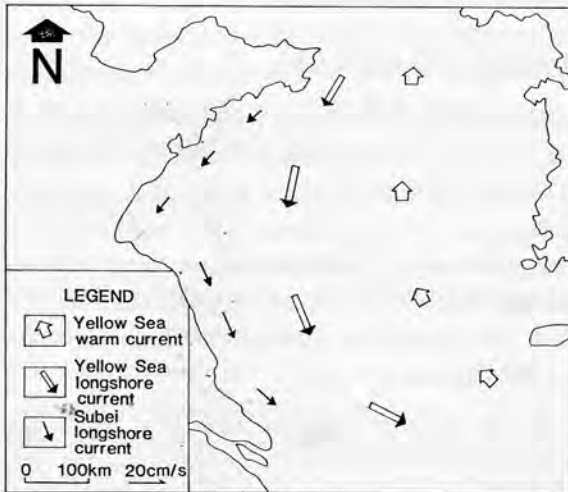


Fig.2 The current system in the southern Yellow Sea.

area. This is also confirmed by satellite photo (Yun et al., 1981). The satellite photo off Changjiang River Mouth shows that the northern boundary for the distribution of the sediments from present-day Changjiang River lies near Liuse of Subei (about 100 km southeast of the Jianguang), where the tone of sea water in MSS-5 photo is two level lower than that near Changjiang mouth, indicating that the sediments from Changjiang River are not transported to the Jianguang area in large quantities.

The distribution of sediment grain sizes in Jianguang Radial Sand Ridges and adjacent area (Fig.3) shows that Jianguang Radial Sand Ridges consist of coarse sediments of sands. The abandoned Old Huanghe River Delta to the north, however, consists of fine-grained sediments of silt and mud. The modern Changjiang Subaqueous Delta to the south also consists mainly of fine sediments of silt, only river mouth sand bars contain sands. This pattern suggests that Jianguang Radial Sand Ridges do not receive sands from Changjiang River or abandoned Old Huanghe River Delta at the present-day conditions.

In fact some of the sand bodies in Jianguang Radial Sand Ridges have been buried in Subei Coastal Plain. The above discussion indicates: (1) Jianguang Radial Sand Ridges are not formed in modern environments, its formation was earlier than modern Changjiang River Delta. (2) Jianguang Radial Sand Ridges are not the associated facies of modern Changjiang River Delta, it is a huge delta by itself.

Detailed investigations revealed that the Late-Pleistocene palaeo-channels of the Changjiang River on the present-day shelf were buried under the Radial Sand Ridges near Jianguang. This is clear evidence that Jianguang Radial Sand Ridges were deposited on the Palaeo-geomorphological surface of Late-Pleistocene. Available data show that the

25 cm/s) and variable directions. In winter it flows southward and may pass the present-day Changjiang River Mouth and join southward flowing Changjiang Dilute Current. In summer the current near sea surface is dominated by Changjiang Dilute Current which turns to the NE, near bottom, however, Subei Longshore Current still flow to the southeast. Such a current is unlikely to cause the northward transport of large amount of fine sands from Changjiang River Mouth to the Jianguang



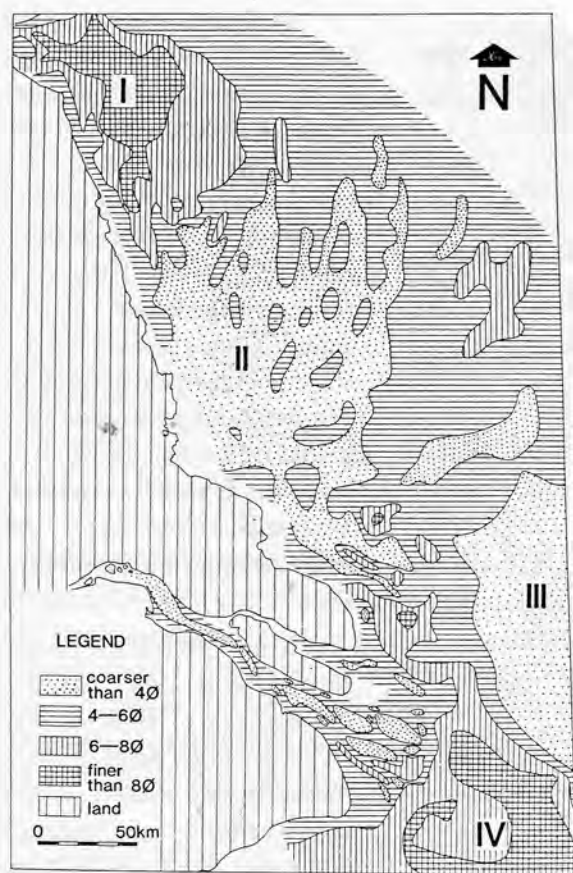


Fig.3 Grain size of the surficial sediments in Jianggang Radial Sand Ridges and adjacent area. I: Old Huanghe River Delta; II: Jianggang Radial Sand Ridges; III: Late Pleistocene Changjiang River Delta; IV: Modern Changjiang River Subaqueous Delta (data from unpublished report of Marine Geological Survey and Li et al., 1979).

Holocene deltaic, nearshore and shallow marine deposits are widely distributed in the area around Jianggang Radial Sand Ridges. Their thicknesses are 20-40 m in coastal area of Subei, 20-35 m in Shanghai area (Guo et al., 1979), and less than 10 m to more than 30 m in modern Changjiang Subaqueous Delta (unpublished report of Marine Geological Survey, 1984). The boundary between Holocene and underlying Pleistocene is characterized by a layer of terrestrial dark-green stiff clay or yellowish-green stiff clay at the top of Late Pleistocene. This key horizon is present in Shanghai and Subei area. It has been found also in modern subaqueous delta of the Changjiang River (unpublished report of Marine Geological Survey, 1984), northern shelf of the East China Sea as well as the shelf of Southern Yellow Sea (Yang, 1983; Wang et al., 1984). Shallow boreholes in Jianggang Radial Sand Ridges have revealed an underlying yellowish brown stiff clay layer with

ferruginous nodules and rootlets. It is comparable to the dark-green stiff clay at the top of Late-Pleistocene, representing palaeo-soil horizon. These data indicate that Jianggang Radial Sand Ridges belong to Holocene.

In Late Pleistocene Changjiang River passed the area of Jianggang. During Early-Holocene transgression, the sea-level rose to -30 m at about 10000 years B.P. and the Changjiang River entered the sea near Jianggang, where a wide funnel-shaped estuary was established. The sands from Changjiang River were deposited in estuary mouth and the adjacent shallow shelf area under the control of strong tidal currents, forming a large tidal delta.



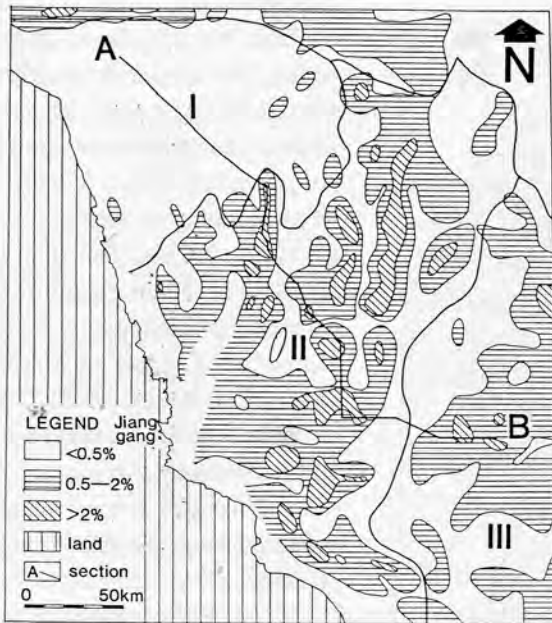


Fig.4 Contents and assemblages of heavy minerals in the surficial sediments of Jianggang Radial Sand Ridges and adjacent area. I: Old Huanghe River Delta; II: Jianggang Radial Sand Ridges; III: Late Pleistocene Changjiang River Delta (data from Luo et al., 1983).

amount of sands from the Changjiang River. The sand supply to Jianggang area was then reduced and the tidal delta underwent a stage of abandonment. Tidal processes became dominant and modified this tidal delta further into radial sand bodies. The major sand ridges extended to the north and northeast, whereas those in southeast direction are relatively small. Fine-grained sediments were brought further offshore and deposited in the Central Basin of the Southern Yellow Sea.

In present-day environment the Jianggang Radial Sand Ridges undergoes the modification by tidal currents and the destruction by storms, waves and longshore currents. As the coastal line prograded gradually, part of the sand ridges were buried in Coastal Plain of Subei.

## THE SOURCE OF THE SEDIMENTS OF JIANGGANG RADIAL SAND RIDGES

There were two important sediment sources around the west coast of the Southern Yellow Sea, i.e. the Changjiang River and the Old Huanghe River. Data on heavy minerals

From 10000 B.P. to 7500 B.P. was the development stage of this Early Holocene tidal delta. During this period the sea-level rose slowly (about 1.1 cm/year on average) and came to a standstill at -30 m and -20 m for some time (Wang, 1982). As a result of large amount of sand supply from the Changjiang River, depositional rates in Jianggang area were rather high, producing a certain thickness of Early Holocene deltaic and shallow marine deposits on the Late Pleistocene morphological surface.

After 7500 B.P. the further rise of the sea-level caused a westward shift of the depocenter for about 150 km, forming a wide funnel-shaped estuary mouth with Zhenjiang and Yangzhou as the apex, which trapped large

TABLE 1

The average contents of some heavy minerals in the surficial sediments of Jianggang Radial Sand Ridges and adjacent area (data from Luo et al., 1983).

Areas	Old Huanghe River Delta (%)	Jianggang Radial Sand Ridges (%)	Late-Pleistocene Changjiang Delta (%)	Modern Changjiang River Sediments (%)
Total heavy minerals	0.1341	0.9945	0.6366	
Ilmenite	0.0069	0.1057	0.0954	0.1107
Claenite	0.00001	0.0001	0.0002	0.0001-0.001
Staurolite	0.00008	0.0005	0.0005	0.0001-0.001

in surficial sediments of SW Southern Yellow Sea (Luo et al., 1983) indicate that the sediments of the Jianggang Radial Sand Ridges were mainly derived from Changjiang River. The Jianggang Radial Sand Ridges and the Late Pleistocene Changjiang Delta show a high content of heavy minerals, while the Old Huanghe River Delta has a low content of heavy minerals (Fig.4). The average contents of heavy minerals are as high as 0.9945% and 0.6360% in Jianggang area and Late Pleistocene Changjiang Delta respectively, but only 0.1341% in Old Huanghe River Delta area (Table 1). Such a variation pattern in heavy

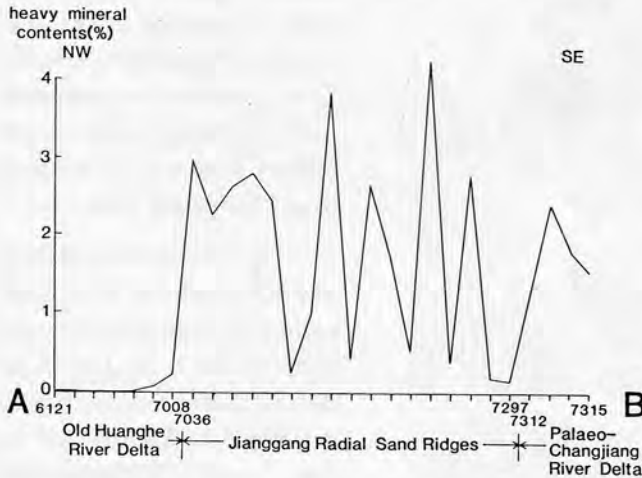


Fig.5 Heavy mineral contents in the surficial sediments from Stations 6121 to 7315 in SW Southern Yellow Sea. The location of the section is shown in Fig.4 as A-B.

mineral contents is also obvious in the cross-section of the surficial sediments of SW Southern Yellow Sea (Fig.5). The northwestern part of the section (Stations 6121 to 7008) shows low contents of heavy minerals of the Old Huanghe River Delta, which consists mainly of muddy silt and sandy silt. The section between Stations 7036 and 7297 shows high contents of heavy minerals of the Jianggang Radial Sand Ridges, which consist

mainly of fine sand, silty sand and sandy silt. The southeastern part of the section (Stations 7312 to 7315) shows high contents of heavy minerals of the Late Pleistocene Changjiang River Delta, which consists mainly of fine sand and silt. These data indicate that the sediments from the Huanghe River are mainly silt with a low content of heavy minerals, whereas those from Changjiang River has a higher content of heavy minerals which is similar to that of Jianggang Radial Sand Ridges.

The assemblage features of heavy minerals also show a clear pattern (Fig.4). The Old Huanghe River Delta shows an assemblage of hornblende-epidote-garnet-ilmenite, and the Late Pleistocene Changjiang River Delta exhibits an assemblage of hornblende-epidote-ilmenite-staurolite-cianite. The Jianggang Sand Ridges show an assemblage of hornblende-epidote-ilmenite-staurolite, which is similar to that of Late Pleistocene Changjiang River Delta.

Compared with the Huanghe River, the sediments from the Changjiang River have relatively higher contents of ilmenite, cianite and staurolite, which are characteristic of metamorphic source rocks (Table 1). The average contents of ilmenite, cianite and staurolite in Jianggang Radial Sand Ridges are much higher than those of the Old Huanghe River Delta, whereas similar to those in the Late Pleistocene Changjiang River Delta and the modern Changjiang River sediments (Table 1). The distribution pattern of ilmenite in surficial sediments shows relative high contents of ilmenite in Jianggang Radial Sand Ridges and the Late Pleistocene Changjiang River Delta, and much lower contents of ilmenite in the Old Huanghe River Delta (Fig.6).

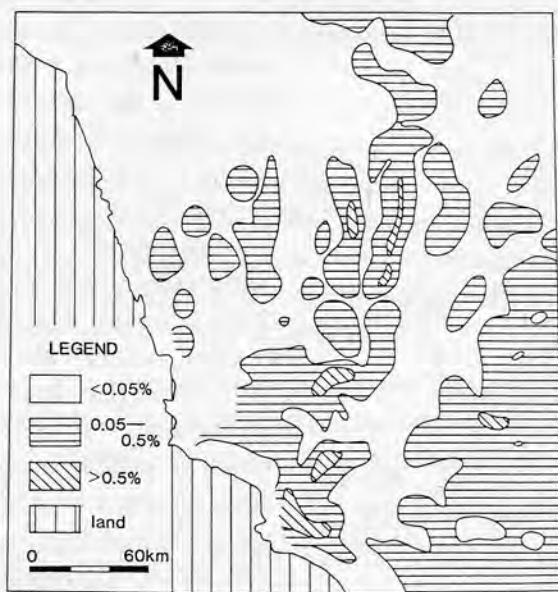


Fig.6 Contents of ilmenite of the surface sediments in Jianggang Radial Sand Ridges and adjacent areas (data from Luo et al., 1983).

Ridges and the Late Pleistocene Changjiang River Delta, and much lower contents of ilmenite in the Old Huanghe River Delta (Fig.6). This illustrates that sediments in Jiang-gang Radial Sand Ridges were mainly derived from Chang-jiang River.

Fig.7 shows the variation of  $\text{CaCO}_3$  contents in surficial sediments. The average contents of  $\text{CaCO}_3$  are 10.50% in the Old Huanghe River Delta, but only 8.20% and 6.68% in the Late Pleistocene Changjiang Delta and the modern Chang-jiang River Delta, respectively. This may reflect the influence of cal-

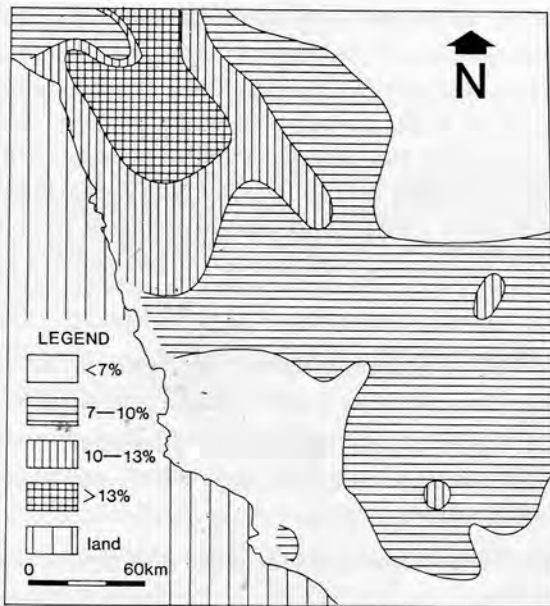


Fig.7 Contents of  $\text{CaCO}_3$  of the surface sediments in Jianggang Radial Sand Ridges and adjacent areas.

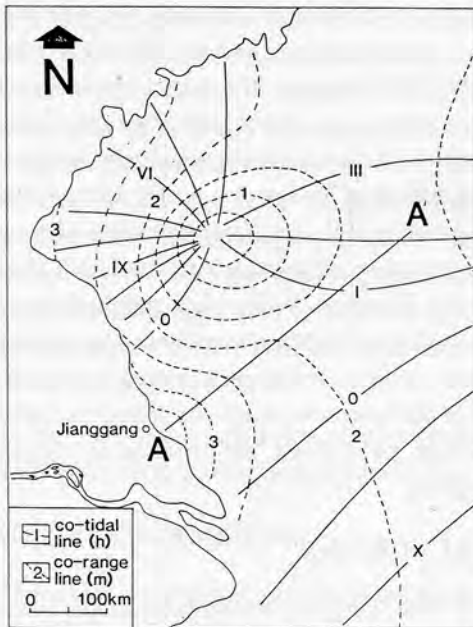


Fig.8 Co-tidal lines (h) of the  $M_2$  tide and co-range lines (m) of semi-diurnal tide in SW Southern Yellow Sea (phases referred to the 135 E, modified from Defant, 1960).

careous sediments in the middle reach of the Huanghe River. The average  $\text{CaCO}_3$  content in Jianggang Radial Sand Ridges is only 6.66%, much lower than that of the Old Huanghe River Delta whereas similar to that of the modern Changjiang River Delta. This indicates again that the sediments of Jianggang Radial Sand Ridges are derived mainly from the Changjiang River.

### HYDRODYNAMIC CONDITION

A distinctive feature of the Jianggang Radial Sand Ridges is the radial distribution pattern of the sand bodies, which is different from many other tidal deltas. This can be attributed to the unique hydrodynamic conditions. The shallow shelf off Jianggang is dominated by semi-diurnal tidal processes and controlled by two tidal wave systems (Fig.8), i.e. the East China Sea progressive tidal wave and the Southern Yellow Sea amphidromic tidal wave. The former propagates from the southeast into the study area. The latter formed due to the reflection of the incident tidal wave by Shandong Peninsula and the coriolis effects. It propagates from the north into

the study area with a speed  $c$  determined by water depth  $d$  and gravitational acceleration  $g$  in the equation (Harvey, 1976):

$$c = \sqrt{gd} \quad (1)$$

Assuming a mean water depth of 25 m in the west part of southern Yellow Sea and a distance  $L$  of 340 km between A-A' line in the study area and the southern coastal line of Shandong Peninsula, the travelling time  $t$  for an incident tidal wave to propagate from A-A' line to Shandong Peninsula and then to be reflected back to A-A' can be estimated as:

$$t = 2L/\sqrt{gd} = 12.1 \text{ h} \quad (2)$$

This indicates that the southern Yellow Sea amphidromic tidal wave arrives at Jianggang area about 12 hours later than the East China Sea progressive tidal wave. The phase difference is approx. a flood/ebb period of semidiurnal tides (12.4 h). These two sets of tidal waves could therefore interfere constructively with each other, causing the resonance and increase of tidal ranges off Jianggang (Fig.8).

The presence of two tidal wave systems also determines the radial flow field of tidal currents (Fig.9). The northern part of the study area is dominated by the Southern Yellow Sea amphidromic tidal wave with N-S oriented long axis of tidal ellipse. The southeastern part is dominated by the Eastern China Sea progressive tidal wave with long axis of tidal ellipse in a NW-SE direction. The northeastern part, however, is the transitional area between the two tidal wave systems and the long axis of tidal ellipse is in a NE-SW direction. The maximum tidal currents are more than 1 m/s. Since similar geomorphological boundary conditions should exist in the western area of the Southern Yellow Sea during Early Holocene transgression, it is considered that there also existed the progressive tidal wave from the East China Sea and the Southern Yellow Sea amphidromic tidal wave reflected by Shandong Peninsula, causing the increase of tidal ranges and forming the radial flow field of tidal currents, which controlled the radial distribution pattern of the tidal sand ridges off Jianggang.

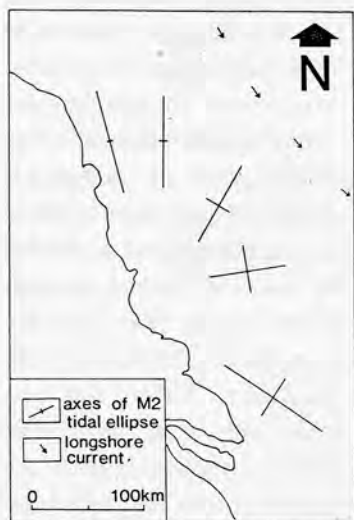


Fig.9 Flow field of tidal currents in Jianggang Radial Sand Ridges area (after Li & Li, 1981).

## CONCLUSIONS

1. The Jianggang Radial Sand Ridges belong to Holocene. It was formed mainly in Early Holocene, i.e. in the period from about 10000 B.P., when the Holocene transgression reached this area, to about



7500 B.P. before the maximum Holocene transgression. In recent environment (after the maximum Holocene transgression) the sediment supply from Recent Changjiang River Delta or abandoned Old Huanghe River Delta to Jianggang Radial Sand Ridges is low and has no direct relation with the formation of the Jianggang Radial Sand Ridges.

2. The sediments of both the Jianggang Radial Sand Ridges and the Late Pleistocene Changjiang River Delta differ from those of the Old Huanghe River Delta by coarse grain size, high content of heavy minerals, low content of  $\text{CaCO}_3$  and the presence of the accessory minerals characteristic of the metamorphic source rocks (Table 1). The sediments of the Jianggang Radial Sand Ridges were derived mainly from the Changjiang River. The sediments from the Huanghe River did not contribute significantly to the formation of the Jianggang Radial Sand Ridges.

3. The major hydrodynamic factor responsible for the development of Jianggang Radial Sand Ridges was not longshore currents, but tidal currents. Because of the geomorphological boundary conditions of this area in Early Holocene, the tides were semidiurnal and dominated by the East China Sea progressive tidal wave and the southern Yellow Sea amphidromic tidal wave. They met off Jianggang coast, where the two sets of tidal waves had a phase difference of about an ebb-flood period and therefore could interfere constructively with each other, causing the increase of tidal range and forming the radial flow field of tidal currents, which controlled the radial distribution pattern of the tidal sand ridges.

4. The above discussion indicates that the Jianggang Radial Sand Ridges are not the associated facies with sediments derived from Recent Changjiang River Delta, Old Huanghe River Delta or Late Pleistocene Changjiang River Delta. It represents an Early Holocene tidal delta of the Changjiang River characterized by huge radial sand ridges, which has already formed before the development of Recent Changjiang River Delta. During Late Pleistocene palaeo-Changjiang passed Jianggang area. When Early Holocene transgression reached this area, a wide estuary was established and a large tidal delta begun to develop as the sands from the Changjiang River were deposited in estuary mouth and the adjacent shallow shelf area under the control of strong tidal currents. During the subsequent abandonment state tidal processes became dominant and modified this tidal delta further into radial sand ridges.

5. In present-day environment the Jianggang Radial Sand Ridges undergo the modification by tidal currents and the destruction by storms, waves and longshore currents.

## **ACKNOWLEDGEMENTS**

Data from unpublished reports of the Bureau of Marine Geological Survey are used. I am grateful to the technique team and crew members of the Bureau of Marine Geological Survey in Shanghai, Ministry of Geology and Mineral Resources for field investigations at sea. Special appreciation and thanks are due to Prof. Nio, S.D. of the Sedimentology

Division, University of Utrecht, and my colleagues in the Bureau of Marine Geological Survey in Shanghai for valuable discussions.

## REFERENCES

- Defant, A., 1960. Physical oceanography. Pergamon press, pp.423.
- Guo, X.M., Xue, S.Y., Wang, J.T. & Li, C.X., 1979. Stratigraphy and areal subdivision of Holocene deposits of Yangtze Estuary region. *Journal of Tung-Chi University*, No.2, p.15-26 (in chinese).
- Harvey, J.G., 1976. Atmosphere and ocean: our fluid environments. The Artemis press, pp.74.
- Li, C.X., Wang, J.T. & Li, P., 1979. Preliminary study on sedimentary facies and sequence of the Yangtze Delta. *Journal of Tung-Chi University*, No.2, p.1-14 (in chinese).
- Li, C.Z. & Li, B.C., 1981. Studies on the formation of Subei Sand Cays. *Oceanologia ET Limnologia sinica*, 12(4): 321-331 (in chinese).
- Luo, M.Y., Shi, S.Q. & Lin, J.Y., 1983. Distribution and zoning of heavy minerals in surficial sediments in the western part of southern Yellow Sea. *Marine Geology and Quaternary Geology*, 3(1): 55-65 (in chinese).
- Wang, K.F. et al., 1984. Quaternary spore-pollen assemblages of Changjiang Delta and the stratigraphical and palaeo-geographical implications. *ACTA oceanologia sinica*, 6(4): 485-496 (in chinese).
- Wang, Z.Y., 1982. Discussion on the characteristics and origin of the relict sand of western Souther Yellow Sea. *Marine Geological Research*, 2(3): 63-70 (in chinese).
- Yang, W.D., 1983. The age and dynamical sedimentary features of the shelf sand out of Yangtze Estuary. *Marine Geology and Quaternary Geology*. 3(2): 41-49 (in chinese).
- Yun, C.X., Cai, M.Y. & Wang, B.Q., 1981. An analysis of the diffusion of suspended sediment discharged from the Changjiang River based on the satellite images. *Oceanologia ET Limnologia sinica*, 12(5): 391-401 (in chinese).
- Zhang, G.D., Wang, Y.Y., Zhu, J.C., Dong, Y.X. & Wu, P., 1984. Modern tidal flat deposits of Jianggang, Subei. *ACTA sedimentologica sinica*, 2(2): 39-49, (in chinese).
- Zhou, C.Z. & Sun, J.S., 1981. On the origin of shallow shoals off Subei coast. *Marine Geological Research*, 1(1) (in chinese).

## Chapter 7

# Tidal sand ridges on the East China Sea shelf

This chapter is published as:

Yang, C.S. & Sun, J.S., 1988. Tidal sand ridges on the East China Sea shelf. In: P.L. de Boer, A. van Gelder and S.D. Nio (eds.), *Tide-Influenced Sedimentary Environments and Facies*. D. Reidel Publishing Company, pp.23-38.

## TIDAL SAND RIDGES ON THE EAST CHINA SEA SHELF

Yang Chang-shu & Sun Jia-song  
Ministry of Geology and Mineral Resources  
Bureau of Marine Geological Survey  
526 Yan An Road West  
Shanghai, China

**ABSTRACT.** Widespread investigations have revealed sand ridges on the shelf of the East China Sea. They occur mainly in the submerged palaeovalley of the Changjiang River and the adjacent area. These huge sand ridges are 10 - 60 km long, 2 - 5 km wide and 5 - 20 m high with a spacing of 8 - 14 km. They extend ESE - WNW (about 120° - 300°). They have asymmetrical profiles in transverse sections, with steeper slopes facing SSW. They mainly consist of well-sorted fine sands (grain size of 2.5 - 3.0 $\phi$ ) with abundant debris of intertidal to shallow water marine shells. The shallow seismic profiles show an unconformity between the sand ridges and the underlying strata, and the very low-angle inclined layers within the sand ridges.

The sand ridges on the shelf of the East China Sea occur mainly in four groups. The depths to the top of these groups are 96 - 115 m, 75 - 90 m, 58 - 70 m and 45 - 55 m. This corresponds to the palaeocoastlines of -100 m, -80 m, -60 m and -50 m respectively, reflecting the history of the post-glacial transgression in the East China Sea.

The shallow marine fossils and the moribund morphology suggest that the tidal sand ridges on the East China Sea shelf probably developed during the post-glacial transgression when water depths were shallower and tidal currents were stronger than those of the present-day. As the sea level rose and the tidal currents became weaker, the sand ridges gradually ceased growing and became 'relict' sand bodies on the shelf of the East China Sea. When covered by fine-grained sediments of late Holocene age in the nearshore area, they were preserved in the stratigraphical section and became an important type of sand body formed in estuary to shallow shelf tidal environments. Evidence of such buried sand bodies can be found in some shallow seismic profiles from the Bureau of Marine Geological Survey.

## INTRODUCTION

The shelf of the East China Sea extends from the mainland of China to a maximum width of 400 - 500 km. It is bounded to the east by the Okinawa Trough. The entire northwestern section of this shelf is less than 100 m deep, and the shelf edge is at a depth of about 150 m. Large-scale sealevel fluctuations since the late-Pleistocene caused the observed geomorphology and sediment distribution pattern on the present-day shelf of the East China Sea. Previous marine geological

investigations of the East China Sea concentrated mainly on the distribution of palaeodeltas and palaeovalleys, sealevel changes and palaeoshoreline migrations since the late-Pleistocene, and the distribution and characteristics of the sediments on the shelf. The results show that a large part of this area was covered by sands. The characteristics and distribution pattern of these sands are of great interest to Chinese marine geologists. Zhu, Zeng & Feng (1983) reported comb-like assemblages of sand ridges on the shelf off the Zhejiang coast. They considered these to be a relict coastal geomorphological type. Gen (1982) and Li & Chen (1984) discussed the sand barrier-lagoon systems which are parallel with the coastline. They proposed that sand barrier-lagoon systems developed not only as one of the major sedimentary units along the present-day Chinese coast, but also on the East China Sea shelf during the post-glacial transgression. These studies revealed some genetic types of the surficial sandy deposits in certain environments of the East China Sea shelf (mainly nearshore area). In general, however, the investigations of the East China Sea shelf are still limited. Further research is therefore necessary concerning the type, thicknesses, distribution pattern, sedimentary characteristics, internal structures and genesis of the surficial sandy deposits in a large area of the East China Sea shelf, which are generally referred to as 'relict sands'.

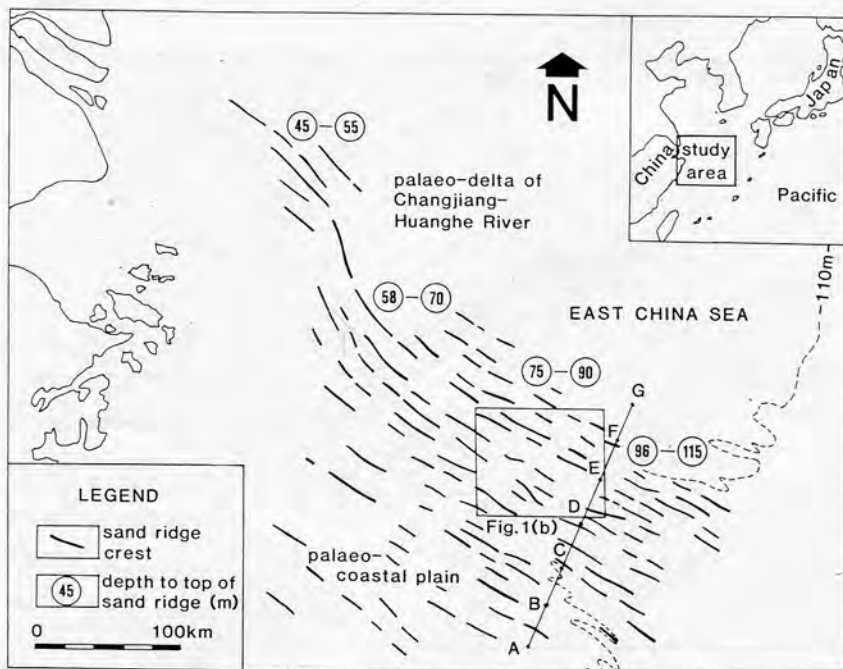


Figure 1a. Tidal sand ridges on the shelf of the East China Sea.



Extensive echo-sounding has been carried out by the Bureau of Marine Geological Survey in Shanghai, Ministry of Geology and Mineral Resources, on the shelf of the East China Sea, along with grab and vibrocore sampling, shallow drilling and shallow seismic profiling in some areas. About 190,000 km of echo-sounding data were obtained. Grab and vibrocore samples were collected with a spacing of 5 to 20 km on the inner shelf, and a wider spacing on the outer shelf. A shallow seismic survey was conducted using E.G. & G.'s uniboom system, which operated with an output power of 300 J. The seismic signals have a bandwidth of 300 - 4,000 Hz. The results revealed for the first time the presence of large-scale tidal sand ridges on the shelf of the East China Sea which probably developed during the post-glacial transgression. Based on unpublished data from the Bureau of Marine Geological Survey, this paper discusses the distribution, morphological features, sediment composition, internal structures, origin, evolution and the present-day stability of these large-scale tidal sand ridges. The research into these large-scale tidal sand ridges is essential to the study of the relict sand genetic type. It is also of great importance to the evaluation of geotechnical conditions and the study of depositional models of these large sand bodies in shelf environments.

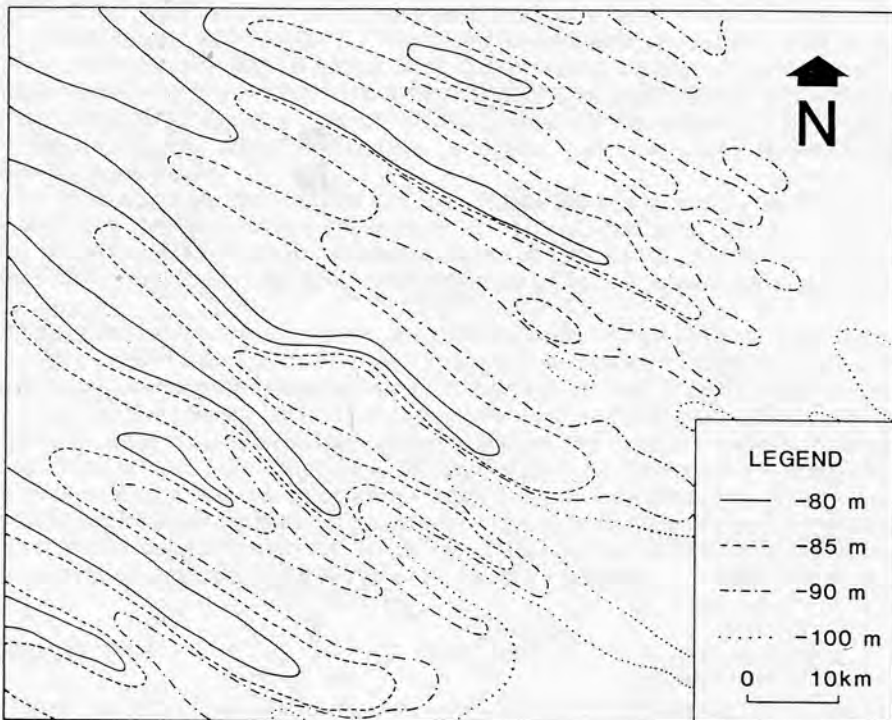


Figure 1b. Sea floor topographic map of the tidal sand ridge area.  
For location see figure 1a.

## MORPHOLOGY OF THE SAND RIDGES

The sand ridges on the shelf of the East China Sea occur mainly in the submerged palaeovalley of the Changjiang River and the adjacent area. They start in the SE from the palaeoestuary mouth of the Changjiang River at the shelf edge (approx.  $125^{\circ} 30' E$ ,  $28^{\circ} N$  to  $126^{\circ} 30' E$ ,  $29^{\circ} N$ ), and end in the NW, at the palaeovalley of the Changjiang River outside the recent subaqueous delta of the Changjiang River (approx.  $122^{\circ} 45' E$ ,  $31^{\circ} 30' N$ ), extending from the SE towards the NW across the shelf of the East China Sea (Fig. 1a). The area of sand ridges is bounded to the NE by the southern edge of the palaeodelta of the Changjiang-Huanghe River, and to the west by -60 to -70 m isobaths.

The sand ridges on the East China Sea shelf are distributed at present-day water depths of 45 m to 115 m. These ridges occur mainly in four groups, with present-day water depths to the top of the groups 96 - 115 m, 75 - 90 m, 58 - 70 m and 45 - 55 m respectively. Individual sand ridges are 10 - 50 km long (maximum length 60 km), 2 - 5 km wide and 5-20 m high (Fig. 1b). The average spacing between ridges is 8 - 14 km. They are roughly parallel to each other, extending mainly ESE - WNW (approx.  $120^{\circ}$  -  $300^{\circ}$ ). However, locally, sand ridges may also occur in a SSE - NNW direction due to the change of the palaeovalley direction (Fig. 1a). In transverse sections these sand ridges exhibit asymmetrical profiles with flat crests. The gentle slopes face NNE (approx.  $30^{\circ}$ ) at an angle of about  $0.5^{\circ}$ , and the steeper slopes dip SSW (approx.  $210^{\circ}$ ) at an angle of about  $2^{\circ}$ .

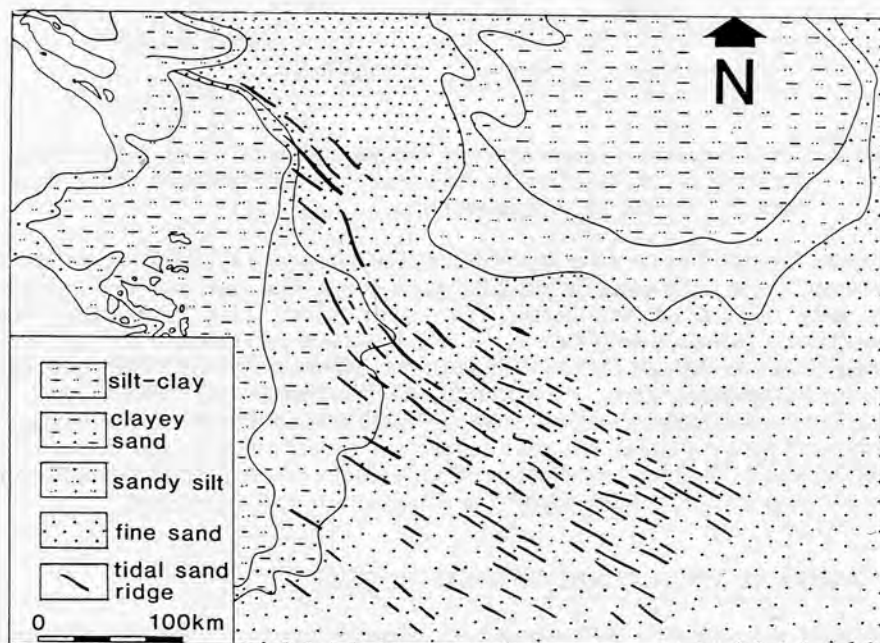


Figure 2. The types of surficial sediments on the East China Sea shelf (data from the Bureau of Marine Geol. Survey and the Second Inst. of Oceanogr.).

### THE SEDIMENTARY CHARACTERISTICS OF THE SAND RIDGES

The surficial sediments in the area of sand ridges are mainly well-sorted, fine grey sands (Fig. 2, data from the Bureau of Marine Geological Survey and the Second Institute of Oceanography). The mean grain sizes are 177 - 125 micron. The sand contents are 70% to more than 90%, while the mud contents are generally less than 10%. The grain size is indicative of transportation and deposition by currents in excess of 0.5 m/s (Miller et al., 1977). This does not tally with the present-day environment and weak currents. These sediments commonly contain foraminifera and abundant shell debris, such as *Ostrea*, *Balanus*, *Solen*, *Anadara subcrenata* and *Mactra*, which are mainly intertidal to shallow marine (less than 30 m deep) species. The ecological environments of these fossils do not agree with the present-day water depth.

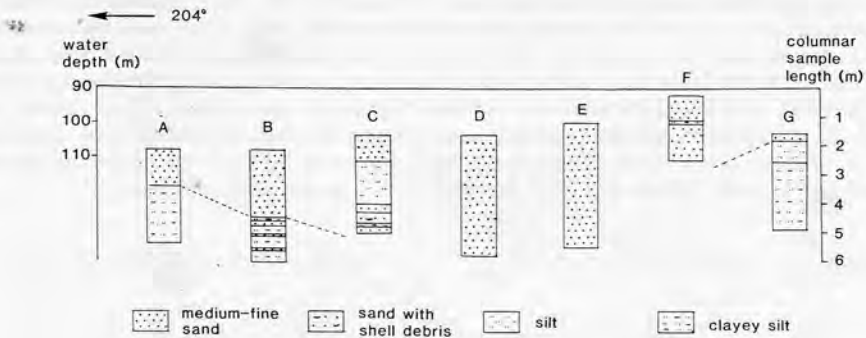


Figure 3. Cross-section of core samples across the tidal sand ridge area. The location of the section is shown as A-G in figure 1a (data from the Second Institute of Oceanography).

Figure 3 shows the transverse section of the vibrocore samples across the sand ridge area. These core samples are 2.3 - 4.2 m deep. The core samples in the sand ridge area consist of well-sorted, fine grey sand. They show the slightly coarsening-up sequence with fine sands at the bottom and medium to fine sands at the top. These sands are rich in foraminifera and contain abundant shell debris. The sand layer thicknesses are variable. At stations D and E (near sand ridge crests) the core samples are more than 4 m deep and do not penetrate through the sand layer. This shows that the sand layers are rather thick at the crests of sand ridges. However, in the troughs between sand ridges the sediments become thinner and finer in grain size, mainly consisting of sandy silt and clayey silt.

### THE INTERNAL STRUCTURES OF SAND RIDGES

Because of the sampling difficulties, the interpretation of the internal structure of the sand ridges is based mainly on the shallow seismic profiling data. The profiles across the sand ridges show large-scale, very low-angle inclined layers within the sand ridges (Figs. 4, 5). In all the shallow seismic profiles, these very

low-angle inclined layers dip SSW (approx.  $210^\circ$ ), in the same direction as the steeper slopes of the sand ridges. In the profiles these very low-angle inclined depositional surfaces appear rather steep because of the exaggeration of the vertical scale, whereas the actual dip angles are only about  $2^\circ$ . The reflections of these surfaces in the shallow seismic profiles suggest the halt of deposition on these surfaces or a change of sediments.

The shallow seismic profiles also show unconformities between sand ridges and underlying strata of late Pleistocene age. Some unconformities were produced by erosion in the trough during the sand ridge development. Major unconformities are those between sand ridges and the underlying deposits of the late-Pleistocene, which were produced during the low sea-level period and the post-glacial transgression. Above this unconformity, sand ridge deposits can be more than 10 m thick at sand ridge crests with internal continuous, very low-angle inclined layers. These deposits thin out in the troughs between sand ridges. The seismic records agree well with the relative heights of sand ridges as revealed by echo-sounding, and also confirm the thickness variations of sand ridge deposits as shown in the

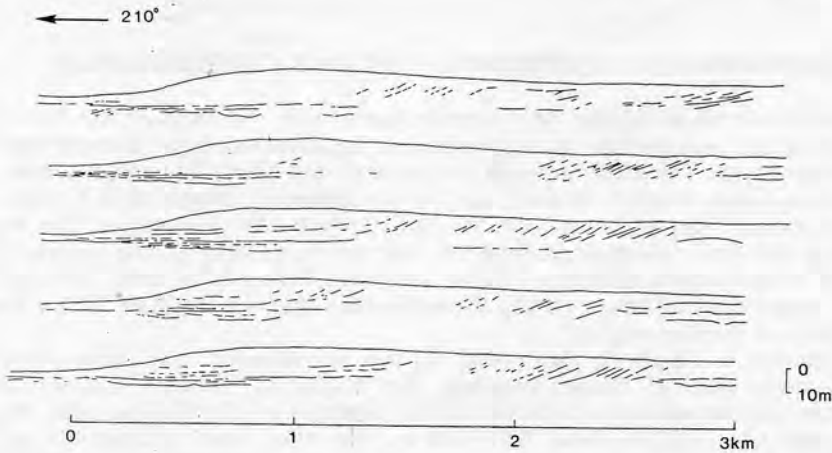


Figure 4. Cross-sections showing internal structures of the tidal sand ridge (present-day water depth of about 90 m) as revealed by high resolution seismic profiler. For the location, see figure 1a.

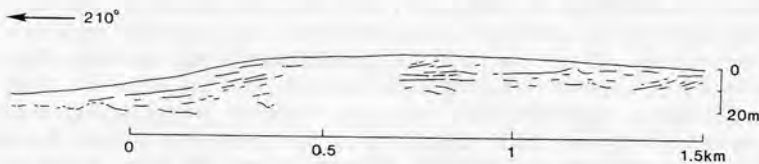


Figure 5. Cross-section showing internal structures of the tidal sand ridge (present-day water depth of about 60 metre) as revealed by high resolution seismic profiler. Location: II in figure 1a.

cross-section of core samples. These data indicate that more than 10 m of deposits might have been formed due to the development of sand ridges during post-glacial transgression (Figs. 4, 5).

### THE SOURCE OF THE SANDS

Large amounts of sand are present on the East China Sea shelf. These sands were derived from the mainland of China and delivered to the present-day East China Sea shelf by rivers. As a result of the low sealevel, the Changjiang River extended across the present-day East China Sea shelf for about 400 - 500 km and its base level was lowered by more than 100 m. Its gradient was much steeper than that in the middle-lower reaches of the present-day Changjiang River. This increased its capacity for erosion and transportation. The transportation of the sands was mainly along the palaeovalley of Changjiang River, which extended from the NW to the palaeo-Changjiang estuary mouth at the shelf edge in the SE. The terrestrial fluvial sands of the late-Pleistocene and the sands from the Changjiang River during the post-glacial transgression provided abundant material for the development of sand ridges.

### THE HYDRODYNAMIC CONDITIONS OF THE EAST CHINA SEA SHELF

A general impression of the tidal current pattern on the shelf of the East China Sea during the post-glacial transgression can be obtained from present-day tidal current patterns. The tidal wave in the present-day East China Sea comes from the northwestern Pacific through the straits between Taiwan and Kyushu. The water transport during 6 h of the  $M_2$ -tide through the passages of the Ryukyu Islands is  $350 \text{ km}^3$ , whereas through the northern entrance of the Taiwan Strait and the southwestern entrance of the Tsushima Strait it is only  $130 \text{ km}^3$  and  $20 \text{ km}^3$  respectively (Defant, 1960). Therefore the tides of the East China Sea are essentially of Pacific origin.

As shown in figure 6, the crest of the semidiurnal tidal wave from the northwestern Pacific Ocean reaches the chain of Ryukyu islands almost simultaneously at about 7 h (referred to the meridian of  $135^\circ\text{E}$ ). The tidal range of spring tide  $2(M_2 + S_2)$  is about 1.25-1.80 m. The tidal wave propagates into the East China Sea as a progressive wave with a wide NE-SW oriented front. It reaches the line from Shanghai to the SW tip of Korea with the phase 0 h, while the range  $2(M_2 + S_2)$  increases to about 2.50 m. As for the K<sub>1</sub> tide, the entire East China Sea has the phase 14.5 h with ranges  $2(K_1 + O_1)$  of 0.7 - 0.8 m (Defant, 1960). The ratio of the diurnal to the semidiurnal tides indicates mixed, predominantly semidiurnal to exclusively semidiurnal tide in the East China Sea.

The tidal currents on the East China Sea shelf are basically rotatory with the long axis of the tidal ellipse NW to SE. The maximum flood currents flow towards the NW and the maximum ebb currents towards the SE (Fig. 7). Near estuary mouths in the west, however, tidal currents become progressively bidirectional and their orientations may turn according to the geomorphological boundaries of the estuaries. But the general NW-SE orientation of the tidal currents remains very distinct (Fig. 7).

In the relatively deep area of the mid- or outer- shelf of the East China Sea, the present-day tidal currents are rather weak. For example, figure 8 shows the



vectorial presentation of the currents measured in the sand ridge area of the outer-shelf of the East China Sea. In this area, the present-day hydrodynamic conditions near the sea surface are dominated by the Kuroshio Current (an important warm, saline current flowing to the north and northeast over the mid- and outer-shelf of the East China Sea). The currents measured at 3 m below sea surface show a clear direction towards the N and NE, coincident with the direction of the Kuroshio. With increasing water depth, the influence of the Kuroshio decreases while rotatory tidal currents become more important. The current directions measured near the sea bed (at a water depth of 80 m) turn through 360 degrees during a flood-ebb cycle. Within a flood-ebb cycle, the maximum current velocity is only about 0.35 m/s near the sea surface (water depth of 3 m), and even less (0.16 m/s) near the sea bed (water depth of 80 m).

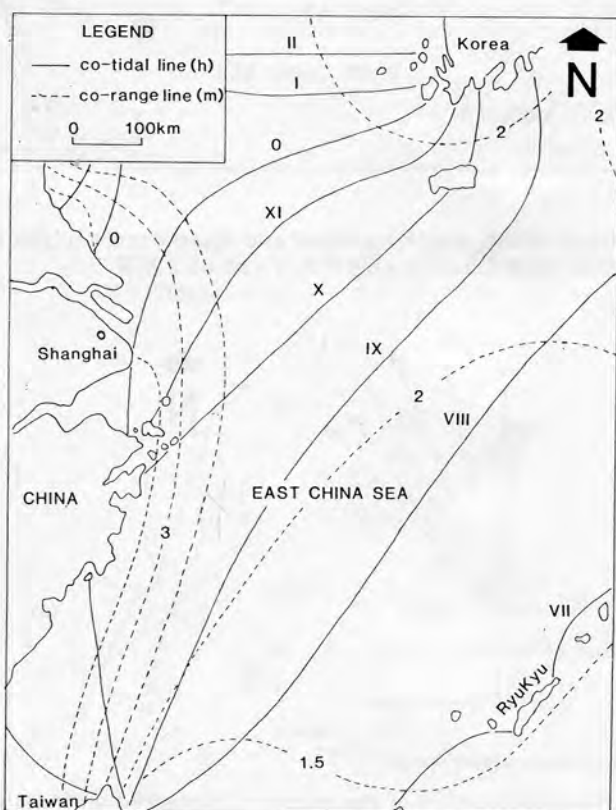


Figure 6. Co-tidal lines of the  $M_2$  tide (h) and co-range of the semidiurnal tide  $2(M_2 + S_2)$  (m) in the East China Sea (phases referred to the  $135^\circ$  E meridian) (modified after Defant, 1960).

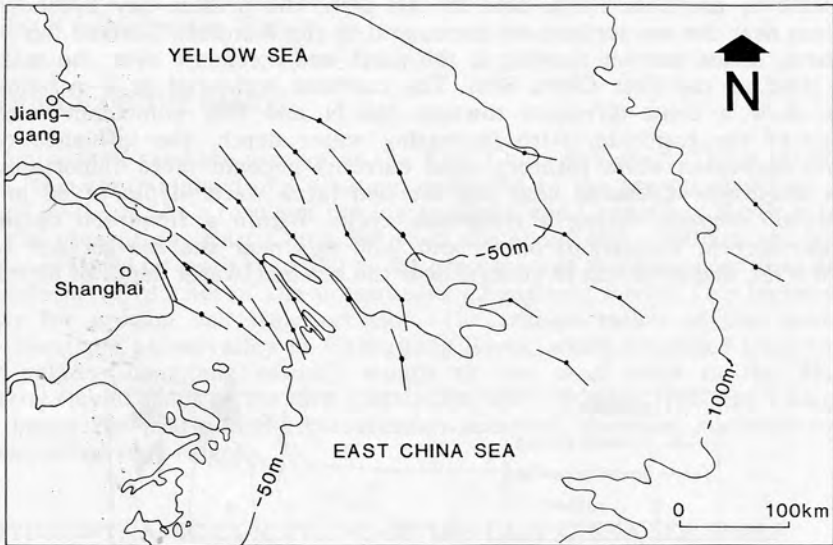


Figure 7. Directions of the maximum flood and ebb currents in the East China Sea (Modified after Chen et al. 1983; Ye et al. 1983).

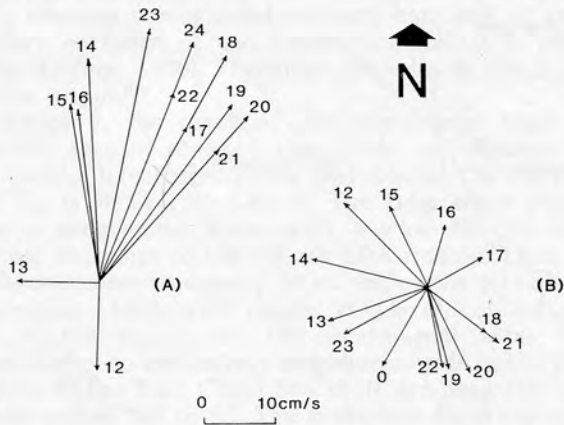


Figure 8. Vectorial presentation of the currents measured during a flood-ebb cycle in tidal sand ridge area on the shelf of East China Sea. The present-day water depth of the measuring station is over 80 m. Figures beside the vector show the time of measurements (h). (a) currents measured at 3 m below sea surface. (b) currents measured at 80 m below sea surface.

### MIGRATION OF THE PALAEOCOASTLINE AND THE DEVELOPMENT OF TIDAL SAND RIDGES SINCE THE END OF THE LATE-PLEISTOCENE

The development of tidal sand ridges was closely related to the history of the post-glacial transgression in the East China Sea (Fig. 9). The rate of post-glacial sealevel rise was not constant. There were standstills and fluctuations during the sealevel rise, resulting in corresponding palaeocoastlines and tidal sand ridges. Tidal sand ridges in the deeper areas developed during an early stage of the post-glacial transgression, and those in shallower areas formed during a late stage.

It has been reported that the lowest sealevel of the East China Sea was -140 m to -160 m at the end of the late-Pleistocene (approx. 18,000 - 15,000 yrs BP) (Feng, 1983). Sand layers with abundant shell debris and some gravels occur widely at locations which are at present depths of 139 m to 155 m. Most shells are worn. They consist mainly of *Mactra*, *Anadara subcrenata*, *Ostrea*, *Solen*, *Balanus* and other intertidal and shallow marine (less than 30 m deep) species, which make up 40% - 90% of the whole sample. These represent the deposits along the coastline

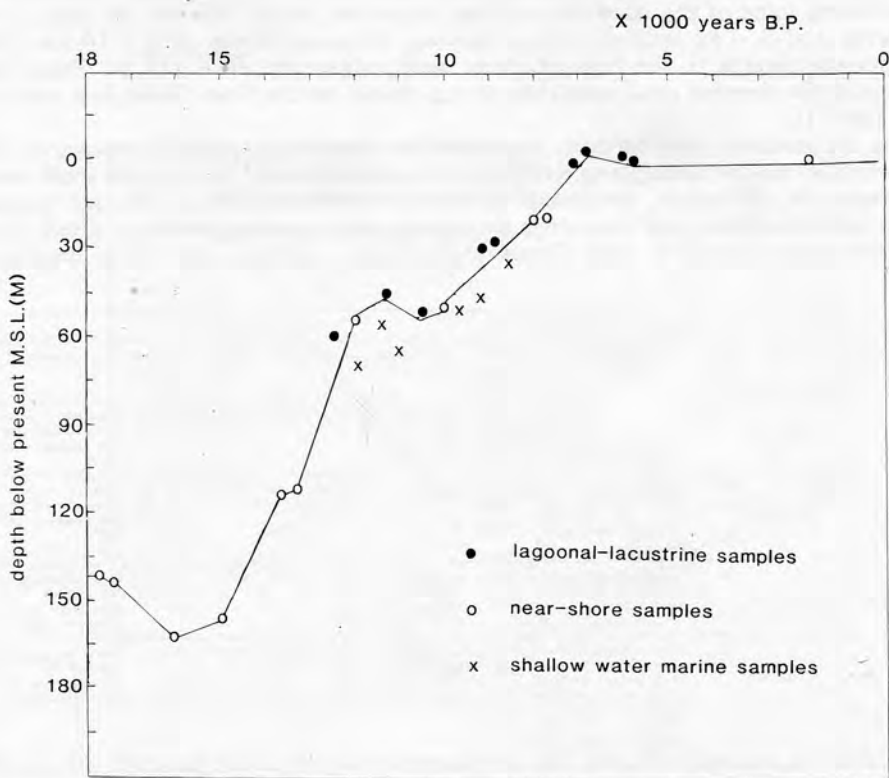


Figure 9. Sea-level rise curve in the East China Sea since 18,000 years BP based on C-14 dating (after Feng, 1983).

during that period. At about 15,000 yrs BP, the sealevel began to rise rapidly, first inundating the late-Pleistocene Changjiang River valley. This palaeovalley was bounded to the north by a palaeodelta of the Changjiang-Huanghe River, and to the south by a broad palaeocoastal plain.

Around 13,500 yrs BP the sealevel rose to about -100 m and came to a standstill period. Available data from the Bureau of Marine Geological Survey and the Second Institute of Oceanography indicate an obvious palaeocoastline at about -100 m, which was characterized by a shelly sand layer rich in spore-pollen, fresh water pediatrum, brackish water *Ostrea*, and *Corbicula* which grew in lagoons. Detailed echo-soundings by the Bureau of Marine Geological Survey show that the mouth of the Changjiang River was situated between 125°30'E, 28°N and 126°30'E, 29°N during this period, forming a wide funnel-shaped estuary (Fig. 10a). The maximum width of the estuary reached 140 km at the mouth. However upstream it gradually became narrower. Therefore the tidal waves from the SE were enhanced in the estuary mouth. The fluvial sands deposited during previous regression and the sands from the Changjiang River during transgression were reworked and deposited by strong tidal currents during this period, forming group I of the tidal sand ridges (Fig. 10a). These sand ridges extend ESE-WNW (approx. 120° - 300°). The sand ridges are elongate, only occasionally can a minor curved crestline be found along some of the sand ridges. The ridges are about 10 - 40 km long, 2 - 4 km wide and 5 - 12 m high with a spacing between ridges of 8 - 10 km. The present-day depths to the tops of these sand ridges are 96 - 115 m. Thus they represent the deepest tidal sand ridge group found on the East China Sea shelf so far (Table 1).

As the sealevel rose further, the coastline migrated gradually westward. The palaeovalley of the Changjiang River and the palaeocoastal plain in the south were inundated by sea water, becoming shallow shelf environments. The terrigenous sands were reworked and deposited by strong tidal currents, forming group II of the tidal sand ridges (Fig. 10b). These ridges occur at present-day water depths of

Tidal sand ridge group	Age	Palaeo-coastal line		Tidal sand ridge						
		Water depth (m)	Morphology	Water depth (m)	Morphology	Length (km)	Width (km)	Height (m)	Spacing (km)	Trend
I	13500 BP	-100	Funnel-shaped estuary mouth, 140 km wide at the mouth, becoming narrower upstream	-96 -115	elongate, minor curved crests along some ridges	10-40	2-4	5-12	8-10	Parallel to each other, trend SEE-NWW (approx. 120°-300°)
II	12750 BP	-80	Estuary mouth bounded in the NE by palaeo-delta, and in the SW by palaeo-coastal plain	-75 -90	elongate	10-40	2-4	8-16	10-12	Parallel to each other, trend SEE-NWW (approx. 120°-300°)
III	12000 BP	-60	Funnel-shaped estuary mouth, 140 km wide at the mouth	-58 -70	elongate, minor curved crests along some ridges	12- more than 50	3-5	8-16	12-14	Trend changing to SEE-NWW (in accordance with palaeo-valley)
IV	11000 BP	-50	Funnel-shaped estuary mouth, bounded in the NE by palaeo-delta of Changjiang River, and in the SW by recent subaqueous delta of Changjiang River, 120 km wide at the mouth	-45 -55	elongate, minor curved crests along some ridges	18- more than 60	3-5	8-20	11-12	Trend changing to SEE-NWW (in accordance with palaeo-valley)

Table 1. The migration of palaeocoastlines and the major features of the tidal sand ridges on the East China Sea shelf since the end of the late-Pleistocene.

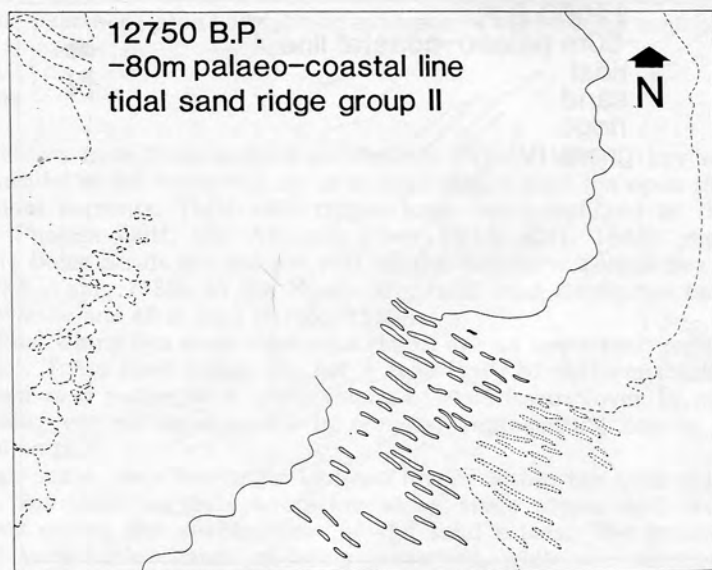
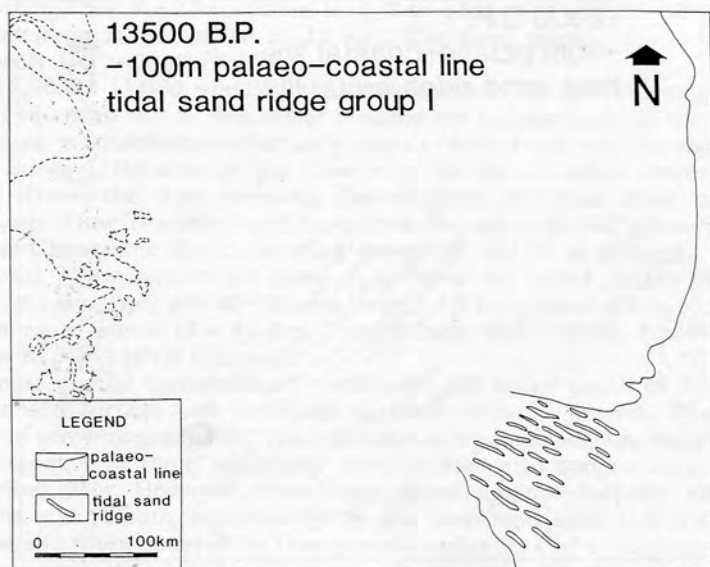


Figure 10. The migration of palaeocoastlines and the development of tidal sand ridges on the East China Sea shelf since the end of late Pleistocene. (a) -100 m palaeocoastline at about 13,500 BP, tidal sand ridge group I. (b) -80 m palaeocoastline at about 12,750 BP, tidal sand ridge group II.



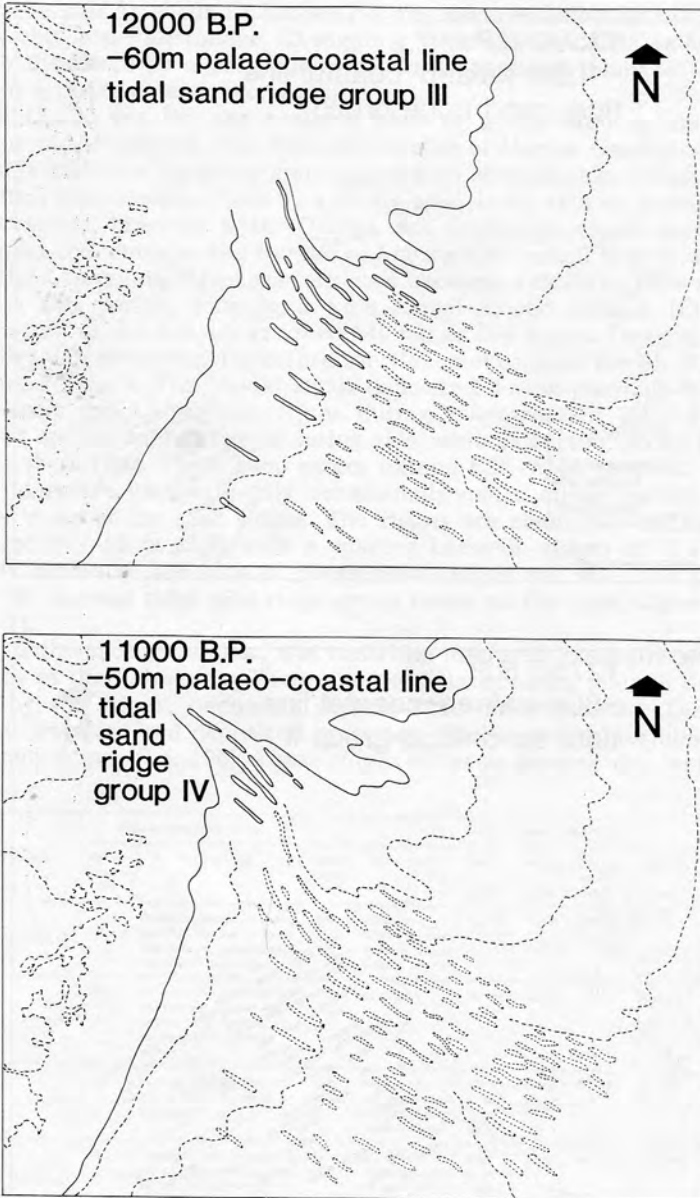


Figure 10 (continued)

- (c) -60 m palaeocoastline at about 12,000 BP, tidal sand ridge group III.
- (d) -50 m palaeocoastline at about 11,000 BP, tidal sand ridge group IV.

-75 m to -90 m. They are 10 to 40 km long, 2 to 4 km wide and 8 - 16 m high with a spacing between ridges of 10 to 12 km. The sand ridges extend ESE - WNW (approximately  $120^{\circ}$  -  $300^{\circ}$ ) (Table 1).

About 12,000 - 11,000 yrs BP, the sealevel rose further, forming a palaeo-coastline at -60 m to -50 m. Sea water invaded the palaeovalley of the Changjiang River, forming a funnel-shaped estuary mouth (data from the Bureau of Marine Geological Survey). Because of the change in the palaeovalley directions of the Changjiang River, the tidal currents also changed direction after entering the estuary mouth. They reworked and deposited the sands in the submerged palaeo-valley of the Changjiang River, forming groups III and IV of the tidal sand ridges (Fig. 10c, 10d). These sand ridges occur at present-day water depths of 58 - 70 m and 45 - 55 m resp. They are 12 - 60 km long, 3 - 5 km wide and 8 - 20 m high and show a spacing of about 11 - 14 km. They extend ESE - WNW, however, locally, they change to SSE - NNW (Table 1).

As the post-glacial transgression continued, the water depth of the tidal sand ridges increased further and the tidal currents became weaker. The tidal sand ridges ceased growing gradually. Their characteristic morphology was modified to a certain extent, and their sediments were mixed with some fine-grained sediments supplied later. However, their basic morphological features and sediment compositions still remain, represented by the moribund sand ridges on the East China Sea shelf. When covered by fine-grained sediments of Late Holocene age in the nearshore area, they were preserved in the stratigraphical section and became an important type of sand body formed in estuary-shallow shelf tidal environments. Shallow seismic data obtained by the Bureau of Marine Geological Survey in the nearshore area have shown evidence of such buried sand bodies.

## DISCUSSION

Tidal sand ridges have been studied extensively (Stride, 1982). They extend in a direction parallel to (in estuaries), or at a small angle with (on open shelves), the dominant tidal currents. Tidal sand ridges have been reported in the Gulf of Korea, the Persian Gulf, the Amazon River Delta (Off, 1963); the Strait of Malacca; the Bohai Strait and the SW part of the Southern Yellow Sea (Sun, Zhou & Feng, 1984; Yang, 1985). In the North Sea, tidal sand ridges can be as long as 50 km, 6 km wide and 40 m high (Stride, 1982).

On the East China Sea shelf tidal sand ridges are an important genetic type of 'relict sands'. These sand ridges are not a sand layer of uniform thickness. They are elongated sand bodies with a thickening of sand layers (over 10 m) at crests and a thinning out of sand layers in troughs, representing one of the major depositional units.

The large-scale, very low-angle inclined layers within the sand ridges on the East China Sea shelf suggests accretion along steep slopes and erosion along gentle slopes during the development of the sand ridges. The erosional gentle slopes have very little chance of being preserved, while the accretional steep slopes have a high preservation potential, producing very low-angle inclined layers in the same direction as the steep slopes. The unidirectional SSW dipping low-angle layers might be related to the regional hydrodynamic conditions and sediment transport pattern. Similar low-angle inclined layers were observed in some tidal sand ridges of the North Sea (Houbolt, 1968).

The moribund morphology, however, suggests that these sand ridges are relict

sand bodies left on the shelf of the East China Sea, similar to the moribund linear sand ridges in the outer Celtic Sea (Belderson, this volume). The shallow marine species of the fossils in the sand ridge deposits show that these sands were probably deposited during the post-glacial transgression when the water depths were shallower than at present.

The present-day tidal currents over the sand ridges in the East China Sea are too weak to form and maintain these huge tidal sand ridges. There is very little data on the tidal current patterns at low sealevels. Some general estimations, however, can be made from a comparison of the present-day shallow shelf area of the East China Sea and the Southern Yellow Sea. A good example is the shallow shelf area in the SW part of the Southern Yellow Sea off Jianggang (approximately 121° - 122° E, 32° 30' - 33° 30' N) where strong tidal currents normally exceed 1 m/s. They rework large amounts of sand deposits, build up and maintain huge tidal sand ridges in an area of less than 20 m waterdepth. These tidal sand ridges exhibit very distinct morphology and active sedimentary processes. Their scales are generally comparable with, or even larger than those of the tidal sand ridges on the East China Sea shelf (Yang, 1985). Such active tidal sand ridges are strongly reminiscent of the formation of tidal sand ridges on the East China Sea shelf, which are presumed to have developed in a similar environment during post-glacial transgression when the East China Sea shelf had shallower water depths and stronger tidal currents than at present. This is also comparable with the modern tidal sand ridges in the North Sea, where the near surface maximum tidal current velocity of the mean spring tide is about 0.75 - 1.30 m/s. In the area with near-surface maximum tidal current velocity less than 0.75 m/s, no tidal sand ridges have developed (Stride, 1982).

Research into the stability of sea floor sedimentary bodies is essential for the evaluation of sea bottom geotechnical conditions. It has been reported that on the East China Sea shelf sandwaves migrated at a mean rate as high as 1376 m/year (Ye, Jin, Lei & Chen, 1983). This could cause serious geotechnical problems. However, in our investigations of tidal sand ridges on the shelf of the East China Sea, no such migrations have been observed for the sand ridges. The present-day hydrodynamic conditions and the moribund sand ridge morphology suggest that these sand ridges are probably relatively stable. Long term observations are still needed to assess the present-day stability of these sand ridges.

#### ACKNOWLEDGEMENTS

The authors are grateful to the technical team and crew members of the Bureau of the Marine Geological Survey in Shanghai, Ministry of Geology and Mineral Resources for field investigations at sea, and to Zhou Changzhen, Huang Yongsheng, Feng Dongzhi, Gao Hongan, Wu Zhiguo and Mao Huimin for data processing and map compilations. We are greatly indebted to Prof. Nio, S.D., Prof. Liu Guangding, Senior Engineer Yang Qilun, P.L. de Boer and the reviewers and our colleagues in the Bureau of Marine Geological Survey for critically reading the manuscript and their valuable suggestions. Miss Yolanda kindly typed this manuscript.

## REFERENCES

- Chen Jiyu, Zhu Huifang, Dong Yongfa & Sun Jiemin (1983) Development of the Changjiang Estuary and its subaqueous Delta. Proc. Int. Symp. on sedimentation on the continental shelf with special reference to the East China Sea. China ocean press, Beijing, vol. 1, 37 - 55.
- Defant, A. (1960) Physical Oceanography. Vol. 2. Pergamon Press. 598 pp.
- Feng Yingjun (1983) Sea-level changes and the lowest sea-level of the East China Sea in the last 40,000 years. Donghai Mar. Sci. 2, 36 - 42 (in Chinese).
- Gen Xiushan (1982) Marine transgression and regression in East China Sea since late-Pleistocene Epoch. Collected oceanic works 5 (1), 100 - 123 (in Chinese).
- Houbolt, J.J.H.C. (1968) Recent sediments in the Southern Bight of the North Sea. Geol. Mijnb. 47, 245 - 273.
- Li Congxian & Chen Gang (1984) Post-glacial transgression-regression and sand barrier-lagoon depositional system. Acta Oceanologica Sinica 6 (5), 657 - 662 (in Chinese).
- Miller, M.C., McCave, I.N. & Komar, P.D. (1977) Threshold of sediment motion under unidirectional currents. Sedimentology 24, 507 - 527.
- Off, T. (1963) Rhythmic linear sand bodies caused by tidal currents. Bull. A.A.P.G. 47, 324 - 341.
- Stride, A.H. (1982) Offshore tidal sands, processes and deposits. Chapman and Hall. 222 pp.
- Sun Jiasong, Zhou Changzhen & Feng Dongzhi (1984) On effects of hydrodynamic processes on the development of some submarine geomorphological features. Mar. Sci. Bull. 3(2), 54 - 61 (in Chinese).
- Yang Changshu (1985) On the origin of Jianggang Radial Sand Ridges in Yellow Sea. Mar. Geol. & Quatern. Geol. 5(3), 35 - 44 (in Chinese).
- Ye Yincan, Jin Changmao, Lei Zhiyan & Chen Xitu (1983) Bedform morphologies of the continental shelf off Changjiang River mouth and their environmental conditions. Proc. Int. Symp. on sedimentation on the continental shelf with special reference to the East China Sea. China Ocean Press, Beijing, 2, 762 - 774.
- Zhu Yongqi, Zeng Chengkai & Feng Yun (1983) The geomorphic types and origin of the East China Sea continental shelf. Proc. Int. Symp. on sedimentation on the continental shelf with special reference to the East China Sea. China Ocean Press, Beijing, 2, 663 - 672.

## Chapter 8

# Active, moribund and buried tidal sand ridges in the East China Sea and the Southern Yellow Sea

Chang-Shu Yang

Ministry of Geology and Mineral Resources, Bureau of Marine Geological Survey, 526 Yan An Road West, Shanghai, China

### ABSTRACT

Shallow seismic profiles and borehole data revealed active, moribund and buried tidal sand ridges in the East China Sea and the Southern Yellow Sea. The ridges consist of relatively clean, well-sorted sands with rather uniform sequences. The microfossil assemblage exhibits a high diversity including both euryhaline and stenohaline species. The ridges are huge elongated sand bodies (several km wide, 10-60 km long and up to 20 m thick) and occur in groups with a spacing of several to 10 km. Normally they are parallel with each other, extending in the direction of the tidal currents. The field of tidal sand ridges on the East China Sea shelf covers an area of 57,000 sq km.

Tidal sand ridges in the East China Sea and the Southern Yellow Sea were formed in estuarine and shallow shelf environments, where strong tidal currents reworked, transported and redeposited large amounts of relict sands from older deltaic and fluvial sediments. The development of tidal sand ridges in estuary-mouth areas is accompanied by a net sand transport from the shelf into the estuary.

The evolution of tidal sand ridges is closely related to transgressions. Active tidal sand ridges are formed during sea level rises. They show distinct morphology and active migrations in a lateral as well as in a landward direction. They are generally in equilibrium with present-day tidal processes and their distribution patterns are related to the flow field of the tidal currents. As the sea level rises further, these tidal sand ridges become moribund

---

This chapter has been accepted for publication as:

Yang, C.S., 1989. Active, moribund and buried tidal sand ridges in the East China Sea and the Southern Yellow Sea. *Marine Geology* (in press).



sand bodies with less distinct morphologies. Their upper surfaces are covered by a thin calcareous-rich layer with very high contents of foraminifera tests, reflecting a submarine hiatus condition on the shelf during the highstand period. During the subsequent steady fall in sea level, tidal sand ridges are often buried by fine-grained shelf and prodelta sediments. They have, therefore, a good chance of being preserved in stratigraphic records.

The sequential buildup during a sea level rise (TR-tract) and a subsequent sea level fall (HS- and LS-tract) would consist of estuarine channel and tidal flat facies, tidal sand ridge facies, shelf mud facies, delta facies, and fluvial facies in an ascending order.

Tidally-dominated estuary conditions may also occur when a major distributary is abandoned, such as at the Northern Branch of the modern Changjiang River mouth, where the accumulation of sand from an abandoned delta lobe and the development of tidal sand ridges have been observed.

The observed features have important implications for the subsurface recognition of fossil tidal sand ridges, for the reconstruction of the regional palaeogeography and transgressive history and for the prediction of potential reservoir sandstones.

## INTRODUCTION

Tidal sand ridges have been reported in the East China Sea and the Southern Yellow Sea (Zhou & Sun, 1981; Sun et al., 1984; Yang, 1985; Yang & Sun, 1988). However, previous studies focused on the morphologies and surficial sediments of the tidal sand ridges, which were formed during the post-glacial transgression (early Holocene). The internal structures of these tidal sand ridges are not very clear, and also, the preservation potential and the sequential buildup are unknown.

During recent investigations conducted by the Bureau of Marine Geological Survey, Ministry of Geology and Mineral Resources of China, new seismic profiles were collected that penetrated about 100 m below the sea bottom. In addition, a shallow borehole was drilled in a sand ridge area in the outer shelf of the East China Sea (Fig.1). These have revealed not only the details of the Holocene tidal sand ridges, but also the presence, characteristics, and sequential buildup of buried Pleistocene sand ridges. Based on these new data, this study is a follow up of previous studies (Zhou & Sun, 1981; Yang, 1985; Yang & Sun, 1988). The present paper documents active, moribund and buried tidal sand ridges found in the Southern Yellow Sea and the East China Sea. The formation, sequential buildup, preservation, stratigraphic record, and reservoir potential of such tidal sand ridges are described and discussed. These tidal sand ridges have important implications for the subsurface recognition of fossil tidal sand ridges in hydrocarbon exploration.

## SEISMIC STRATIGRAPHY

In recent years large-scale shallow marine geophysical surveys have been conducted

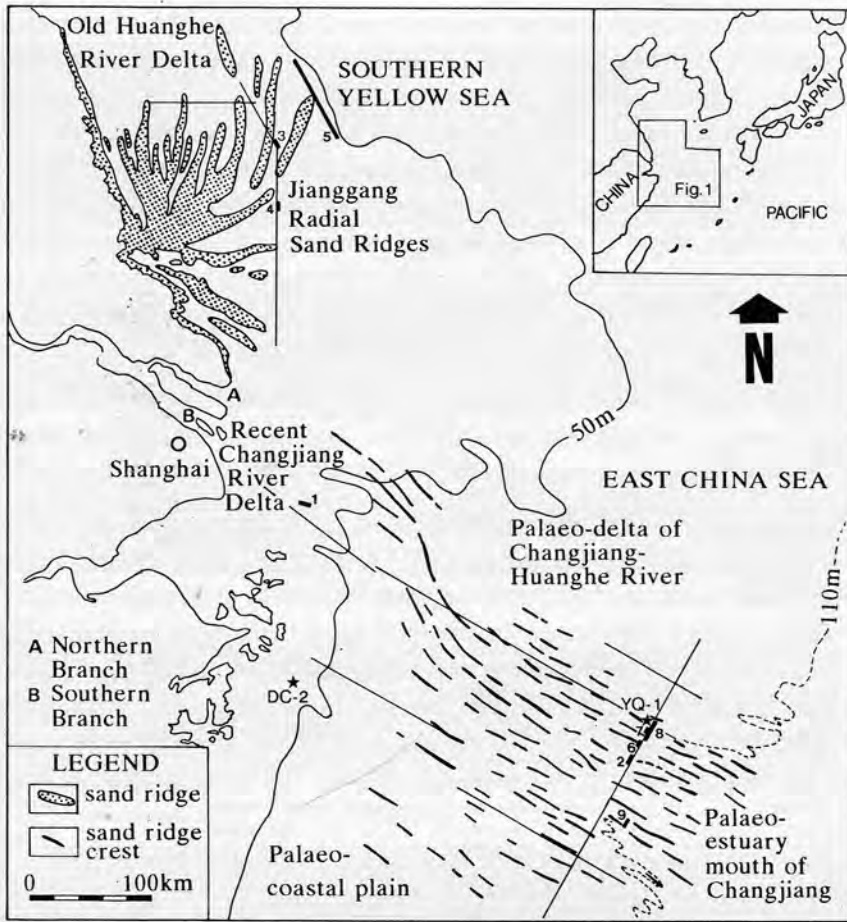


Fig.1 Map of the study area showing tidal sand ridges in the East China Sea and the Southern Yellow Sea. Stars indicate the locations of the shallow boreholes YQ-1 and DC-2. Shallow seismic tracklines are shown as thin lines. Thick bars with numbers represent locations of profiles shown in this paper.

by the Bureau of Marine Geological Survey on the shelf of the East China Sea and the Southern Yellow Sea. The purpose of these surveys was to investigate bathymetric, geomorphological and geological conditions, and to provide basic data for the study of regional engineering geology and Quaternary geology.

The water depth of the studied areas ranges from less than 20 m in the nearshore area to more than 100 m on the outer shelf of the East China Sea (Fig.1). The general trend of the shelf is characterized by a gradual deepening from the northwest towards the southeast, with an average gradient of 0.3 m/km. The shelf has a maximum width of 550 km in its north-eastern part, off the Changjiang River mouth, but it becomes narrower towards the southwest. The shelf edge is at water depths of about 140-160 m. Surface sediments are Holocene terrigenous mud on the inner shelf, and late Pleistocene relict sand on the outer shelf.

Shallow seismic surveys were conducted using an O.R.E. Geopulse system with a pulse energy of 280-350 J and a frequency band of 200-2000 Hz. In shallow water areas, an E.G. & G. Uniboom system was used with a pulse energy of 200-300 J and a frequency band of 300-3000 Hz. The energy level and the frequency band were varied according to bottom conditions and required penetrations. The system was towed by the survey vessels Fendou-3 and Fendou-2 at a speed of 9 km/h (5 knots) in conditions of less than 16 knots wind speed. Ship positions were determined by an Argo-Maxiran positioning system with an accuracy of 10 m. The profiles were displayed on an EPC recorder with negative half-wave mode. Resolution varied from less than 1 m to 3 m. Bottom penetration varied in different types of sea-bottom sediments, and often reached 50-100 m below the seafloor.

The two-way-travel times measured from the profiles were converted to sediment thicknesses using an average velocity of 1700 m/s. This seismic velocity was determined from the shallow borehole stratigraphy data.

Shallow seismic profiles obtained on the East China Sea and Southern Yellow Sea shelf revealed the details of the stratigraphic sequence (Fig.2). A seismic stratigraphy analysis is beyond the scope of this paper and, therefore, will be presented elsewhere (Yang & Shi, in prep.). Only a brief summary is presented below to illustrate the stratigraphic setting of tidal sand ridges. The observed seismic sequences can be divided by seismic unconformities or disconformities into a number of units. These seismic units can be correlated across major seismic profiles over the surveyed area. Shallow seismic profiles revealed great

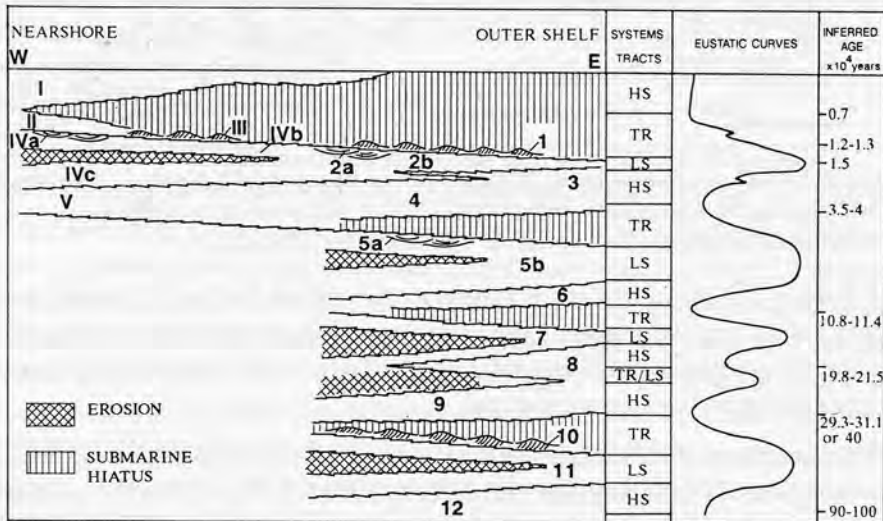


Fig.2 Interpreted seismic stratigraphic sequence based on regional correlations of major seismic profiles in the East China Sea, their proposed correlation, and their relationship with sea-level fluctuations since Pleistocene time. Numbers denote seismic facies units. Systems tracts follow the definition of Vail (1987): HS-Highstand systems tract; TR-Transgressive systems tract; LS-Lowstand systems tract.

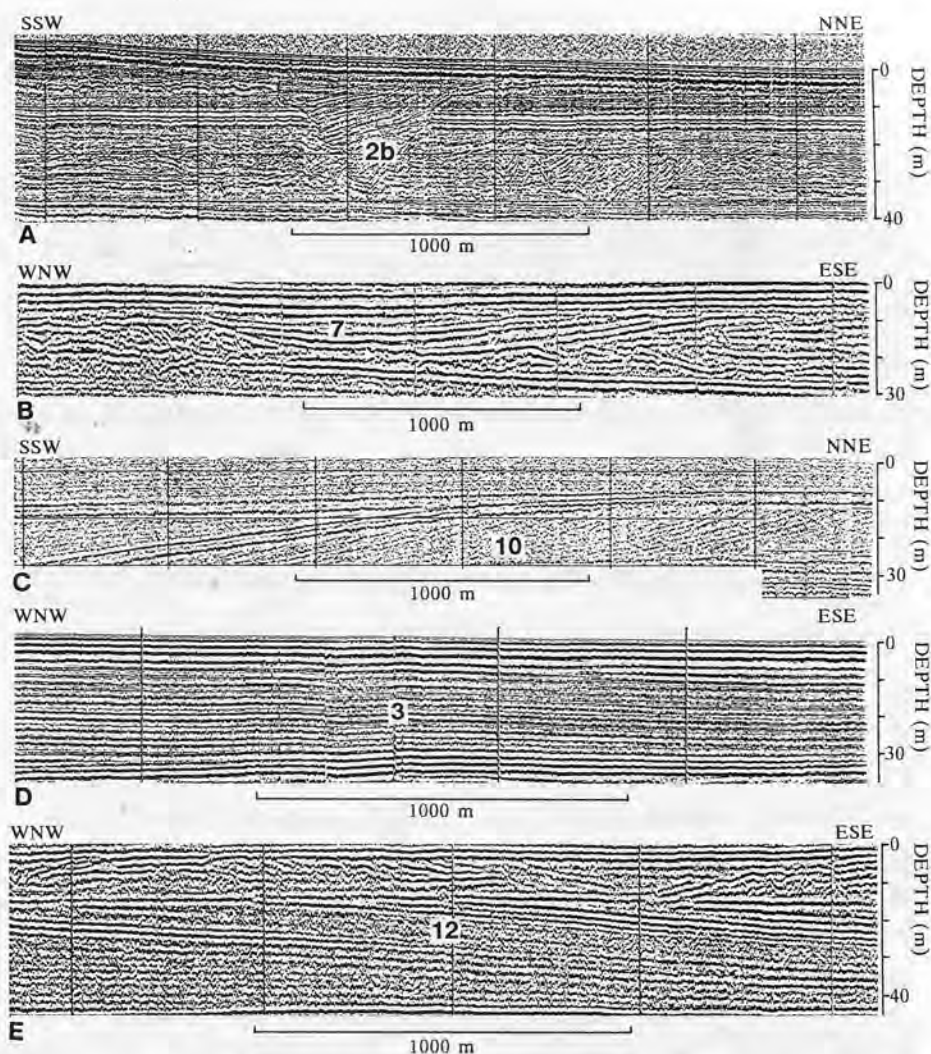


Fig.3 Typical seismic facies patterns in the East China Sea. A. Fluvial or estuarine channel facies (Unit 2b). B. Lacustrine and swamp facies (Unit 7). C. Tidal sand ridge facies (Unit 10). D. Shelf mud facies (Unit 3). E. Deltaic facies (Unit 12) (data from the Bureau of Marine Geological Survey).

details in various seismic facies patterns, such as the external shape; internal reflection configuration, continuity, amplitude and frequency; top and bottom contacts; lateral variations as well as regional distribution patterns of the units. An interpretation of the seismic units was therefore attempted, primarily based on seismic facies analysis, with the aid of additional data on seafloor morphology, surficial sediments and shallow borehole stratigraphy to check facies interpretations. 5 sedimentary facies were identified: fluvial and estuarine channel facies; lacustrine and swamp facies; tidal sand ridge facies; shelf mud facies and



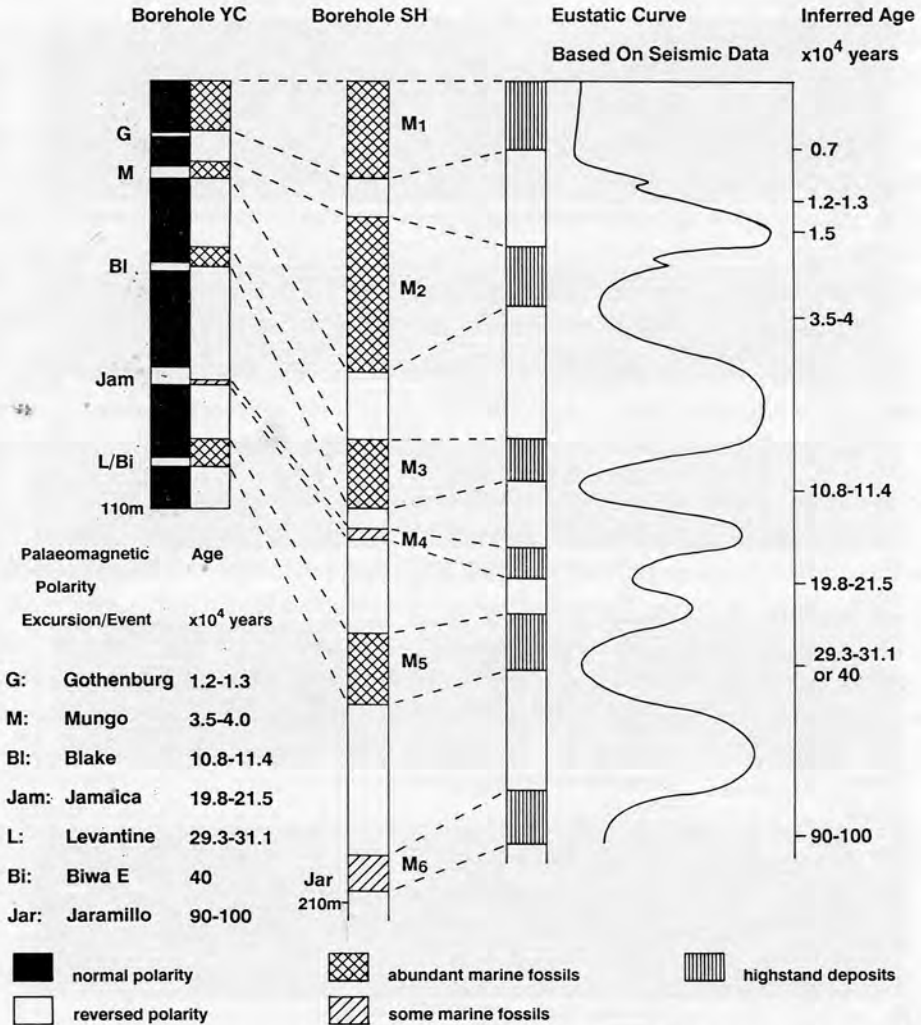


Fig.4 Proposed correlation between the eustatic curve based on seismic data and the borehole stratigraphy sequences in nearshore and coastal Quaternary basins. Six marine layers (labelled M1-M6) have been recognized and correlated between the boreholes according to biostratigraphic data. These marine layers show a good correlation to highstand periods in the eustatic curve. The ages were based on magnetostratigraphic data (Borehole stratigraphy data from Qian (1984) and Zhao & Qin (1986)).

deltaic facies (Fig.3). The ages of these units were inferred from the correlation between the eustatic curve based on seismic data and the known stratigraphy sequences (Fig.4) which have been established from borehole data in nearshore and coastal Quaternary basins (Qian, 1984; Zhao & Qin, 1986). The determination of more reliable ages of these units is delayed until direct correlations between seismic profiles and borehole data are available.

An interpreted seismic stratigraphic sequence based on regional correlations of major



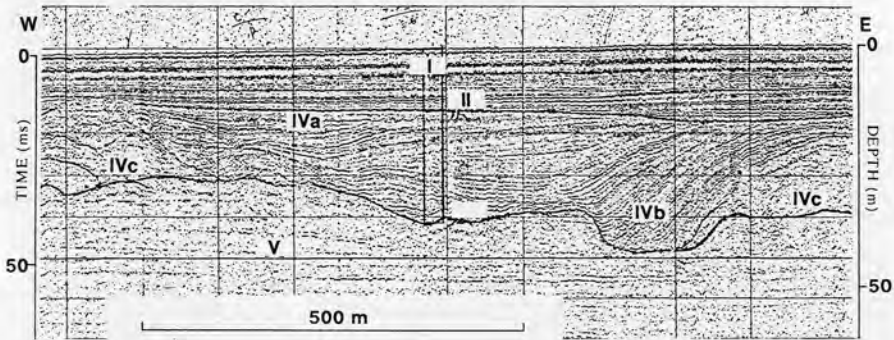


Fig.5 Shallow seismic profile in the nearshore area. Roman numbers denote seismic facies units. For location see bar 1 in Fig.1.

seismic profiles in the East China Sea is shown in Fig.2. In the nearshore area, at least five units have been recognized in seismic profiles (Fig.5):

Unit I. Prodelta to shelf fine-grained deposits of late Holocene age.

Unit II. Shallow marine fine-grained deposits of early Holocene age.

Unit III. Tidal sand ridges of early Holocene age (not shown in Fig.5).

Unit IV. Lacustrine (IVa) and estuarine (IVb) sediments deposited during the early Holocene transgression and fluvial sediments of late Pleistocene age (IVc).

Unit V. Prodelta to shallow-marine sediments of late Pleistocene age.

In the outer shelf area, twelve units have been identified within the limits of seismic penetration (about 100 m below the sea bottom) (Fig.6):

Unit 1. Tidal sand ridges formed during the Holocene transgression.

Unit 2. Swamp, lacustrine (2a) and estuarine channel and fluvial (2b) deposits of late Pleistocene age. There was erosion in the western parts of the basin during this period.

Unit 3. Prodelta and shelf fine-grained sediments of late Pleistocene age.

Unit 4. Prodelta sediments of late Pleistocene age (not shown in Fig.6).

Unit 5. Swamp-lacustrine (5a) and fluvial (5b) sediments of late Pleistocene age. The western parts of the basin were eroded during this period.

Unit 6. Shallow-marine fine-grained deposits of late Pleistocene age.

Unit 7. Fluvial and lacustrine sediments of middle Pleistocene age, with erosion in the western parts of the basin (not shown in Fig.6).

Unit 8. Large delta complex of middle Pleistocene age.

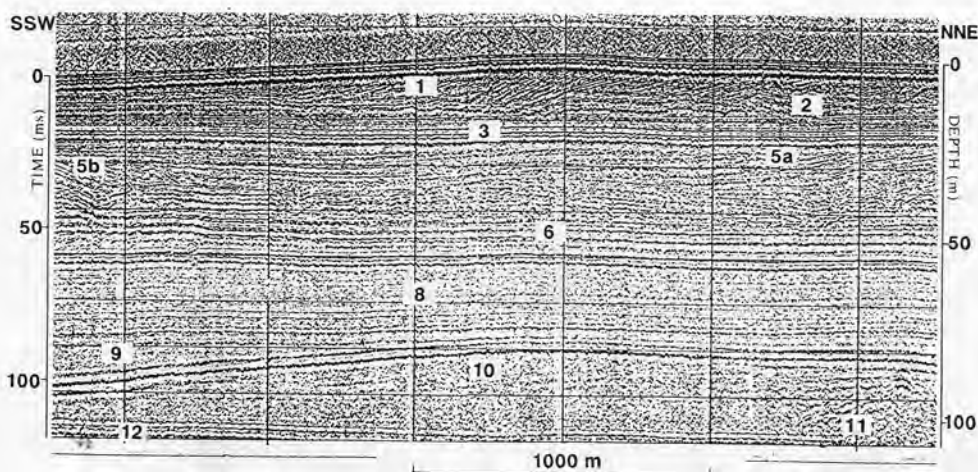


Fig.6 Shallow seismic profile in the outer shelf of the East China Sea. Numbers denote seismic facies units. For location see bar 2 in Fig. 1.

Unit 9. Shelf fine-grained sediments of middle Pleistocene age, passing towards the west into a large delta complex.

Unit 10. Tidal sand ridges of middle Pleistocene age.

Unit 11. Fluvial deposits of middle Pleistocene age, there was erosion in the western parts of the basin.

Unit 12. Large delta complex of early-middle Pleistocene age.

As shown in Fig.2, tidal sand ridges have been observed in Unit III in the nearshore area, and in Units 1 and 10 in the outer shelf area.

## HOLOCENE JIANGGANG RADIAL SAND RIDGES IN THE SOUTHERN YELLOW SEA

The Jianggang Radial Sand Ridges are situated to the north of the Recent Changjiang River Delta and south of the Old Huanghe River Delta, off the Subei coast. These huge sand ridges cover a shallow shelf area of about 35,000 sq km (250 km N-S and 140 km E-W) in the Southern Yellow Sea (Fig.1). By implication, the most striking feature of the Jianggang Radial Sand Ridges is the radial distribution pattern of the main sand ridges, with Jianggang as the apex (Fig.1). This pattern can be attributed to the radial flow field of the tidal currents in this area (Yang, 1985). Individual sand ridges are 60-100 km long, 10-15 km wide and 10-15 m high. Water depths to the top of these sand ridges range from 5 to 20 m. Approaching the apex near Jianggang, individual sand ridges merge together, forming large shallow subtidal to intertidal shoals which emerge during low tides. A part of the shoals in the apex extends onto the present-day coastal plain. The major sand ridges consist of grey,

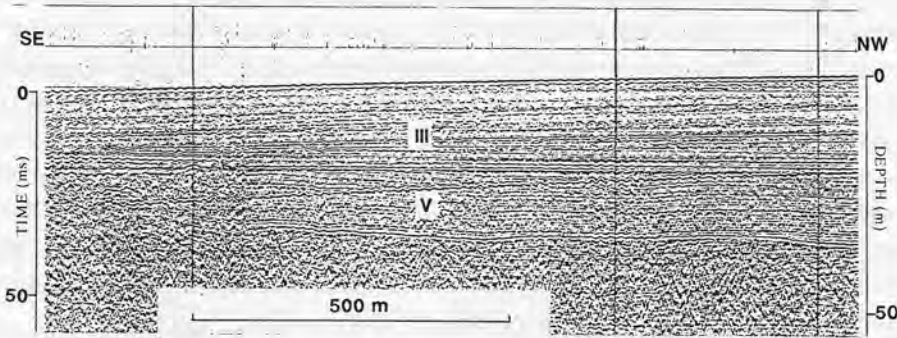


Fig.7 Shallow seismic profile in the Jianggang Radial Sand Ridges. Roman numerals denote seismic facies units. For location see bar 3 in Fig.1.

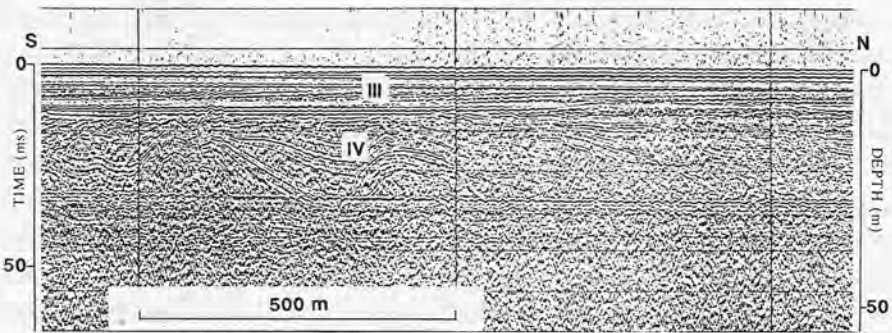


Fig.8 Shallow seismic profile in the Jianggang Radial Sand Ridges. Roman numerals denote seismic facies units. For location see bar 4 in Fig.1.

well-sorted fine sands, silty sands and sandy silt with shell debris. There is a gradual decrease in the grain size from well-sorted fine sands with enrichment of heavy minerals in the shoals near the apex to silty sands and sandy silt in distal parts of the sand ridges. Deposits in the troughs, however, are mainly clayey silt and silty clay.

Shallow seismic profiles across the sand ridges show that the major sand ridge unit (Unit III in Figs. 7 and 8) is 10-20 m thick. They lie unconformably over late Pleistocene-early Holocene fluvial and estuarine channel deposits (Unit IV in Fig.8). This relationship clearly suggests that the Jianggang Radial Sand Ridges were formed during the early Holocene transgression. The internal structure of the sand ridges is characterized by large-scale, low-angle inclined beds, which dip towards the southeast, parallel to the ridge flanks (Unit III in Fig.7), indicative of lateral migrations of the ridges.

Detailed investigations of the seafloor morphology, surficial sediments and shallow stratigraphy revealed that the late Pleistocene palaeochannels of the Changjiang River were

buried beneath the Radial Sand Ridges near Jianggang (Zhou & Sun, 1981; Yang, 1985; Yang et al. 1985). This indicates that the Changjiang River passed through the area of Jianggang in late Pleistocene times. During the post-glacial transgression, a wide funnel-shaped estuary was established in this area. A large-scale prograding delta complex of the Changjiang River was formed during the subsequent highstand, depositing a huge amount of sand within the area (Zhou & Sun, 1981; Yang, 1985; Yang et al. 1985). Subsequently, when the Changjiang River shifted more to the south, the sand supply was depleted. Tidal erosion became dominant, modifying the deltaic features into radial sand ridges (Fig.9). Fine-grained sediments were transported further offshore and deposited in the Central Basin of the southern Yellow Sea (Zhou & Sun, 1981; Yang, 1985; Yang et al. 1985).

The present-day Jianggang Radial Sand Ridges are actively moved by strong tidal currents, which normally exceed 1 m/s. Comparisons with historical data (Li & Li, 1981) indicate a general trend of landward migrations of sand ridge bodies, which merge with each other, or merge into shoreline-attached intertidal-subtidal shoals. This trend indicates the landward transportation of the relict deltaic sand from the shelf during sand ridge development. Such a pattern of sand movement may reflect the effects of tidal wave distortion in the shallow-water area. The flood current has the shorter duration but a higher current velocity. Since the sediment transport rate depends on the third or fourth power of the current velocity, a relatively minor difference in tidal current velocity can result in a major difference in sediment transport rate. Although the net fluid flux over a tidal cycle is zero, the sediment transport by flood currents will be much higher than that by ebb currents, resulting in the net sediment transport in the landward direction. Actual measurements at a coastal station north of Jianggang show just such an asymmetrical tidal current pattern with a maximum flood current velocity of 1.25 m/s and a maximum ebb current velocity of 0.53 m/s (Li & Li, 1981).

Similar processes can also be observed in the present-day Changjiang River mouth,

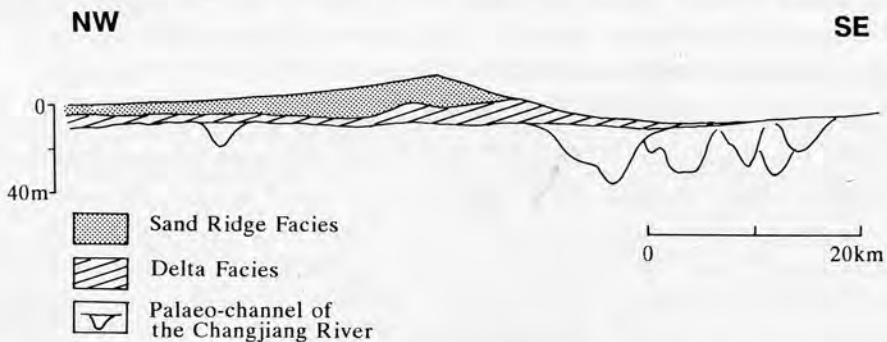


Fig.9 Schematic section across a sand ridge in the southern Yellow Sea, showing palaeochannels of the Changjiang River buried beneath deltaic sediments, which were partly reworked into sand ridge deposits (after Yang et al., 1985). For location see bar 5 in Fig.1.



which consists of two major distributaries, the Northern Branch and the Southern Branch (Fig.1). As the major fluvial discharge was shifted to the Southern Branch, the Northern Branch gradually lost its identity as a major river distributary, and became a funnel-shaped estuary dominated by tidal processes. Due to shallow water distortions of tidal waves, depth-averaged velocities of flood currents there are much higher than those of ebb currents. Consequently abandoned deltaic sands at the mouth of the Northern Branch are being reworked and transported into the estuary, and sand ridges have been observed. This is similar to the situation in the Jianggang area and has important implications for the Changjiang River Delta model.

### MORIBUND TIDAL SAND RIDGES OF EARLY HOLOCENE AGE ON THE EAST CHINA SEA SHELF

The sand ridges on the shelf of the East China Sea mainly occur over the submerged palaeovalley of the Changjiang River and the adjacent area (Fig.1). Detailed echosoundings by the Bureau of Marine Geological Survey show that they start in the southeast from the palaeoestuary mouth of the Changjiang River at the shelf edge, and end in the northwest, at the palaeovalley of the Changjiang River east of the recent subaqueous delta of the Changjiang River.

The sand ridges on the East China Sea shelf are distributed in present-day water depths of 45-115 m. They cover an area of 57,000 sq km. Individual sand ridges are 10-50 km long (maximum length 60 km), 2-5 km wide and 5-20 m high. The average spacing between ridges is 8-14 km. They are roughly parallel to each other, mainly extending ESE-WNW (approx.  $120^{\circ}$ - $300^{\circ}$ ). Locally, however, sand ridges may also occur in a SSE-NNW direction due to the change of the palaeovalley direction. In transverse sections these offshore sand ridges exhibit asymmetrical profiles with flat crests. The gentle slopes face north-northeast (approx.  $30^{\circ}$ ) at an angle of about  $0.5^{\circ}$ , and the steeper slopes dip south-southwest (approx.  $210^{\circ}$ ) at an angle of about  $2^{\circ}$ .

In shallow seismic profiles, these offshore tidal sand ridges comprise Unit 1. The profiles across the sand ridges reveal large-scale, very low-angle inclined layers, which show a convergent pattern at the base of this unit (Figs.6 and 10). These very low-angle inclined layers dip towards the south-southwest (approx.  $210^{\circ}$ ), in the same direction as the steeper slopes of the sand ridges.

The shallow seismic profiles also show an unconformity between the sand ridges (Unit 1) and underlying lacustrine (Unit 2a) estuarine channel and fluvial (Unit 2b) deposits of late Pleistocene age (Figs.6 and 10). This is also quite distinct in the line drawing of a seismic section (Fig.11). This unconformity represents periods of erosion during the post-glacial transgression. Above this unconformity, sand ridge deposits are more than 10 m thick at the ridge crests.



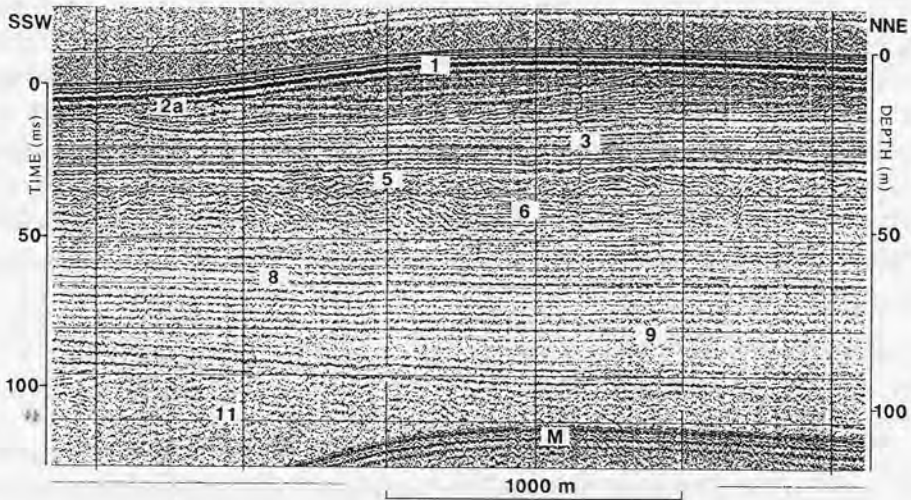


Fig.10 Shallow seismic profile from the outer shelf of the East China Sea showing large-scale, low-angle inclined layers in a sand ridge of Unit 1. Numbers denote seismic facies units. M is seafloor multiple. For location see bar 6 in Fig.1.

Shallow borehole data indicate that the tidal sand ridges of Unit 1 mainly consist of fine sands with abundant shell fragments. They were formed during the post-glacial transgression when the East China Sea shelf had shallower water depths and stronger tidal currents than now. This is comparable with the present-day shallow shelf off Jianggang in the Southern Yellow Sea. On the East China Sea shelf, however, as the post-glacial transgression continued, the water depth of the tidal sand ridges increased and the tidal currents became weaker. The tidal sand ridges gradually ceased growing and became moribund sand ridges. It is noteworthy that these moribund sand ridges still retain an asymmetrical shape, although less distinct. This is true even for some buried tidal sand ridges (Fig.11). The extremely high contents of foraminifera tests at their upper surfaces, however, indicate that

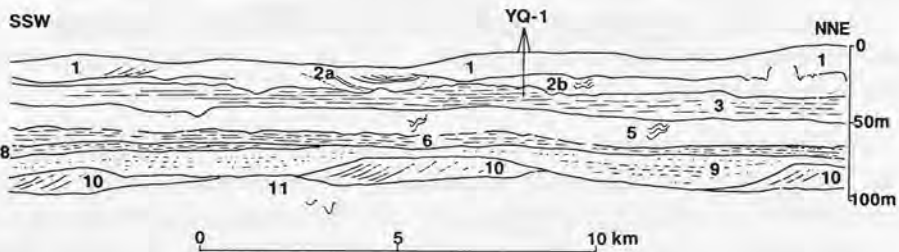


Fig.11 Line drawing of a seismic section over the outer shelf of the East China Sea showing three sand ridges of Unit 1 and three sand ridges of Unit 10. Numbers denote seismic facies units. The projected position of the nearby borehole YQ-1 is also shown in the section. For location see bar 8 in Fig.1.

movement, if any, would influence no more than a mobile surface layer, and the sand ridges as a whole remain moribund.

## BURIED TIDAL SAND RIDGES OF MIDDLE PLEISTOCENE AGE IN THE EAST CHINA SEA

Recent shallow seismic profiles acquired on the East China Sea shelf show that the Holocene tidal sand ridges of Unit 1 are not the only example there. A similar group of tidal sand ridges has been observed in the same area, but at a depth of 60-80 m below the sea bottom. They comprise Unit 10 (Figs.6 and 12).

In seismic profiles, Unit 10 lies unconformably over the delta complex of Unit 12 and the fluvial deposits of Unit 11, and it, in turn, is overlain disconformably by the fine-grained shelf deposits of Unit 9 (Figs.6 and 12). This stratigraphic sequence suggests that the sand ridges of Unit 10 may have been formed during a transgressive stage, like those of Unit 1.

Figure 12 shows the details of Unit 10. This unit also shows a ridge-like shape with a significantly undulating upper surface. It is 15-20 m thick at the crests, but thins out in the troughs. The internal structure of Unit 10 is characterized by low-angle inclined reflectors which dip towards the southwest and show a convergent pattern at the base of the ridge, identical to that of Unit 1.

The line drawing of a seismic section (Fig.11) shows the lateral distribution of three sand ridge bodies of Unit 10. The sand ridge shape and the internal low-angle, southwest-dipping structures are very distinct. Individual sand ridges are 3-6 km wide and 15-20 m thick. The spacing between the sand ridges is 8-12 km, similar to that of Unit 1. The similarities in overall shape, internal structure, scale, distribution pattern and stratigraphic

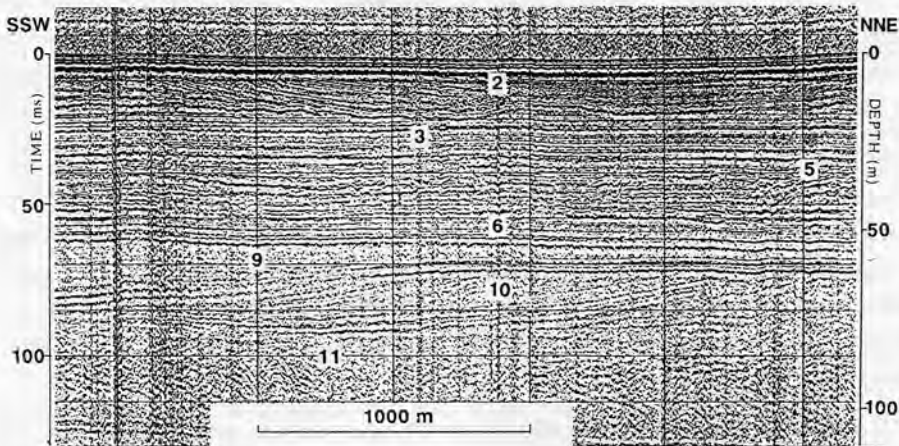


Fig.12 Shallow seismic profile from the outer shelf of the East China Sea showing details of a sand ridge (Unit 10). Numbers denote seismic facies units. For location see bar 7 in Fig.1.

position between Unit 1 and Unit 10 are obvious when comparing the three sand ridges of Unit 10 with the three in Unit 1 in Fig.11.

Regional seismic data recently collected by the Bureau of Marine Geological Survey revealed that the sand ridges of Unit 10 occur in an area approximately coincident with, but further north of the area of tidal sand ridges in Unit 1. Based on the correlation between the seismic data and the established stratigraphic sequences in nearshore Quaternary basins, the age of Unit 10 has been inferred as middle Pleistocene, probably 0.3 or 0.4 Ma B.P. (Fig.2).

## A VERTICAL SEQUENCE OF TIDAL SAND RIDGE DEPOSITS

A borehole (YQ-1) was drilled through a tidal sand ridge on the outer shelf of the East China Sea, where the water depth is about 90 m (Fig.1). Samples for grain size and for spore-pollen and foraminifera analyses were collected from the borehole (Figs.13 and 14).

The stratigraphic sequence in the borehole can be compared with a nearby seismic profile (Fig.11). With a total depth of 25.75 m, this borehole penetrated three units, i.e. the tidal sand ridge deposits of Unit 1, estuarine channel deposits of Unit 2b and prodelta fine-grained sediments of Unit 3.

### Interval C (25.75-20.55 m)

This interval mainly consists of silt (53-64%) and clay (36-44%) with minor sand (1-4%) (Fig.13). It can be correlated with the highstand prodelta-shallow shelf fine-grained sediments of Unit 3 (Fig.11).

The spore-pollen assemblage of this interval mainly consists of tree pollen (55.1-60.9%) with some herb pollen (17.6-26.7%) and spores (13.0-25.0%) (Fig.13, Zone C). The abundant *Pinus*, *Quercus*, *Juglans*, *Ulmus*, *Castanea* and *Polypodiaceae* indicate a warm climate. A similar spore-pollen assemblage characterized by *Pinus*, *Quercus*, *Juglans* and *Pterocarya* in the 38.2-33.4 m interval of borehole DC-2 in the nearshore area of the East China Sea has been correlated to a warm climate period (Huang et al., 1984; the location of DC-2 is shown in Fig.1).

About 20-40 foraminifera species were observed in this interval. The number of foraminifera tests per 50 g of dry sediment is about 60-360 (Fig.14, Zone C). The important species include *Ammonia compressiuscula*, *Quinqueloculina lamarckiana*, *Textularia foliacea*, *Bulimina marginata*, and *Elphidium advenum*, which represent an inner-shelf environment. The presence of *Pseudonionella variabilis* indicates that this area was not far from an estuary mouth.

The above observations indicate that Interval C represents prodelta-shallow shelf fine-grained sediments deposited during a highstand in an inner shelf environment not very far from an estuary mouth.

### Interval B (20.55-8.5 m)

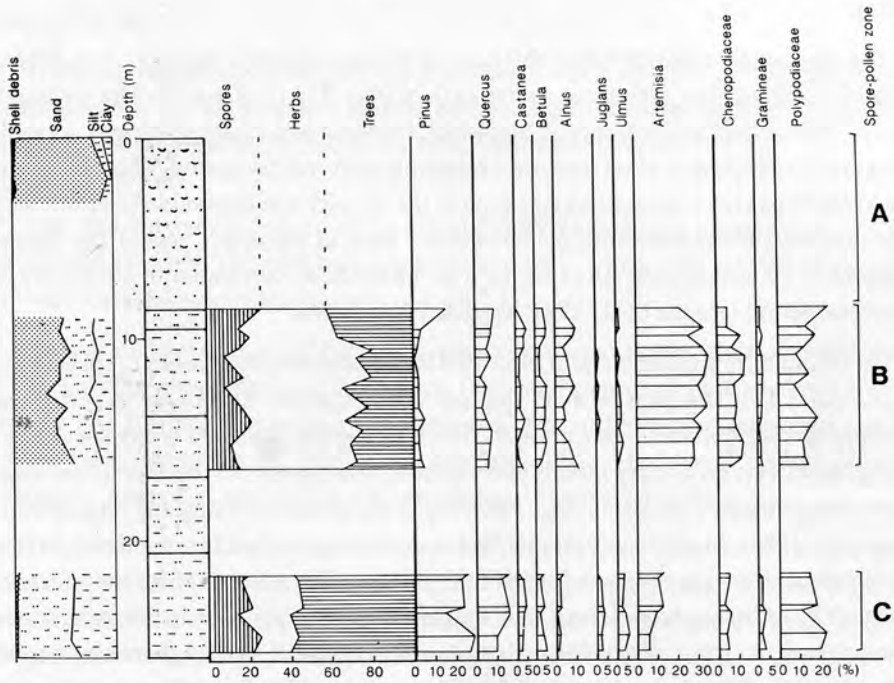


Fig.13 Grain size and spore-pollen zonation in borehole YQ-1. The location of the borehole is shown in Fig.1.

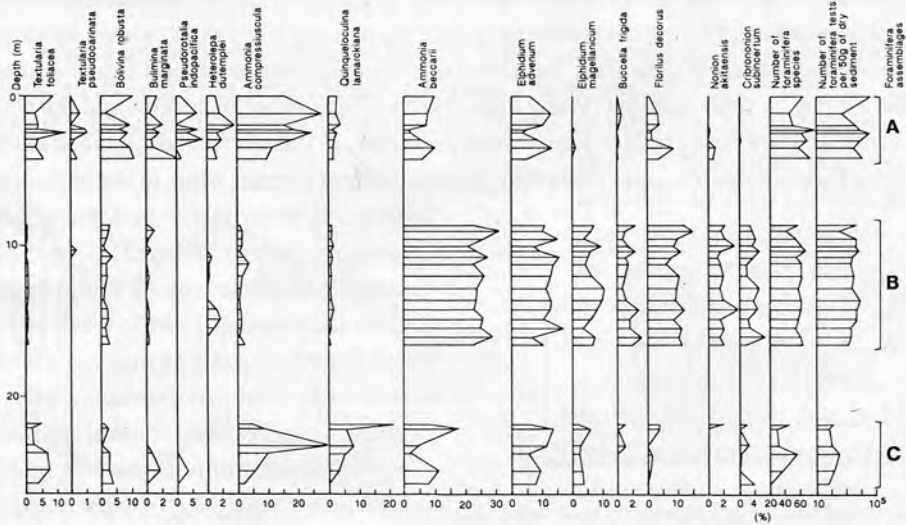


Fig.14 Foraminifera zonation in borehole YQ-1. The location of the borehole is shown in Fig.1.

This interval mainly consists of fine sand (43-58%) and silt (27-43%) with some clay (12-25%) (Fig.13). It can be correlated with the estuarine channel deposits of Unit 2b



(Fig.11).

The spore-pollen assemblage of this interval mainly consists of herb (31.7-64.5%) and tree (20.0-42.3%) pollen with some spores (8.0-26.0%) (Fig.13, Zone B). The obvious increase in herb pollen, the presence of abundant *Artemisia* and *Chenopodiaceae*, as well as the increase in *Betula* and *Alnus* indicate a relatively cold and dry period. This can be compared to the *Artemisia-Chenopodiaceae* zone in the 33.4-29.1 m interval in borehole DC-2 and to the *Gramineae-Artemisia-Chenopodiaceae* zone in the upper part of the Sheshan Formation in the Changjiang River Delta, which have been correlated to a cold, dry late Pleistocene period (Huang et al., 1984; Tang & Zhan, 1986).

The foraminiferal assemblage of Interval B is characterized by a variety of foraminifera (Fig.14, Zone B). The presence of shallow water species *Elphidium magellanicum*, euryhaline species *Ammonia beccarii* and *Nonion akitaensis*, and cold-water species *Buccella frigida* reflects an estuary mouth environment, comparable to the *Elphidium magellanicum-Ammonia beccarii* assemblage observed in the modern Changjiang estuary mouth (Wang et al., 1986). In addition, Interval B also shows stenohaline foraminifera. As many as 40-65 foraminifera species were found in this interval. The number of foraminifera tests per 50 g of dry sediment ranges from 1300 to 6300. This is very similar to the foraminiferal thanatocoenoses in the modern Changjiang estuary. Detailed studies there show a clear salinity zonation of the living foraminifera (Wang et al., 1986). Even the euryhaline *Ammonia beccarii* and *Elphidium magellanicum* are only found in the area outside the estuary. There are no living foraminifera within the estuary (Fig.15). Abundant foraminifera tests, however, can be found in bottom sediments within the estuary. They show no salinity zonation, but a clear sorting of their sizes, indicative of the transportation of tests from the shelf into the estuary by tidal currents (Wang et al., 1986). The number of species and the content of foraminifera tests are functions of tidal processes. In the microtidal Zhujiang River mouth, surficial sediments contain less than 10 foraminifera species, while in the mesotidal

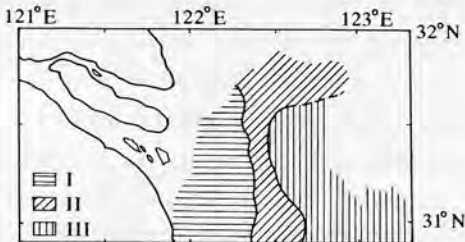


Fig.15 Distribution of living foraminifera in surface sediments of the Changjiang River estuary. I = *Elphidium magellanicum-Ammonia beccarii* var. assemblage; II = *Ammobaculites* sp.-*Arenoparella asiatica* assemblage; III = *Nonionella jacksonensis-Hanzawaia nipponica* assemblage (after Wang et al., 1986).

Changjiang River mouth and macrotidal Qiantang River mouth, over 40 foraminifera species can be found in the bottom sediments (Li, 1985; Wang et al., 1986). Even in the same estuary, seasonal variations in tidal processes may have a clear influence on foraminiferal distribution. The number of tests per 50 g of dry sediment in Changjiang Estuary reached 1,300 during the dry season of 1982 when tidal currents had a strong influence, but decreased to 81 during the flood season of 1983 when tidal currents were relative-



ly weak (Fig.16).

The foregoing indicates that Interval B was deposited in an estuary setting with a strong tidal influence, which developed in the area of the present-day outer shelf of the East China Sea during low sea level at the end of the late Pleistocene (Fig.1).

#### Interval A (8.5-0 m)

This interval mainly consists of fine sand (88-95%) with only minor silt (4-10%) and clay (0-11%) (Fig.13). The sand contains abundant shell debris. This interval can be correlated with the tidal sand ridge deposits of Unit 1 (Fig.11).

Only some spores (mainly *Polypodiaceae*) were found in this interval (not shown in Fig.13). This can be compared with the early Holocene spore-pollen zone above 16.3 m in borehole DC-2, which is dominated by spores (62.8%, including *Polypodiaceae* and *Dennstaedtiaceae*) (Huang et al., 1984; Zhao and Qin, 1986). The lack of a spore-pollen assemblage in Interval A may reflect the reworking of these sediments.

The foraminiferal assemblage of Interval A (Fig.14, Zone A) is characterized by *Ammonia compressiuscula*, *Textularia foliacea*, and *Bulimina marginata*, representing a shelf environment. Some warm-water species, such as *Pseudorotalia indopacifica* and *Heterolepa dutemplei*, were also found. These species may have been deposited at a later stage when this shelf area was influenced by the warm Kuroshio current. Their presence in the upper part of this interval indicates the reworking of the upper layer, probably by tidal currents or storm-driven currents.

The foraminifera assemblage of Interval A also shows a high diversity. Between 35 and 78 foraminifera species were found in this zone. The number of tests per 50 g of dry sediment ranges between 2800 and 41700 (Fig.14). These features are characteristic of the relict

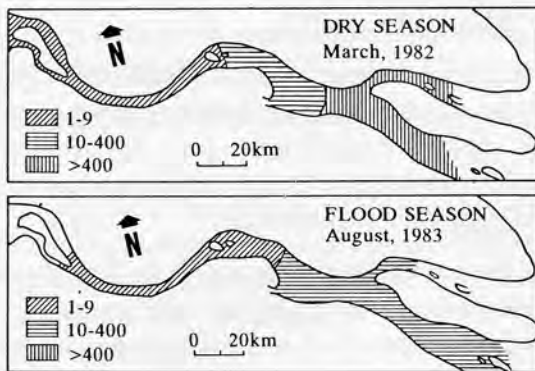


Fig.16 Foraminiferal abundance in surface sediments in the Changjiang River estuary showing a comparison between dry and flood seasons. Numbers denote number of tests per 50g of dry sediment (after Wang et al., 1986).

sands, which were subsequently reworked by tidal currents. In the Southern Yellow Sea, as many as 90 foraminifera species can be found in reworked relict sands, and the number of tests per 50 g of dry sediment can reach 7000 (Wang, 1982). In the East China Sea, reworked relict sands contain both relict tests of euryhaline species and modern tests of stenohaline species. The number of tests per 50 g of dry sediment ranges from 1000 to over 10000. The sizes of the tests show a sorting in accordance with sand

grain size (Shen, 1985).

The top of Interval A is a very thin layer characterized by (1) a wide lateral continuity, (2) little terrigenous sedimentation and (3) an extremely high content of foraminifera. The number of tests per 50 g of dry sediment reached 41700. This reflects the submarine hiatus condition on the shelf during the Holocene high sea level. This fossil-rich surface layer is less than 1 m thick, indicating that movement, if any, would influence no more than a mobile surface layer. Such a thin calcareous-rich layer can be preserved in stratigraphic records as a submarine hardground.

The above discussion shows that Interval A was deposited as tidal sand ridges during the post-glacial transgression. The sharp decrease in mud content, the high diversity of foraminifera species and the high content of tests are comparable with the features of the relict sands, which were subsequently reworked by tidal currents. The calcareous-rich layer on the upper surface reflects a submarine hiatus condition during the subsequent high sea level.

## DISCUSSION

### Origin of Tidal Sand Ridges

The tidal sand ridges in the East China Sea and the Southern Yellow Sea represent an important type of tidal sand ridge.

Since the 1960's tidal sand ridges have been widely reported (Off, 1963; Stride, 1982; de Boer et al., 1988). Three types of tidal sand ridges are commonly observed.

(1) Tidal sand ridges may develop along sand transport paths on the shelf, e.g., in the present-day North Sea. Their formation may be ascribed to pairs of helical cells rotating in opposite directions with axes parallel or at a small angle to the peak tidal currents (Belderson et al., 1982).

(2) Tidal sand ridges can also be formed at the outlet of a strait. The tidal sand ridges in the Bohai Sea are a good example. The lateral constraints of the strait may increase tidal current velocities, causing the erosion of bottom sediments in the strait. At the outlet, however, the widening of the strait will result in the decrease in tidal current velocities and the deposition of sands, forming tidal sand ridges (Sun et al., 1984).

(3) Tidal sand ridges may develop in the estuary-mouth area, e.g., in the East China Sea and the Southern Yellow Sea. The estuary conditions may occur during a sea-level rise (such as the case of offshore sand ridges in the East China Sea), or during the abandonment of major distributaries (such as the cases in the Jianggang and in the Northern Branch of the modern Changjiang River mouth). Consequently, tidal processes become dominant, modifying older deltaic and fluvial deposits into tidal sand ridges. Tidal sand ridges in such a setting show a trend of landward migration, indicating net sand transport into the estuary,

which is most probably caused by tidal wave distortions in shallow-water areas.

### **Evolution of Tidal Sand Ridges**

The evolution of tidal sand ridges was closely related to sea-level fluctuations. Active tidal sand ridges are formed during a sea-level rise. They show distinct morphology and active migrations in a lateral as well as in a landward direction. They are generally in equilibrium with present-day tidal processes and their distribution patterns are related to the flow field of the tidal currents. As the sea level rises further, these tidal sand ridges become moribund sand bodies with a less distinct morphology. Their upper surfaces are covered by a thin calcareous-rich layer with a very high content of foraminifera tests, reflecting a submarine hiatus condition on the shelf during the highstand. During the subsequent steady fall of sea level, the tidal sand ridges can be buried by fine-grained shelf and prodelta sediments. They have, therefore, a good chance of being preserved in the stratigraphic record.

### **Sequential Buildup**

A basic model can be summarized for the sequential development of the tidal sand ridges. The sequential buildup during a sea-level rise (TR-tract) and a subsequent sea-level fall (HS- and LS-tract) would consist of the following depositional facies in an ascending order:

(1) The estuarine channel and tidal flat facies were formed at the onset of the sea-level rise (the early stage of the TR-tract), indicating that the previous fluvial system was changed to an estuarine system during a brackish transgression.

(2) The tidal sand ridge facies was formed during a sea-level rise (TR-tract). During this marine transgression, a modification of the in-situ sediments by tidal currents occurred.

(3) Fine-grained shelf and prodelta mud facies may cover tidal sand ridge deposits, representing the highstand stage (early HS-tract).

(4) Large-scale prograding delta complexes were developed during a steady sea-level fall (HS-tract).

(5) Continental deposits mainly consisting of fluvial facies represent a lowstand (LS-tract).

The total thickness of a vertical sequence for a complete cycle of sea-level rise and fall may reach 50-60 m. Due to the limited lateral extent, however, some facies are often missing. Incomplete sequences, therefore, are more common with erosional surfaces, abandonment surfaces and palaeosoil horizons.

### **Reservoir Potential**

Tidal sand ridges are huge sand bodies containing well-sorted sands. They have therefore a good reservoir potential.

Figure 17 shows a bright spot observed at the crest of a buried Pleistocene tidal sand

ridge in the East China Sea. The bright spot can be identified by polarity reversal, amplitude anomaly, and the velocity pull-down of the reflection from the base. This indicates porous gas-filled sands at the sand ridge crest. The top and the base of the gas sand are shown as the "white" and the "black" respectively (Fig.17). This gas-filled sand layer is 1650 m wide across the sand ridge crest. By measuring the time between the reflections from the top and the base, the thickness of the gas sand is estimated as 5.5 m. The gas in this case has a biogenic origin. It was most probably derived from the overlying shelf mud deposits of Unit 9, and filled only the uppermost part of the sand ridge crest. The accumulation of such shallow gas has also been proved by shallow boreholes drilled by the Bureau of Marine Geological Survey in nearshore areas.

## SUMMARY

Tidal sand ridges in the East China Sea and the Southern Yellow Sea have important implications for ancient analogues in terms of the external shape, dimensions, distribution patterns, internal structural organization, sequential construction and reservoir quality. Some important aspects of these sand ridges include:

(1) They consist of relatively clean, well-sorted fine sands with fairly uniform sequences. The sands were reworked by tidal currents and show low contents of clay. The microfossil assemblage exhibits a high diversity including both euryhaline and stenohaline species.

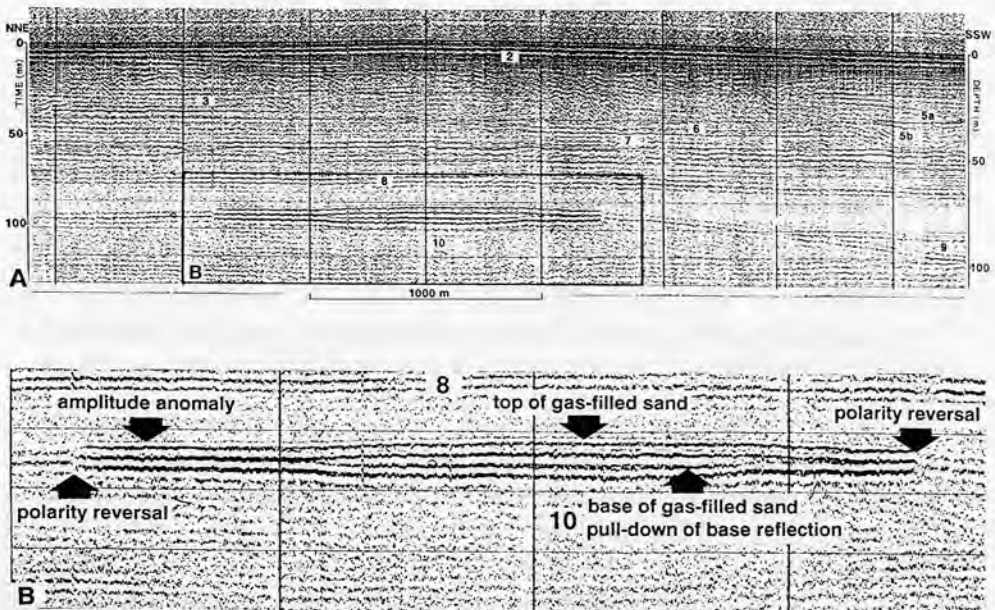


Fig.17 A bright spot at the crest of a buried Pleistocene tidal sand ridge. The bright spot can be identified by polarity reversal, amplitude anomaly and the velocity pull-down of the reflection from the base. It indicates a gas-filled sand layer about 1,650 m wide and 5.5 m thick. For location see bar 9 in Fig.1.



(2) The ridges are huge elongated sand bodies, several km wide, 10-60 km long and up to 20 m thick.

(3) They normally occur in groups. Individual sand ridges are spaced at several to more than 10 km. The sand ridge field on the East China Sea shelf covers an area of 57,000 sq km.

(4) The distribution pattern of the sand ridges is controlled by the regional tidal current pattern. Normally, they are parallel with each other and extend in the direction of the tidal currents. Due to the radial flow field of tidal currents, however, a radial distribution pattern may develop.

(5) The internal structure of these tidal sand ridges often show unidirectional-dipping layers inclined at low angles (a few degrees).

(6) The ridges are preserved within a transgressive sequence related to a period of sea-level rise. They overlie continental sediments deposited during low sea level, and are covered by shelf mud deposited during the subsequent highstand. They have, therefore, a high preservation potential in the stratigraphic record.

(7) Fossil tidal sand ridges are potential stratigraphic traps of hydrocarbon. The well-sorted fine sands often show good porosity. The overlying shelf and prodelta mud may provide source rock and seal conditions. The upper surfaces of the sand ridges were often preserved as submarine hardgrounds with low permeabilities, which may also provide seal conditions.

These features have important implications for the subsurface recognition of the fossil tidal sand ridges, a factor critical to the reconstruction of the regional palaeogeography and transgressional history and the prediction of potential reservoir sandstones and stratigraphic traps.

## **ACKNOWLEDGEMENTS**

I would like to thank the technical team and crew members of the Bureau of Marine Geological Survey in Shanghai (Ministry of Geology and Mineral Resources of China) for the shallow seismic surveys and drilling. I would also like to thank Li Weixian for collecting samples from the borehole and the Bureau's laboratory for analyzing the samples. Special thanks are due to Prof.S.D. Nio of the Sedimentology Division, State University of Utrecht, and Sun Jiasong, Shi Siqi, Wei Binyan, Zhou Yonglin, Jiangjian and many other colleagues in the Bureau of Marine Geological Survey for valuable discussions. International Geoservices BV of the Netherlands kindly provided word-processing and other facilities. The manuscript benefitted substantially from valuable comments by the reviewers.



## REFERENCES

- Belderson, R.H., Johnson, M.A. & Kenyon, N.H., 1982. Bedforms. In: A.H. Stride (Editor), *Offshore Tidal Sands, Processes and Deposits*. Chapman & Hall, London, pp.27-57.
- De Boer, P.L., Van Gelder, A. & Nio, S.D., 1988. *Tide-Influenced Sedimentary Environments and Facies*. Reidel, Dordrecht, 530 pp.
- Huang Qingfu, Gou Shuming, Sun Weimin, Shen Xunxi, Xu Shanmin & Cang Shuxi, 1984. The stratigraphical division of DC-2 columnar core from the East China Sea. *Mar. Geol. Quat. Geol.*, 4(1): 11-26 (in Chinese).
- Li Chengzhi & Li Benchuan, 1981. Studies on the formation of Subei sand cays. *Oceanol. Limnol. Sin.*, 12(4): 321-331 (in Chinese).
- Li Shuluan, 1985. Distribution of the foraminiferal thanatocoenosis of Pearl River estuary. *Mar. Geol. Quat. Geol.*, 5(2): 83-104 (in Chinese).
- Off, T., 1963. Rhythmic linear sand bodies caused by tidal currents. *Bull. Am. Assoc. Pet. Geol.*, 47: 324-341.
- Qian Fang, 1984. A preliminary study on magnetostratigraphy of Quaternary transgressive series in China. *Mar. Geol. Quat. Geol.*, 4(3): 89-100 (in Chinese).
- Shen Huati, 1985. The age and origin of the relict sediments on the continental shelf of the East China Sea. *ACTA Oceanol. Sin.*, 7(1): 67-77 (in Chinese).
- Stride, A.H., 1982. *Offshore Tidal Sands, Processes and Deposits*. Chapman and Hall, London, 222pp.
- Sun Jiasong, Zhou Changzhen & Feng Dongzhi, 1984. On effects of hydrodynamic processes on the development of some submarine geomorphological features. *Mar. Sci. Bull.*, 3(2):54-61 (in Chinese).
- Tang Baogen & Zhan Yiping, 1986. Stratigraphic division of cores from shallow holes in Changjiang River subaqueous delta. *Mar. Geol. Quat. Geol.*, 6(2): 41-52 (in Chinese).
- Vail, P.R., 1987. Seismic stratigraphy interpretation using sequence stratigraphy, Part 1: Seismic stratigraphy interpretation procedure. In: A.W. Bally (Editor), *Atlas of Seismic Stratigraphy (American Association of Petroleum Geologists Studies in Geology, No.27)*. Am. Assoc. Pet. Geol., Tulsa, Okla., Vol.1, pp. 1-10.
- Wang Pinxian, Min Qiubao, Bian Yunhua, Cheng Xinrong & Zhu Xiaodong, 1986. Transport of foraminiferal tests in estuaries and its paleoenvironmental implications. *Mar. Geol. Quat. Geol.*, 6(2): 53-66 and 6(3): 83-92 (in Chinese).
- Wang Zhenyu, 1982. Discussion on the characteristics and origin of the relict sand of western South Yellow Sea. *Mar. Geol. Res.*, 2(3): 63-70 (in Chinese).
- Yang Changshu, 1985. On the origin of Jianggang radial sand ridges in the Yellow Sea. *Mar. Geol. Quat. Geol.*, 5(3): 35-44 (in Chinese).
- Yang Changshu & Shi Siqi, in prep. Late Quaternary seismic stratigraphy and facies in the East China Sea shelf.
- Yang Changshu & Sun Jiasong, 1988. Tidal sand ridges on the East China Sea shelf. In: P.L.de Boer, A. Van Gelder & S.D. Nio (Editors), *Tide-Influenced Sedimentary Environments and Facies*. Reidel, Dordrecht, pp.23-38.
- Yang Zigeng, Sun Jiashi & Gao Jinman, 1985. Sedimentology and environment in south Huanghai Sea shelf since late Pleistocene. *Mar. Geol. Quat. Geol.*, 5(4): 1-19 (in Chinese).
- Zhao Songling & Qin Yunshan, 1986. Transgressions and sea-level changes in the eastern coastal region of China in the last 300,000 years. In: *China Sea Level Changes*. China Ocean Press, Beijing, pp.115-123 (in Chinese).
- Zhou Changzheng & Sun Jiasong, 1981. On the genesis of the shoal off north Jiangsu. *Mar. Geol. Res.*, 1(1): 83-91 (in Chinese).

## Samenvatting

Het doel van dit proefschrift is een kwantitatieve analyse van de dynamiek van getijdenafzettingen en de toepassing van de resultaten in fossiele getijdenafzettingen. In dit onderzoek zullen drie aspecten aan de orde komen. Deel 1 (Hoofdstuk 2 en 4) behandelt twee fundamentele problemen van vloeistof- en sedimentbeweging. De toepassing van deze methoden leidt tot de reconstructie van de hydrodynamische omstandigheden bij paleogetijden in fossiele afzettingen (Deel 1, hoofdstuk 3) en de identificatie, interpretatie en voorspelling van getijdenafzettingen in recente en fossiele getijdenmilieus (Deel 3, Hoofdstuk 4,5, 6, 7 en 8).

Een van de fundamentele problemen van vloeistof en sedimentbeweging betreft het veld van schuifspanningen in een laag en de stroomsnelheid in de grenslaag (Hoofdstuk 4). In ondiep mariene milieus met kleinschalige ruwheidselementen (kleiner dan 10cm hoog), kunnen stroomsnelheden worden gemeten op 100 cm boven de zee bodem, waarbij een enkelvoudige sleepcoëfficiënt kan worden gebruikt. In gebieden met megaribbels of "sandwaves" daarentegen, rijzen grote vraagtekens wat betreft het snelheidsveld boven de zeebodem en de determinatie van de beddingschuifspanning uit de snelheidsverdelingen in de grenslaag. Uit metingen in het veld en gepubliceerde gegevens is een samengesteld grensbeddingmodel, bestaand uit twee gebieden, ontwikkeld dat in deze studie wordt gebruikt om het plaatselijk gemiddelde van de beddingschuifspanning te relateren aan de snelheidsverdelingen bij grote beddingvormen. The twee gebieden zijn verdeeld op 100 cm boven het beddingvlak, in een buitenste gebied met ruwheidselementen van 1.5cm, en een binnenste gebied met ruwheidselementen van 0.15cm lang.

Een ander fundamenteel probleem dat in deze studie wordt behandeld heeft te maken met de formule van sediment transport (Hoofdstuk 2). De sedimenttransport formule van Bagnold is belangrijk gebleken in getijden milieus, maar enige daarbij opgeroepen vragen behoeven discussie. In hun theoretische vorm zijn Bagnolds formules voor transport van gesuspendeerde vracht  $q_s = \omega e_s \bar{U}_s (1 - e_b) / W$  en totale vracht  $q = \omega (e_b / \tan \alpha + e_s \bar{U}_s (1 - e_b) / W)$  niet correct wat betreft de wet behoud van energy. De juiste vorm zou moeten zijn  $q_s = \omega e_s \bar{U}_s / W$  voor het transport van gesuspendeerde vracht en  $q = \omega (e_b / \tan \alpha + e_s \bar{U}_s / W)$  voor de totale vracht. Wat betreft de praktische vorm, is de algemeen gebruikte Bagnoldse transportcoëfficiënt is op exponentiële wijze afhankelijk van de dimensieloze schuifspanning. Sediment transport-hoeveelheden die zijn voorspeld met deze aangepaste totale vracht formule van Bagnold komen zeer goed overeen met de getallen die afkomstig zijn uit metingen van beddingvorm migraties. Deze vergelijking maakt het verschil tussen de termen beddingvracht ("bed-load") duidelijk wanneer deze gebruikt worden bij beddingvorm migratie en in sediment transport formules. Om verwarring te voorkomen, bed-

dingmateriaal transporthoeveelheid ("bed-material transport rate") zou een betere term zijn voor de sedimenttransport hoeveelheden die worden geschat uit metingen van beddingvorm migraties.

Met de huidige kennis van getijden hydrodynamiek en sediment transport kunnen de fossiele hydrodynamische condities worden gereconstrueerd van de bewaarde fossiele getijden afzettingen. In hoofdstuk 3 wordt tijdserieanalyse toegepast om de paleogetijdenbewegingen uit te splitsen in verschillende periodische variaties. Hierbij wordt gebruik gemaakt van (1) Fourier analyse om de periodiciteit van de opeenvolgende bundeldiktes te testen en de periodes en fases van de belangrijkste periodische elementen af te schatten, en (2) filter analyse om de opeenvolging van bundeldiktes in verschillende componenten op te splitsen (bv. dagelijkse schommelingen, willekeurige variaties, variaties in dood- en springtij en variaties over langere perioden) en eveneens de relatieve waarde van elke component (bv. amplitude). Uit deze analyses kan bruikbare informatie worden gewonnen wat betreft de hydrodynamiek van het paleogetijdenmilieu (zoals het paleogetijdenbereik, stroomsnelheden, paleogetijden componenten en getijden karakter) en niet getijden gebonden processen zoals de sterkte, duur, frequentie en mogelijke richting van stormen.

Het belang van deze kwantitative studie is tweeledig. Ze geeft niet alleen een nieuw middel om paleogetijdenprocessen en -milieus te reconstrueren vanuit een sedimentologisch gezichtspunt, maar ook een nieuwe mogelijkheid om getijden afzettingen te identificeren, interpreteren en te voorspellen in termen van hydrodynamica.

Hoofdstuk 4 bespreekt het voorspellen van sedimentbeweging in recente getijdeafzettingen. Metingen aan getijdestromen in de Oosterschelde zijn gebruikt voor de regionale beschrijving van zandbewegingen en voor de schatting van zandtransport. De berekeningen duiden op zeer actieve zandbeweging in het huidige getijdebekken van de Oosterschelde. Plaatselijke sediment circulatie kan zich ontwikkelen om zandbanken. Erosie van de geulbodem kan ontstaan in die gebieden waar verschillende stromen van elkaar afstromen ("parting areas"). Het netto sediment transport vindt voornamelijk plaats in de ebrichting. De zandhuishouding over langere perioden wijst op een snelle aanpassing van het getijde bekken / zandbank systeem op variaties van het getijdenprisma.

In hoofdstuk 5 worden de afzonderlijke opeenvolging, de externe geometrie, de interne structurele organisatie en de sequentiële opbouw van een ebgetijdedelta en daarmee geassocieerde zandlichamen van estuariene geulen in de Onder Eocene Roda Zandsteen in de zuidelijke Pyreneën in Spanje gedocumenteerd en geïnterpreteerd. Dit gebeurt in de vorm van een vergelijkend onderzoek tussen de bewaard gebleven opeenvolgingen van dit fossiele voorbeeld en de sedimentaire processen in het huidige estuariene en ebdeltaïsche milieu van het mesogetijde bekken van de Oosterschelde in zuidwest Nederland. Voor de ebdelta en het geassocieerde estuariene geulstelsel is een afzettingsmodel ontwikkeld dat is gebaseerd op de overeenkomsten en verschillen tussen de twee eerder genoemde ebdel-

tas. Dit model bestaat voornamelijk uit prograderende eindlobben aan het delta front, uitgestrekte ebgedomineerde onder het getijdeniveau liggende zandbanken en brede, ondiepe ebgeulen op het delta platform, zowel als uitgestrekte tussen de eb en vloedlijn liggende zandbanken en relatief diepe actief migrerende getijden geulen in het estuariene bekken. Het veel voorkomen van mariene verlatings ("abandonment") oppervlakken en erosieve oppervlakken is een belangrijk kenmerk van de ebdelta en de estuariene geulopeenvolgingen. Hun sequentiële opbouw is in sterke mate afhankelijk van de invloed van mariene transgressies en tektonische bewegingen van het getijdebekken.

Hoofdstuk 6 beschrijft een voorbeeld met een sterke getijdeinvloed, de Jianggang Radial Sand Ridges aan de Jiangsu kust van de zuidelijke Gele Zee. Deze gigantische zandruggen werden verondersteld te zijn gevormd door kustparallele stromen die het sediment transporteerden van de verlaten Oude Huanghe rivierdelta in het noorden en de recente Changjiang rivier delta in het zuiden. Onze onderzoeken daarentegen veronderstellen dat de Jianggang zand ruggen een vroeg Holocene getijdedelta van de Chiangjiang rivier voorstellen die wordt gekenmerkt door reusachtige radiale getijdezandruggen. Getijdestromen zijn de voornaamste hydrodynamische faktor die verantwoordelijk is voor de ontwikkeling van de Jianggang Radial Sand Ridges. Vanwege de geomorfologische grensvoorwaarden in dit gebied ontmoetten de progressieve getijden golf van de oostelijke Chinese Zee en de amphidromische getijden golf van de zuidelijke Gele Zee elkaar voor de kust van Jiangsu. Op dit punt hadden deze twee getijdengolven een faseverschil van ongeveer één eb-vloed periode en daarom, konden ze met elkaar op konstruktieve wijze met elkaar interfereren, waarbij het getijdebereik werd vergroot en een radiaal veld van getijdestromen werd gevormd, dat het radiale verdelingspatroon van de getijdezandruggen beheerste.

Een voorbeeld van "moribund" (relicte) getijdezandruggen wordt behandeld in Hoofdstuk 7. Uitgebreid onderzoek heeft voor het eerst de aanwezigheid onthuld van deze reusachtige getijdezandruggen op het continentaal plat van de Oost Chinese Zee. Ze zijn 10-60km lang, 2-5km breed en 5-20m hoog met een onderlinge afstand van 8-14km. Ze strekken zich uit van OZO-WNW (ongeveer  $120^{\circ}$ - $300^{\circ}$ ) en hebben een asymmetrisch profiel in dwarsdoorsneden met de stijlere hellingen naar het ZZW gericht. Ze bestaan voornamelijk uit goed gesorteerde fijne zanden met overvloedig debris van intergetijden- en mariene ondiepwaterschelpen. De ondiepe seismische profielen laten een discordantie zien tussen de zandruggen en de onderliggende lagen, en de flauw hellende lagen die in de zandruggen zitten. De ondiep mariene fossielen en de relicte morfologie doen veronderstellen dat de getijdezandruggen op het continentaal plat van de Oost Chinese Zee zich waarschijnlijk hebben ontwikkeld gedurende de post-glaciale transgressie toen de waterdiepte geringer was en de getijdenstromen sterker dan tegenwoordig. Met het stijgen van het zeeniveau werden de getijdestromen zwakker, geleidelijk aan stopte de groei van



de zandruggen zodat deze relicte structuren werden op het kontinentaal plat van de ost Chinese Zee.

Hoofdstuk 8 is een vervolg op de studies in Hoofdstuk 6 en 7. Nieuwe ondiepe seismiek met een penetratie van ongeveer 100m onder het zeebodemoppervlak en gegevens van ondiepe boringen hebben niet alleen de details onthuld van de actieve en de relicte Holocene getijdenezandruggen, maar ook de aanwezigheid, kenmerken en sequentiële ontwikkeling van begraven Pleistocene zandruggen. Ze bestaan uit relatief schone, goedgesorteerde zanden in tamelijk uniforme opeenvolgingen. Hun microfossiele gemeenschap vertoont een grote diversiteit die zowel euryhaliene als stenohaliene soorten omvat. Ze vormen reusachtig grote elongate zandlichamen (verscheidene km breed, 10-60km lang en to 20m dik) en komen voor in groepen met een onderlinge afstand van enige tot meer dan 10 km. Normaal gesproken strekken ze zich uit in de richting van de getijdestromen. De interne structuren worden gekenmerkt door flauw hellende interne lagen.

Deze getijdezandruggen werden gevormd in estuariene en ondiep continentaal plat milieus, waar sterke getijdestromen grote hoeveelheden relicte zanden van oudere delta en rivier sedimenten remanieëerde, transporteerde en weer afzette. De ontwikkeling van getijdezandruggen in de monding van estuaria wordt vergezeld van een netto zandtransport van het continentale plat naar het estuarium. De evolutie van getijdezandruggen is nauw verbonden met transgressies. Actieve getijdezandruggen worden gevormd tijdens een relatieve zeespiegelrijzing. Zij vertonen een typische morfologie en migreren actief in zowel laterale als landwaartse richting. Zij zijn over het algemeen in evenwicht met de huidige getijdeprocessen en hun distributie patronen zijn gerelateerd aan het stromingsveld van de getijdestromen. Als het zeeniveau verder stijgt worden deze ruggen inactief waarbij hun morfologie minder markant wordt. Hun bovenoppervlak wordt bedekt door een dunne kalkhoudende laag met een hoog gehalte aan mariene fossielen, wat duidt op een submariene hiaat gedurende de perioden van hoge zeewaterstand. Gedurende de daaropvolgende gestage daling van het zeeniveau worden getijdezandruggen vaak bedekt door fijnkorrelige continentaal plat en prodeltasedimenten. Zij hebben daarom een goede kans om bewaard te worden in de stratigrafische overlevering.

De bovengenoemde kenmerken hebben belangrijke implicaties voor het herkennen van fossiele getijdezandruggen in de ondergrond, voor de rekonstruktie van de regionale paleogeografie en de geschiedenis van de transgressies en voor de voorspelling van potentiële reservoir zandstenen.



## Acknowledgements

I wish to thank all persons and institutions that contributed to the research described in this thesis.

The help of S.D. Nio has been crucial for the completion of this thesis. He introduced to me the fascinating tidal environment. He created a stimulating atmosphere for comparative sedimentological research not only through his interesting lectures, but also from his enthusiastic presence in the field and the brain-storming discussions. The help of J.B. Southard is especially valuable. Despite his heavy schedule, he reviewed the thesis in great detail with very helpful comments. His scientific attitude is a great example for me. G.V. Middleton, J.H.J. Terwindt, T. Elliott, M.R. Leeder, P.A. Allen, J.S. Bridge, D.A. McManus, A.D. Miall and many others kindly reviewed the early version of the thesis and/or the paper in the thesis. Their valuable comments and suggestions are of great help. I am greatly indebted to K.J. Hsu for his enthusiastic help and encouragement. Appreciation and thanks are also due to P.L. de Boer, T. de Mowbray, M.J. Visser, C. Siegenthaler, A. van Gelder, J.H. van den Berg, C. Laban, D.B. Smith, Sun Jiasong, Shi Siqi and many others for fruitful discussions and valuable suggestions. H. Dronkert helped with the Dutch translation of the summary.

The Bureau of Marine Geological Survey in the Ministry of Geology and Mineral Resources of China, the Ministry of Transport and Public Works of The Netherlands, and the Geological Survey of the Netherlands (Division of Marine Geology and Quaternary Geology) kindly offered me the opportunity to work in the East China Sea, in the Oosterschelde of SW Netherlands, and in the North Sea.

The research has been supported by the fellowship from the Ministry of Education and Science of The Netherlands, Sedimentology Consultants B.V., and International Geoservices B.V. of The Netherlands.

## Curriculum Vitae

- January 27, 1947      Born in Jiangsu, China
- 1964-1969:            study at the Department of Geology, Nanjing University, China
- 1969-1976:            field geological work in northern China
- 1976-1981:            work in marine geology and petroleum geology in China  
offshore areas at the Bureau of Marine Geological  
Survey, Ministry of Geology, China
- 1981-1984:            research in marine clastic sedimentation in Spain, SW  
Netherlands and the North Sea at the Sedimentology  
Division, Institute of Earth Sciences, State University  
of Utrecht, the Netherlands
- 1984-1987:            work in marine geology and shallow seismic survey in China  
offshore areas at the Bureau of Marine Geological  
Survey, Ministry of Geology and Mineral Resources,  
China
- 1987-1989:            work on Ph.D. program in the Netherlands